Development of Abdominal MRI at 7 Tesla.

by

Emma Doran, M.Sci

Thesis submitted to
The University of Nottingham
for the degree of
Doctor of Philosophy

4th May 2020

Contents

Acknowledgements **10**

Abstract **11**

List of Abbreviations **12**

1 General Introduction **16**

1.1 Historical Perspective 16

1.2 Existing Abdominal MRI Work at 7 T 17

1.3 Overview of Thesis 18

2 Theory **26**

2.1 Nuclear Magnetic Resonance 26

2.1.1 Nuclear Magnetisation 26

2.1.2 Precession in a Magnetic Field 27

2.1.3 Energy Quantization 29

2.1.4 Energy Level Populations 29

2.1.5 Excitation and Detection in NMR 32

2.1.5.1 RF Pulses 32

2.1.5.2 Signal Detection 34

2.1.5.3 Free Induction Decay 35

2.1.6 Relaxation 35

2.1.6.1 The Bloch Equations 35

2.1.6.2 Longitudinal Recovery 36

2.1.6.3 Measurement of T_1 Relaxation 36

2.1.6.4 Transverse Relaxation 37

2.1.6.5 Measurement of T_2 Relaxation 39

2.1.6.6 Measurement of T_2^* Relaxation 40

2.1.6.7 Correlation Time 40

2.1.7 Chemical Shift 41

2.1.8 Contrast in MRI 42
2.2 Magnetic Resonance Imaging 42
2.2.1 MR Encoding 42
2.2.1.1 Spatial Encoding using Gradients 42
2.2.1.2 Gradient Coils 43
2.2.1.3 Slice Selection 43
2.2.1.4 Frequency Encoding 46
2.2.1.5 Phase Encoding 49
2.2.1.6 k-Space 50
2.2.2 MR Imaging Sequences and Techniques 52
2.2.2.1 Spin Warp Imaging 52
2.2.2.2 Echo Planar Imaging 54
2.2.2.3 Fast Low Angle Shot Imaging 55
2.2.2.4 Parallel Imaging 57
2.2.3 Field Mapping 58
2.2.3.1 B_0 Mapping 59
2.2.3.2 B_1^+ Mapping 59
2.2.4 Dixon Method 59
2.3 Conclusion 60

3 Principles of 7 T Body Imaging 62
3.1 MRI at Ultra-High Field 62
3.2 Parallel Transmission 64
3.2.1 Static pTx 65
3.2.2 Dynamic pTx 66
3.2.3 Summary 67
3.3 Overview of Parallel Transmit System 69
3.3.1 Scanner Operation 69
3.3.2 Main Magnetic Field 69
3.3.3 Gradient and Shim Coils 70
3.3.4 RF Transmit Chain 71
3.4 RF Coil for 7 T Body Imaging 72

3.4.1 Transmit Phase Settings 72
3.4.2 Coil Scattering Matrix 74
3.4.3 Receive Coil Array 76
3.4.3.1 Investigation of Receive Coil Configurations . 76
3.5 RF Power Optimisation 79
3.6 SENSE for 7 T Body Imaging 80
3.7 Creating a 7 T Body Phantom 80
3.8 Specific Absorption Rate 83
3.9 RF Modelling 86
3.9.1 EM Simulations using FDTD 86
3.9.2 Local SAR Calculation 88
3.9.2.1 Q-Matrix Formalism 89
3.9.3 Effective Methods for Calculating Local SAR 90
3.9.3.1 Development Work 93
3.9.4 Virtual Observation Points 94
3.10 MR Safety at UHF 95
3.11 Discussion and Conclusion 99

4 B_1^+ Mapping for 7 T Body Imaging 111
4.1 Introduction 111
4.2 Background and Theory 111
4.2.1 Conventional Methods 112
4.2.1.1 VFA 112
4.2.1.2 AFI 116
4.2.1.3 DREAM 118
4.2.2 B_1^+ Mapping for pTx Systems 120
4.2.2.1 Linear Combination Approach 121
4.2.2.2 Relative B_1^+ Mapping 124
4.2.3 Advanced B_1^+ Mapping for pTx Systems 126
4.2.3.1 Multiple LFA-SPGR's for B_1^+ Mapping 126
4.2.3.2 B1TIAMO 127
4.2.4 Summary 128

4.3 Methods . . . 128
4.3.1 AFI . . . 128
4.3.1.1 Error Propagation . . . 128
4.3.1.2 AFI Reconstruction Comparisons . . . 128
4.3.1.3 AFI Spoiling . . . 129
4.3.2 DREAM . . . 130
4.3.2.1 Error Propagation . . . 130
4.3.2.2 DREAM Reconstruction Comparison . . . 130
4.3.3 Comparing VFA, AFI and DREAM . . . 131
4.3.4 Linearity of B_1^+ Response . . . 131
4.3.5 Single Channel versus Linear Combination B_1^+ Maps . . . 132
4.3.6 Adapting B_1^+ Mapping for Body Imaging . . . 132
4.3.6.1 Combining Different Transmit Phases . . . 133
4.3.6.2 Combining Different RF Powers . . . 134
4.4 Results . . . 135
4.4.1 AFI . . . 135
4.4.1.1 Error Propagation . . . 135
4.4.1.2 AFI Reconstruction Comparison . . . 136
4.4.1.3 AFI Spoiling . . . 136
4.4.2 DREAM . . . 138
4.4.2.1 Error Propagation . . . 138
4.4.2.2 DREAM Reconstruction Comparison . . . 138
4.4.3 Comparing VFA, AFI and DREAM . . . 140
4.4.4 Linearity of B_1^+ Response . . . 142
4.4.5 Single Channel versus Linear Combination B_1^+ Maps . . . 144
4.4.6 Adapting B_1^+ Mapping for Body Imaging . . . 145
4.4.6.1 Combining Different Transmit Phases . . . 149
4.4.6.2 Combining Different RF Powers . . . 150
4.5 Discussion . . . 151
4.5.1 AFI . . . 151
4.5.2 DREAM . . . 151

4.5.3 Comparing VFA, AFI and DREAM . . . 152
4.5.4 Linearity of B_1^+ Response . . . 152
4.5.5 Single Channel versus Linear Combination B_1^+ Maps . . 152
4.5.6 Adapting B_1^+ Mapping for Body Imaging . . . 153
4.5.6.1 Approaches for Combining B_1^+ Maps . . . 153
4.6 Conclusion . . . 154

5 Robust RF Modelling for Evaluation of 7 T Body Imaging 159
5.1 Introduction . . . 160
5.1.1 Outline . . . 164
5.2 Methods . . . 166
5.2.1 Simulations . . . 166
5.2.2 Data Processing . . . 167
5.2.3 Comparing Simulated and Experimental B_1^+ Distributions 167
5.2.4 Simplified Dipole Model Verification . . . 168
5.2.5 Development of Simplified Body Models . . . 171
5.2.5.1 Truncation . . . 171
5.2.5.2 Repeatability and Coil Model Position . . . 171
5.2.5.3 Reduced Tissue Complexity . . . 173
5.2.5.4 Automatic Segmentation . . . 173
5.2.6 Intra-subject Variability: Respiration Study . . . 175
5.2.7 Inter-subject Variability . . . 179
5.3 Results . . . 180
5.3.1 Comparing Simulated and Experimental B_1^+ Distributions 180
5.3.2 Simplified Dipole Model Verification . . . 181
5.3.3 Development of Simplified Body Models . . . 185
5.3.3.1 Truncation . . . 185
5.3.3.2 Repeatability and Coil Model Position . . . 187
5.3.3.3 Reduced Tissue Complexity . . . 192
5.3.3.4 Automatic Segmentation . . . 197
5.3.4 Intra-subject Variability: Respiration Study . . . 201
5.3.5 Inter-subject Variability . . . 207

5.4 Discussion 210
5.5 Conclusion 217

6 High Resolution MR Angiography for Imaging Small Vessels 223
6.1 Introduction 223
6.2 Clinical Applications 226
6.2.0.1 Kidney Function and Vasculature 226
6.2.0.2 Liver Function and Hepatic Vasculature 229
6.2.0.3 Blood Supply to the Lower Abdominal Wall . 230
6.3 Magnetic Resonance Angiography 233
6.3.1 Contrast vs. Non-Contrast Enhancement 233
6.3.2 Phase Contrast Angiography 234
6.3.3 Time-of-Flight (TOF) Angiography 236
6.3.4 Benefits of 7 T 239
6.3.5 Challenges at 7 T 240
6.3.6 Outline 240
6.4 Materials and Methods 241
6.4.1 Study Population 241
6.4.2 MRI and Coil System 241
6.4.3 Sequence Optimisation and Imaging 242
6.4.3.1 Development 242
6.4.3.2 Localiser Scans 247
6.4.3.3 B_0 and B_1^+ Mapping 248
6.4.3.4 B_1^+ Optimisation 249
6.4.3.5 Final Imaging Parameters 250
6.4.4 Qualitative and Quantitative Image Analysis 251
6.4.5 Assessment of Vessel Radii 252
6.4.6 Liver Angiography 254
6.4.7 Lower Abdominal Wall Angiography 255
6.5 Results 256
6.5.1 Localiser Scans 256
6.5.2 B_1^+ Optimisation 257

6.5.3 Qualitative image analysis . . . 258
6.5.4 Quantitative image analysis . . . 263
6.5.5 Assessment of Vessel Radii . . . 268
6.5.6 Liver Angiography . . . 270
6.5.7 Lower Abdominal Wall Angiography . . . 273
6.6 Discussion . . . 277
6.7 Conclusion . . . 280

7 T_2^*-Weighted Body MRI 290
7.1 Introduction . . . 290
7.2 Methods . . . 292
7.2.1 T_2^*-Weighted Imaging . . . 292
7.2.2 Fat-Water Imaging . . . 292
7.2.3 T_2^* measurements at 3 and 7 T . . . 293
7.2.3.1 Image Acquisition . . . 293
7.2.3.2 Data Analysis . . . 294
7.3 Results and Discussion . . . 295
7.3.1 T_2^*-Weighted Imaging . . . 295
7.3.2 Fat-Water Imaging . . . 298
7.3.3 T_2^* measurements at 3 and 7 T . . . 299
7.4 Conclusion . . . 302

8 Conclusion 309

A Error Propagation in AFI Sequence 312

"Study hard what interests you the most in the most undisciplined, irreverent and original manner possible." - *Richard Feynman*

Acknowledgements

First, I would like to thank my supervisors Professor Penny Gowland and Professor Sue Francis for their help, guidance and inspiration throughout my PhD. I am also extremely thankful for the valuable input from Paul Glover, Andrew Peters, Matthew Clemence, Steve Bawden and Oliver Mougin. Thank you all for your help and advice when I needed it.

Before I came to Nottingham everyone said that SPMIC was special, and it really is. The SPMIC has been like family. Lesley, your wee face at reception in the mornings kept me going every day. To all the other PhD students and post-docs, past and present; Andrew, Ben, Alex, Fed, Daisie, Lucrezia, Gill, Becky, Lauren, Elena, Laura, Jodi, Tommy, Henry, Gita, George O, George H, Jim, Andy, Simon, Chris B, Charlotte, Rich - I have so much respect for you all and think you are incredibly clever. It has been fun!

A special thank you to Christopher Mirfin for discovering the multix system with me and for the afternoon trips to Portland for coffee. Hannah Williams - you have been the best office/ISMRM buddy a PhD student could ask for. I have also loved being an exclusive Below the Neck member and hope that one day there will be a thriving Below the Neck, Above 3 T crew.

Thank you, Mum, Dad and Megan, for your love and support that lead me into this PhD and has enabled me to finish it. I am also extremely grateful to the rest of my family and all of my friends - I love you all.

Finally, thank you Chris, for sharing this crazy PhD journey with me and telling me that I'm a strong, independent, intelligent woman when I needed to hear it the most.

Abstract

This thesis covers the development of abdominal magnetic resonance imaging (MRI) at the ultra-high field (UHF) of 7 Tesla (7 T). The advantages and challenges of MR imaging at 7 T are introduced alongside an overview of a parallel transmit system and its associated applications. Methods for mapping the B_1^+ field are outlined with a focus on the further adaptations required to obtain accurate measurements at UHF.

Radio frequency (RF) safety is a major limiting factor for body imaging at 7 T as the higher frequency can result in increased RF power deposition and potentially dangerous temperature increases in biological tissue during imaging. This heating effect is quantified by specific absorption rate (SAR) and is particularly problematic for body MRI as traditional methods to mitigate risk result in longer scan times or the sacrifice of spatial resolution. It is important to have accurate SAR estimates to ensure subject safety and optimise imaging performance without being over conservative. This thesis aimed to address this by developing a pipeline for performing subject-specific local SAR simulations. Both intra- and inter- subject variability in peak local SAR was investigated to assess the safety factors in place for current average power limits and to inform future MR safety decisions for body imaging at 7 T.

Development work and initial body imaging studies are presented. This includes results from high resolution MR angiography of the kidneys, liver and abdominal wall. T_2^*-weighted images were also used to obtain T_2^* measurements in the kidneys, liver, adipose and muscle tissues together with fat-water images. Clinical applications of the developed imaging protocols and the techniques used to overcome the challenges encountered at 7 T are discussed throughout.

List of Abbreviations

AFI Actual Flip Angle Imaging.

AKI Acute Kidney Injury.

ARVD Atherosclerotic Renovascular Disease.

ASL Arterial Spin Labelling.

BMI Body Mass Index.

BOLD Blood Oxygen Level Dependent.

CKD Chronic Kidney Disease.

CLD Chronic Liver Disease.

CNR Contrast-to-Noise Ratio.

CT Computed Tomography.

CTA Computed Tomography Angiography.

DIEA Deep Inferior Epigastric Artery.

DIEP Deep Inferior Epigastric Perforator.

DREAM Dual Refocusing Echo Acquisition Mode.

EDT Euclidean Distance Transform.

EM Electromagnetic.

EPI Echo Planar Imaging.

ESKD End Stage Kidney Disease.

FDTD Finite-Difference Time-Domain.

FID Free Induction Decay.

FLASH Fast Low Angle Shot.

fMRI Functional Magnetic Resonance Imaging.

FOV Field of View.

FRE Flow Related Enhancement.

GFR Glomerular Filtration Rate.

GI Gastrointestinal.

GRE Gradient Recalled Echo.

HA Hepatic Arteries.

HV Hepatic Veins.

ISMRM International Society for Magnetic Resonance in Medicine.

IVC Inferior Vena Cava.

LFA Low Flip Angle.

MIP Maximum Intensity Projection.

MLE Maximum Likelihood Estimation.

MRA Magnetic Resonance Angiography.

MRI Magnetic Resonance Imaging.

MRS Magnetic Resonance Spectroscopy.

NMR Nuclear Magnetic Resonance.

PCA Phase Contrast Angiography.

PNS Peripheral Nerve Stimulation.

PO Power Optimisation.

PSD Phase Sensitive Detectors.

pTx Parallel Transmission Technology.

PV Portal Vein.

QBC Quadrature Body Coil.

RAD Renal Artery Disease.

RAS Renal Artery Stenosis.

RBF Renal Blood Flow.

RF Radiofrequency.

ROI Region of Interest.

SAR Specific Absorption Rate.

SE Spin-Echo.

SIEA Superficial Inferior Epigastric Artery.

SIEV Superficial Inferior Epigastric Vein.

SNR Signal-to-Noise Ratio.

SPGR Spoiled Gradient Echo.

SSFP Steady-State Free Precession.

STE Stimulated Echo.

STEAM Stimulated Echo Acquisition Mode.

TIAMO Time Interleaved Acquisition of Modes.

TOF Time-of-Flight.

UHF Ultra-High Field.

VFA Variable Flip Angle.

1 General Introduction

1.1 Historical Perspective

Magnetic Resonance Imaging (MRI) is a relatively recent addition to the world of medical physics. X-ray imaging was discovered and applied to the human body by Wilhelm Röntgen in 1895; ultrasound was first applied in the body for medical purposes by George Ludwig in the late 1940's, and Computed Tomography (CT) was conceived by Godfrey Hounsfield in 1967. MRI requires no ionising radiation, which can be a disadvantage of x-ray and CT, and produces sub-millimetre resolution images with high contrast that cannot be achieved with ultrasound. It provides a diverse range of contrast mechanisms and this allows for excellent soft tissue differentiation aiding diagnosis of disease and the understanding of anatomy and pathology in the human body.

MRI is the imaging application of the Nuclear Magnetic Resonance (NMR) method which can be dated back to 1938. This was when Rabi extended the Stern-Gerlach experiment (which had proved that angular momentum is quantized in 1922) and demonstrated that molecules could be made to emit radio waves at specific frequencies when in a magnetic field. Rabi was awarded the Nobel Prize in Physics for this work in 1944. Then, in 1952, Bloch and Purcell were awarded the Nobel Prize in Physics for NMR precision measurements in solids and liquids.

After several more fundamental advancements in the field of NMR, in 1971 Damadian discovered that biological tissues had different relaxation properties that could potentially be exploited to distinguish between cancerous and healthy tissues [1]. This was shortly followed in 1973 by the first use of NMR to perform imaging by Lauterbur [2] and the demonstration of the use of linear gradients to localise the NMR signal on a slice-by-slice basis by Mansfield [3]. By the end of the 1970's whole-body MR images could be acquired. The 2003 Nobel Prize in Physiology and Medicine was jointly awarded to Paul Lauterbur and Sir Peter

Mansfield for their discoveries concerning MRI.

MRI pulse sequence developments such as spin warp imaging in 1980 by Edelstein [4] and Echo Planar Imaging (EPI) by Mansfield [3] secured the continued clinical interest in the new medical technology. The advent of parallel imaging techniques such as SENSE in 1999 [5] and GRAPPA in 2002 [6] accelerated image acquisition and made whole-body MRI in the clinic possible [7].

Methods to exploit different contrast mechanisms have been developed for multiple clinical applications. Prominent techniques include fat-water imaging; developed by Dixon in 1984 [8], MR angiography; first described in 1985 [9], diffusion weighted imaging (DWI); established in 1985 [10], BOLD Functional Magnetic Resonance Imaging (fMRI); reported in 1992 [11] and Chemical Exchange Dependent Saturation Transfer (CEST); demonstrated in 2000 [12]. All of these methods have allowed MRI to provide quantitative evaluation of biological function at macroscopic, microscopic and molecular scales.

Key advancements in engineering include the introduction of superconducting magnets; these enabled MR scanners to be produced with higher, more homogenous magnetic fields [13]. Since then, more sophisticated magnets have been refined and shielding and magnetic gradient performance has improved. All this, together with novel RF applications, has pushed MRI to increasingly high magnetic field strengths.

1.2 Existing Abdominal MRI Work at 7 T

Research on 7 T MR systems originally focused on neurological and musculoskeletal imaging [14] making significant diagnostic advancements in medicine and psychology [15, 16]. Research and development have been focused on improving the homogeneity of the excitation field to decrease artefacts experienced at Ultra-High Field (UHF). This has made it possible to consider imaging over larger fields of view, paving the way for body imaging research at 7 T.

As with the progression from 1.5 to 3 T [17], moving whole-body in vivo research

from 3 to 7 T has required investigation of the safety implications and overall benefits of imaging the body at higher field strengths [18]. Preliminary imaging carried out by Metzger et al. in 2008 displayed the use of novel RF methods to image the prostate [19]. In 2009, Vaughn et al. and Snyder et al. published preliminary results from abdominal, thorax, cardiac and breast imaging [20] [21]. Following on from their initial work, Metzger et al. published results from non-contrast renal angiography [22] demonstrating superior images to contrast enhanced images at lower field strengths. Wu et al. published 7 T liver images in 2011 and addressed the challenges of imaging large organs using RF pulse design to improve uniform excitation [23]. Despite the technical challenges of imaging the body at 7 T, these results showed the potential for gaining additional clinical insight compared to 3 T data.

Advanced coil design and RF engineering concepts have been applied to enable imaging of the whole body, spine and hip joints [24–26], pelvis [27], uterus and rectum [28], heart [29, 30], liver [31–33] and breast [34]. Orzada et al. adopted an alternative image reconstruction approach to mitigate the inhomogeneity in 7 T body images and have demonstrated the advantages of this approach by imaging the liver [35].

7 T systems are now widely available internationally and were recently given FDA approval to be used clinically for imaging the head and extremities to provide diagnostic information that cannot be obtained or made available at 3 T. This demonstrates the potential advantages for using 7 T systems as a diagnostic tool for abdominal applications.

1.3 Overview of Thesis

The work in this thesis describes the development of abdominal imaging on a Philips 7 T Achieva Multi-Transmit MR system. The following section outlines the material covered in the remainder of this thesis.

Chapter 2 outlines the basic principles of NMR and describes the necessary

background theory regarding spatial encoding, imaging sequences and imaging techniques that underlie MRI.

Chapter 3 introduces concepts relevant to MRI in the context of UHF. This includes the effect of the high magnetic field on relaxation mechanisms, the advantages and disadvantages of imaging at 7 T and techniques developed to overcome technical challenges. Parallel transmission technology (pTx) is introduced and the differences between static and dynamic approaches are explained. An overview of a parallel transmit MR system is given and includes an outline of basic scanner operation and the hardware and software referenced throughout this thesis.

The RF coil used for body imaging at 7 T is described providing details about the transmit and receive modes of the coil and an investigation of the available receive coil configurations is presented. The adaptations to RF power optimisation and SENSE methods that are required for 7 T body imaging are summarised followed by the process used to construct a 7 T body phantom that was used for calibration methods and assessing MR sequence development. Safety considerations of 7 T MRI are explained, starting with the definition of Specific Absorption Rate (SAR). RF modelling concepts including electromagnetic simulations using numerical methods and calculation of local SAR are covered and include an investigation into an effective method for averaging SAR. Other safety considerations concerning 7 T MRI are also discussed.

Chapter 4 gives an overview of B_1^+ mapping techniques that are employed on conventional and pTx systems. This includes descriptions of the variable flip angle (VFA), actual flip angle imaging (AFI) and dual refocusing echo acquisition mode (DREAM) methods; linear combination and relative B_1^+ mapping approaches; and additional techniques developed to improve the acquisition of B_1^+ information for pTx and 7 T body imaging applications. The work performed to validate and develop B_1^+ mapping in the body at 7 T is presented and methods are proposed that have the potential to address the difficulties outlined.

Chapter 5 covers RF modelling work performed for the evaluation of 7 T body imaging. This involves the study of the variation in peak local SAR values in a library of subject-specific body models. The underlying investigations required to carry out this analysis are presented extensively in this chapter and include the following sections; the comparison of simulated and experimental B_1^+ distributions, the creation and validation of a simplified RF coil model, the development of simplified subject-specific models and a study into intra-subject variability with respect to changes induced in local SAR and B_1^+ during respiration.

Chapter 6 outlines a high resolution, multi-echo, time-of-flight MR angiography study in the kidneys, liver and abdominal wall of healthy subjects. The concept of non-contrast MRA is described along with phase contrast angiography (PCA) and time-of-flight (TOF) techniques. The advantages and challenges of MRA at 7 T are discussed and initial PCA results in the liver are presented.

Chapter 7 presents preliminary quantitative abdominal imaging results which include T_2^* measurements in abdominal tissues. Related results comprised of fat-water images together with interesting anatomical findings in T_2^* weighted images are also shown.

Chapter 8 concludes with an overview of the work in this thesis. An outline of the future directions for B_1^+ mapping and local SAR modelling are suggested and how the MRI methods developed in healthy volunteers could be applied in 7 T patient body imaging studies.

References

[1] R Damadian. Tumor Detection by Nuclear Magnetic Resonance. *Science*, 147(3659):738–739, 1971.

[2] P. C. Lauterbur. Image Formation by Induced Local Interactions: Examples Employing Nuclear Magnetic Resonance. *Nature*, 242:190–191, 1973.

[3] P Mansfield. Multi-planar image formation using NMR spin echoes. Technical report, 1977.

[4] W A Edelstein, J M S Hutchinson, G Johnson, and T Redpath. Spin warp NMR imaging and applications to human whole-body imaging. Technical report, 1980.

[5] Klaas P. Pruessmann, Markus Weiger, Markus B. Scheidegger, and Peter Boesiger. SENSE: Sensitivity encoding for fast MRI. *Magnetic Resonance in Medicine*, 42(5):952–962, 1999.

[6] Mark A. Griswold, Peter M. Jakob, Robin M. Heidemann, Mathias Nittka, Vladimir Jellus, Jianmin Wang, Berthold Kiefer, and Axel Haase. Generalized Autocalibrating Partially Parallel Acquisitions (GRAPPA). *Magnetic Resonance in Medicine*, 47(6):1202–1210, 2002.

[7] Anagha Deshmane, Vikas Gulani, Mark A Griswold, and Nicole Seiberlich. Review: MR Physics for Clinicians Parallel MR Imaging. *Journal of Magnetic Resonance Imaging*, 36:55–72, 2012.

[8] W Dixon, Thomas. Simple Proton Spectroscopic Imaging. *Radiology*, 153:189–194, 1984.

[9] J. R. Singer and L. E. Crooks. Nuclear magnetic resonance blood flow measurements in the human brain. *Science*, 221(4611):654–656, 1983.

[10] John Lygouras, Vassilis Kodogiannis, Theodoros Pachidis, and Panagiotis Liatsis. Terrain-based navigation for underwater vehicles using an ultrasonic scanning system. Technical Report 11, 2008.

[11] S Ogawa, D W Tank, R Menon, J M Ellermann, S Kim, H Merkle, and K Ugurbil. Intrinsic Signal Changes Accompanying Sensory Stimulation: Functional Brain Mapping with Magnetic Resonance Imaging. *Proc Natl Acad Sci USA*, 89(13):5951–5, 1992.

[12] K.M Ward, A.H Aletras, and R.S Balaban. A New Class of Contrast Agents for MRI Based on Proton Chemical Exchange Dependent Saturation Transfer (CEST). *Journal of Magnetic Resonance*, 143(1):79–87, 2000.

[13] R J Alfidi, J R Haaga, S J El-Yousef, P J Bryan, B D Fletcher, J P LiPuma, S C Morrison, B Kaufman, J B Richey, W S Hinshaw, D M Kramer, H N Yeung, A M Cohen, H E Butler, A E Ament, and J M Lieberman. Preliminary experimental results in humans and animals with a superconducting, whole-body, nuclear magnetic resonance scanner. *Radiology*, 143(1):175–81, 1982.

[14] J.T. Vaughan, M. Garwood, C.M. Collins, W. Liu, L. DelaBarre, G. Adriany, P. Andersen, H. Merkle, R. Goebel, M.B. Smith, and K. Ugurbil. 7T vs. 4T: RF power, homogeneity, and signal-to-noise comparison in head images. *Magnetic Resonance in Medicine*, 46(1):24–30, 2001.

[15] Hyeong Cheol Moon, Hyeon-Man Baek, and Young Seok Park. Comparison of 3 and 7 Tesla Magnetic Resonance Imaging of Obstructive Hydrocephalus Caused by Tectal Glioma. *Brain tumor research and treatment*, 4(2):150–154, 2016.

[16] Siegfried Trattnig, Elisabeth Springer, Wolfgang Bogner, Gilbert Hangel, Bernhard Strasser, Barbara Dymerska, Pedro Lima Cardoso, and Simon Daniel Robinson. Key clinical benefits of neuroimaging at 7 T. *NeuroImage*, 168:477–489, 2018.

[17] Fritz Schick. Whole-body MRI at high field: Technical limits and clinical potential. *European Radiology*, 15(5):946–959, 2005.

[18] Christopher M. Collins and Michael B. Smith. Calculations ofB1 distribution, SNR, and SAR for a surface coil adjacent to an anatomically-accurate human body model. *Magnetic Resonance in Medicine*, 45(4):692–699, 2001.

[19] Gregory J. Metzger, Carl Snyder, Can Akgun, Tommy Vaughan, Kamil Ugurbil, and Pierre Francois Van De Moortele. Local B1+ shimming for prostate imaging with transceiver arrays at 7T based on subject-dependent transmit phase measurements. *Magnetic Resonance in Medicine*, 59(2):396–409, 2008.

[20] J. Thomas Vaughan, Carl J. Snyder, Lance J. Delabarre, Patrick J. Bolan, Jinfeng Tian, Lizann Bolinger, Gregor Adriany, Peter Andersen, John Strupp, and Kamil Ugurbil. Whole-body imaging at 7T: Preliminary results. *Magnetic Resonance in Medicine*, 61(1):244–248, 2009.

[21] C J Snyder, L DelaBarre, G J Metzger, P-F van de Moortele, C Akgun, K Ugurbil, and J T Vaughan. Initial results of cardiac imaging at 7 Tesla. *Magnetic resonance in medicine*, 61(3):517–24, 2009.

[22] Gregory J Metzger and Pierre-François Van de Moortele. Non-Contrast Enhanced Renal MRA at 7T. *Magnetic Resonance in Medicine*, 19(4):7–9, 2011.

[23] X. Wu, S. Schmitter, E. J. Auerbach, J. Pfeuffer, M. Hamm, K. Ugerbil, and P-F. Van de Moortele. Parallel Transmission in Liver MRI at 7T: Initial Results. *Proc Intl Soc Mag Reson Med*, 19:2940, 2011.

[24] J. Ellermann, U. Goerke, P. Morgan, K. Ugurbil, J. Tian, S. Schmitter, T. Vaughan, and P. F. Van De Moortele. Simultaneous bilateral hip joint imaging at 7 Tesla using fast transmit B1 shimming methods

and multichannel transmission - a feasibility study. *NMR in Biomedicine*, 25(10):1202–1208, 2012.

[25] Cem Murat Deniz, Ryan Brown, Riccardo Lattanzi, Leeor Alon, Daniel K. Sodickson, and Yudong Zhu. Maximum Efficiency RF Shimming: Theory and Initial Application for Hip Imaging at 7 Tesla. *Magn Reson Med.*, 69(5):1379–1388, 2013.

[26] Oliver Kraff, Andrea Lazik-Palm, Rahel Heule, Jens M. Theysohn, Oliver Bieri, and Harald H. Quick. 7 Tesla quantitative hip MRI: a comparison between TESS and CPMG for T2 mapping. *Magnetic Resonance Materials in Physics, Biology and Medicine*, 29(3):503–512, 2016.

[27] Lale Umutlu, Oliver Kraff, Anja Fischer, Sonja Kinner, Stefan Maderwald, Kai Nassenstein, Felix Nensa, Johannes Grüneisen, Stephan Orzada, Andreas K. Bitz, Michael Forsting, Mark E. Ladd, and Thomas C. Lauenstein. Seven-Tesla MRI of the female pelvis. *European Radiology*, 23(9):2364–2373, 2013.

[28] I.M.L. van Kalleveen, J.P. Hoogendam, A.J.E. Raaijmakers, F. Visser, C.S. Arteaga de Castro, R.H.M. Verheijen, P.R. Luijten, R.P. Zweemer, W.B. Veldhuis, and D.W.J. Klomp. Boosting the SNR by adding a receive-only endorectal monopole to an external antenna array for high-resolution,T2-weighted imaging of early-stage cervical cancer with 7-T MRI. *NMR in Biomedicine*, 2017.

[29] Sebastian Schmitter, Lance Delabarre, Xiaoping Wu, Andreas Greiser, Dingxin Wang, Edward J. Auerbach, J. Thomas Vaughan, Kâmil Uğurbil, and Pierre François Van De Moortele. Cardiac imaging at 7 tesla: Single- and two-spoke radiofrequency pulse design with 16-channel parallel excitation. *Magnetic Resonance in Medicine*, 70(5):1210–1219, 2013.

[30] Graeme A. Keith, Christopher T. Rodgers, Aaron T. Hess, Carl J. Snyder, J. Thomas Vaughan, and Matthew D. Robson. Automated tuning

of an eight-channel cardiac transceive array at 7 Tesla using piezoelectric actuators. *Magnetic Resonance in Medicine*, 73(6):2390–2397, 2015.

[31] Lale Umutlu, Andreas K. Bitz, Stefan Maderwald, Stephan Orzada, Sonja Kinner, Oliver Kraff, Irina Brote, Susanne C. Ladd, Tobias Schroeder, Michael Forsting, Gerald Antoch, Mark E. Ladd, Harald H. Quick, and Thomas C. Lauenstein. Contrast-enhanced ultra-high-field liver MRI: A feasibility trial. *European Journal of Radiology*, 82(5):760–767, 2013.

[32] Xiaoping Wu, Sebastian Schmitter, Edward J Auerbach, U Kâmil, and Pierre-françois Van De Moortele. Mitigating transmit B1 inhomogeneity in the liver at 7T using multi- spoke parallel transmit RF pulse design. *Quant Imaging Med Surg*, 4(1):4–10, 2014.

[33] Anja Fischer, Oliver Kraff, Stefan Maderwald, Karsten Beiderwellen, Mark E. Ladd, Michael Forsting, Thomas C. Lauenstein, and Lale Umutlu. Non-enhanced T1-weighted liver vessel imaging at 7 Tesla. *PLoS ONE*, 9(6):1–9, 2014.

[34] Mary Preston McDougall, Sergey Cheshkov, Joseph Rispoli, Craig Malloy, Ivan Dimitrov, and Steven M. Wright. Quadrature transmit coil for breast imaging at 7 tesla using forced current excitation for improved homogeneity. *Journal of Magnetic Resonance Imaging*, 40(5):1165–1173, 2014.

[35] Stephan Orzada, Stefan Maderwald, Benedikt Andreas Poser, Andreas K. Bitz, Harald H. Quick, and Mark E. Ladd. RF excitation using Time Interleaved Acquisition of Modes (TIAMO) to address B1 inhomogeneity in high-field MRI. *Magnetic Resonance in Medicine*, 2010.

2 Theory

The following chapter will outline the basic principles behind Nuclear Magnetic Resonance (NMR) and describe the fundamental concepts of Magnetic Resonance Imaging (MRI) that are referenced throughout this thesis.

2.1 Nuclear Magnetic Resonance

2.1.1 Nuclear Magnetisation

NMR is the physical process that describes the behaviour of atomic nuclei when exposed to an external magnetic field. Nuclei which contain an odd number of protons or neutrons, possess intrinsic spin angular momentum $\mathbf{J}$ with magnitude

$$|\mathbf{J}| = \hbar\sqrt{\mathbf{I}(\mathbf{I}+1)} \tag{2.1}$$

where $\mathbf{I}$ is the dimensionless spin quantum number and $\hbar$ is the reduced Planck's constant. The nuclei are charged and so are also associated with a magnetic moment μ through the following relation:

$$\mu = \gamma\mathbf{J} \tag{2.2}$$

The gyromagnetic ratio, γ, is a constant that varies with atomic species. For the hydrogen proton (^{1}H), $\gamma = 42.58$ MHz/T. As γ is positive, μ is parallel to the spin angular momentum. ^{1}H is the most abundant nucleus in organic tissues and generates the greatest NMR signal; for this reason, MRI is based on proton imaging. Therefore, ^{1}H will be the focus for the theory outlined in the following sections.

2.1.2 Precession in a Magnetic Field

A spinning proton with rotating charge can be modelled as a dipole which produces a magnetic field as shown in Figure 2.1. When a dipole is placed into a magnetic field its magnetic moment, μ, experiences a turning force called torque, τ, which tries to align it with the applied field.

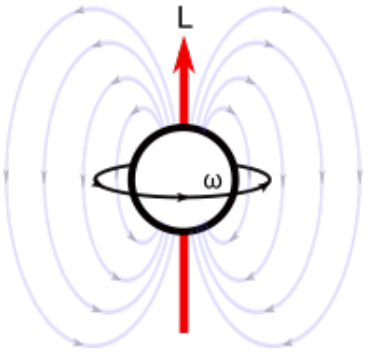


Figure 2.1: A spinning proton rotating with frequency ω and angular momentum L produces a magnetic field. The magnetic moment of the proton is in the same direction as the angular momentum.

When subjected to a magnetic field, $\mathbf{B}$, as the proton is spinning, it undergoes precession which is analogous to the gyroscope effect demonstrated in Figure 2.2. The torque experienced by the proton is:

$$\tau = \mu \times \mathbf{B} \tag{2.3}$$

In classical mechanics, the change in intrinsic spin angular momentum, $\frac{d\mathbf{J}}{dt}$, can also be used to describe torque. Torque is perpendicular to μ and B_0 (and also $\mathbf{J}$ since μ is parallel to $\mathbf{J}$). As $\frac{d\mathbf{J}}{dt}$ is perpendicular to $\mathbf{J}$, it undergoes precession.

$$\tau = \frac{d\mathbf{J}}{dt} = \mu \times \mathbf{B} = \gamma \mathbf{J} \times \mathbf{B} = \gamma \mathbf{J} B sin\theta \tag{2.4}$$

Precession is maintained without loss or gain of energy as long as $\mathbf{B}$ is contin-

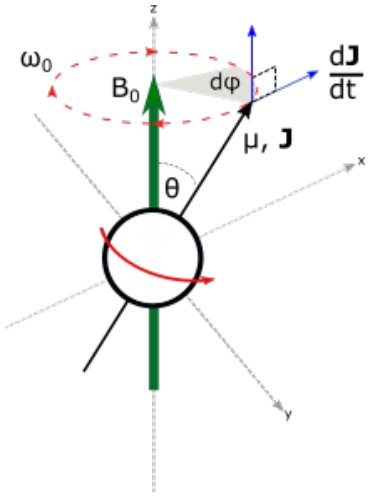


Figure 2.2: Geometry of precession.

uously applied. The geometry in Figure 2.2 shows that:

$$d\mathbf{J} = \mathbf{J}sin\theta d\phi \tag{2.5}$$

The angular frequency of precession is given as the change in ϕ:

$$\omega = \frac{d\phi}{dt} \tag{2.6}$$

By combining Equations 2.4, 2.5 and 2.6 an expression for the Larmor frequency, ω_0 is obtained:

$$\omega_0 = \gamma B \tag{2.7}$$

This frequency is directly proportional to the magnetic field strength and is explained in more detail in subsequent sections.

2.1.3 Energy Quantization

In quantum mechanics a magnetic dipole moment, μ, has a restricted number of orientations defined by the spin quantum number, m_l. The number of possible orientations that correspond to different states is given by $(2\mathbf{I}+1)$. For protons, $\mathbf{I}=\frac{1}{2}$ and so two different possible spin states exist, $m_l=+\frac{1}{2}$ ("spin-up") and $m_l=-\frac{1}{2}$ ("spin-down").

This gives rise to two angular momentum states:

$$\mu = \pm\frac{\gamma\hbar}{2}\hat{z} \tag{2.8}$$

The potential energy of a magnetic dipole in the presence of a static magnetic field with strength B_0 directed along the z direction is the work done rotating the dipole within that field:

$$E = -\mu\cdot\mathbf{B} = -\mu_z B_0 = -\gamma\hbar m_l B_0 \tag{2.9}$$

As $m_l=\pm\frac{1}{2}$, two energy levels exist for protons corresponding to the two spin states that are created when B_0 is applied (this is called the Zeeman effect). These states have energies equal to:

$$E_\pm = \pm\gamma\hbar\frac{B_0}{2} \tag{2.10}$$

The difference in energy between these two levels, ΔE, is equal to hν. Transitions between these energy levels occur when radiation with frequency ν is applied.

2.1.4 Energy Level Populations

Thermal fluctuations mean that spins do not always exist in the lower energy state. At thermal equilibrium there is a net difference in the population of spins

split between the two energy levels. The Boltzmann distribution characterises the number of spins expected in each spin-up (N^+) or -down (N^-) configuration and depends on the difference in energy between the two levels (ΔE), Boltzmann's constant (k_B) and temperature (T):

$$\frac{N^+}{N^-} = exp\Big[\frac{\Delta E}{k_B T}\Big] \tag{2.11}$$

As $\Delta E << k_B$, the population difference is low, and the Boltzmann distribution can be approximated to

$$\frac{N^+}{N^-} \approx 1 + \frac{\Delta E}{k_B T} \tag{2.12}$$

Combining Equations 2.12 and 2.10 gives

$$N^+ - N^- = N^- \frac{\gamma \hbar B_0}{k_B T} \tag{2.13}$$

If the population difference, n, is very small N^- can be approximated to $\frac{N}{2}$ where N is the total number of spins. The expression for population difference then becomes

$$n = N^+ - N^- = N \frac{\gamma \hbar B_0}{2 k_B T} \tag{2.14}$$

When electromagnetic radiation is applied at the Larmor frequency, ω_0, protons transition between the spin-up and spin-down states. Increasing the static magnetic field, B_0, will increase the population difference between the energy levels (by increasing ΔE, see Figure 2.3) and increase the sensitivity of NMR measurements. Decreasing the temperature T will also have a similar effect.

When B_0 is applied proton spins precess with random phase, with an excess of spins in the spin-up state (lower energy state). The population difference leads to generation of net magnetisation, M_0, parallel to B_0 (in the z direction) and

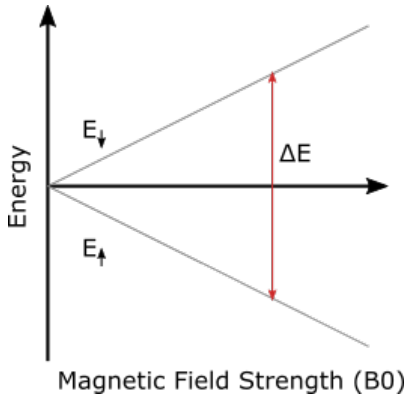


Figure 2.3: Energy difference between spin up and spin down states as a function of magnetic field strength, B_0.

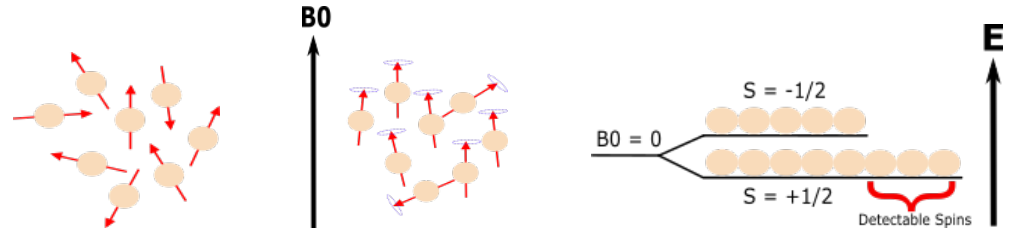
is given by the sum of all the magnetic moments produced by all the spins in the system

$$M_0 = \sum_{n=1}^{N} \mu_z \tag{2.15}$$

Spin up and down states cancel each other out and so it is only the population difference that contributes towards the net magnetisation:

$$M_0 = n\mu_z = N\frac{\gamma^2\hbar^2 B_0}{4k_B T}\hat{z} \tag{2.16}$$

Net magnetisation (or bulk magnetisation) is the concept that explains NMR on a macroscopic scale. The concepts outlined in this section are demonstrated in Figure 2.4.



(a) No external magnetic field applied. Net magnetisation is zero.

(b) External magnetic field, B_0, applied. Net magnetisation $= M_0$. Spins favour the lower energy state of being aligned with B_0.

(c) Population difference between spin-up and spin-down energy states induced by B_0. The excess spins in the lower energy state contribute to the net magnetisation that can be detected.

Figure 2.4: Behaviour of ^{1}H protons in an external magnetic field, B_0.

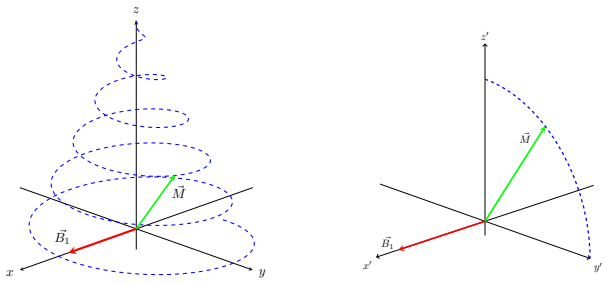
2.1.5 Excitation and Detection in NMR

2.1.5.1 RF Pulses

An additional magnetic field is used to induce transitions between the Zeeman energy levels. This magnetic field is known as $\mathbf{B_1}$ and oscillates at frequency ω_1 close to the Larmor frequency. This ensures that it is synchronised with the precessing spins so that the transfer of energy to the system is maximally efficient. Typically, these frequencies are in the RF range and so $\mathbf{B_1}$ is also referred to as the RF field.

It is easiest to consider RF pulses in a rotating frame of reference. The lab frame is defined with x, y and z coordinates and the $\mathbf{B_1}$ field and spins are rotating around z. In the rotating frame, coordinates defined by x', y' and z' rotate at frequency ω_1 so the $\mathbf{B_1}$ field and spins appear static.

An imaginary field is applied with amplitude ω_1/γ that cancels the precessional motion. As long as $\omega_1 \approx \omega_0$, B_0 transforms approximately to zero and the effect from the main magnetic field disappears. Therefore, the only magnetic field acting is the static $\mathbf{B_1}$ field. The magnetisation, $\mathbf{M}$, now precesses around $\mathbf{B_1}$ in a process called nutation. This is demonstrated in Figure 2.5.



(a) (b)

Figure 2.5: The evolution of net magnetisation $\mathbf{M}$ after the application of an on-resonance RF pulse in the (a) laboratory frame and (b) rotating frame of reference.

The $\mathbf{B_1}$ field is circularly polarised and applied perpendicular to B_0. The $+\omega_1$ component appears static in the rotating frame of reference, whereas the -ω_1 component appears to rotate at -2ω_1. Therefore, only B_1^+ is effective in inducing precession [1, 2]. In summary; considering a $\mathbf{B_1}$ field applied along the x axis, the magnetisation precesses around $\mathbf{B_1}$ and the net magnetisation rotates in the y', z' plane (see Figure 2.5 (b)).

The duration and amplitude of an RF pulse controls the amount that the net magnetisation rotates. This effect is known as tipping and the angle through which the magnetisation is rotated is called the flip angle, α. The flip angle produced depends on the integral of the gyromagnetic ratio, γ and the RF modulation envelope, $B_1(t)$, calculated over the duration of the RF pulse, t_p:

$$\alpha = \gamma \int_{t=0}^{t=t_p} B_1(t)dt \tag{2.17}$$

Conventionally, RF pulses are referred to by the angle through which they rotate $\mathbf{M}$. A 180° pulse tips the magnetisation, originally orientated along +z, along -z so that it is inverted. A 90° pulse tips the magnetisation into the transverse plane where the magnetisation is said to be excited or saturated.

The RF pulses are produced by RF transmit coils which are tuned to the required

resonant frequency. These can be located either within the inner walls of the scanner or as free-standing devices placed on the patient, connected by cables to the scanner. Further details about the RF transmit chain are covered in the Chapter 3.

2.1.5.2 Signal Detection

By the end of the application of a 90° RF pulse, the net magnetisation is tipped into the transverse plane, all the spins are in phase and there is no net population difference. When the RF pulse is turned off, the transverse magnetisation created, M_{xy}, starts to precess about B_0 at the Larmor frequency.

The rotating M_{xy} magnetisation is responsible for generating the NMR signal through Faraday's Law of Induction by inducing an oscillating voltage that causes current to flow in a pick-up coil that is tuned to RF frequencies (see Figure 2.6). The induced voltage is the NMR signal and is detected via a process called phase sensitive detection.

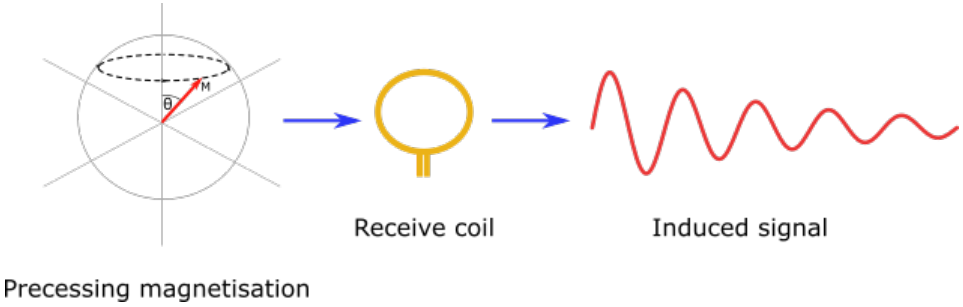


Figure 2.6: MR signal detection: precessing magnetisation induces a current in a receive coil that creates a FID signal.

The NMR signal is also an RF signal, just like the excitation pulse. However, the excitation pulse is many magnitudes greater than the induced signal. To avoid the RF pulse damaging the receiver, the signal detection hardware is gated off during the RF pulse.

2.1.5.3 Free Induction Decay

The NMR signal generated by a single RF pulse is a free induction decay (FID). This is a damped oscillatory signal recorded when the net magnetisation is tipped into the transverse plane. The signal decays exponentially due to interactions between individual spins and their surrounding environments.

2.1.6 Relaxation

As the NMR signal decreases over time, energy is released, and the magnetisation $\mathbf{M}$ returns to thermal equilibrium (parallel to B_0) with a magnitude equal to M_0. This process is called relaxation and is the phenomenon that gives rise to the contrast generated in MR images.

2.1.6.1 The Bloch Equations

The rate of change of magnetisation (with components M_x, M_y and M_z) due to the magnetic field $\mathbf{B(t)}$, was originally described by Bloch as

$$\frac{d\mathbf{M}}{dt} = \gamma|\mathbf{M} \times \mathbf{B}| \tag{2.18}$$

This can be extended to characterise the relaxation process, in the rotating frame, using two time constants, T_1 and T_2.

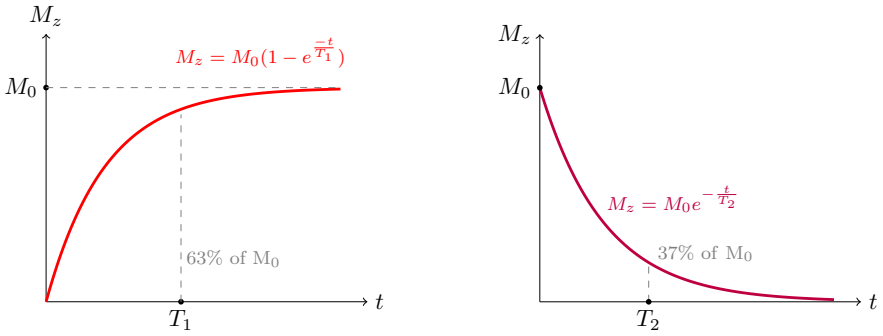
$$\frac{d\mathbf{M}}{dt} = \gamma(\mathbf{M} \times \mathbf{B}) - \frac{M_x}{T_2}\hat{x} - \frac{M_y}{T_2}\hat{y} - \frac{(M_z - M_0)}{T_1}\hat{z} \tag{2.19}$$

These are empirical equations that describe the magnetisation of a spin system over time during relaxation which is determined by various physical processes.

2.1.6.2 Longitudinal Recovery

The process through which the spin system returns to equilibrium after absorbing RF energy from the application of the RF pulse is called longitudinal recovery and is described by the relaxation time constant T_1. T_1 is a measure of the time that it takes for the net magnetisation to grow to (1 - 1/e), $\sim$ 63 %, of M_0.

This involves relaxing spins transferring heat energy to the surrounding environment and returning $\mathbf{M}$ to the lower energy state parallel to B_0. For this reason, the longitudinal recovery mechanism is also called spin-lattice, thermal or T_1 relaxation. A T_1 recovery curve is demonstrated in Figure 2.7 (a).



(a) (b)

Figure 2.7: (a) T_1 Recovery and (b) T_2 Decay Curves.

2.1.6.3 Measurement of T_1 Relaxation

The recovery of the longitudinal magnetisation $M_z(t)$ after an RF pulse can be described by solving Equation 2.19 to obtain the following expression:

$$M_z(t) = M_0\Big[1 - exp\Big(-\frac{t}{T_1}\Big)\Big] + M_z(0)exp\Big(-\frac{t}{T_1}\Big) \tag{2.20}$$

where $M_z(0)$ is the longitudinal magnetisation at t = 0. In a saturation recovery

experiment, a 90° RF pulse is used to tip the magnetisation into the xy plane. Here, at t = 0, $M_z(0) = 0$ and therefore the equation above can be simplified to:

$$M_z(t) = M_0[1 - exp(-\frac{t}{T_1})] \tag{2.21}$$

Usually, an inversion recovery experiment is used for measuring T_1. A 180° RF pulse fully inverts the magnetisation to -M_z before returning to M_0 with time constant T_1. After a specified time TI (inversion time) a 90° RF pulse is applied to flip longitudinal magnetisation into the transverse plane to create signal. In this case the boundary conditions assume that $M_z(0)$ = -M_0 and that at TI time later the longitudinal magnetisation has recovered to an arbitrary value of $M_z(t)$. Equation 2.20 can then be simplified to:

$$M_z(t) = M_0[1 - 2exp(-\frac{t}{T_1})] \tag{2.22}$$

The signal depends on the size of M_z prior to the 90° pulse. To fully characterise T_1, TI is varied and multiple measurements are made to sample M_z during the full recovery of longitudinal magnetisation. An example of a T_1 inversion recovery curve is shown in Figure 2.8.

2.1.6.4 Transverse Relaxation

Once the spins have been tipped into the transverse plane, they precess around the z-axis at the Larmor frequency. Changes in the local magnetic fields alter the precession frequencies of individual spins causing the spins lose their overall phase coherence and to fan out as demonstrated in Figure 2.9. It is this dephasing of the spins in the xy-plane that causes transverse relaxation. The contribution to the decay of the NMR signal is modelled as an exponential decay with time constant T_2.

In real systems the observed T_2 decay is quicker than predicted due to additional

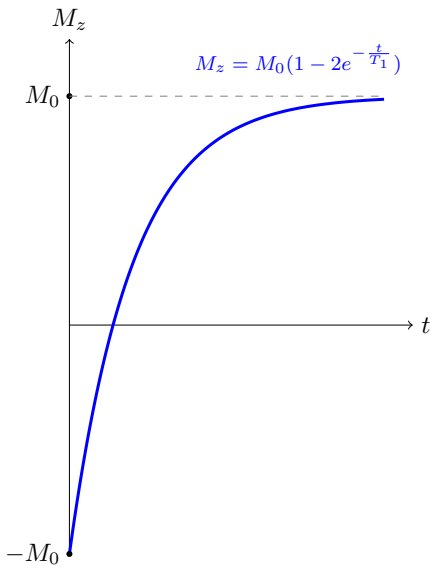


Figure 2.8: Example of T_1 Inversion Recovery Curve

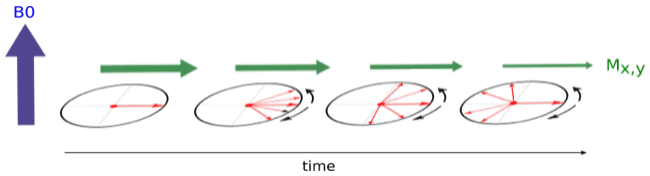


Figure 2.9: T_2 relaxation: loss of phase coherence and decay of transverse magnetisation, M_{xy}.

dephasing effects from local field inhomogeneities. Therefore, the observed decay is described by the time constant T_2^*. The T_2^* decay results from additional static B_0 inhomogeneities caused by underlying imperfections in the magnet or changes in magnetic susceptibility that induce a variation in the applied field. The relaxation time associated with the additional dephasing effects due to static field inhomogeneities is T_2'. The T_2' processes do not vary with time and so it is possible to rephase these effects. However, true T_2 processes cannot be rephased as they are related to time-varying effects (such as spin exchange or moving spins). The relationship between true T_2, observed T_2^* and T_2' is

$$\frac{1}{T_2^*} = \frac{1}{T_2} + \frac{1}{T_2'} \tag{2.23}$$

2.1.6.5 Measurement of T_2 Relaxation

In order to measure T_2, the static field inhomogeneity effects, T_2', need to be eliminated. This can be achieved by using a spin-echo sequence to refocus the additional dephasing allowing for the quantitative measurement of T_2.

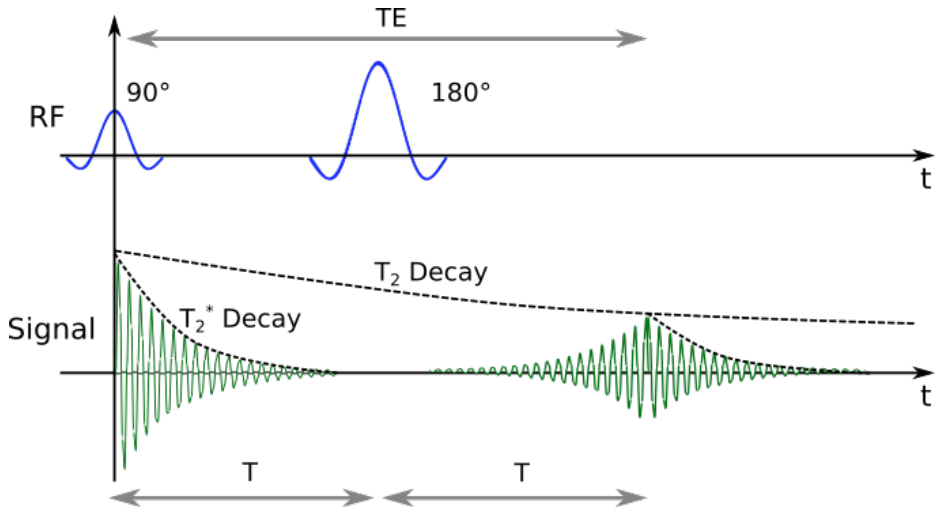


Figure 2.10: Spin echo sequence: a spin echo is created by two RF pulses. The first 90° RF pulse generates an FID, while the second 180° pulse generates the spin echo. The echo time (TE) is twice the interval between these two pulses.

Figure 2.10 displays a spin-echo sequence; at t = 0 a 90° RF pulse creates M_{xy} and all spins are in-phase. Inhomogeneities in the B_0 field mean that spins exposed to a higher magnetic field precess faster than the Larmor frequency whereas spins in lower magnetic fields precess slower than the Larmor frequency. This results in the spins fanning out and losing their phase coherence (see Figure 2.11).

At time t = T later each spin has accrued a phase shift of ϕ and a 180° refocusing RF pulse is applied. This reverses M_{xy} so that the phase shift is also reversed.

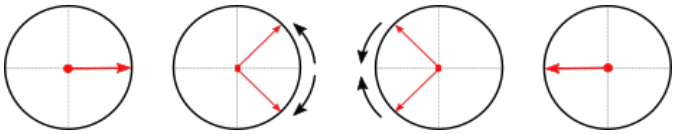


Figure 2.11: Spin echo formation: after a 90° pulse spins are initially all in-phase. As time evolves spins fan out due to phase accumulation. After the 180° pulse spins are flipped and come back into phase and form a spin echo which induces a detectable signal.

At t = 2T, the spins have accumulated a phase shift of -ϕ and the signal is refocused.

However, time dependent T_2 processes mean that the fields are constantly varying and so not all spins are rephased exactly. This causes a decay in signal which can be described by exp($\frac{-t}{T_2}$). Multiple measurements of the signal decay are made by varying the echo time (TE) in the spin-echo sequence. An exponential fit is applied to fit for T_2 which corresponds to the time it takes for M_{xy} to decay to 1/e ($\sim$ 37 %) of its initial maximum value.

2.1.6.6 Measurement of T_2^* Relaxation

After a 90° RF pulse is applied, an FID signal results that can be described by exp($\frac{-t}{T_2^*}$). By measuring the amplitude of the signal at different times, t, an exponential fit can be applied and T_2^* can be quantified.

2.1.6.7 Correlation Time

There are many processes that cause T_1 and T_2 relaxation; the main one of interest for ^{1}H is the dipole-dipole interaction. The rotational motion of a molecule has the greatest influence on the dipole-dipole interactions and is known as the molecular tumbling rate. Molecular tumbling is determined by the correlation time, τ_c, which is defined as the time it takes a molecule to rotate 1 radian. Larger molecules have longer correlation times as they tend to rotate more slowly. Correlation time also depends on the kinetic energy of each individual molecule which can vary with a sample.

The dependence of the T_1 and T_2 of protons on molecular tumbling rate is demonstrated in Figure 2.12. Macromolecules with slow molecular tumbling rates have high T_1 and low T_2, as opposed to free water which has both a long T_1 and T_2. Relaxation rates therefore have dependence on the applied magnetic field strength (B_0) due to its direct influence on the Larmor frequency (ω_0).

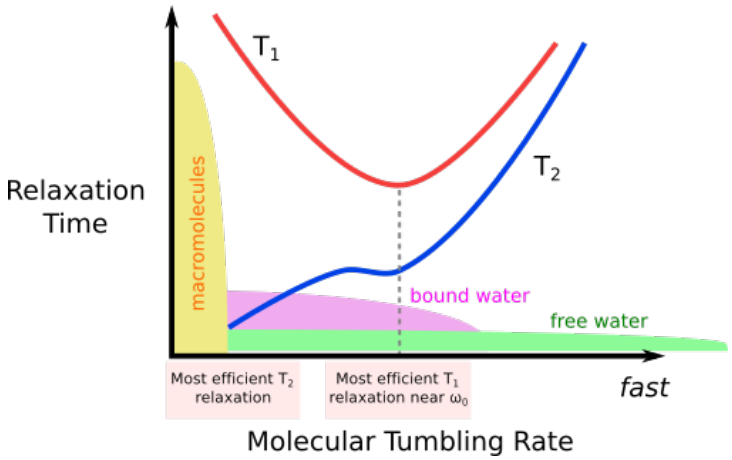


Figure 2.12: T_1 and T_2 vs. molecule size and molecular tumbling rate.

2.1.7 Chemical Shift

The resonance frequency of ^{1}H is determined not just by B_0, but by the local field (B_{loc}) created by the atomic scale chemical environment that it experiences. Electrons shield the nuclei from the magnetic field (characterised by the shielding factor, σ) and this results in a difference between B_{loc} and B_0:

$$B_{loc} = B_0(1 - \sigma) \tag{2.24}$$

Therefore, ^{1}H nuclei attached to different molecules experience their own particular magnetic fields and do not have the same resonant frequency. The difference between the Larmor frequencies is exploited in Magnetic Resonance Spectroscopy (MRS) to identify the relative abundance of chemical species within a

sample. This is achieved by collecting a spectrum and comparing the peaks to a reference standard. The chemical shift of a particular species, δ, is measured in parts per million (ppm) and calculated as

$$\delta = \frac{f_{signal} - f_{reference}}{f_{reference}} \tag{2.25}$$

2.1.8 Contrast in MRI

MR images have different T_1 and T_2 weighting depending on which MR pulse sequence and timings were used to generate the NMR signals. For example, in an inversion recovery sequence the inversion time (TI) controls the T_1 contrast between tissues; whereas in a spin-echo sequence it is the echo time (TE) that controls the T_2 contrast in the final image. The ability to vary the contrast between different soft tissues is a unique component of MR imaging.

2.2 Magnetic Resonance Imaging

2.2.1 MR Encoding

2.2.1.1 Spatial Encoding using Gradients

MRI employs spatially varying magnetic field gradients, $\mathbf{G}$, to change the Larmor frequency across a sample. These gradients can be written as a tensor

$$\mathbf{G} = \begin{bmatrix} \hat{i}\hat{i}\frac{\delta B_x}{\delta x} & \hat{i}\hat{j}\frac{\delta B_x}{\delta y} & \hat{i}\hat{k}\frac{\delta B_x}{\delta z} \\ \hat{j}\hat{i}\frac{\delta B_y}{\delta x} & \hat{j}\hat{j}\frac{\delta B_y}{\delta y} & \hat{j}\hat{k}\frac{\delta B_y}{\delta z} \\ \hat{k}\hat{i}\frac{\delta B_z}{\delta x} & \hat{k}\hat{j}\frac{\delta B_z}{\delta y} & \hat{k}\hat{k}\frac{\delta B_z}{\delta z} \end{bmatrix} \tag{2.26}$$

Since the direction of the main magnetic field is along the z axis, B_x and B_y are generally neglected and the tensor can be reduced to

$$\mathbf{G} = \frac{\delta B_z}{\delta x}\hat{\mathbf{i}} + \frac{\delta B_z}{\delta y}\hat{\mathbf{j}} + \frac{\delta B_z}{\delta z}\hat{\mathbf{k}} \tag{2.27}$$

B_0 is directed along the z axis and the gradients alter its strength. This results in the change of precession frequencies of the transverse magnetisation in each unique location. The effective magnetic field produced by the main magnetic field, B_0, and the applied gradients at location $\mathbf{r}$ is

$$B(\mathbf{r}) = B_0 + \mathbf{G}.\mathbf{r} \tag{2.28}$$

Which means the associated Larmor frequency at this point is

$$\omega_0(\mathbf{r}) = \gamma(B_0 + \mathbf{G}.\mathbf{r}) \tag{2.29}$$

Spatial alteration of the Larmor frequency is the basis of MR imaging and allows for 3D samples to be imaged.

2.2.1.2 Gradient Coils

Gradient coils lie inside the bore of the MR scanner and are designed such that they produce the required linearly varying magnetic fields. The gradient fields distort the main magnetic field in predetermined patterns, causing the resonance frequency of protons to vary as a function of their position. Three sets of gradient coils are used in standard MR systems; the x-, y- and z-gradients (G_x, G_y and G_z). Common coil designs used in cylindrical whole-body imaging systems are the Maxwell pair and Golay configurations.

2.2.1.3 Slice Selection

When a magnetic field gradient is applied along an axis perpendicular to the plane of the desired slice (this would be the z direction for an axial slice) this causes the the Larmor frequency to vary along the axis. To select the desired slice for imaging, a tailored RF pulse is applied over a narrow bandwidth of frequencies that excites the spins within the specific frequency range that corresponds to the target slice. This process selects the image slice perpendicular to the z axis (for the axial slice) as shown in Figure 2.13.

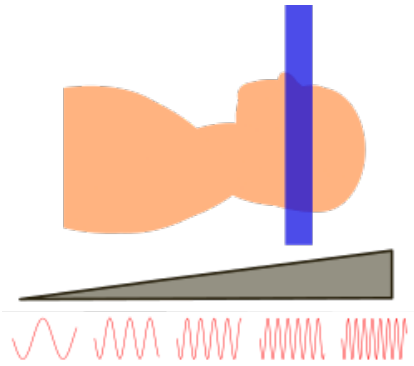


Figure 2.13: Demonstration of slice selection gradient.

The Fourier transform of the RF pulse shape can approximate the excited slice profile in the case of small flip angles and this is described by the small tip angle approximation. This approximation breaks down for larger flip angles due to the non-linearities of the Bloch equations. The ideal slice profile excites all spins within the slice and leaves all spins outwith the desired frequency range unaffected; i.e. a "top-hat" profile. The Fourier transform of this shape is a sinc function with an infinite number of side lobes. In practice, adopized sinc RF pulses are used which are truncated and so the top hat excitation profile is imperfect as it is missing the high frequency information required to produce the sharp edges of the desired profile (this is illustrated in Figure 2.14).

The thickness of the imaging slice, Δz, is determined by the strength of the gradient in the z direction, G_z, and the bandwidth of the RF pulse $\Delta\omega$. G_z determines the range of Larmor frequencies across the sample and $\Delta\omega$ determines the range of frequencies that are excited through the following expression

$$\Delta z = \frac{\Delta\omega}{\gamma G_z} \tag{2.30}$$

Figure 2.15 demonstrates the effect of increasing the gradient strength, G_z, and RF pulse bandwidth, $\Delta\omega$, on slice thickness. Increasing the gradient strength produces a thinner imaging slice and increasing the bandwidth produces a thicker imaging slice.

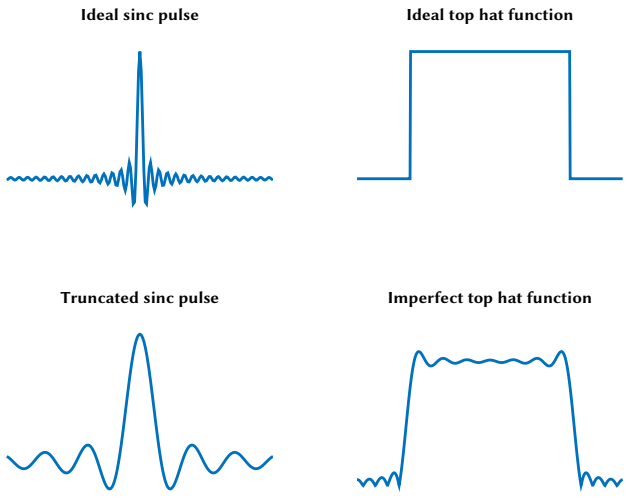
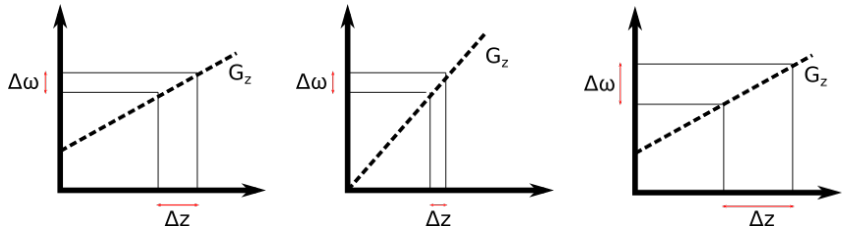


Figure 2.14: Illustration of ideal versus achievable excitation profiles. In the ideal case, the excitation profile produced in response to a sinc pulse resembles a top hat function. In reality, an infinite number of lobes in the sinc pulse is not possible and so an apodized, truncated sinc pulse is used which produces an imperfect excitation profile.



(a) Default G_z and bandwidth.

(b) Increased G_z results in thinner Δz.

(c) Increased bandwidth results in thicker Δz.

Figure 2.15: Effect of gradient strength G_z and bandwidth of the RF pulse, $\Delta\omega$, of slice thickness Δz.

Selective excitation is achieved by applying the gradient and RF pulse at the same time. After the RF pulse has been applied the magnetic field gradient in the z direction can be turned off as the required spins have already been excited. However, the application of RF pulse and magnetic field gradient will have produced phase differences across the slice which causes additional spin

dephasing and signal loss. Therefore, a gradient of equal and opposite magnitude of half the original duration is applied so that the dephasing effect is reversed. Figure 2.16 illustrates the pulse sequence required for slice selection.

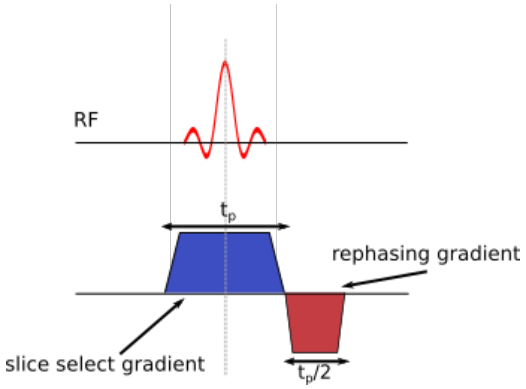


Figure 2.16: Demonstration of RF excitation pulse and slice selection gradients used to rephase spins and maximise resulting signal. t_p is the duration of the RF pulse and slice select gradient.

2.2.1.4 Frequency Encoding

Once an imaging slice has been selected, only the spins within this region will be affected by the magnetic field gradients. The resulting magnetisation can be detected using the same principals as slice selection and spatially encoding the slice using the magnetic field gradients.

Frequency encoding gradients are applied in the x direction so that the Larmor frequency of spins along the x plane vary as

$$\omega(x) = \gamma(B_0 + xG_x) \tag{2.31}$$

In the rotating frame of reference this can be simplified to:

$$\omega(x) = \gamma x G_x \tag{2.32}$$

The measured signal, $S(\mathbf{r}, t)$, is a function of position, $\mathbf{r}$, sample time t, spin density $\rho(\mathbf{r})$ and the integral over all the distinct precessional frequencies of the spins in the slice during readout duration, τ:

$$S(\mathbf{r}, t) \propto \rho(\mathbf{r}) e^{i \int \omega(\mathbf{r}, \tau) d\tau} \tag{2.33}$$

The signal from a whole sample volume V can be expressed as:

$$S(t) \propto \int_V \rho(\mathbf{r}) e^{i \int_0^t \omega(r, \tau) d\tau} dV \tag{2.34}$$

The precession frequency of each spin is determined by the magnetic field experienced at its specific location. Therefore, Equations 2.32 and 2.34 can be combined as

$$S(t) \propto \int_V \rho(\mathbf{r}) e^{i\gamma \int_0^t \mathbf{r}.G(\tau) d\tau} dV \tag{2.35}$$

where $\mathbf{G}(\tau)$ is the total gradient applied in all directions. The phase accumulated by the spins due to $\mathbf{G}(\tau)$ can be described using the wave number, k:

$$k(t) = \gamma \int_0^t \mathbf{G}(\tau) d\tau \tag{2.36}$$

Combining these equations gives

$$S(k) \propto \int_V \rho(k) e^{(i\mathbf{r}k(t))} dV \tag{2.37}$$

Equation 2.37 has the form of an inverse Fourier Transform. A Fourier Transform takes time domain information and converts it to the frequency domain, which is key to the spatial encoding required in MRI (see Figure 2.17). Applying a Fourier Transform to the signal results in the proton density:

$$\rho(k) \propto \int S(k) e^{(-i\mathbf{r}k(t))} dV \tag{2.38}$$

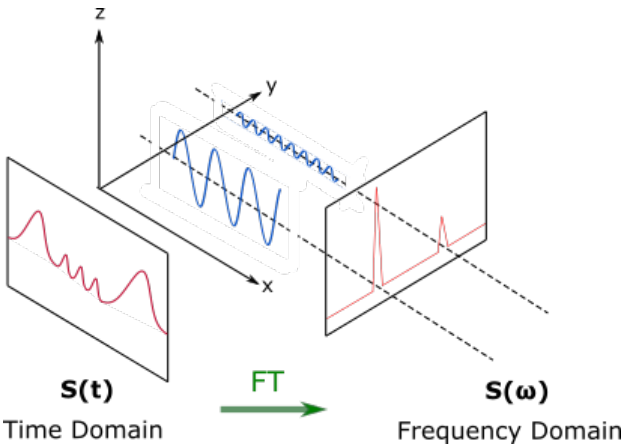


Figure 2.17: Illustration of Fourier transform operation converting time domain signals into the space domain.

This is how an MR image is produced, by acquiring NMR signals at a range of different frequencies and solving the Fourier Transform for proton density information at each location. A schematic demonstration of frequency encoding is shown in Figure 2.18.

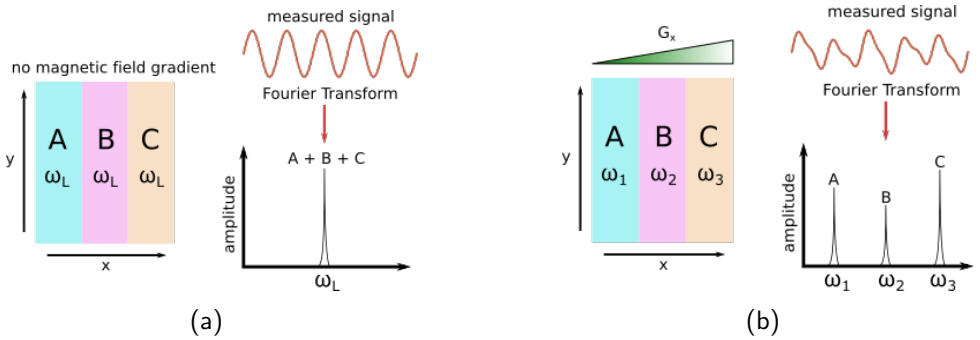


Figure 2.18: Frequency encoding: when a magnetic field gradient is applied along the x direction, the Larmor frequencies (ω_L) vary with x position. The measured signal is a function of all detected spin frequencies, a Fourier Transform is used to calculate the proton density at each specific location.

2.2.1.5 Phase Encoding

Phase encoding is used to spatially encode the spins in a sample in the y direction in order to localise the signal fully in 3D space. It involves applying a second magnetic field gradient along the y direction (or perpendicular to the frequency encoding gradient) temporarily so that the precessional frequencies are temporarily increased before returning to the Larmor frequency.

The precession frequency whilst the gradient is applied, is given by

$$\omega(y) = \gamma(B_0 + yG_y) \tag{2.39}$$

A phase shift, $\phi(y)$, at position y, is induced in the detected signal which is dependent on the duration and magnitude of the of the applied gradient:

$$\phi(y) = \gamma y \int_0^t G_y(t)dt \tag{2.40}$$

Which can be simplified using Equation 2.36 to

$$\phi = yk_y \tag{2.41}$$

The magnitude of the gradient is successively changed, and its duration kept constant, so that different phase shifts are applied to the signal. The position along the y axis can then be identified as the rate that the phase changes depends on its location along the y direction (see Figure 2.19 for demonstration of phase encoding).

In the centre of the gradients used for frequency and phase encoding there is no frequency or phase shifts in the sample. This allows for gradients that range from a negative to an equal but positive amplitude.

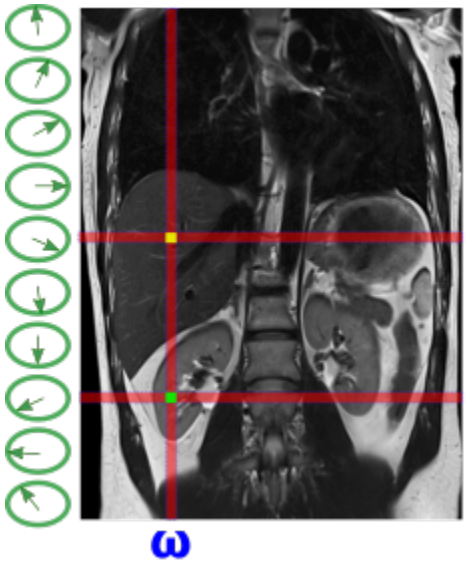


Figure 2.19: Demonstration of phase encoding; a gradient applied in the y direction induces a linear phase shift in the detected ω signal which depend on the position of the spins in the y direction. This allows the distinct yellow and green box locations to be identified.

2.2.1.6 k-Space

MR encoding is best understood using the concept of k-space where k is the wave number (the number of waves per unit space also known as the spatial frequency) which is inversely proportional to wavelength. k is characteristic of the signal being collected and is directly related to the gradient applied across a sample. By changing the amplitude and duration of the gradients over time (by applying frequency and phase encoding), points in k-space can be sampled along certain paths called k-space trajectories.

Figure 2.20 demonstrates how k-space is sampled on a Cartesian grid, starting at the centre of k-space where the spins are in phase following application of the slice select gradients. Applying identical x and y direction gradients (blue gradients) results in a diagonal route across k-space (blue line). A negative x gradient (red gradient) results in movement along the -k_x direction (red line). Similarly, a negative y gradient (orange gradient) causes movement in the -k_y

direction. Finally, both negative x and y gradients (green gradients) cause a reverse diagonal route through k-space (green line).

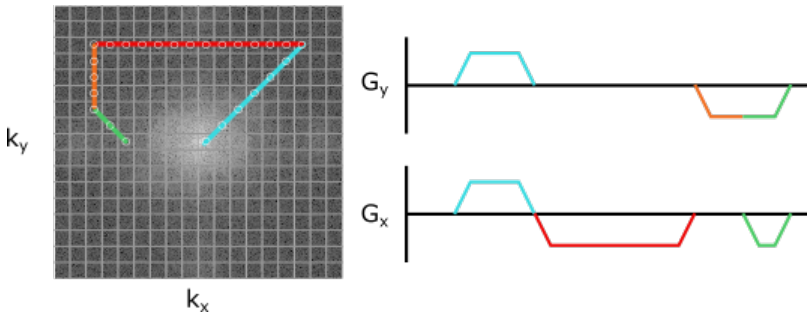


Figure 2.20: Demonstration of how gradients are used to traverse k-space. The pattern in which this is performed is called a k-space trajectory.

Each sample of signal is directly projected onto a specific location in k-space. Once k-space has been sampled to the desired extent an inverse Fourier Transform is applied to convert the measured spatial frequency content into image space (see Figure 2.21). The higher spatial frequencies that are responsible for sharp edges and high-resolution details originate from the outer regions of k-space and require higher and longer gradients.

The field of view of the image is given by

$$FOV_x = \frac{1}{\Delta k_x} \qquad FOV_y = \frac{1}{\Delta k_y} \tag{2.42}$$

The resolution of k-space is given by the maximum value of k-space.

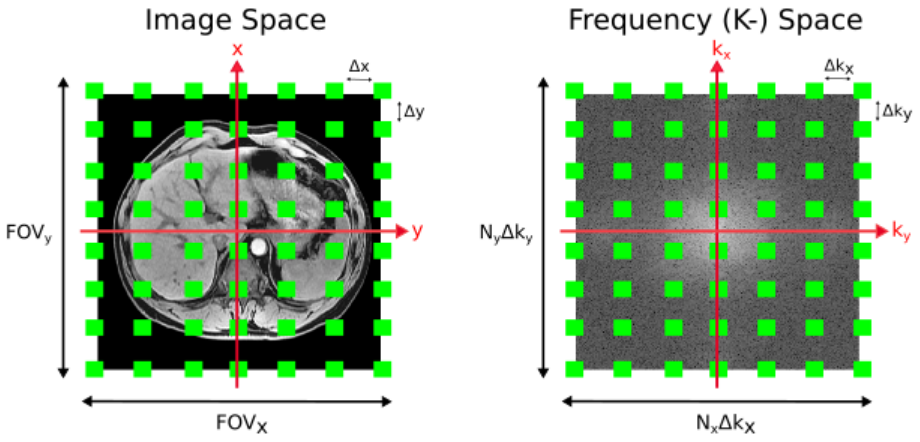


Figure 2.21: Image space and k-space are related through the Fourier Transform. The field of view of the image is linked to the sampling of k_x and k_y.

2.2.2 MR Imaging Sequences and Techniques

Many MR imaging sequences have been introduced that vary the way in which k-space is sampled. There are roughly two classes of sequences; the Gradient Recalled Echo (GRE) and Spin-Echo (SE). GRE based sequences provide T_1 and T_2^* weighted image contrast depending on MR parameters selected for the acquisition and SE sequences generate T_2 weighted images. Only GRE sequences were used for the work in this thesis and are outlined in this section. Spin warp imaging, EPI and FLASH imaging sequences are explained; then parallel imaging is presented followed by the concept of field mapping and finally this section concludes with an overview of Dixon imaging.

2.2.2.1 Spin Warp Imaging

An early development in MR imaging was that of spin warp imaging. It is considered the "bread and butter" MR encoding method and uses successive application of phase- and frequency-encoding gradients. It is a 2D acquisition method which means the signals are acquired for each slice individually and

requires multiple RF excitations in order to fully sample a single slice.

A 2D gradient echo pulse sequence using spin-warp imaging is illustrated in Figure 2.22. An RF pulse is applied to excite the slice (using slice select gradients), followed by short phase and frequency encoding gradients which spatially encode the signal in x and y directions. Applying a second frequency encoding gradient reverses the frequency dephasing and produces an echo. Conventionally, there is one readout measurement per RF excitation which means that in every excitation the spatial frequencies of the readout direction are fully sampled.

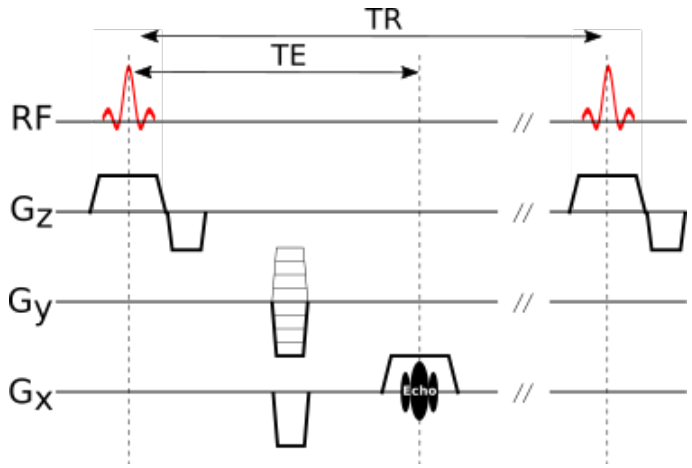


Figure 2.22: Illustration of k-space trajectory and MR pulse sequence diagram for a 2D-spin warp imaging sequence.

The echo produced represents a single phase encoding step. Therefore, in order to produce a complete image, this sequence is repeated multiple times with different phase encoding amplitudes in order to sample all the spatial frequencies required to build up k-space. It is also necessary to wait for magnetisation to fully recover before the next line of k-space can be sampled. This waiting time is known as the repetition time (TR) and can be long when large flip angles are used. These reasons mean that acquisition times for spin warp imaging can be very slow for high-resolution images.

2.2.2.2 Echo Planar Imaging

EPI is a fast acquisition method which samples the whole of k-space following a single RF excitation pulse. It was first conceived by Sir Peter Mansfield in 1977 [3].

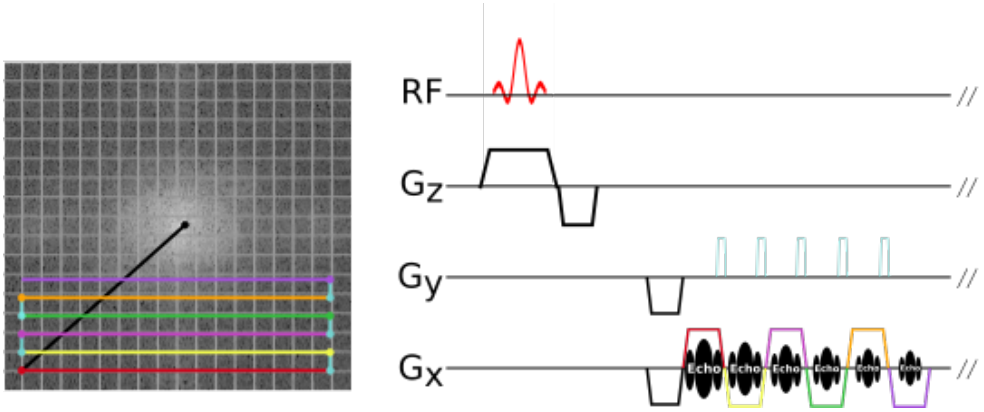


Figure 2.23: Illustration of k-space trajectory and MR pulse sequence diagram for a 2D-EPI sequence. The recorded signal decays according to T_2^*.

Similar to spin warp imaging, EPI starts with an RF excitation pulse and slice select gradients followed by short duration phase and frequency encoding gradients that spatially encode the signal in x and y directions. This sends the k-space trajectory to the edge of k-space (Figure 2.23 - black line). A frequency gradient of equal but opposite magnitude is applied to rephase the signal in the k_x direction and the signal is acquired (Figure 2.23 - red line). A small phase encoding blip is then applied which causes the k-space trajectory to move up a line in k-space (Figure 2.23 - light blue line). Practically, this is achieved by adjusting the phase shifts of the signals. Another frequency encoding gradient of equal but opposite magnitude is then applied to sample the next line of k-space in the opposite direction (Figure 2.23 - yellow line). The process of applying the phase encoding blips and switching the polarity of the frequency encoding gradients eventually results in the full coverage of k-space.

Signal is recorded during each of the alternating frequency encoding gradients where the maximum amplitude of the echo occurs at the mid-point of each lobe.

The amplitude of the recorded signal decays at a rate defined by T_2^*.

Total scan time for EPI can be less than 100 ms, which means that motion artefacts can be reduced, and the temporal resolution (SNR/time) is high compared with other imaging methods making it highly favourable for dynamic studies. However, these advantages depend on the intrinsic SNR and high gradient switching rates which are required to sample the entirety of k-space. EPI is also very sensitive to B_0 homogeneity and is prone to signal loss and distortion artefacts. 2D EPI is not implemented in this thesis but is included for its historical significance and use in body imaging applications at conventional field strengths.

2.2.2.3 Fast Low Angle Shot Imaging

Fast Low Angle Shot (FLASH) imaging is an extension of the 2D gradient echo spin warp imaging sequence outlined at the beginning of this section. FLASH uses low flip angle RF pulses which allow for the TR to be shorter and spoiler gradients combined with incremental phase shifts to remove unwanted stimulated echo effects that may arise and corrupt the final image. Stimulated echoes occur due to the refocusing of magnetisation that was initialised by RF excitation in earlier repetitions[1].

The FLASH sequence is illustrated in Figure 2.24. The spoiler gradients dephase the spins in each voxel so that there is no transverse magnetisation left by the time the next RF excitation pulse is applied in the next TR. Additional rewinder gradient lobes are introduced that are opposite to the phase encoding gradients and these restore spin coherence in the phase encode direction.

The spoiler gradients destroy any remaining spin coherence at the end of the TR, without affecting the longitudinal component of magnetisation. After several repetitions a steady state of magnetisation, M_{ss}, is reached where both T_1 relaxation and excitation effects are stabilised. In the steady state the following

[1] Stimulated echoes are not always considered an artefact, some sequences use them to their advantage [4]

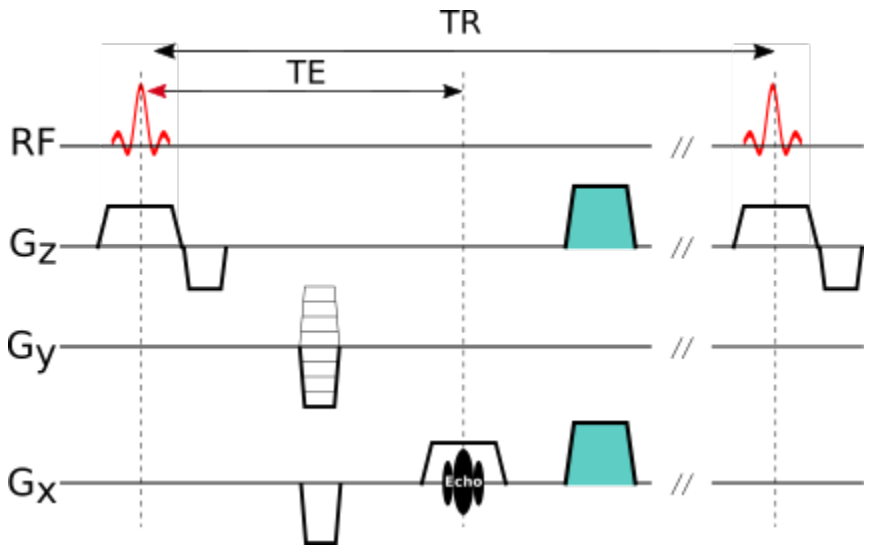


Figure 2.24: FLASH MR sequence diagram. Spoiler gradients along the slice select and readout directions are shaded turquoise.

equation for M_{ss} applies:

$$M_{ss} = \frac{M_0(1 - e^{\frac{-TR}{T_1}})}{1 - e^{\frac{-TR}{T_1}} cos(\theta)} \tag{2.43}$$

This allows for the Ernst angle corresponding to the maximum signal for a given TR to be calculated via:

$$\theta_E = arccos(e^{\frac{-TR}{T_1}}) \tag{2.44}$$

This shows that maximum signal can be achieved for a small flip angle and short TR.

2.2.2.4 Parallel Imaging

Rapid image acquisition is necessary for using MRI for routine clinical use. Shorter imaging times result in higher patient throughput, potential for dynamic imaging and improved imaging of organs susceptible to motion. However, there is a trade-off between imaging speed and the signal and contrast to noise ratios (SNR/CNR). In normal MR imaging multiple receiver coils collect the signals and then these are combined to produce the full signal to form an image. Using multiple receiver coils improves SNR but does not make use of the varying sensitivity of each coil.

Parallel imaging reduces scan time by reducing the number of phase encoding lines in a Cartesian acquisition by an acceleration factor, R. The theoretical maximum value of R is equal to the number of receive coils however, achieving this artefact free is dependent on the overall geometry of the coils. Spatial resolution (coverage of k-space) is kept constant thus reducing the total scan time by R. An effect of increasing the distance between phase encoding lines Δk is that the FOV is reduced. Therefore, if an object extends beyond the FOV wrap around artefacts (also known as aliasing) can occur.

The spatial sensitivities of each receive coil are used to prevent this artefact and provide information about the localisation of the signals. There are different strategies that can be used for this; SiMultaneous Acquisition of Spatial Harmonics (SMASH) [5], GeneRalized Autocalibrating Partially Parallel Acquisitions (GRAPPA) [6] and SENSitivity Encoding (SENSE) [7]. Only SENSE is used for the work in this thesis and is described in the rest of this section with reference to Figure 2.25.

SENSE is an image space method where each receive coil k-space data sets are Fourier transformed separately. This results in aliased images which are then combined using weights calculated from coil sensitivity maps to give a single final image with the wrap around artefact removed.

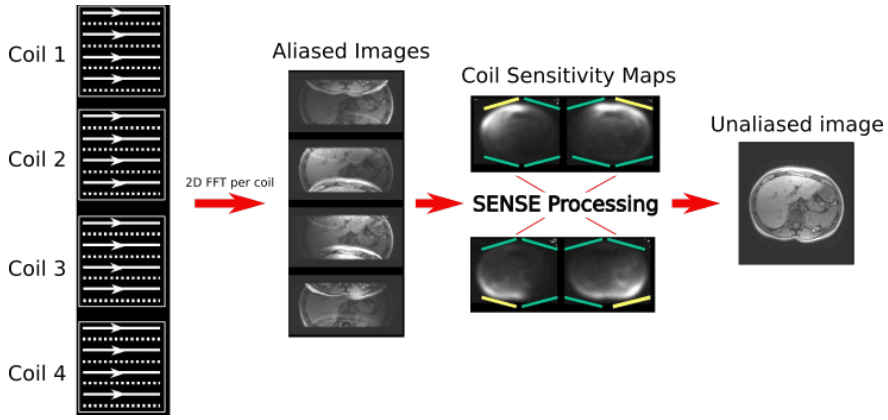


Figure 2.25: Demonstration of sensitivity encoding using four coils and a SENSE reduction factor of 4. Figure adapted from [8].

In each aliased image, the signal in each voxel, P, is the sum of the true signal from voxels in the unaliased image, A and B.

$$P = A.S_A + B.S_B \tag{2.45}$$

Using the relative coil sensitivity at each location of voxels A and B (S_A and S_B respectively) the aliased images can be unfolded using simultaneous equations. If a voxel contains signal from n parts of the image, there must be at least n receive coils to unwrap it.

Unwrapping the aliased image magnifies the image noise which is spatially varying across the FOV. The noise is enhanced in areas where coil sensitivity is low. The geometry factor, g, is used to express this noise enhancement.

2.2.3 Field Mapping

Mapping of both the main magnetic field, B_0, and the applied radiofrequency field, B_1^+, is necessary for the respective shimming calculations that are implemented to homogenise both fields. This is essential for uniform excitation and contrast in the final generated image.

2.2.3.1 B_0 Mapping

A map of the B_0 distribution is acquired using a gradient echo sequence repeated with two different echo times that are separated by a time ΔTE. The difference in the phase $\Delta\phi$ of the nuclei at the two different echo times is directly proportional to the B_0 inhomogeneity, $\Delta B_z(r)$, at that location and is given by

$$\Delta\phi(r) = \gamma \Delta B_z(r) \Delta TE \tag{2.46}$$

The local deviation of the B_0 field is then calculated as

$$\Delta B_z(r) = \frac{\Delta\phi(r)}{\gamma \Delta TE} \tag{2.47}$$

2.2.3.2 B_1^+ Mapping

B_1^+ mapping is necessary when the exact flip angle distribution generated across a field of view is required. This is the subject of Chapter 4 and is covered extensively.

2.2.4 Dixon Method

The Dixon method [9] exploits the chemical shift properties of fat to produce separate fat and water images. The resonant frequencies of fat and water are different and therefore the fat and water signals go in and out of phase with each other over time.

Two images are collected with different echo times (TE); the first image is collected when fat (F) and water (W) are in-phase (IP), the second image is collected when they are out-of-phase (OP) (see Figure 2.26). The signals in IP and OP images can be described as:

$$\begin{aligned} S_{IP} &= S_W + S_F \\ S_{OP} &= S_W - S_F \end{aligned} \tag{2.48}$$

These equations can be rearranged and solved for S_W and S_F:

$$\begin{aligned} S_W &= \tfrac{1}{2}(S_{IP} + S_{OP}) \\ S_F &= \tfrac{1}{2}(S_{IP} - S_{OP}) \end{aligned} \tag{2.49}$$

This allows for separate fat and water images to be reconstructed.

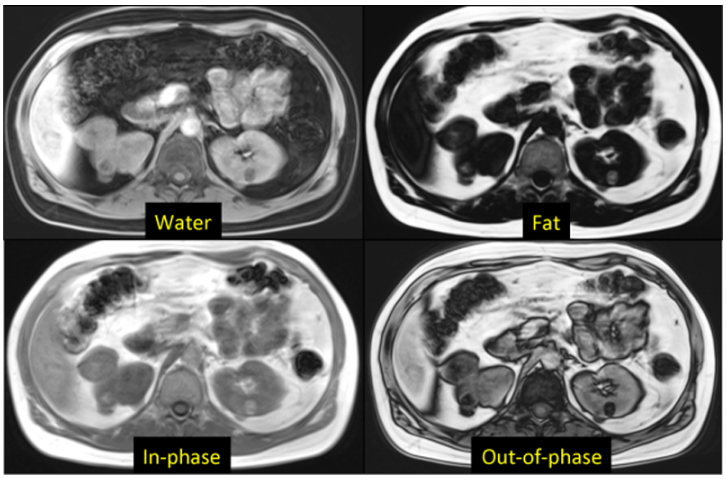


Figure 2.26: Example of Dixon method applied at 3 Tesla. Figure from `http://mriquestions.com/dixon-method.html`

More sophisticated Dixon methods acquire multiple images at different echo times in order to gain more information about the fat composition of the sample, as well as B_0 inhomogeneities [10]. On Philips systems this scan is known as mDIXON.

2.3 Conclusion

This chapter has introduced the basics of NMR required to understand how MRI works. It has also discussed the physics behind the MR acquisition techniques that are used throughout this thesis.

References

[1] Tamer S. Ibrahim. Analytical approach to the MR signal. *Magnetic Resonance in Medicine*, 54(3):677–682, 2005.

[2] Rudolf Stollberger and Paul Wach. Imaging of the active B1 field in vivo. *Magnetic Resonance in Medicine*, 35(2):245–251, 1996.

[3] P Mansfield. Multi-planar image formation using NMR spin echoes. Technical report, 1977.

[4] J. Frahm, K. D. Merboldt, W. Hanicke, and A. Haase. Stimulated echo imaging. *Journal of Magnetic Resonance (1969)*, 64(1):81–93, 1985.

[5] Daniel K. Sodickson and Warren J. Manning. Simultaneous acquisition of spatial harmonics (SMASH): Fast imaging with radiofrequency coil arrays. *Magnetic Resonance in Medicine*, 38(4):591–603, 1997.

[6] Mark A. Griswold, Peter M. Jakob, Robin M. Heidemann, Mathias Nittka, Vladimir Jellus, Jianmin Wang, Berthold Kiefer, and Axel Haase. Generalized Autocalibrating Partially Parallel Acquisitions (GRAPPA). *Magnetic Resonance in Medicine*, 47(6):1202–1210, 2002.

[7] Klaas P. Pruessmann, Markus Weiger, Markus B. Scheidegger, and Peter Boesiger. SENSE: Sensitivity encoding for fast MRI. *Magnetic Resonance in Medicine*, 42(5):952–962, 1999.

[8] Vimal M. Aga. Structural and Functional Imaging, 2018.

[9] W Dixon, Thomas. Simple Proton Spectroscopic Imaging. *Radiology*, 153:189–194, 1984.

[10] Jingfei Ma. Dixon techniques for water and fat imaging. *Journal of Magnetic Resonance Imaging*, 28(3):543–558, 2008.

3 Principles of 7 T Body Imaging

This chapter introduces the advantages and challenges of imaging at 7 T and the methods designed to overcome these difficulties. The concept of Parallel Transmission Technology (pTx) is introduced and it is explained how pTx systems are necessary to achieve body imaging at 7 T compared with conventional imaging at lower magnetic field strengths. An overview of the 7 T Multi-Transmit Philips Achieva MRI system is given, outlining aspects of scanner operation, hardware and software that are referred to throughout the rest of this thesis. The theory of Specific Absorption Rate (SAR) and the regulatory limits placed upon it for MR scanning is defined. Problems associated with SAR at 7 T and on pTx systems are explained in addition to how SAR distributions are modelled in order to monitor and assess MR safety.

3.1 MRI at Ultra-High Field

There are several advantages of 7 T compared to lower field strengths. The intrinsic Signal-to-Noise Ratio (SNR) is greater meaning that higher spatial resolutions can be used for studying small-scale anatomical structures and reducing partial volume effects. Greater SNR also means that scan times can be shorter as less averaging is required to collect the equivalent signal.

At UHF the underlying contrast mechanisms in MRI change. The effects of fundamental dipole-dipole interactions increase with B_0 which leads to an increase in the T_1 relaxation time. Longer T_1's are beneficial for MR techniques which require signal suppression such as Time-of-Flight (TOF) and Arterial Spin Labelling (ASL), but mean that longer scan times are required to avoid suppression in other imaging sequences. T_2 relaxation times decrease with increasing B_0, and shorter T_2^* times occur due to the rise in susceptibility effects which can cause additional geometric distortions and increased intravoxel dephasing. However, the shorter T_2^* times are beneficial for techniques like Blood Oxygen Level Dependent (BOLD) imaging as the sensitivity of measurements is increased.

Lastly, the chemical shift effect is increased at UHF and can cause misregistration of fat and water in reconstructed images (see Figure 3.1) or alternatively can be exploited for better fat saturation [1].

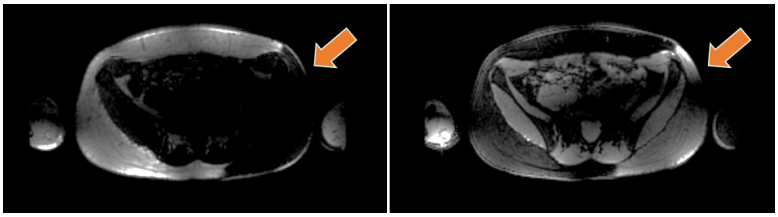


Figure 3.1: Demonstration of fat and water misregistration in reconstructed Dixon images at 7 T.

The higher Larmor frequency, and consequently shorter Radiofrequency (RF) wavelength (approximately 11 cm as demonstrated in Figure 3.2), produces non-uniformities in the RF transmit and receive fields which are much greater than those experienced at 1.5 and 3 T. This means that conventional RF excitation strategies become inefficient and can lead to low SNR and signal voids in the resultant MR images. Spatially varying flip angles are also produced which can result in poor inversion efficiency and unexpected contrast. Furthermore, due to the shortened wavelength the RF penetration is limited which hinders MRI acquisition of organs located deep within the body [2].

There are a number of methods that have been designed to address these challenges. These include applying adiabatic RF pulses that are insensitive to inhomogeneities in the B_1^+ field [4, 5]; using dielectric pads that alter the underlying Electromagnetic (EM) fields to improve the spatial homogeneity [6–8]; and designing coils to optimise the transmit RF homogeneity [9, 10]. However, the implementation of multiple RF transmission channels is the most promising approach for mitigating the B_1^+ inhomogeneity experienced at 7 T and is the subject of the next section.

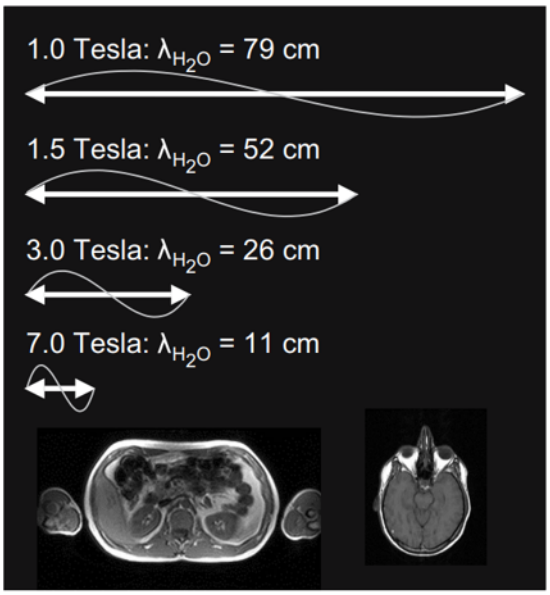


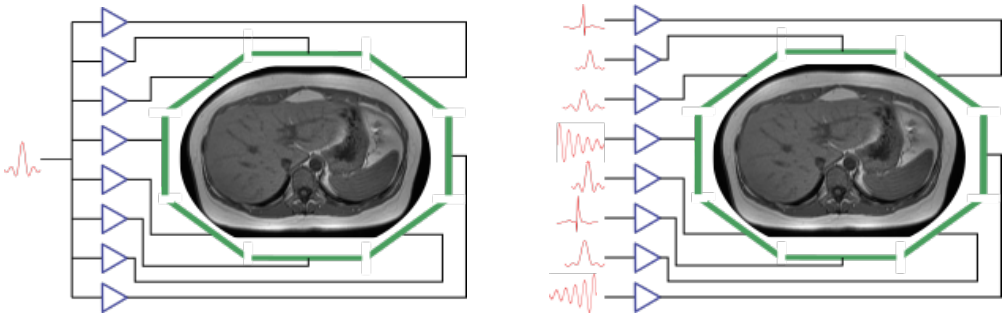
Figure 3.2: Demonstration of the RF wavelengths at common field strengths relative to standard body dimensions. Quoted wavelengths calculated for proton Larmor frequency in water. Figure from: [3].

3.2 Parallel Transmission

Parallel Transmission Technology (pTx) uses N multiple transmit channels to independently adjust the amplitude and phase of N individual RF waveforms to improve the B_1^+ homogeneity in an excited volume of interest [11]. The complex superposition of the fields generated by each coil element, $B_{1,n}^+(\boldsymbol{r},t)$, each with transmit sensitivity, $S_n(\boldsymbol{r})$, and driven by RF pulses, $b_n(t)$, determines the net field $B_1^+(\boldsymbol{r},t)$ produced inside the subject [12].

$$B_1^+(\boldsymbol{r},t) = \sum_{n=1}^{N} B_{1,n}^+(\boldsymbol{r},t) = \sum_{n=1}^{N} b_n(t) S_n(\boldsymbol{r}) \tag{3.1}$$

By modifying $b_n(t)$ the resulting total B_1^+ field can be controlled both spatially and temporally using either static or dynamic pTx.



(a) (b)

Figure 3.3: Schematic diagrams of (a) static and (b) dynamic pTx. In static pTx the same RF waveform is applied to each transmit channel; the magnitude and phase of the waveform can be adjusted on a per channel basis. In dynamic pTx, different RF waveforms can be applied through each transmit channel.

3.2.1 Static pTx

Static pTx (also known as B_1^+ or RF shimming) considers each RF pulse from the different transmit channels, $b_n(t)$, to be identical with a profile $b(t)$, weighted by a time independent amplitude and phase term, $w_n = a_n e^{i\phi_n}$ [1, 13]. Therefore, the net B_1^+ field is:

$$B_1^+(\boldsymbol{r}, t) = b(t) \sum_{n=1}^{N} w_n S_n(\boldsymbol{r}) \tag{3.2}$$

The goal is to optimise the spatial field, $S(\boldsymbol{r}) = \sum_{n=1}^{N} w_n S_n(\boldsymbol{r})$, in terms of homogeneity, peak local B_1^+ or power by finding a shim set, $\boldsymbol{w} = (w_1, ..., w_n)^T$, (corresponding to optimal a_n and ϕ_n) for each transmit channel. The temporal profile of the RF pulse $b(t)$ is not affected by the RF shimming. B_1^+ maps are required for each channel to determine the transmit sensitivity $S_n(\boldsymbol{r})$ and are explained in more detail in the next chapter.

RF shimming is usually applied to improve the B_1^+ inhomogeneity within a Region of Interest (ROI). The success of an RF shim scales inversely with the size of the ROI. In localised regions, for example the prostate, a homogenous B_1^+ distribution can be achieved with phase only shimming which involves optimising

ϕ_n by aligning the average phase of each channel such that all channels are constructively interfering within the ROI. Higher transmit efficiency is achieved by maintaining $a_n = 1$ for each w_n.

RF shimming can also be used to maximise the transmit efficiency, as opposed to maximising the homogeneity of the field, within the ROI. This is desirable when using adiabatic RF pulses that require high B_1^+ values and rely less on a uniform distribution. Shim sets can also be used to trade off B_1^+ homogeneity for SAR minimisation [14] (see Section 3.8 for explanation of SAR).

The optimum weightings for RF shimming, w_n, are usually determined using numerical optimisation algorithms that iteratively minimise a chosen cost function. There are many different cost functions that have been explored in the literature such as linear least squares [15], magnitude least squares [16], coefficient of variation [17] and MaxMin which maximises the minimum [18]. In general, most functions consist of an error term that control the B_1^+ spatial distribution, a term related to SAR limits and a term related to hardware limits such as peak power.

The application of RF shimming does not require any changes to be made to the MR sequence. Different RF shim settings can be employed for different RF pulses (excitation, refocusing, inversion, saturation etc.) within a sequence using dynamic B_1^+ shimming. This is desirable when there are different ROIs for different pulses or when homogeneity or efficiency requirements change throughout the sequence.

3.2.2 Dynamic pTx

Dynamic pTx approaches are not covered in this thesis, however this section provides a basic overview for further context of the field. Dynamic pTx differs from static pTx such that the weights of the RF shim set change over the duration of a given RF pulse, or there are different RF pulses for each transmit channel. Dynamic approaches focus more on the optimisation of the resultant flip angle distribution as opposed to the resultant B_1^+ field. Therefore, the B_0

field and gradient trajectory are also optimised as these also affect the flip angles that are produced. Dynamic pTx approaches can be applied to non-selective, slice or slab-selective, and 2D or 3D local excitation.

Non-selective excitation uses k_T-points pulses to achieve spatially uniform excitation within a 3D volume [19, 20]. Rectangular sub-pulses are applied with no slice select gradients so that all RF power is deposited at specific locations in transmit k-space. Gradient blips are applied between the sub-pulses in all three spatial directions to create a volume excitation.

Spokes RF pulses are used in slice or slab-selective excitation [21–23]. These RF pulses utilise successive selective sub-pulses, each with different shim sets. Both slice-select gradients during the applied RF pulses and gradient blips between sub-pulses are applied. The trajectory of excitation k-space results in multiple "spokes" along the k_z direction sparsely distributed in the $k_{x,y}$ plane [24].

2D and 3D local excitation is achieved using 2D and 3D spatially selective pTx RF pulses. This is feasible with single channel transmit systems but requires long gradient trajectories that are practically unfeasible. pTx allows shorter gradient trajectories and oversampling of the excitation k-space. This shortens the lengths of the RF pulses (and subsequently acquisition times) without forfeiting spatial resolution. This application is called "Transmit SENSE" [25, 26].

3.2.3 Summary

This section has reviewed the two pTx approaches that allow for spatial and temporal control over individual B_1^+ fields generated by separate transmit elements that can be used to mitigate the inhomogeneity experienced at 7 T. For the work performed in this thesis, only static pTx is employed. In the sections that follow, the hardware and software used to implement this method during imaging is explained.

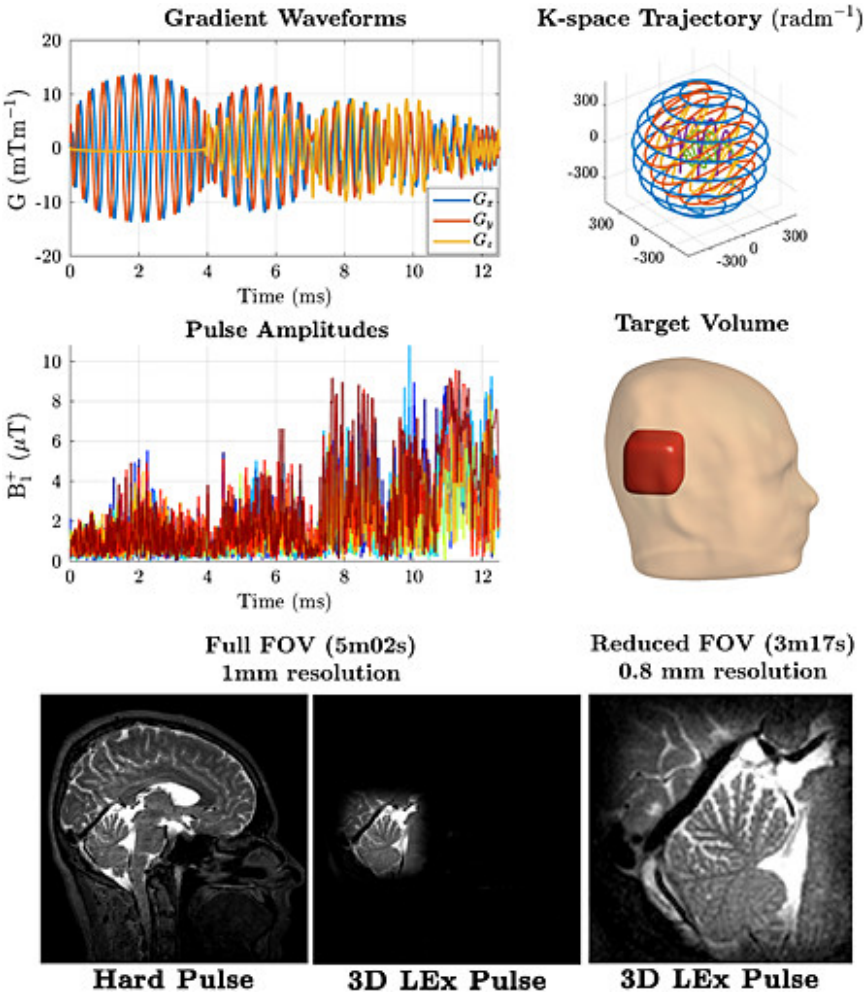


Figure 3.4: Examples of dynamic pTx applications; optimised gradient waveforms, excitation k-space trajectories and B_1^+ waveforms based on a given target volume for local excitation and reduced FOV imaging. Figure from [12].

3.3 Overview of Parallel Transmit System

This section covers the hardware and software that control the 7 T Multi-Transmit Philips Achieva MRI system used to collect experimental results presented throughout this thesis. Each subsection provides details concerning the MR components most relevant to the work presented in the succeeding chapters with reference to Figure 3.5.

3.3.1 Scanner Operation

The scanner is operated by the user from the console computer. This is where the MR pulse sequences are generated; the appropriate RF pulses are defined and gradient magnitudes and timings are calculated. Once the pulse sequence is finalised the relative signals are passed from the console to the analogue system via digital to analogue converters (DAC).

The gradient waveforms are sent to the gradient amplifier and the necessary currents generate the gradient fields at the times calculated. Only information regarding the shape of the RF pulse is passed to the DAC. In order to achieve excitation the RF pulse must oscillate at the Larmor frequency. Therefore, it has to be modulated by the carrier frequency which is determined by the frequency synthesizer. The RF pulses are then directed to the RF amplifiers that amplify the waveforms such that they reach amplitudes of μT in the coil.

3.3.2 Main Magnetic Field

The system is built around an unshielded 90 cm diameter bore superconducting magnet (Magnex Scientific, Oxford, England). Liquid helium is used to cool the coils wound around the bore that create the superconducting solenoid generating the static magnetic field, B_0. The entire setup is enclosed within a Faraday cage to minimise RF noise and suppress stray fields from the outside the magnet room. Approximately 200-ton of iron lines the walls of the room to reduce the magnetic field from 7 T to 5 mT within a safe distance of the building.

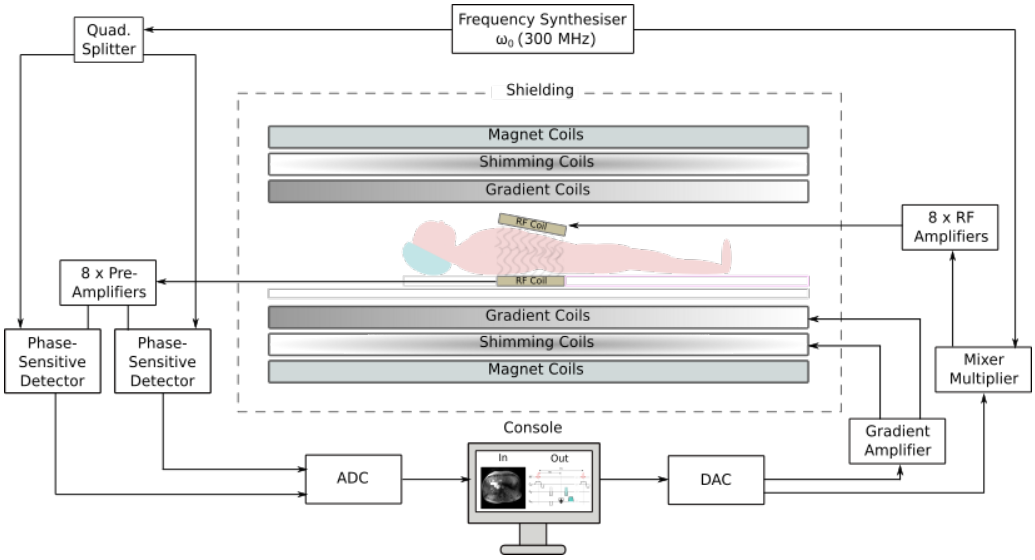


Figure 3.5: Schematic diagram of 7 T pTx system.

3.3.3 Gradient and Shim Coils

Three layers of gradient coils, each with different geometries, are used to spatially encode the MR signal in x, y and z directions. Alternating currents rapidly switch the gradients needed to produce an image; this can cause creation of intense temperatures within the coil wires. A liquid cooling system is used to minimise this heating effect. On the Philips 7 T system, the maximum gradient that can be produced is 40 mT/m, and the maximum rate of change (slew rate) is 200 mT/m/ms.

It is not possible to construct a magnet with a perfectly homogenous magnetic field. Shim coils are used to improve the homogeneity of the main magnetic field B_0 which is already imperfect and then further degraded when a subject (or phantom) is placed within the scanner. Shimming can be either be passive or active; passive shimming is normally performed during installation of the magnet by placing metal at specific locations on the outer surface of the scanner; active shimming optimises the homogeneity of the field by adjusting the electrical currents running through the shim coils.

This is an important calibration step performed at the beginning of each scan session as if B_0 is not homogenous, the Larmor frequency will spatially vary resulting in poor image quality. The frequency shift cannot be removed during post-processing and so it is essential to achieve an effective shim when imaging. B_0 calibration is subject-dependent and so B_0 shimming calculations are applied at the start of each scanning session.

The shim coils are designed similar to the gradient coils and the magnetic field generated by each coil is proportional to the electrical current running through it. The currents required to optimise the homogeneity of B_0 are determined by a specific algorithm that analyses the B_0 distribution within a given 3D volume. The B_0 distribution is characterised by a Taylor series expansion and is measured using the B_0 mapping method outlined in Section 2.2.3.1.

3.3.4 RF Transmit Chain

There are eight independent RF transmit channels each controlled by a standalone 2 kW amplifier. The RF amplifiers generate the RF waveforms and power supply for each transmit channel of the RF coil. During the evolution of the RF pulse the power is monitored by bi-directional couplers on each channel that measure the forward and reflected power at the coil connection plane (CCP). This is a virtual plane between the RF interface box and the RF coil. CCP calibration is a manufacturer routine check essential for ensuring power monitoring is accurate. The signals detected by the bi-directional couplers are sent to a software power monitoring unit (SPMU) where the peak and average power for each channel at the CCP is determined. If either of these measurements exceeds average or peak power limits for the RF coil, then the power to generate the desired the RF pulses in the MR sequence is reduced or the scan is aborted. The SPMU is always active during scanning and accumulates average power measurements over a time period of 15 seconds.

3.4 RF Coil for 7 T Body Imaging

The RF coil used for body imaging at 7 T throughout this thesis is an 8 channel transmit, 32 channel receive body array (MRCoils, Zaltbommel, Netherlands). The eight transmit elements are placed around a subject, four on the posterior and four on the anterior side in two separate arrays. Each element has a plastic casing that encompasses a fractionated dipole antenna for RF transmission [27] and along the length of each dipole are four receive loops. Fractionated dipoles have high transmit efficiency at UHF which is beneficial for imaging deeply located organs in the body and they also produce lower peak local SAR values [27].

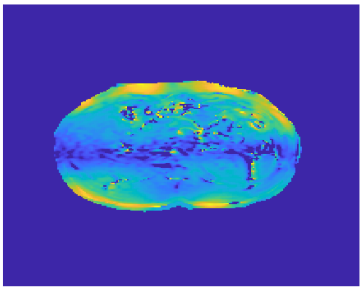
The body coil arrays are identified by the scanner with a coil ID dongle which is plugged into the side of the scanner bed at the start of each scanning session. This allows specific settings and power limits associated with the coil (stored in a specific coil file) to be applied at the scanner.

3.4.1 Transmit Phase Settings

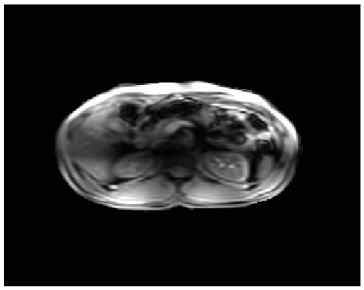
The coil file associated with the body array contains the default transmit RF phase settings used during calibration scans at the start of each protocol, before an RF shim is calculated and the phase settings are altered. Throughout initial work with the body array, these transmit phase settings were calibrated to minimise the phase difference in the image in the areas between individual transmit channels. This effective quadrature mode was achieved with the following relative phases applied to each transmit channel: [0° -246° -131° -129° 218° 165° -134° 252°]. Over time, the MR system and body array underwent separate recalibrations. To achieve the same effect, the transmit phase settings were replaced with: [0° 0° 0° 0° 0° 0° 0° 0°]. As all transmit phases were set to 0°, this mode was termed "linear mode" and it generated homogenous signal over most of the field of view, apart for a band of destructive interference in the middle of the subject. Linear mode was desirable for most calibration scans, such as B_1^+ mapping and renal localiser scans (see Figures 3.6 (a) and (b) for

examples acquired in this mode).

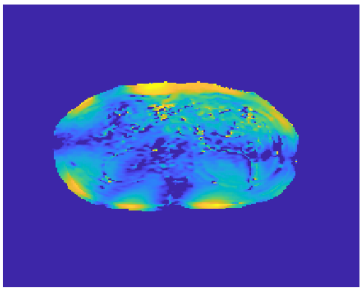
An alternative quadrature mode where the transmit phase on each channel was 45° out of phase with its neighbouring element, (theoretically minimising the variation in phase and the destructive interference between adjacent elements) was used to acquire the B_1^+ map and survey image shown in Figures 3.6 (c) and (d). This mode was undesirable for calibration scans as there were more distinct RF interference bands across the Field of View (FOV) and the default transmit phase settings were set in the linear mode.



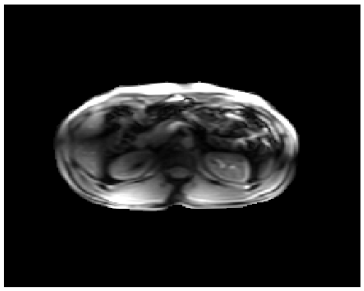
(a) B_1^+ map acquired with linear mode transmit RF phase settings.



(b) Gradient echo image acquired with linear mode transmit RF phase settings.



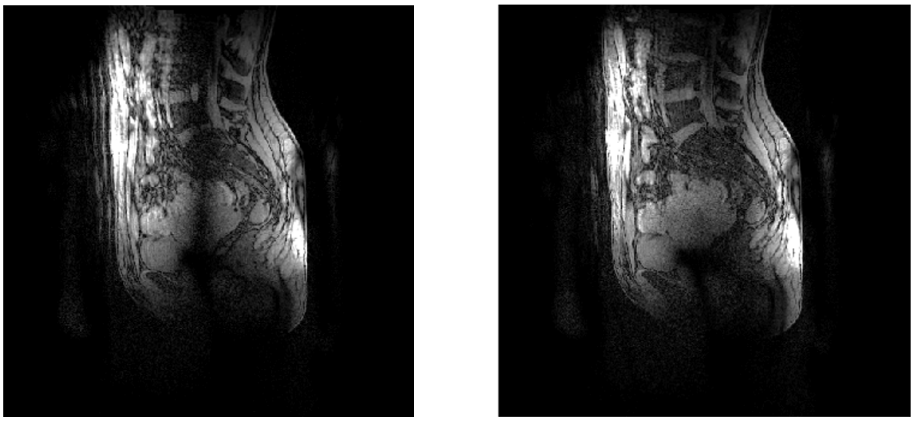
(c) B_1^+ map acquired with quadrature mode transmit RF phase settings.



(d) Gradient echo image acquired with quadrature mode transmit RF phase settings.

Figure 3.6: Example of the importance of transmit RF phase settings for calibration scans.

However, the 45° quadrature mode was used when imaging the centre of the body and when calibration scans were degraded due to the common band of destructive interference identified through the centre of subjects. This was the case when attempting to image the uterus within healthy volunteers (see Chapter 7). Figure 3.7 (a) shows a sagittal image acquired using the linear mode phase settings, and (b) shows the same image slice acquired with the 45° quadrature mode. The 45° quadrature mode was essential for the sagittal images that used as localiser and calibration scans performed before RF shimming was implemented.



(a) Linear mode. (b) Quadrature mode.

Figure 3.7: Examples of linear and quadrature mode transmit RF settings used in localiser scans for uterus imaging.

3.4.2 Coil Scattering Matrix

The scattering parameter (S-parameter) is the complex ratio of the reflected signal on a particular transmit channel to the incident signal on the same or a different transmit channel [28]. It can be measured physically from the forward and reflected power measurements made by the bi-directional couplers on each transmit channel. S-parameters are commonly quoted in units of decibels (dB).

They can be presented as N_{TX} x N_{TX} matrices (where N_{TX} is the total number of transmit RF channels) and provide a way of demonstrating the coupling that exists between the elements of a pTx array. S-matrices also offer insight to the robustness of fixed tuning for specific loading conditions of the body array. The S-matrices can vary across subjects with different BMI's which means that the power characteristics and coil coupling vary on a subject basis. S-matrices extracted from the log files compiled from scan sessions with four different volunteers are presented in Figure 3.8 and show how the coupling between elements can change, particularly between nearest neighbour elements.

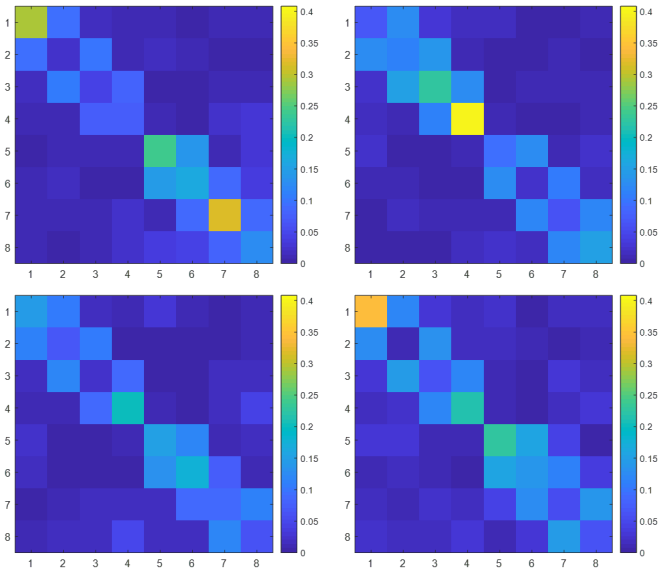


Figure 3.8: Example of S-matrices acquired in different in vivo scanning sessions.

S-matrices can have other applications such as detecting cardiac and respiration motion which have shown promising results for use in cardiac gating and diaphragm tracking on pTx systems [29–31]. They have also been used to inform local SAR measurements and improve the accuracy of the predictions [28].

3.4.3 Receive Coil Array

The RF transmit dipoles and RF receive coils are located within the same volume. The voltages required to transmit the RF fields are many times the magnitude of the induced signal from precessing spins within the sample, and the receive coils are gated off during transmission to avoid damaging the equipment. The induced signals detected by each receive coil are amplified by pre-amps before being recorded. This creates recorded signals large enough to overcome any noise that can be generated by the electronics.

Signals are detected using quadrature phase sensitive detection which uses two Phase Sensitive Detectors (PSD) with reference signals 90° out-of-phase from each other. The reference signals are produced by the frequency synthesizer and so are close to the Larmor frequency. The detected signals are mixed with the reference frequency in each PSD to demodulate the signal to audio frequencies. Once the signals have been processed, they are fed to an analogue to digital converter (ADC) and then sent back to the console where the signals are processed to form images of the sample.

The body array is designed to detect signal with the 32 receive loops distributed across all the elements. Loops are commonly used as receive elements at all field strengths [32, 33]. Alternatively, the eight dipoles can also be used in receive mode. The fractionated dipoles in the RF coil have been shown to present homogenous receive sensitivity [27] and it has been suggested that receiving on dipoles improves performance compared to receiving on loops at UHF [34].

3.4.3.1 Investigation of Receive Coil Configurations

An experiment was performed to assess the receive options available on the scanner with the body phantom (see Section 3.7). Normalised SNR was calculated from two data sets of gradient echo images (flip angle = 3°, TR = 30 ms, voxel size = 2.3 x 2.3 x 10 mm^3, number of slices = 10, slice gap = 125 mm) acquired (1) with the 32 receive loops, SNR_{32}, and (2) with the 8 dipoles as receive elements, SNR_8. The images were acquired in a coronal geometry with

slice 1 adjacent to anterior array, and slice 10 closest to the posterior array (see Figure 3.10 (a)).

Noise was calculated as the voxel-by-voxel difference between consecutive acquisitions. The ratio of SNR_{32}:SNR_8 was calculated and is presented in Figure 3.9. A ratio value greater than 1 reflects regions where the receive loops have outperformed the dipole receive configuration ($SNR_{32} > SNR_8$). This is the case for most areas in slices 1 to 8, especially around the periphery of the elements. However, in slices 9 and 10 (closest to the posterior array) the ratio is less than 1 suggesting that for posterior imaging (e.g. imaging or spectroscopy of the back muscle and superficial adipose layers) that using the dipole receive configuration might be advantageous in terms of SNR.

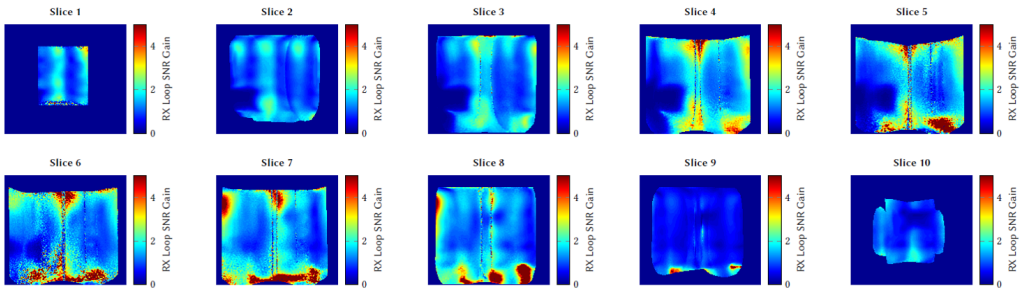


Figure 3.9: Ratio of loop receive to dipole receive SNR data in each slice. In regions where the ratio is greater than 1 the loop receive outperforms the dipole receive mode. Voxels with values less than 1 reflect where the SNR in the dipole receive data is greater.

SNR values were sampled along the length of the four dipole positions (A-D) in the foot-head direction in each image as shown in Figure 3.10 (a). The mean SNR_{32} and SNR_8 profiles were sampled and plotted for slices 1 to 10; these results are shown in Figure 3.10 (b). The mean SNR profiles decrease towards the centre of the phantom as expected due to the decrease in signal further from the transmit elements. SNR_8 profiles appear smoother than the SNR_{32} profiles along the lines of interest, particularly in slices 2 and 3. The higher mean SNR_8 values in slices 9 and 10 reinforce the findings that higher SNR is achieved with the dipole receive configuration posteriorly.

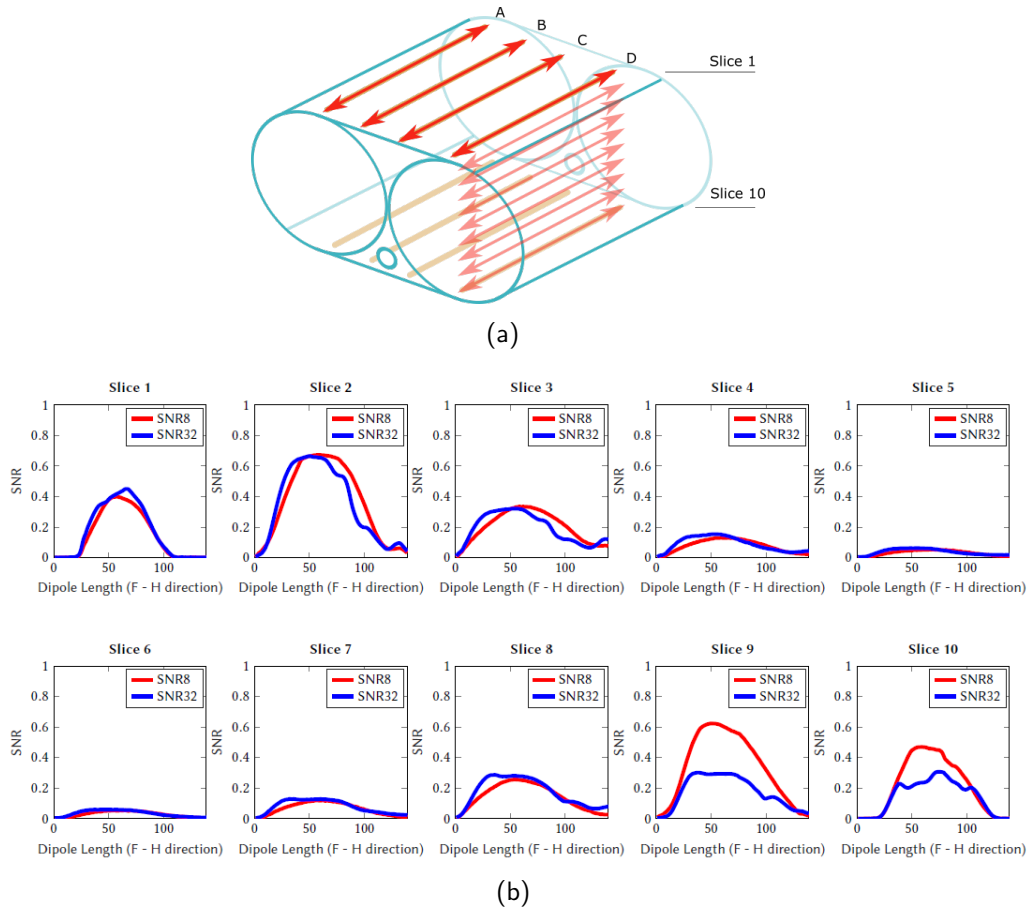
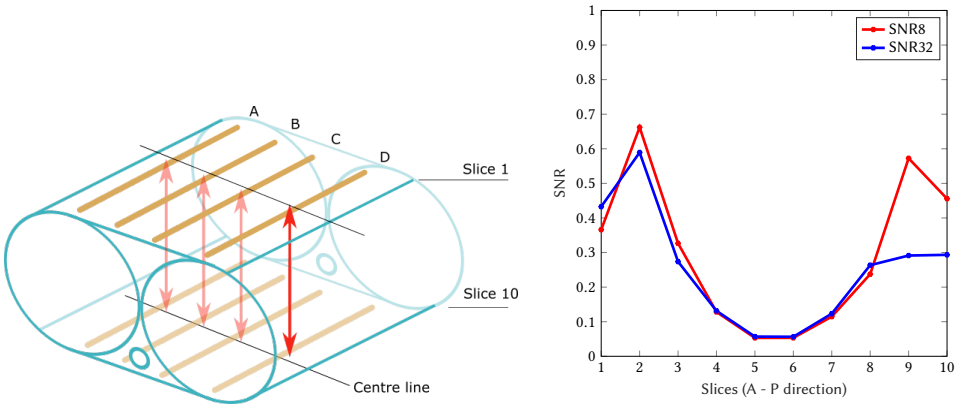


Figure 3.10: Coil SNR measured along length of each dipole (F - H direction) from coronal SNR maps. (a) Red arrows indicate the location of the SNR measurements. (b) Subplots from left to right display data from nearest the transmit arrays to the centre of the phantom. Slices for anterior and posterior elements taken nearest to respective arrays (subplot1: slices 1 & 10, subplot2: slices 2 & 9, subplot3: slices 3 & 8, subplot4: slices 4 & 7, subplot5: slices 5 & 6).

SNR values were then studied in the anterior-posterior direction along the centre line of the phantom at each of the four dipole positions (A-D) as shown in Figure 3.11 (a). The mean SNR_{32} and SNR_8 profiles were calculated over the four dipole positions and plotted as a function of slice number (see Figure 3.11 (b)). Both mean SNR profiles present similar drop-off characteristics towards the centre of

the phantom from the anterior and posterior slices. The mean SNR_8 data is higher towards the posterior slices (slices 9 and 10).



(a) (b)

Figure 3.11: Coil SNR measured in each slice (A - P direction) from coronal SNR maps at the mid-point of the F - H line of the phantom. (a) Red arrows indicate the location of the SNR measurements. (b) SNR from dipole and loop receive data.

In conclusion, in some cases it may be beneficial to use the dipoles for both transmit and receive configurations, particularly for posterior imaging applications. RF coil models do exist that receive with a combination of both loops and dipoles [35, 36]. These types of coils can yield enhanced SNR values compared with receiving with loops or dipoles only [37].

3.5 RF Power Optimisation

Power Optimisation (PO) is always problematic at 7 T systems due to the high variability of the RF transmit field. PO is normally performed by the MR system on a central, transversal slice adopting the method used at 3 T (where there is a Quadrature Body Coil (QBC)) by implementing a double spin-echo stimulated-echo sequence in which the echo amplitudes have a simple relationship to flip angle. A reference scale related directly to the power that comes from the amplifier is then adjusted so that the desired flip angle is achieved.

However, variation in flip angle across the FOV at 7 T makes an image based PO desirable. This is especially the case for body imaging where a larger dynamic range of flip angles, severe B_1^+ inhomogeneities and effects from the local transmit coil give rise to complicated spatial distributions. Therefore, for the work throughout this thesis the PO step for body imaging at 7 T is performed manually by the scanner operator as opposed to the scanner software. A B_1^+ map is acquired, and the percentage of the requested flip angle is measured in a ROI. The drive scale is a scale factor related to the RF demand that can be adjusted to cater for variations in load across subjects. This is adjusted so that the actual flip angle is equal to 100 % of the requested flip angle in the ROI used for the PO calibration.

3.6 SENSE for 7 T Body Imaging

Coping with the absent QBC: there is no QBC on the 7 T and so the SENSE reconstruction algorithm uses an alternative QBC image. A synthetic QBC image is created from the sum of squares of the individual receive coil images.

RF shimming considerations: the SENSE reconstruction algorithm knows nothing about the actual RF shim values in the coil file. Therefore, SENSE reference scans need to be repeated after the desired RF shim has been calculated.

3.7 Creating a 7 T Body Phantom

When assessing MR sequences and calibrating and checking MRI equipment it is useful to first test these on phantoms that are designed to have similar loading and relaxation properties as the organs of interest. For work performed with the 7 T body array, a phantom designed to replicate the loading conditions of a human torso was constructed to aid in the calibration of the body array and development of imaging protocols.

The phantom is constructed from three acrylic cylinders and two acrylic sheets to form a water-tight container. A schematic of the phantom design can be

seen in Figure 3.12. The measurements of the phantom are 40 cm x 37 cm x 20 cm.

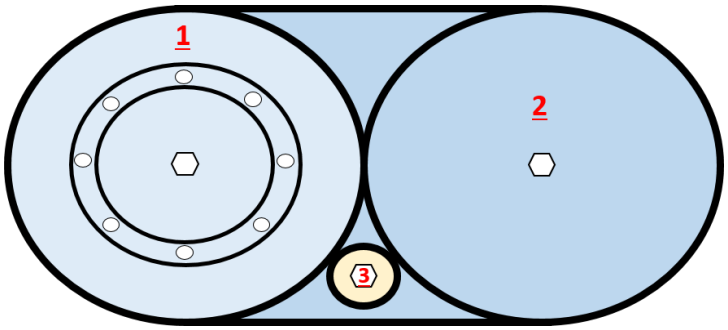


Figure 3.12: Schematic diagram of body phantom: consists of three compartments (1) left hand cylinder holds 9 litres of solution and has removable lid section for potential inserts to be administered (2) right hand cylinder attached to mid-section holds 11 litres of solution (3) small column along central posterior of phantom with potential to mimic spinal fluid, currently filled with vegetable oil for fat/water applications.

The left hand side cylinder has a removable lid for access which allows for the capability for placing objects within the phantom. This allowed for the insertion of plastic balls containing fat emulsions to do preliminary fat quantification work and will be useful for future applications such as flow and studying smaller regions of varying relaxation times. This compartment is labelled 'Section 1' of the phantom.

The right hand side cylinder is connected to the mid-section of the phantom via holes in the top and bottom of the acrylic cylinder. Therefore, the solution that fills this cylinder, also fills the middle remaining section. Collectively, this compartment is labelled 'Section 2'. Finally, the small column in the middle of the posterior side of the phantom extends along its full length to mimic the spine. This cylinder, labelled as 'Section 3', contains vegetable oil and has allowed for observations of chemical shift and provides a region of interest for setting up MR spectroscopy scans for investigating fat spectra. The three sections of the phantom can be identified in Figure 3.12 and a photograph of the phantom can be seen in Figure 3.13.

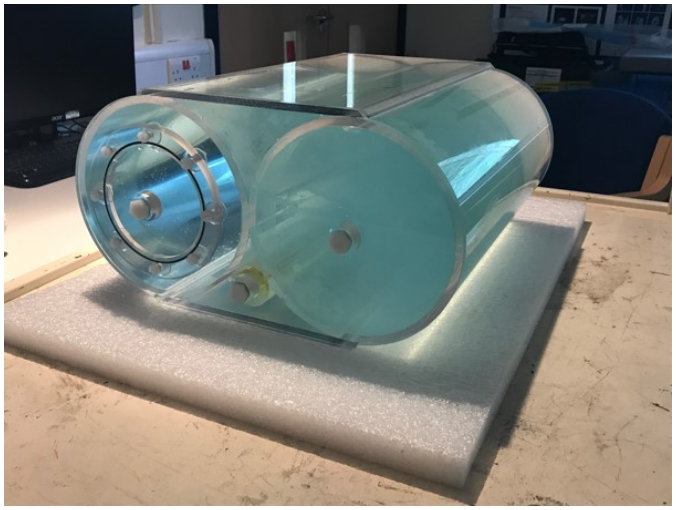


Figure 3.13: Photograph of the body phantom.

Sections 1 and 2 were both filled with physiological saline solution (9g/L NaCl). Section 1 contained 1 mM of copper sulphate (mM, Copper (II) sulphate pentahydrate 98%, Acros Organics), and section 2 contained 0.5 mM of the same copper sulphate compound. Section 3 was filled with pure vegetable oil.

All solutions and oils were siphoned into the phantom. Due to the small access holes to each of the sections it was decided that using agar solutions would restrict the use of the phantom. Keeping the phantom in a liquid state would mean each of the sections could be altered for future experiments and replaced if required.

The phantom was generally free from air bubbles and homogenous within each of the sections. Therefore, it performed well as a sequence development aid. A single transverse slice through the phantom is shown in Figure 3.14.

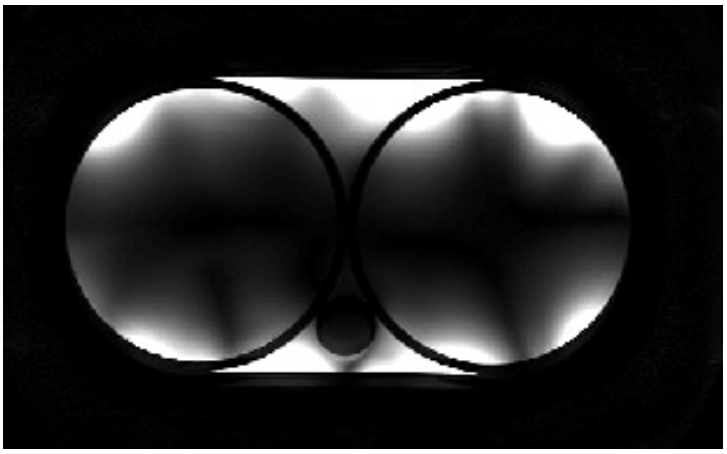


Figure 3.14: Image from survey scan on the body phantom.

3.8 Specific Absorption Rate

The Specific Absorption Rate (SAR) is a measure of the energy deposited by RF in biological tissue. The transfer of RF radiation energy can cause heating effects that arise from the interaction of the electric fields. SAR is proportional to the product of conductivity, σ, and square of the electric field, E, and inversely proportional to the material density, ρ [12, 38, 39]. At a specific location $\mathbf{r}$, SAR is described with the following equation:

$$SAR(\mathbf{r}) = \frac{\sigma(\mathbf{r})}{2\rho(\mathbf{r})}|E(\mathbf{r})|^2 \tag{3.3}$$

Global SAR is averaged over the subject's whole-body or certain body sections and local SAR is typically averaged over 1g or 10g of biological tissue. Local and global SAR limits are governed by international standards and adhered to in all clinical and research settings. Local SAR limits exist for the head, trunk and extremities [40]. These limits are established by the International Electrotechnical Commission (IEC) and outlined in guidance document IEC 2010 60601-2-33 [41]. The commission recommends different limits depending on use of volume transmit and local transmit coils and these are summarised in Tables 3.1 and

3.2. For the work relevant in this thesis the limit of interest is the 10 Wkg^{-1} local SAR limit placed on the trunk in the normal operating mode.

Table 3.1: SAR Limits for volume transmit coils: ^{a}These limits scale dynamically with the ratio "exposed patient mass/patient mass". In the "Normal Operating Mode": Partial body SAR = 10 Wkg^{-1} - (8 Wkg^{-1}*exposed patient mass/patient mass).

Averaging Time	6 minutes		
	Whole Body SAR	Partial Body SAR	Head SAR
Body Region →	Whole Body	Exposed Body Part	Head
Operating Mode ↓	(Wkg^{-1})	(Wkg^{-1})	(Wkg^{-1})
Normal	2	2-10^a	3.2
First level controlled	2	4-10^a	3.2
Second level controlled	>4	>(4-10)^a	>3.2
Long MR Examination	Max allowed SAR is 240 W.min.kg^{-1} per MR exam		
Short duration SAR	SAR limits over any 10 second period should not exceed 2 x stated values		

Table 3.2: SAR Limits for local transmit coils: ^{a}NOTE in cases where the orbit is in the field of a local RF transmit coil, care should be taken to ensure that the temperature rise is limited to 1°C.

Averaging Time	6 minutes		
	Local SAR		
Body Region →	Head	Trunk	Extremities
Operating Mode ↓	(Wkg^{-1})	(Wkg^{-1})	(Wkg^{-1})
Normal	10^a	**10**	20
First level controlled	20^a	20	40
Second level controlled	>20^a	>20	>40
Short duration SAR	SAR limits over any 10 second period should not exceed 2 x stated values		

At 1.5 and 3 T (conventional, single channel MR systems) it is adequate to calculate the ratio of peak SAR to $(B_1^+)^2$ from simulated data and use this to determine the peak and time averaged SAR for different estimates of B_1^+ in real time [40]. Traditional methods to lower the SAR for a given MR sequence include adjusting imaging parameters to reduce the overall RF power deposition during

scanning. This might include scaling down the requested flip angle, increasing echo (TE) and repetition (TR) times and implementing parallel imaging [42]. This approach to reducing SAR can limit scanner performance and image quality. Therefore, there are also more innovative methods for reducing SAR that include novel coil design, manipulation of imaging sequences and optimised RF pulse design [43–45].

On moving to 7 T, SAR becomes a major limiting factor for scanner performance. SAR increases quadratically with B_0^2 and so it is inherently greater compared to SAR at lower fields; local transmit coils are used at 7 T which means there is more localised power deposition which can lead to high SAR; and, the shorter RF wavelengths cause inhomogeneities not only in the resultant B_1^+ field but also the electric field distribution which can produce complicated, unpredictable SAR distributions. The increase in SAR at 7 T can result in the acquisition of fewer slices, reduction of flip angles and longer TR's; these steps can often counteract the gain in intrinsic SNR.

When using a conventional 7 T system in quadrature mode the Philips scanner uses a similar approach to estimate SAR as at 1.5 and 3 T by estimating the relationship between B_1^+ and SAR for the coil. For pTx systems the electric fields produced by each transmit element are spatially and temporally variable. Therefore, the superposition of these fields can be complex due to the multiple degrees of freedom available [46]. Unexpected hotspots can occur in different locations due to constructive interference of the electric fields generated by each transmit element. These SAR hotspots can also occur in different areas in different subjects due to variation in the positioning of the subject and individual body tissue compositions [47].

It is impossible to know the locations of these hotspots a priori and it is no longer feasible to simply scale the global and local SAR according to the B_1^+ of the RF waveform applied as the SAR patterns can vary with the relative phase settings of the transmit coil elements [40]. Therefore, for pTx it is especially important to accurately simulate the expected SAR from different profiles of

electric fields [12]. There is also a need for accurate predictions of SAR for individualised models and experimental situations that accurately reflect specific coils, RF pulses, body compositions and subject positioning within the bore of the scanner.

pTx can also be used to lower SAR and local SAR hotspots. Reducing SAR is a major target in both static and dynamic pTx optimisations [26, 48] and it has been shown that improving B_1^+ homogeneity whilst simultaneously controlling RF power and lowering SAR within localised ROIs is possible [17].

3.9 RF Modelling

3.9.1 EM Simulations using FDTD

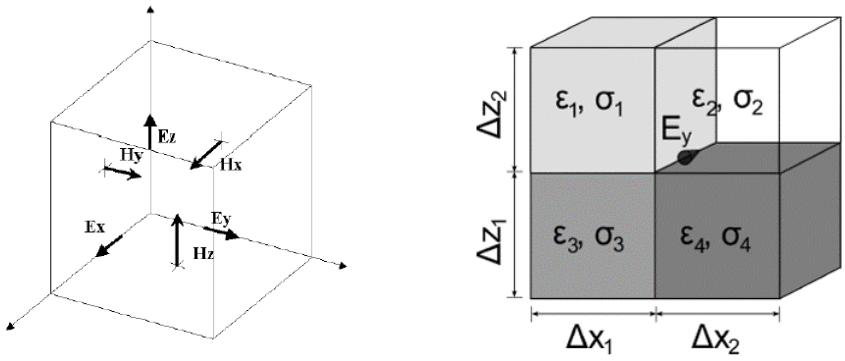
Local SAR distributions are investigated by modelling the excitation magnetic field, $\boldsymbol{B_1}$, and electric field, $\boldsymbol{E}$, in EM simulations using the Finite-Difference Time-Domain (FDTD) method. This is a numerical analysis technique used for modelling computational electrodynamics. It is a time domain method and so can be used to investigate large frequency ranges within a single simulation run and deal with non-linear material properties [49].

The FDTD method is based on a finite difference approximation of Maxwell's time domain equations:

$$\nabla \times \boldsymbol{E} = -\mu \frac{\partial \boldsymbol{H}}{\partial t} \tag{3.4}$$

$$\nabla \times \boldsymbol{H} = \sigma \boldsymbol{E} + \epsilon \frac{\partial \boldsymbol{E}}{\partial t} \tag{3.5}$$

These equations are solved by updating the field quantities in a leapfrog manner such that electric and magnetic field vectors are solved at every time step, but interlaced half-a-step apart in both time and space [50]. This process is repeated until the steady-state EM field behaviour has finally evolved [51].



(a) Yee cell with labelled field components.

(b) E_y component enclosed by four Yee cells with different dielectric components [52].

Figure 3.15: (a) Demonstration of FDTD 3D Yee cell and (b) how these are used to make up the computational grid in EM simulations.

Computational space is based on a Cartesian rectangular grid composed of Yee cells (named after the mathematician, Yee, who first described the FDTD technique [53]). The electric field vectors are derived along the edges of these cells and the magnetic field vectors are derived at the centre of the electric field surfaces in perpendicular directions as shown in Figure 3.15 (a). Due to the nature of how the total electric field is calculated on the edge of the Yee cell, the electric field corresponding to one Yee cell is based on the weighted average of the dielectric properties of the material that occupies the four adjacent cells. This concept is illustrated in Figure 3.15 (b).

Boundary conditions are important in FDTD simulations as they are used to truncate computational space in open region problems. The perfectly matched layer (PML) technique places an artificial layer of absorbing material around the outer boundary of the computational domain to completely absorb incident waves at all frequencies and incidence angles [49].

To ensure accuracy of the computed results, spatial increments must be small compared to the operating wavelength (typically $\leq \lambda/10$) [54] and selected to fully characterise minimum feature sizes, particularly subwavelength structures.

However, small cell sizes come at the cost of large runtimes and memory consumption [55]. This can be problematic for models with curved surfaces where small cell sizes are desired in order to fully characterise the shape of an object. Cartesian FDTD methods can only provide a "stair-case" approximation to these models [56]. Tetrahedral grids have been developed (for FDTD simulations) offering cells that conform to curved objects whilst maintaining stable results [57].

It is necessary to verify the results from FDTD simulations before local SAR predictions can be used for setting power limits for in vivo exams. The simulation models are normally verified by comparing simulated B_1^+ field distributions to experimentally acquired B_1^+ distributions on the same object of interest (for example, a phantom or a specific subject model). If the B_1^+ distributions are similar then it provides some confidence that the simulated electric fields are modelled accurately. However, similarity between simulated and measured B_1^+ fields does not always guarantee similar agreement in the electric fields as different B_z components can generate different electric fields. Numerical results can be verified more directly using field probe measurements and MR thermometry [58] but such experiments are time consuming and can be difficult to perform in vivo.

3.9.2 Local SAR Calculation

This section uses the notation presented by Graesslin et al. [39].

The SAR at location x during transmit period, t_i can be calculated from the electric field information, **E**, mass density, ρ, electrical conductivity, σ and averaging volume, V

$$\mathrm{SAR}_{\mathsf{sample}}(\mathbf{x}, t_i) = \frac{1}{V}\int_V \frac{\sigma(\mathbf{x})}{2\rho(\mathbf{x})}.||\mathbf{E}(x, t_i)||_2^2 \mathrm{dV} \tag{3.6}$$

This expression is modified for pTx where N_c is the number of transmit RF channels and $\mathbf{E}_c$ is the electric field generated by each transmit element, c.

$$\mathrm{SAR}_{\mathrm{sample}}(\mathbf{x}, t_i) = \frac{1}{V}\int_V \frac{\sigma(\mathbf{x})}{2\rho(\mathbf{x})}.\left|\left|\sum_{c=1}^{N_c}\mathbf{E}_c(\mathbf{x}, t_i)\right|\right|_2^2 \mathrm{dV} \tag{3.7}$$

3.9.2.1 Q-Matrix Formalism

Local and global SAR can be calculated from simulated electric fields. First, the electric fields, $\mathbf{E}_c$, are scaled to 1 W input power per channel. This leads to an electric field vector $\tilde{\mathbf{E}}_c$ that summarises the three orthogonal components in a 3 x N_c matrix for each location, **x**. The RF waveforms produced by each individual transmit element are proportional to the currents within the elements, therefore the waveforms can be represented by a phasor $\mathbf{I}(t_i)$ at each time point t_i

$$\mathbf{E}(\mathbf{x}, t_i) = \sum_{c=1}^{N_c}\mathbf{E}_c(\mathbf{x}, t_i) = \tilde{\mathbf{E}}(\mathbf{x}).\mathbf{I}(t_i) = \begin{pmatrix} \tilde{\mathbf{E}}_{x,1}(\mathbf{x}) & \cdots & \tilde{\mathbf{E}}_{x,N_c}(\mathbf{x}) \\ \tilde{\mathbf{E}}_{y,1}(\mathbf{x}) & \cdots & \tilde{\mathbf{E}}_{y,N_c}(\mathbf{x}) \\ \tilde{\mathbf{E}}_{z,1}(\mathbf{x}) & \cdots & \tilde{\mathbf{E}}_{z,N_c}(\mathbf{x}) \end{pmatrix} . \begin{pmatrix} \mathbf{I}_1(t_i) \\ \vdots \\ \mathbf{I}_{N_c}(t_i) \end{pmatrix} \tag{3.8}$$

$\mathbf{I}(t_i)$ represents the relationship between the amplitude and phase of the time varying signals and the RF waveform on each channel produced following RF shimming or pulse design.

$\tilde{\mathbf{E}}_{i,N_c}(\mathbf{x})$ is the amplitude and phase of each x, y and z component of the electric field produced from each transmit channel in the unshimmed, default setting.

The expression for SAR is now

$$\mathrm{SAR}_{\mathrm{sample}}(\mathbf{x}, t_i) = \frac{1}{V}\int_V \frac{\sigma(\mathbf{x})}{2\rho(\mathbf{x})}.\left|\left|\tilde{\mathbf{E}}(\mathbf{x}).\mathbf{I}(t_i)\right|\right|_2^2 \mathrm{dV} \tag{3.9}$$

Whilst $\mathbf{I}(t_i)$ can change between RF pulses, $\tilde{\mathbf{E}}(\mathbf{x})$ is constant for a given coil geometry **x**; so, to speed up SAR calculation a Q-matrix is calculated at each

x location on the simulation grid. The Q-matrix summarises the SAR in each location for a unit power supplied on each transmit element, averaged over a volume, V, or a certain mass, m. Methods used to perform mass averaging are discussed in the next section.

$$\boldsymbol{Q}(\boldsymbol{x}) = \frac{1}{V}\int_V \frac{\sigma(\boldsymbol{x})}{2\rho(\boldsymbol{x})}.\tilde{\boldsymbol{E}}^{\dagger}(\boldsymbol{x}).\tilde{\boldsymbol{E}}(\boldsymbol{x})dV \tag{3.10}$$

As the integral only depends on the normalised electric field and local tissue properties the local **Q** matrix of size N_c x N_c can be calculated independent of t_i. The local SAR at location **x**, at time t_i is expressed as

$$\mathrm{SAR}_{\mathsf{sample}}(\mathbf{x}, t_i) = \mathbf{I}^{\dagger}(t_i).\boldsymbol{Q}(\mathbf{x}).\mathbf{I}(t_i) \tag{3.11}$$

where the phasors are given from the specific RF setting under investigation.

3.9.3 Effective Methods for Calculating Local SAR

The IEC and FDA require that SAR is averaged over 10 gram mass volumes to calculate local SAR as it directly relates to local temperature elevation which is the limiting factor for MR safety protocols [59]. Commercially available RF numerical simulators (for example XFDTD (Remcom, Inc.; State College, PA; USA)) have built-in algorithms that compute the local n-gram average SAR. These algorithms are based on the method presented in the IEEE Std C95.3-2002(R2008) documentation [60], where a cubical volume centred in a voxel of interest is expanded in all directions until the volume encompasses the desired mass. If the cubical volume does not extend beyond the surface of the body the volume is classed as valid, and all voxels in the volume are used to compute the averaged SAR for the voxel of interest. An example of this is shown in the upper cube of Figure 3.16.

However, the cubical volume is built around a central voxel and expands until it reaches the total required mass, regardless of the amount of air enclosed in the

volume (as is the case for the middle and bottom squares in Figure 3.16). As long as the surface boundaries do not extend beyond the most exterior surface of the body, the cubical volume is considered valid and all voxels contained within the volume are included in the averaging process (middle cube, Figure 3.16).

A cubical volume is considered invalid if the volume has external surfaces with no voxels internal to the body (bottom cube, Figure 3.16). In this case, the averaged SAR value assigned to the central voxel is the maximum averaged SAR value of the valid voxels which can lead to problems in the resulting local SAR distribution.

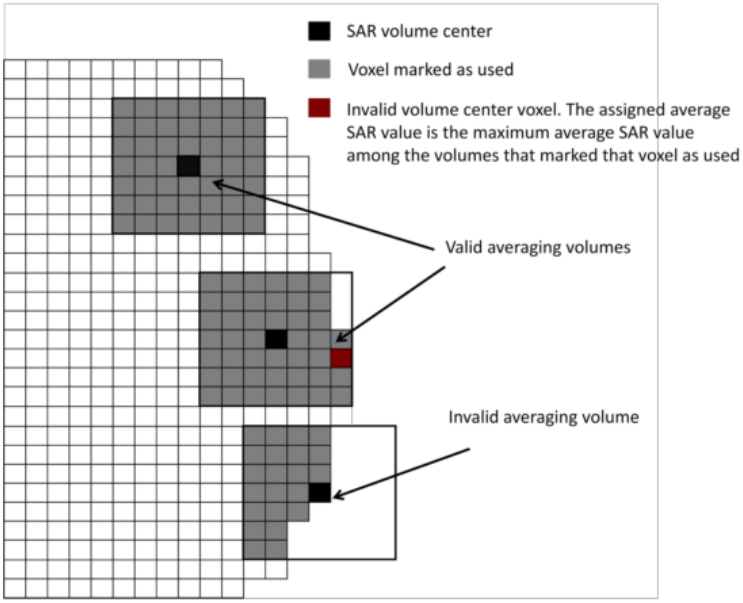
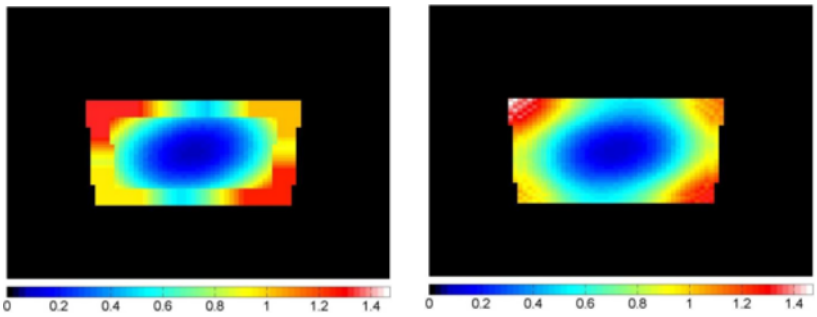


Figure 3.16: Demonstration of cubical mass averaging method. Figure from: [61]

An example of this cubical averaging method applied to a SAR distribution simulated by Carluccio et al. [61] is presented in Figure 3.17 (a). The SAR distribution was generated by a birdcage coil on a box of water. It demonstrates the discontinuities present in the computed averaged SAR that arise due to the most external voxels being assigned the highest SAR value within their respective

valid mass volume. This is particularly problematic when the method is applied to large average mass volumes (i.e. 10 g average). The 10g averaging mask is relatively large which results in more voxels in the final averaged SAR map with values that are calculated within volumes that are not centred on them. This causes highly conservative and inaccurate results in external voxels which is undesirable. These voxels are highly relevant in MR safety as they are nearest to the coil and exposed to high RF energy.



(a) Cubical averaging method. (b) Adaptive Spherical averaging method.

Figure 3.17: Local SAR distributions generated by a birdcage coil on a box of water. (a) local SAR distribution calculated using standard cubical averaging method, (b) local SAR distribution calculated using adaptive spherical averaging method. Figures from: [61]

An improved method for mass averaging is the adaptive spherical method and is presented in Figure 3.18 [62, 63]. This implements an algorithm that sequentially increases the radius of a spherical volume centred on the voxel of interest. Using a spherical volume minimises the distance between the central voxel and the other voxels within the volume, improving the accuracy of the SAR averaging (upper sphere, Figure 3.18). The adaptive aspect of this method ensures that the spherical volumes grow according to the shape of the model (see bottom sphere with adapted geometry in Figure 3.18).

The mass and the summed SAR of all the voxels in the most external voxel layer (m_s and SAR_s) and the interior volume (m_i and SAR_i) are calculated. When the total mass ($m_s + m_i$) exceeds 10 g, the SAR of the external layer is weighted so

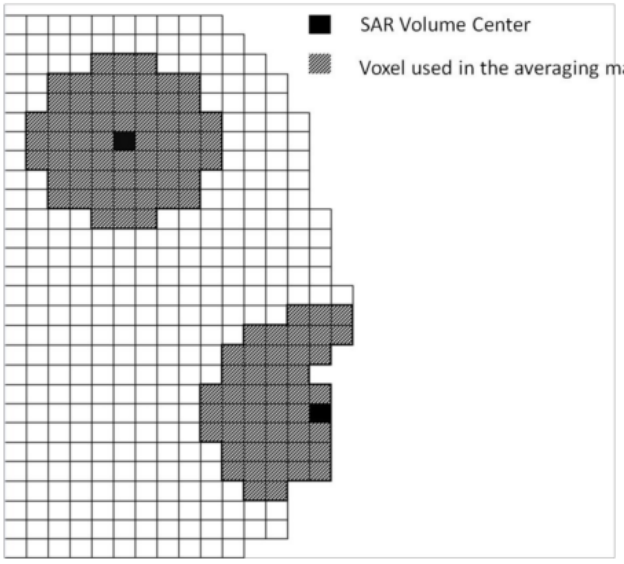


Figure 3.18: Demonstration of adaptive spherical mass averaging method. Figure from: [61]

that the total mass equals 10 g. The number of voxels contained in the external and internal layers are n_s and n_i respectively and the 10 g averaged local SAR is calculated as follows:

$$SAR_{10g} = \frac{\frac{10g-m_i}{m_s}(SAR_s + SAR_i)}{\frac{10g-m_i}{m_s}(n_s + n_i)} \tag{3.12}$$

This method overcomes the artificial inflation of high SAR values near surface-air interfaces and reduces the presence of discontinuities in the local SAR distribution (see Figure 3.17 (b)).

3.9.3.1 Development Work

For the work in this thesis, an alternative mass averaging method was implemented when calculating local SAR from the simulated electric field distributions. FDTD simulations were performed using optimised mesh settings that varied the cell sizes across computational space. This shortened the runtime of

the simulations and reduced the size of the data output from the EM software. Using the previously described methods to calculate 10 g averaged local SAR resulted in banding artefacts in the final results (see Figure 3.19 (a)). This was found to be due to the anisotropy of the voxel shapes.

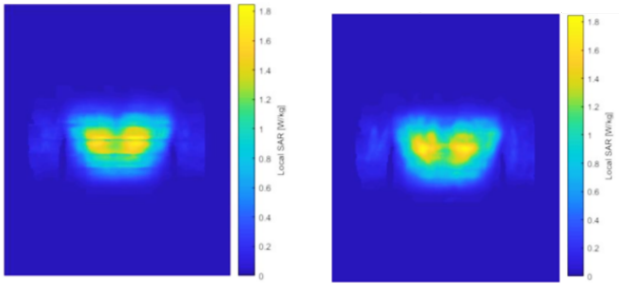
A method was developed to average SAR distributions based on an approximate 10 g spherical volume with a fixed predetermined radius that was calculated from the density of muscle tissue used in the human body models ($\rho = 1090$ kgm^{-3}). Muscle tissue has high density and therefore, the fixed sphere has a conservative 10 g volume, ensuring the averaged local SAR values assigned to each voxel throughout the model are not underestimated. Initially, this approach had a considerably long runtime (approximately 22 hours for one SAR distribution on the HPC) due to the anisotropic voxels and therefore was not practical for efficient online local SAR evaluation

To overcome this, the SAR distributions and density information were interpolated onto a 2 x 2 x 2 mm^3 grid using a cubic interpolation function (*interpn* function, Matlab R2018b). This increased the efficiency of this approach for calculating conservative local SAR distributions. To avoid any further overestimation of SAR values around the edges of the body, the fixed sphere was expanded until the region of the volume containing voxels within the body was equal to the number of voxels in the fixed sphere volume. This method removed the banding artefact in the final local SAR results (see Figure 3.19 (b)).

3.9.4 Virtual Observation Points

Virtual Observation Points (VOPs) can be used to reduce the complexity of predicting the peak local SAR in a given volume [64]. Rather than considering a Q-matrix in every voxel, VOPs enable a given model to be compressed so that a model-wide peak local SAR value can be estimated within a specified tolerance from the VOPs instead of monitoring the Q-matrices in all voxels in the 3D model [65].

VOPs capture the peaks in the underlying local SAR distribution and are deter-



(a) (b)

Figure 3.19: (a) Mass averaging banding artefact, (b) modified mass averaging method where artefact is removed.

mined by applying a lossy compression algorithm with a specified maximum SAR overestimation factor [66]. VOPs are an efficient method for fast computation of an approximate local SAR distribution. They can be extremely beneficial for real-time RF engineering calculations as they can be pre-computed for a given model and coil geometry and applied to peak local SAR computations for specific RF pulses.

3.10 MR Safety at UHF

The increase in static magnetic field strength at 7 T generates specific MR safety concerns. The risk of ferromagnetic objects interacting with the magnetic field is greatly increased and the fringe fields of the magnet can be considerably extended (see Figure 3.20). The 5 Gauss line is the level of static magnetic field exposure considered to be safe for the general public. No one with loose magnetic objects or implants should pass this line and this should be strictly adhered to especially for individuals with electronic devices such as pacemakers [67].

In terms of physiological effects induced by the increased static magnetic field, some subjects report cases of vertigo, metallic taste, nausea, light flashes and there are also recorded instances of nystagmus [58, 69]. Recent work suggests that experience of these short-term effects differs between active and passively

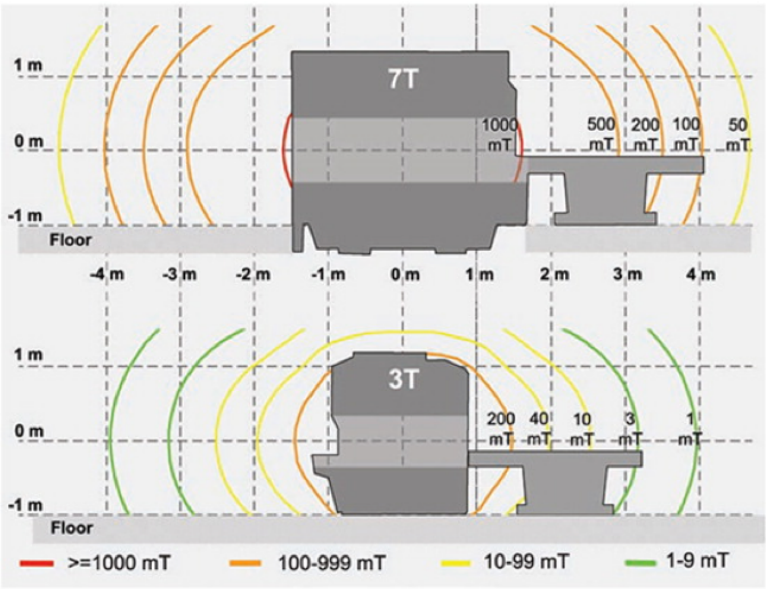


Figure 3.20: Comparison of 3 and 7 T fringe magnetic fields. Figure from [68].

shielded magnets [70] which may be related to the shielding or to other aspects of the system design. However, when compared to subjects' experiences of MRI scanning at lower field strengths these effects are not significantly worse, more likely to occur or less tolerable than those reported at 3 T [71].

Areas of concern also include increased blood pressure and heart rate [72] and effects on the cognitive system [73]. There are no reported instances of this being a clinical issue, but it is important to monitor these effects, particularly in patient volunteers. For the in vivo work performed throughout this thesis, subjects were put into the scanner bore foot first exposing the subjects' head to reasonable $\frac{dB}{dz}$. It was anticipated that subjects would be more likely to experience vertigo in this orientation but no instances were reported. Figure 3.21 shows a subject positioned foot first towards the bore of the 7 T scanner.

Peripheral Nerve Stimulation (PNS) occurs when time-varying magnetic fields generate electric fields inside the body which can interact with the normal function of nerve cells and muscle fibres to cause twitching and general discomfort during scanning. The gradient magnetic fields at 7 T are equivalent to those

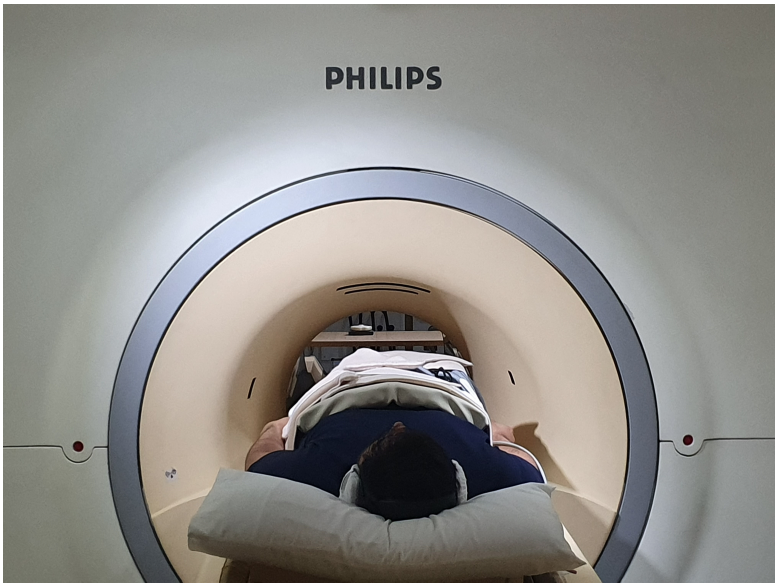


Figure 3.21: Demonstration of subject positioned in the foot first orientation before being entered into the bore of the scanner. Anterior section of body array is observed as well as ear protection for the subject.

used at lower field strengths and so the likelihood of experiencing PNS at 7 T is equivalent to the risk at 1.5 and 3 T [74, 75].

The limits placed on the RF fields which aim to lower the likelihood of excessive energy deposition in biological tissue are unchanged from lower field strengths. There is a shortage of research into how implants and tattoos that are MR safe at 1.5 and 3 T are affected by RF fields at 7 T [76–78]. This interaction requires accurate modelling of orientation and placement of the specific structures as well of the transmit mode of the scanner (see Figure 3.22 for an example of RF safety simulations concerning hip implants at 7 T). Therefore, subjects with these contraindications are usually excluded from scans at 7 T or local decisions are made on a case by case basis if the scan is required for clinical benefit.

At 7 T, the size of the scanner's bore and resonant RF frequency induces EM wave propagation along the longitudinal axis of the bore. The scanner bore acts as a waveguide and the propagating wave is known as a travelling wave. These

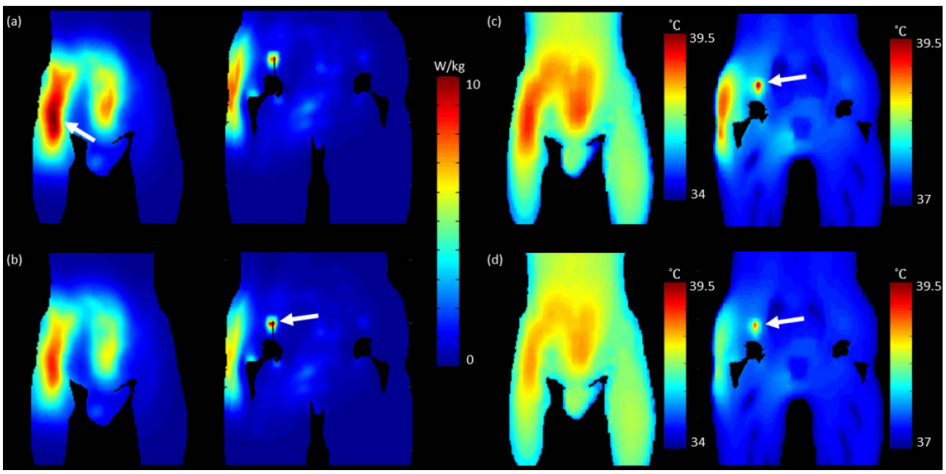


Figure 3.22: Example of simulated SAR (Wkg^{-1}) and associated RF heating ($^{\circ}C$) in patients with hip implants at 7 T [79].

waves mean that the RF fields can extend further than the local RF transmit coil which can be an additional source of deposited RF energy or can be exploited for imaging applications [80].

At 7 T local transmit RF coils and experimental hardware tend to be custom made and so require site specific safety checks and risk assessment. These include accurate modelling of the electromagnetic fields and validation with experimental measurements; hazard analysis and mechanical safety checks such as power measurements and built-in failure modes. International regulatory limits concerning MR safety put in place by governing bodies include the IEC EN 60601-2-33 [81], FDA [82] and ICNIRP (2009). A White Paper specifically on MRI safety at 7 T is due to be submitted by the ISMRM MR Safety Study Group.

3.11 Discussion and Conclusion

This chapter has outlined the advantages of imaging at 7 T and discussed the challenges associated with the higher Larmor frequency and the approaches that have been developed to overcome this. PTx and the associated hardware and software used throughout this thesis was described. Examples of the difference between receive loop and receive dipole configurations was given and images obtained with different transmit RF phase settings highlight the ability of the RF coil settings to influence the quality of images obtained. Therefore, knowledge of how the RF coil operates is key to 7 T body imaging.

The methods for RF power optimisation and SENSE at 7 T has been described, along with the construction of the body phantom that has been used extensively throughout this thesis. A summary of SAR and the associated theory related to RF modelling and local SAR calculation that was given which will be relevant to the work in Chapter 5. Finally, the safety considerations concerning 7 T MRI were discussed and conclude that if correct monitoring of the gradient and RF fields is in place, 7 T MRI applied to brain, musculoskeletal and whole-body imaging is not dangerous and induces the same level of physiological effects that are experienced at 1.5 and 3 T.

References

[1] Mark E. Ladd, Peter Bachert, Martin Meyerspeer, Ewald Moser, Armin M. Nagel, David G. Norris, Sebastian Schmitter, Oliver Speck, Sina Straub, and Moritz Zaiss. Pros and cons of ultra-high-field MRI/MRS for human application. *Progress in Nuclear Magnetic Resonance Spectroscopy*, 109:1–50, 2018.

[2] Andrew G Webb and Christopher M Collins. Parallel Transmit and Receive Technology in High-Field Magnetic Resonance Neuroimaging. *Int J Imaging Syst Technol*, 20:2–13, 2010.

[3] Fritz Schick. Whole-body MRI at high field: Technical limits and clinical potential. *European Radiology*, 15(5):946–959, 2005.

[4] David G. Norris. Adiabatic radiofrequency pulse forms in biomedical nuclear magnetic resonance. *Concepts in Magnetic Resonance*, 14(2):89–101, 2002.

[5] Priti Balchandani, Gary Glover, John Pauly, and Daniel Spielman. Improved slice-selective adiabatic excitation. *Magnetic Resonance in Medicine*, 71(1):75–82, 2014.

[6] Wei Luo, Michael T Lanagan, Christopher T Sica, Yeunchul Ryu, Sukhoon Oh, Matthew Ketterman, Qing X Yang, and Christopher M Collins. Permittivity and Performance of Dielectric Pads with Sintered Ceramic Beads in MRI: Early Experiments and Simulations at 3 T. 2012.

[7] Qing X. Yang, Weihua Mao, Jinghua Wang, Michael B. Smith, Hao Lei, Xiaoliang Zhang, Kamil Ugurbil, and Wei Chen. Manipulation of image intensity distribution at 7.0 T: Passive RF shimming and focusing with dielectric materials. *Journal of Magnetic Resonance Imaging*, 24(1):197–202, 2006.

[8] A G Webb. Dielectric Materials in Magnetic Resonance. *Concepts in Magnetic Resonance Part A*, 38A(4):148–184, 2011.

[9] David C. Alsop, Thomas J. Connick, and Gabor Mizsei. A spiral volume coil for improved rf field homogeneity at high static magnetic field strength. *Magnetic Resonance in Medicine*, 40(1):49–54, 1998.

[10] J Thomas Vaughan, Hoby P Hetherington, Joe Otu, Jullie W Pan, and Gerald M Pohost. High Frequency Volume Coils. *Spectroscopy*, C:206–218, 1994.

[11] Ulrich Katscher and Peter Börnert. Parallel RF transmission in MRI. *NMR in Biomedicine*, 19(3):393–400, 2006.

[12] Francesco Padormo, Arian Beqiri, Joseph V. Hajnal, and Shaihan J. Malik. Parallel transmission for ultrahigh-field imaging. *NMR in Biomedicine*, 2015.

[13] Gregor Adriany, Pierre Francois Van De Moortele, Florian Wiesinger, Steen Moeller, John P. Strupp, Peter Andersen, Carl Snyder, Xiaoliang Zhang, Wei Chen, Klaas P. Pruessmann, Peter Boesiger, Tommy Vaughan, and Kamil Uğurbil. Transmit and receive transmission line arrays for 7 tesla parallel imaging. *Magnetic Resonance in Medicine*, 53(2):434–445, 2005.

[14] Cem Murat Deniz, Ryan Brown, Riccardo Lattanzi, Leeor Alon, Daniel K. Sodickson, and Yudong Zhu. Maximum Efficiency RF Shimming: Theory and Initial Application for Hip Imaging at 7 Tesla. *Magn Reson Med.*, 69(5):1379–1388, 2013.

[15] Weihua Mao, Michael B. Smith, and Christopher M. Collins. Exploring the limits of RF shimming for high-field MRI of the human head. *Magnetic Resonance in Medicine*, 56(4):918–922, 2006.

[16] Kawin Setsompop, L. L. Wald, V. Alagappan, B. A. Gagoski, and E. Adalsteinsson. Magnitude least squares optimization for parallel radio frequency

excitation design demonstrated at 7 tesla with eight channels. *Magnetic Resonance in Medicine*, 59(4):908–915, 2008.

[17] Bob van den Bergen, Cornelis A T Van den Berg, Lambertus W Bartels, and Jan J W Lagendijk. 7 T body MRI: B1 shimming with simultaneous SAR reduction. *Physics in Medicine and Biology*, 52(17):5429–5441, 2007.

[18] Kawin Setsompop, Lawrence L Wald, and Elfar Adalsteinsson. Reduced-Voltage RF Shimming for Adiabatic Pulse Design in Parallel Transmission. *Proc Intl Soc Mag Reson Med 15 (2007)*, 15:1687, 2007.

[19] M. A. Cloos, N. Boulant, M. Luong, G. Ferrand, E. Giacomini, D. Le Bihan, and A. Amadon. K T-points: Short three-dimensional tailored RF pulses for flip-angle homogenization over an extended volume. *Magnetic Resonance in Medicine*, 67(1):72–80, 2012.

[20] Vincent Gras, Franck Mauconduit, Alexandre Vignaud, Alexis Amadon, Denis Le Bihan, Tony Stöcker, and Nicolas Boulant. Design of universal parallel-transmit refocusing k T -point pulses and application to 3D T 2 -weighted imaging at 7T. *Magnetic Resonance in Medicine*, 80(1):53–65, 2018.

[21] Chao Ma, Dan Xu, Kevin F. King, and Zhi-Pei Liang. Joint design of spoke trajectories and RF pulses for parallel excitation. *Magnetic Resonance in Medicine*, 65(4):973–985, 2011.

[22] M M Khalighi, M Saranathan, W Grissom, A B Kerr, R Watkins, and B K Rutt. Parallel Transmit using 3D Spokes RF Pulses for Improved B1+ Homogeneity over 3D Volumes. Technical Report 6, 2006.

[23] Lawrence. L. Wald and Elfar Adalsteinsson. Parallel Transmit Technology for High Field MRI. Technical report, 2009.

[24] William A Grissom, Laura Sacolick, and Mika W Vogel. Improving high-field MRI using parallel excitation. *Imaging Med*, 2(6):675–693, 2010.

[25] Ulrich Katscher, Peter Börnert, Christoph Leussler, and Johan S. Van den Brink. Transmit SENSE. *Magnetic Resonance in Medicine*, 49(1):144–150, 2003.

[26] Yudong Zhu. Parallel Excitation with an Array of Transmit Coils. *Magnetic Resonance in Medicine*, 51(4):775–784, 2004.

[27] Alexander J.E. Raaijmakers, Michel Italiaander, Ingmar J. Voogt, Peter R. Luijten, Johannes M. Hoogduin, Dennis W.J. Klomp, and Cornelis A.T. van den Berg. The fractionated dipole antenna: A new antenna for body imaging at 7 Tesla. *Magnetic Resonance in Medicine*, 75(3):1366–1374, 2016.

[28] Matthew Restivo, Alexander Raaijmakers, Cornelis van den Berg, Peter Luijten, and Hans Hoogduin. Improving peak local SAR prediction in parallel transmit using in situ S-matrix measurements. *Magnetic Resonance in Medicine*, 77(5):2040–2047, 2017.

[29] Aaron T. Hess, Elizabeth M Tunnicliffe, Christopher T. Rodgers, and Matthew D. Robson. Diaphragm position can be accurately estimated from the scattering of a parallel transmit RF coil at 7 T. *Magnetic Resonance in Medicine*, 79(4):2164–2169, 2018.

[30] Sven H.F. Jaeschke, Matthew D. Robson, and Aaron T. Hess. Cardiac gating using scattering of an 8-channel parallel transmit coil at 7T. *Magnetic Resonance in Medicine*, 80(2):633–640, 2018.

[31] Sven H. F. Jaeschke, Matthew D. Robson, and Aaron T. Hess. Scattering matrix imaging pulse design for real-time respiration and cardiac motion monitoring. *Magnetic Resonance in Medicine*, (May):1–9, 2019.

[32] Andreas Graessl, Wolfgang Renz, Fabian Hezel, Matthias A. Dieringer, Lukas Winter, Celal Oezerdem, Jan Rieger, Peter Kellman, Davide Santoro, Tomasz D. Lindel, Tobias Frauenrath, Harald Pfeiffer, and Thoralf

Niendorf. Modular 32-channel transceiver coil array for cardiac MRI at 7.0T. *Magnetic Resonance in Medicine*, 72(1):276–290, 2014.

[33] Bernd J. Wintersperger, Scott B. Reeder, Konstantin Nikolaou, Olaf Dietrich, Armin Huber, Andreas Greiser, Titus Lanz, Maximilian F. Reiser, and Stefan O. Schoenberg. Cardiac CINE MR imaging with a 32-channel cardiac coil and parallel imaging: Impact of acceleration factors on image quality and volumetric accuracy. *Journal of Magnetic Resonance Imaging*, 23(2):222–227, 2006.

[34] Riccardo Lattanzi, Graham C Wiggins, Bei Zhang, Qi Duan, Ryan Brown, and Daniel K Sodickson. Approaching Ultimate Intrinsic Signal-to-Noise Ratio with Loop and Dipole Antennas. *Magn Reson Med*, 79(3):1789–1803, 2018.

[35] M. Arcan Ertürk, Alexander J.E. Raaijmakers, Gregor Adriany, Kâmil Uğurbil, and Gregory J. Metzger. A 16-channel combined loop-dipole transceiver array for 7 Tesla body MRI. *Magnetic Resonance in Medicine*, 77(2):884–894, 2017.

[36] Ananda Kumar and Paul A. Bottomley. Optimized quadrature surface coil designs. *Magnetic Resonance Materials in Physics, Biology and Medicine*, 21(1-2):41–52, 2008.

[37] Bart R Steensma, Ingmar J Voogt, Tim Leiner, Peter R Luijten, Jesse Habets, · Dennis, W J Klomp, · Cornelis, A T Van Den Berg, · Alexander, and J E Raaijmakers. An 8-channel Tx/Rx dipole array combined with 16 Rx loops for high-resolution functional cardiac imaging at 7 T. *Biology and Medicine*, 31:7–18, 2018.

[38] Matthias J.P. van Osch and Andrew G. Webb. Safety of Ultra-High Field MRI: What are the Specific Risks? *Current Radiology Reports*, 2(8), 2014.

[39] Ingmar Graesslin, Hanno Homann, Sven Biederer, Peter Börnert, Kay Nehrke, Peter Vernickel, Giel Mens, Paul Harvey, and Ulrich Katscher.

A specific absorption rate prediction concept for parallel transmission MR. *Magnetic Resonance in Medicine*, 68(5):1664–1674, 2012.

[40] H. Homann, P. Börnert, H. Eggers, K. Nehrke, O. Dössel, and I. Graesslin. Toward individualized SAR models and in vivo validation. *Magnetic Resonance in Medicine*, 66(6):1767–1776, 2011.

[41] International Electrotechnical Commission. SAR Compliance Guidance Document 2010 60601-2-33. Technical report.

[42] Jerry Allison and Nathan Yanasak. What MRI sequences produce the highest specific absorption rate (SAR), and is there something we should be doing to reduce the SAR during standard examinations? *American Journal of Roentgenology*, 205(2):W140, 2015.

[43] Matthew F Muldoon, Christopher M Ryan, Jeffrey K Yao, Sarah M Conklin, Stephen B Manuck, and Old Engineering Hall. HHS Public Access. 179(11 0):95–105, 2016.

[44] Radiofrequency Power, David C Alsop, Reed F Busse, Philip M Robson, Neil M Rofsky, and David B Hackney. Brain MR Imaging at Ultra-low Methods : Results : Conclusion :. 259(2), 2011.

[45] Xiaoping Wu, Can Akgün, J. Thomas Vaughn, Peter Andersen, John Strupp, Kâmil Uğurbil, and Pierre-François Van de Moortele. Adapted RF Pulse Design for SAR Reduction in Parallel Exciation with Experimental Verifcation at 9.4 Tesla. *Journal of Magnetic Resonance*, 205(1):161–170, 2010.

[46] Yudong Zhu, Leeor Alon, Cem M. Deniz, Ryan Brown, and Daniel K. Sodickson. System and SAR characterization in parallel RF transmission. *Magnetic Resonance in Medicine*, 67(5):1367–1378, 2012.

[47] R. P. Findlay and P. J. Dimbylow. Effects of posture on FDTD calculations of specific absorption rate in a voxel model of the human body. *Physics in Medicine and Biology*, 50(16):3825–3835, 2005.

[48] Martijn Anton Cloos, Michel Luong, Guillaume Ferrand, Alexis Amadon, Denis Le Bihan, and Nicolas Boulant. Local SAR reduction in parallel excitation based on channel-dependent Tikhonov parameters. *Journal of Magnetic Resonance Imaging*, 32(5):1209–1216, 2010.

[49] Wenhua Yu, Xiaoling Yang, Yongjun Liu, and Raj Mittra. *Electromagnetic Simulation Techniques Based on the FDTD Method*. John Wiley & Sons, Inc., New Jersey, 2009.

[50] Jianbao Wang, Bihua Zhou, Lihua Shi, Cheng Gao, and Bin Chen. A novel 3-D HIE-FDTD method with one-step leapfrog scheme. *IEEE Transactions on Microwave Theory and Techniques*, 62(6):1275–1283, 2014.

[51] T. S. Ibrahim, R. Lee, B. A. Baertlein, and P. M.L. Robitaille. B1 field homogeneity and SAR calculations for the birdcage coil. *Physics in Medicine and Biology*, 46(2):609–619, 2001.

[52] Remcom Inc. *XFdtd Reference Manual, Release 7.7.1*. Remcom Inc., State College, PA, 7.7.1.1 edition, 2018.

[53] Kane S. Yee. Numerical Solution of Initial Boundary Value Problems Involving Maxwell's Equations in Isotropic Media. *IEEE Transactions on Antennas and Propagation*, 14(3):302–307, 1966.

[54] Matthew N. O. Sadiku. *Numerical Techniques in Electromagnetics, Second Edition*. CRC Press LLC, 2000.

[55] Tomasz P. Stefański and Timothy D. Drysdale. Large scale ADI-FDTD parallel computations. *Proceedings of 2008 Asia Pacific Microwave Conference, APMC 2008*, pages 8–11, 2008.

[56] Douglas J Riley and C David Turner. Grids to Structured-Grid FDTD. 5(9):284–286, 1995.

[57] Lorenzo Codecasa, Bernard Kapidani, Ruben Specogna, and Francesco Trevisan. Novel FDTD technique over tetrahedral grids for conductive media. *IEEE Transactions on Antennas and Propagation*, 66(10):5387–5396, 2018.

[58] Thomas M. Fiedler, Mark E. Ladd, and Andreas K. Bitz. SAR Simulations & Safety. *NeuroImage*, 168:33–58, 2018.

[59] Akimasa Hirata and Osamu Fujiwara. Physics in Medicine & Biology Modeling time variation of blood temperature in a bioheat equation and its application to temperature analysis due to RF exposure. *MEDICINE AND BIOLOGY Phys. Med. Biol*, 54:189–196, 2009.

[60] Ieee Std, Ieee International Committee, Electromagnetic Safety, Standards Coordinating Committee, Non-ionizing Radiation, and Ieee-sa Standards Board. *IEEE Recommended Practice for Measurements and Computations of Radio Frequency Electromagnetic Fields With Respect to Human Exposure to Such Fields , 100 kHz – 300 GHz*, volume 2002. 2008.

[61] Giuseppe Carluccio. Defense Committee : Danilo Erricolo , Chair and Advisor Rashid Ansari Piergiorgio L . E . Uslenghi Christopher M . Collins , Pennsylvania State University Paolo F . Maccarini , Duke University. 2011.

[62] S Oh, G Carluccio, and C M Collins. Method and Tool for Improved, Rapid N-gram Average SAR Determination. *Ismrm*, 19:1, 2011.

[63] Giuseppe Carluccio, Danilo Erricolo, Sukhoon Oh, and Christopher M. Collins. An approach to rapid calculation of temperature change in tissue using spatial filters to approximate effects of thermal conduction. *IEEE Transactions on Biomedical Engineering*, 60(6):1735–1741, 2013.

[64] Bastien Guérin, Kawin Setsompop, Huihui Ye, Benedikt A Poser, Andrew V Stenger, and Lawrence L Wald. Design of parallel transmission pulses for simultaneous multislice with explicit control for peak power and local specific absorption rate. *Magnetic resonance in medicine*, 73(5):1946–53, 2015.

[65] Joonsung Lee, Matthias Gebhardt, Lawrence L Wald, and Elfar Adalsteinsson. Local SAR in Parallel Transmission Pulse Design.

[66] Andreas K Bitz, Rene Gumbrecht, Stephan Orzada, Hans-Peter Fautz, and Mark E Ladd. Evaluation of Virtual Observation Points for Local SAR Monitoring of Multi-Channel Transmit RF Coils at 7 Tesla. Technical report.

[67] Mark N Keene, D Ph, and John Summers. MRI Safety : Ferromagnetic Detectors ; Patient Monitoring ; and Cardiac Devices. (D), 2014.

[68] Todd D. Greenberg, Michael N. Hoff, Tobias B. Gilk, Edward F. Jackson, Emanuel Kanal, Alexander M. McKinney, Joseph G. Och, Ivan Pedrosa, Tina L. Rampulla, Scott B. Reeder, Jeffrey M. Rogg, Frank G. Shellock, Robert E. Watson, Jeffrey C. Weinreb, and Dina Hernandez. ACR guidance document on MR safe practices: Updates and critical information 2019. *Journal of Magnetic Resonance Imaging*, pages 1–8, 2019.

[69] Mark E. Ladd, Peter Bachert, Martin Meyerspeer, Ewald Moser, Armin M. Nagel, David G. Norris, Sebastian Schmitter, Oliver Speck, Sina Straub, and Moritz Zaiss. Pros and cons of ultra-high-field MRI/MRS for human application. *Progress in Nuclear Magnetic Resonance Spectroscopy*, 109:1–50, 2018.

[70] Boel Hansson, Peter Höglund, Karin Markenroth Bloch, Markus Nilsson, Johan Olsrud, Jonna Wilén, and Isabella M. Björkman-Burtscher. Short-term effects experienced during examinations in an actively shielded 7 T MR. *Bioelectromagnetics*, 40(4):234–249, 2019.

[71] Christina Heilmaier, Jens M. Theysohn, Stefan Maderwald, Oliver Kraff, Mark E. Ladd, and Susanne C. Ladd. A large-scale study on subjective perception of discomfort during 7 and 1.5 T MRI examinations. *Bioelectromagnetics*, 32(8):610–619, 2011.

[72] Daisy van Minde, Laura Klaming, and Hans Weda. Pinpointing moments of high anxiety during an MRI examination. *International journal of behavioral medicine*, 21(3):487–495, 2014.

[73] Marc Schlamann, Min Suk Yoon, Stefan Maderwald, Thomas Pietrzyk, Andreas K. Bitz, Marcus Gerwig, Michael Forsting, Susanne C. Ladd, Mark E. Ladd, and Oliver Kastrup. Short Term Effects of Magnetic Resonance Imaging on Excitability of the Motor Cortex at 1.5T and 7T. *Academic Radiology*, 2010.

[74] C. L.G. Ham, J. M.L. Engels, G. T. Van de Wiel, and A. Machielsen. Peripheral nerve stimulation during MRI: Effects of high gradient amplitudes and switching rates. *Journal of Magnetic Resonance Imaging*, 7(5):933–937, 1997.

[75] Mathias Davids, Bastien Guérin, Matthias Malzacher, Lothar R. Schad, and Lawrence L. Wald. Predicting Magnetostimulation Thresholds in the Peripheral Nervous System using Realistic Body Models. *Scientific Reports*, 7(1):5316, 2017.

[76] Adrienne N Dula, John Virostko, and Frank G Shellock. Assessment of MRI Issues at 7 T for 28 Implants and Other Objects. *AJR*, 202:401–405, 2014.

[77] D X Feng, J P Mccauley, F K Morgan-Curtis, R A Salam, D R Pennell, and M E Loveless. Evaluation of 39 medical implants at 7.0 T. *Br J Radiol*, 88, 2015.

[78] Valentina Hartwig, Giulio Giovannetti, Nicola Vanello, Massimo Lombardi, Luigi Landini, and Silvana Simi. Biological Effects and Safety in Magnetic Resonance Imaging: A Review. *Int. J. Environ. Res. Public Health*, 6:6, 2009.

[79] Aurelien Destruel, Kieran O'Brien, Jin Jin, Feng Liu, Markus Barth, and Stuart Crozier. Adaptive SAR mass-averaging framework to improve pre-

dictions of local RF heating near a hip implant for parallel transmit at 7 T. *Magnetic Resonance in Medicine*, 81(1):615–627, 2019.

[80] David O. Brunner, Jan Paška, Juerg Froehlich, and Klaas P. Pruessmann. Traveling-wave RF shimming and parallel MRI. *Magnetic Resonance in Medicine*, 66(1):290–300, 2011.

[81] International Electrotechnical Commission. (Preview Version) Medical electrical equipment – Part 2-33: Particular requirements for the safety of magnetic resonance equipment for medical diagnosis, 2015.

[82] Jana Delfino Ph.D. Criteria for Significant Risk Investigations of Magnetic Resonance Diagnostic Devices Guidance for Industry and Food and Drug Administration Staff. 2014.

4 B_1^+ Mapping for 7 T Body Imaging

4.1 Introduction

Reliable B_1^+ mapping is extremely important at ultra-high field in order to produce definitive measures of the transmit RF inhomogeneity. Knowledge of the B_1^+ distribution is necessary for RF shimming and RF pulse design techniques which are used to improve the B_1^+ homogeneity crucial for abdominal imaging at 7 T.

This chapter provides an overview of available B_1^+ mapping methods at 7 T. This includes exploring common techniques that are used on conventional MR systems and the development of these techniques for pTx applications. Existing and ongoing novel approaches to B_1^+ mapping are presented with the aim of determining the best method for B_1^+ mapping in 7 T body applications.

4.2 Background and Theory

B_1^+ mapping is a measure of the active magnetic field component of the applied RF field responsible for the excitation of the magnetisation [1]. It is essential to know the B_1^+ distribution, as it has an important influence on the quality of images that are produced in MRI and can be a source of error for quantitative measures [2]. Techniques to determine the distribution involve encoding the B_1^+ into the magnitude or phase of the measured signal. A flip angle map is calculated as an indirect measure of the B_1^+ field. Flip angle maps are commonly presented in units of 'Percentage of Nominal Flip Angle'.

PTx methods such as RF shimming and tailored RF pulse design, rely on prior knowledge of the B_1^+ distributions generated by each individual transmit coil element [3, 4]. This calls for a B_1^+ map to be collected for each transmit channel. Therefore, it is important that appropriate, time efficient methods are applied to ensure as short as possible scan durations [5].

4.2.1 Conventional Methods

This section outlines magnitude based B_1^+ mapping techniques that are commonly used across all field strengths. Conventionally B_1^+ maps are used to correct quantitative measures such as T_1 maps in the liver at 3 T that suffer from moderate B_1^+ heterogeneities [6] and eliminate bias in cortical thickness measurements induced by B_1^+ inhomogeneity effects T_1w images and T_1 maps acquired with the MP2RAGE sequence at 7 T [7].

Examples of B_1^+ maps acquired on a Philips 7 T Achieva MR system with a NOVA 32-channel receive head coil are shown throughout this section.

4.2.1.1 VFA

The Variable Flip Angle (VFA) method is the gold standard technique for mapping B_1^+ and involves acquiring a series of images with different flip angles α. The signal intensity, S, in each voxel is fitted using a least squares algorithm to the function:

$$S = S_0\sqrt{\sin^2(k\theta)} \tag{4.1}$$

S_0 is the initial magnetisation information and k is the scale factor that relates the measured flip angle to the nominal flip angle set, θ, in the scan parameters [8]. A B_1^+ map can then be inferred from the scaling factor, k as this reflects the transmit efficiency of each element.

This B_1^+ mapping technique is reliable due to the high precision of the measurement of k from numerous data points per voxel rather than using a ratio between images. However, the acquisition time for this method can be extensive due to the long TRs required between RF pulses to allow the longitudinal magnetisation to recover fully. The T_1 longitudinal relaxation constant increases with B_0 which means that the TR required for magnetisation to fully recover increases at 7 T. Therefore, the VFA method is not a practical method of measuring B_1^+ in vivo

but it does provide a means for testing the performance of the other techniques explained within this chapter [9].

Equation 4.1 only applies to 3D acquired data. If a 2D acquisition is used then the fitted signal does not fully characterise the acquired signal due to slice profile effects. Figure 4.1 shows an example of a non-linear fit to the signal curve within one voxel of a dataset obtained with a 2D acquisition. The fit does not fully characterise the signal curve.

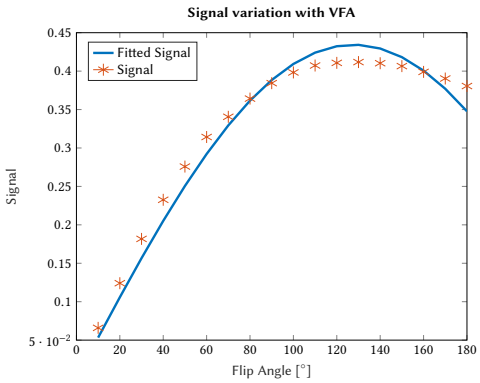


Figure 4.1: Demonstration of a non-linear fit using the single flip angle VFA equation to a signal intensity curve from one voxel in an image slice obtained using a 2D acquisition. The VFA fit does not fully characterise the signal curve due to slice profile effects.

In reality, slice profile effects mean that the signal within each voxel (intra-voxel signal) is the sum of the contributions from individual spins across the thickness of the slice, Δz, due to the variation of $M_{x,y}$ within each voxel.

$$\mathrm{S} = \mathrm{S}_0 \int_0^{\Delta z} \sqrt{\sin^2(\mathrm{k}\theta)} dz \tag{4.2}$$

The slice profile effect was simulated by generating intra-voxel signal curves for different transmit efficiencies, k, which are presented in Figure 4.2. For low k ($k < 1$) the signal is maximum above 90°, for high k ($k > 1$) the signal is maximum below 90° and for $k = 1$ maximum signal is at 90°.

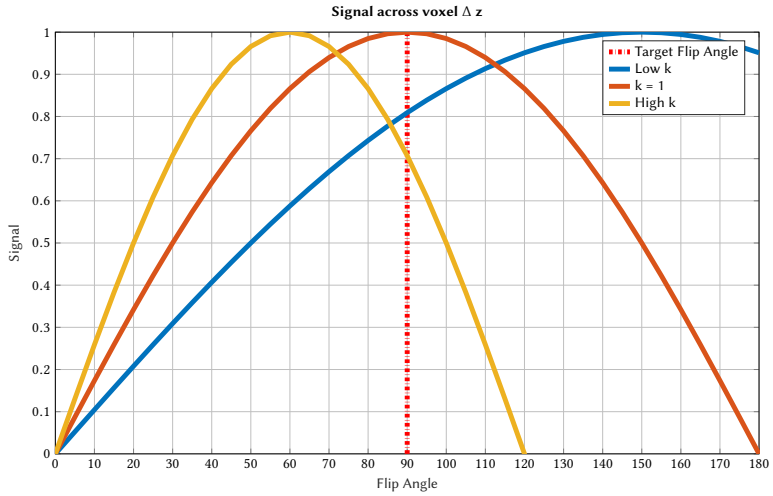


Figure 4.2: VFA Slice Profile Effects: simulated signal curves for different values of k; $k < 1$, $k = 1$ and $k > 1$ respectively.

In Figure 4.3 two signal curves are plotted that correspond to $(k = 1)$ and the sum of $(k > 1) + (k < 1)$ which represents signal corresponding to a mix of transmit efficiencies. Fits were made to each of these signal curves using Equation 4.1. The fit made to the $(k = 1)$ curve characterises the signal fully and shows no slice profile effects. However, the fit to the $(k > 1) + (k < 1)$ signal curve was unsuccessful reflecting similar features to the failed fit in Figure 4.1.

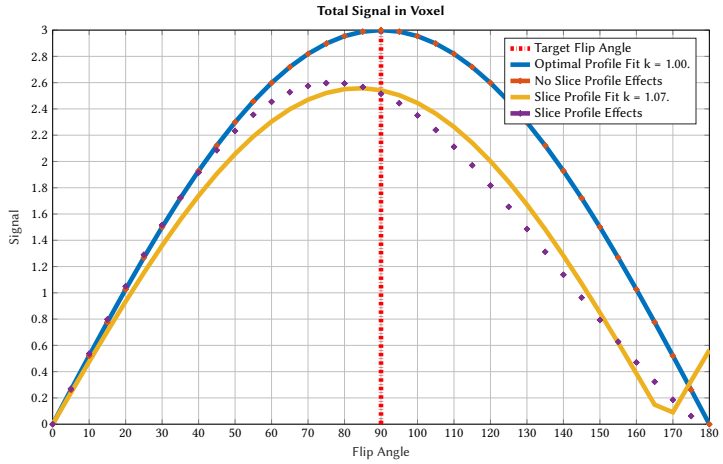


Figure 4.3: VFA Slice Profile Effects: fits made to different signal curves - demonstrates how the model breaks down when applied to the signal curve composed of different transmit efficiencies of intra-voxel signal.

Figure 4.4 shows an example of a fit to the signal curve within one voxel of a dataset obtained with a 3D acquisition. In this case, the fit fully characterises the signal curve and demonstrates the need for 3D acquisition when using the VFA method.

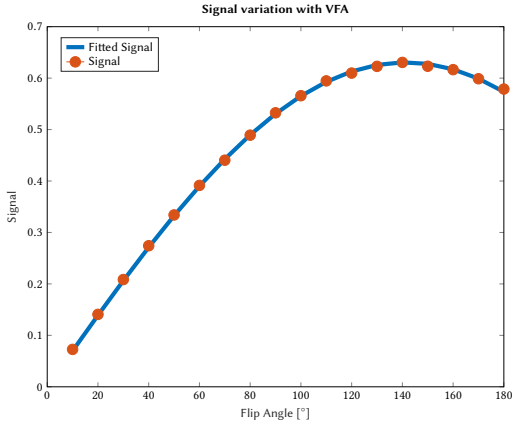


Figure 4.4: Fitting of VFA equation to signal intensity across all sampled points within one voxel in images obtained using a 3D acquisition. VFA fit fully characterises the signal curve due to slice profile effects. This fit can be used to solve for transmit efficiency k.

4.2.1.2 AFI

Actual Flip Angle Imaging (AFI) is a robust and frequently used B_1^+ mapping technique [10, 11]. It is a 3D acquisition method but can be adapted for 2D mapping with an applied slice profile correction [12]. The method uses two identical RF pulses with a flip angle of α each followed by delays, TR_1 and TR_2. This produces two interleaved spoiled gradient echo acquisitions [3]. As can be seen in Figure 4.5, the signals referred to as S_1 and S_2 are Free Induction Decay (FID) signals recorded after each α pulse.

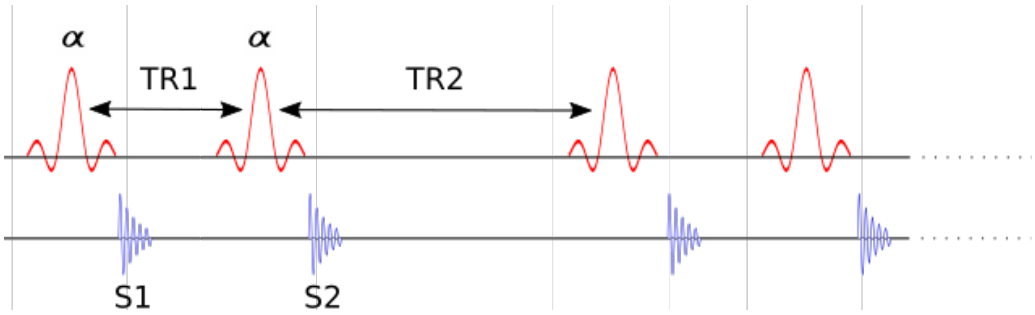


Figure 4.5: Actual Flip Angle Imaging (AFI) Sequence: two identical RF pulses, α are followed by delays TR_1 and TR_2.

Transverse magnetisation is spoiled at the end of the delays TR_1 and TR_2 using an RF phase cycling and gradient spoiling adjustment scheme to avoid off-resonance effects and preserve the ratio of the measured signals [3, 13]. To avoid systematic errors caused by T_1 relaxation the following condition is placed on TR_1 and TR_2 values: ($TR_1 < TR_2 < T_1$). Steady state solutions to the Bloch equations can be calculated based on this condition. The assumption that $TR_{1,2}/T_1 << 1$ allows a first order approximation to be made so that the flip angle, α, can be given by:

$$\alpha \approx arccos\left(\frac{rn-1}{n-r}\right) \tag{4.3}$$

Here, $r = S_2/S_1$ is the ratio between the two signal intensities and $n = TR_2/TR_1$ is the ratio between the two time delays. The ratio n, is the main parameter

that determines the sensitivity of the AFI method to flip angle variations in the excited volume. Optimum parameters for the pulse sequence are given for a 1.5 T MRI scanner by Yarnykh [10]. These include setting TR_1 and TR_2 such that n has a value between 4 - 6 and selecting the flip angle, α, to within a range of 40° - 60°.

The full analytical AFI signal equation is given by:

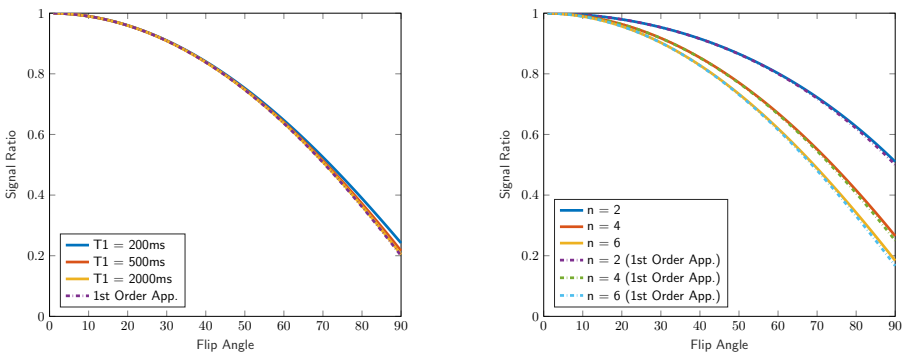
$$\alpha = arccos\left[\frac{1 - E_1 - r - rE_2}{E_1E_2 - rE_1E_2 + rE_2 - E_1}\right] \tag{4.4}$$

where the terms E_1 and E_2 are equal to e^{-TR_1/T_1} and e^{-TR_2/T_1} respectively.

The plot in Figure 4.6 shows the signal ratio, r, calculated for a range of actual flip angles from the approximate (Equation 4.3) and from the full (Equation 4.4) analytical equations (T_1 = 500 ms). In general, the approximation reproduces the full analytical solution except at high flip angles (Figure 4.6) which can be relevant at 7 T where the flip angles can vary considerably across the FOV.

The deviation between approximate and full analytical solutions is more pronounced at shorter T_1 values (Figure 4.6 (a)). At higher values of n, the dynamic range of flip angle measurements is increased (Figure 4.6 (b)). This means there is an increased difference in the signal intensities in the underlying gradient echo images. However, larger n values come at a cost of increased scan time and a choice of n in the range 4 - 6 is sufficient to provide the required sensitivity to variations in flip angle [10].

Acquisition times for AFI can be long, especially over large FOV's. This is a clear disadvantage for abdominal applications in which breath-holds are required during the acquisition of calibration scans [11].



(a) (b)

Figure 4.6: AFI Signal Dependence: (a) Ratio of signal intensities, r, plotted as function of flip angle demonstrating T_1 dependence for full and approximate AFI models, (b) Ratio of signal intensities, r, plotted as function of flip angle demonstrating dependence on the ratio of TRs, n, for full and approximate AFI models.

4.2.1.3 DREAM

Dual Refocusing Echo Acquisition Mode (DREAM) consists of a Stimulated Echo Acquisition Mode (STEAM) magnetisation preparation sequence for B_1^+ encoding followed by a low-angle gradient echo train for spatial encoding [14]. The sequence produces a Stimulated Echo (STE) and FID signal which are both refocused with a temporal offset as gre. Their ratio is then used to calculate the flip angle of the STEAM preparation sequence, α [15].

The DREAM method is a fast 2D technique [15] and to account for slice profile effects the STEAM slice thickness is thicker than the imaging slice [14]. It is significantly faster than AFI since the flip angle encoding depends on a STE and a faster readout can be applied. Therefore, the TR can be shorter and the two signals can be measured almost simultaneously [15]. This means that DREAM is more suited for abdominal imaging as large FOV's can be covered within a breath hold at reasonable spatial resolutions. Additionally, DREAM has a lower total SAR burden also making it favourable for UHF scanning [14].

Figure 4.7 displays the DREAM MR acquisition sequence. In-between the two

α pulses a dephaser gradient (G_{M2}) pre-encodes some of the magnetisation that is then stored in the longitudinal state to enable the detection of the STE signal, I_{STE}, at a controlled time (TE_{STE}) [11]. A spoiler gradient (G_{SPOIL}) is used at the end of the STEAM preparation to spoil any spurious transverse magnetisation, which could be refocused by the readout pulses.

The imaging part of the sequence consists of an excitation pulse β which generates I_{STE} from the STEAM-prepared longitudinal magnetisation and a FID signal, I_{FID}, from the unprepared longitudinal magnetisation.

G_{M2} and prephaser gradient, G_{M1}, control the timing of the STE and FID as GRE's at different echo times, TE_{STE} and TE_{FID} respectively, refocused during a single readout gradient, G_M [15]. By switching the polarity and adjusting these gradients the FID signal can be measured prior to the STE signal giving rise to a 'STE first' or 'FID first' sequence option. The STE first option is preferred as it is less susceptible to T_2 decay effects [14].

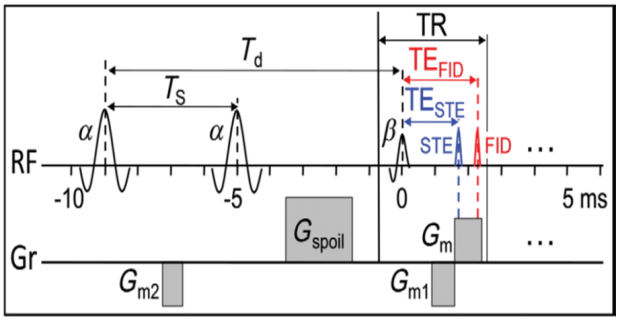


Figure 4.7: DREAM Sequence: STE first. Figure from Nehrke et al. [15]

As with AFI, solutions of the Bloch equations give expressions for the magnetisation at specific time points within the sequence and an analytic expression for the flip angle of the STEAM magnetisation preparation sequence can be determined. A final expression that assumes relaxation effects are negligible is as follows:

$$\alpha = arctan\sqrt{\frac{2I_{STE}}{I_{FID}}} \tag{4.5}$$

However, the longitudinal magnetisation undergoes recovery according to T_1 and the measured signals decay according to T_2 in between STEAM preparation and imaging sequences. This can impact the accuracy of Equation 4.5 in determining α. According to simulation results by Nehrke et al. [14] an underestimation of α is observed when echo number increases and T_1 decreases. Taking these effects into consideration leads to the equation:

$$\alpha = arcsin\sqrt{\frac{1}{E_1(|I_{FID}/2I_{STE}|E_2+1)}} \tag{4.6}$$

where $E_1 = \exp(-T_d/T_1)$ and $E_2 = \exp(-\Delta T_E/T_2)$.

4.2.2 B_1^+ Mapping for pTx Systems

PTx methods require knowledge of the B_1^+ distributions per each individual transmit element. The methods described in the previous section (VFA, AFI, DREAM) can be used to produce B_1^+ maps for each separate transmit channel. Each transmit element is pulsed consecutively and signal is acquired simultaneously through all coil receive elements so that individual transmit profiles are obtained over the entire sample. The complex addition of acquired B_1^+ magnitude and phase maps allows direct comparison with the total volume transmit mode where all transmit elements were used.

Examples of AFI B_1^+ maps acquired in a spherical phantom collected on the eight transmit channels using the NOVA Medical Head Coil 8TX/32RX (NOVA Medical, Wilmington, MA) on the Philips 7 T Achieva pTx system are shown in Figure 4.8. Acquiring B_1^+ field information sequentially on single channels can be time consuming which is undesirable for calibration scans [16].

There is a large dynamic range in pTx systems due to the high signal generated

close the transmit dipole elements and the little to no excitation further from the element. Therefore, methods that can accurately map the B_1^+ distribution rapidly across a wide range of flip angles are essential. This is one of the limitations of using AFI and DREAM for single channel B_1^+ mapping as they are limited in the flip angle regimes that they can accurately measure [17, 18]. Achieving the high flip angle pulses required in these methods is challenging at UHF due to power and in-vivo SAR limits [19], however, they are necessary as the techniques suffer from error propagation at low flip angles [20].

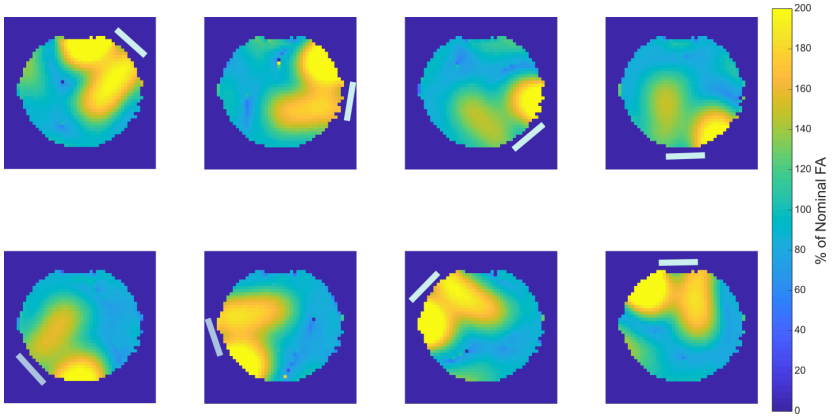


Figure 4.8: Individual B_1^+ maps collected for each channel of NOVA head coil. AFI method was used. Position of each transmit element is shown.

4.2.2.1 Linear Combination Approach

This method provides a way of increasing the SNR across the FOV for B_1^+ mapping methods. Mapping superpositions of individual transmit elements can be used as a means of shifting the B_1^+ field into the operational linear range required for B_1^+ mapping methods [19, 21]. Assuming linear properties of the transmit system, B_1^+ maps for each transmit element can be collected using independent coil combinations which represent the basis functions of a fitting problem. Basis functions with constructive superposition of transmit element B_1^+ sensitivities are favourable. The relationship between the individual transmit element B_1^+ distributions, $(B1_{k,j}^+)$, and measured B_1^+ maps, $B1_{i,j}^{+LC}$, can be described using the following linear combination [22]:

$$B1^{+LC}_{i,j} = \sum_k A_{i,k} B1^{+}_{k,j} \tag{4.7}$$

Indices i and k are equal if the same number of linear combinations as transmit channels is used. Index j is the total number of voxels in each B_1^+ map. Assuming i $= k$, then $A_{i,k}$ is a square, transformation matrix that describes the linear combinations of individual transmit elements. Each entry of A can be described by a single parameter:

$$A_{i,k} = 1 \text{ for i} \neq \text{k} \tag{4.8}$$

$$A_{i,k} = \epsilon \text{ for i} = \text{k} \tag{4.9}$$

- $\epsilon = 1$, corresponds to quadrature excitation.
- $\epsilon = 0$, corresponds to zero RF transmission through the transmit element.
- $\epsilon = \alpha e^{i\phi}$, corresponds to a complex parameter where both the relative amplitude (α) and phase (ϕ) of the RF field transmitted through an element can be adjusted.

B_1^+ maps for individual transmit elements are obtained by taking the following inverse transformation:

$$B1^{+}_{i,j} = \sum_k A^{-1}_{i,k} B1^{+LC}_{k,j} \tag{4.10}$$

It is important that A is an invertible matrix in order to minimise noise amplification in the estimation of the individual transmit element B_1^+ maps.

The "All-But-One" method is a simple example of this approach and involves switching off individual transmit channels in turn during each permutation of coil transmit settings such that:

$$A_{i,k} = 1 \text{ for i} \neq \text{k} \tag{4.11}$$

$$A_{i,k} = 0 \text{ for i} = \text{k} \tag{4.12}$$

The "All-But-One" combination reduces the dynamic range of B_1^+ over the FOV whilst simultaneously increasing SNR and is equivalent to the following transformation matrix A:

$$A = \begin{bmatrix} 0 & 1 & 1 & 1 & 1 & 1 & 1 & 1 \\ 1 & 0 & 1 & 1 & 1 & 1 & 1 & 1 \\ 1 & 1 & 0 & 1 & 1 & 1 & 1 & 1 \\ 1 & 1 & 1 & 0 & 1 & 1 & 1 & 1 \\ 1 & 1 & 1 & 1 & 0 & 1 & 1 & 1 \\ 1 & 1 & 1 & 1 & 1 & 0 & 1 & 1 \\ 1 & 1 & 1 & 1 & 1 & 1 & 0 & 1 \\ 1 & 1 & 1 & 1 & 1 & 1 & 1 & 0 \end{bmatrix} \tag{4.13}$$

B_1^+ maps acquired using the AFI acquisition method and the "All-But-One" configuration were collected with the NOVA head coil. Figure 4.9 presents the eight B_1^+ maps and shows the calculated flip angles obtained across the phantom and the decreased dynamic range of B_1^+ from the centre to the edges of the FOV. This method is also time consuming as a full B_1^+ map is acquired on each channel as required for the single channel mapping methods.

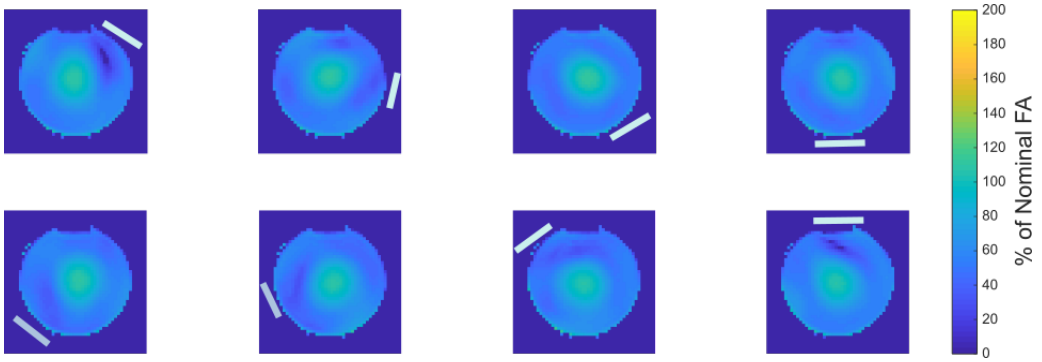


Figure 4.9: AFI B_1^+ maps acquired using 'All-But-One' method.

4.2.2.2 Relative B_1^+ Mapping

Relative B_1^+ mapping is a fast and efficient method for calculating the B_1^+ distributions for multiple transmit channels in pTx systems [23]. It requires acquisition of only a single B_1^+ map in quadrature mode with all transmit channels on simultaneously, $B1^+_{quad}$, plus a set of Low Flip Angle (LFA) Spoiled Gradient Echo (SPGR) images acquired on each individual transmit channel, $Image_{FFE}(n)$ where n is the number of the transmit channels ($n = 1 - TX$). The LFA approximation assumes that the signal intensity in the LFA-SPGR images is directly proportional to the transmit field strength, on the condition that the RF supply system is linear [9].

The LFA-SPGR's are acquired on each transmit channel in turn or by using linear combinations of transmit channels (see Section 4.2.2.1). Ratios of the individual transmit channel images to a calculated quadrature image (from the complex addition of the single channel images) determine the relative B_1^+ distributions for each transmit channel. Any information regarding receive sensitivity or T_1 weighting is neglected.

The relative B_1^+ distributions are then multiplied by $B1^+_{quad}$ to give absolute B_1^+ values for each individual transmit channel map, $B1^+_{ch}(n)$ [23, 24].

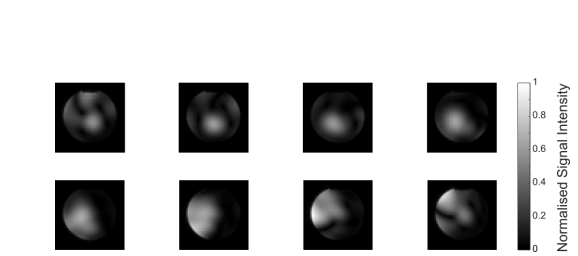
$$\left|B1^{+}_{ch}(n)\right| = \left|\left(\frac{Image_{FFE}(n)}{\sum_{n=1}^{TX} Image_{FFE}(n)}\right)\right| \times \left|B1^{+}_{quad}\right| \tag{4.14}$$

The relative B_1^+ phase maps for each channel are calculated as the difference between the phase of the first transmit channel image ($n = 1$) relative to the phase of each image from the other channels ($n = 1 - TX$).

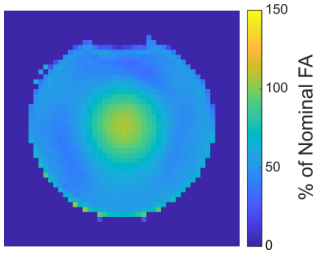
$$\angle B1^{+}_{ch}(n) = \angle Image_{FFE}(1) - \angle Image_{FFE}(n) \tag{4.15}$$

An outline of this method is presented in Figure 4.10 for which the data was collected in a spherical phantom using the NOVA 8TX/32RX head coil. A set of LFA-SPGR images and a quadrature B_1^+ map that are used to calculate the B_1^+ magnitude and phase maps are shown in Figures 4.10 (a), (b), (c) and (d) respectively.

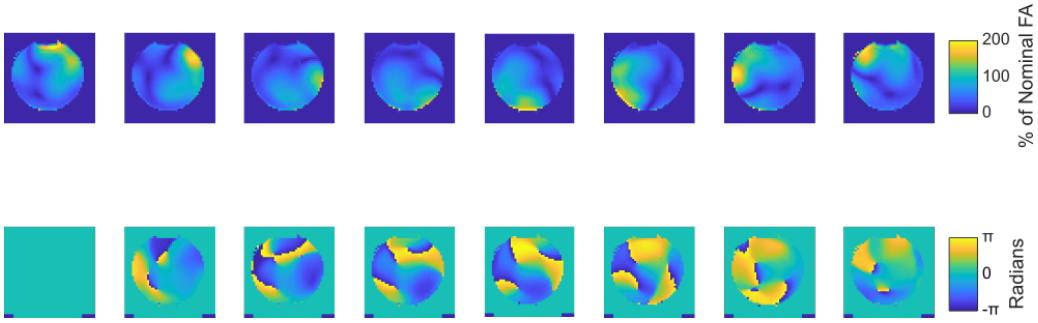
Relative B_1^+ mapping relies on the linear dependence between flip angle and B_1^+ being valid across the full FOV in the LFA images. This is unlikely to be the case for body imaging where the FOV is large and the dynamic range of B_1^+ is even more pronounced. Very large B_1^+ fields can be generated in close proximity to the transmit elements but lower B_1^+ fields are produced at a distance in the centre of the body [22]. Ensuring the LFA approximation is valid adjacent to the transmit elements results in noise dominated measurements from the rest of the object where the transmit field is of low amplitude. Likewise, increasing the flip angle to achieve sufficient signal at greater distances from the transmit element results in violation of the LFA approximation near the transmit element. This poses a problem for B_1^+ mapping over large FOV's in body imaging.



(a) Individual LFA-SPGR images collected for each transmit channel of head coil. Flip angle of 3° was used.



(b) AFI B_1^+ map acquired with all transmit channels on



(c) Absolute relative B_1^+ maps and relative phase maps

Figure 4.10: Data required to calculated relative B_1^+ maps and resulting absolute relative B_1^+ maps for each channel, relative phase information displayed as well.

4.2.3 Advanced B_1^+ Mapping for pTx Systems

The LFA approximation does not hold across the full FOV in situations where the B_1^+ field has large dynamic range. This is the case in body imaging with local transmit coils at 7 T. Two novel methods developed to address this are described in the following sections.

4.2.3.1 Multiple LFA-SPGR's for B_1^+ Mapping

One approach used to combat the large dynamic range of RF fields is the following scheme, developed by Padormo et al. [25]. For each transmit channel, LFA-SPGR images are acquired at different RF pulse amplitudes so that the LFA is satisfied in every region for at least one acquisition.

A reconstruction algorithm combines the images using a Maximum Likelihood Estimation (MLE) statistical framework that estimates the most probable signal for each voxel such that the signal intensities in the resultant image are directly proportional to the B_1^+ field. Relative B_1^+ maps are then obtained by taking the appropriate ratios of the images described in Section 4.2.2.2.

This method addresses the need for the LFA-SPGR images to follow the LFA. However, the validity of the quadrature B_1^+ map across the large FOV's typical in body imaging which are used to calculate the absolute B_1^+ values is still problematic due to effects of low SNR in the middle of the body. The following sections look at schemes that can be used to address this.

4.2.3.2 B1TIAMO

An existing method that has been developed to improve B_1^+ mapping procedures for large body regions at UHF is the B1 Time Interleaved Acquisition of Modes (TIAMO) sequence. This sequence scales single-channel relative B_1^+ maps using two absolute flip angle maps acquired by Pre-Sat TFL [26] which are combined using the TIAMO technique [16, 27, 28]. The two flip angle maps are acquired with different RF transmit phase settings to ensure there is sufficient signal in each voxel in at least one of the maps. The maps are then combined by utilising a local weighting based on the signals in the underlying images.

By using two different B_1^+ modes a complementary RF pattern can be used to improve overall signal homogeneity. Instead of doubling the acquisition time TIAMO exploits parallel imaging algorithms such as GRAPPA [29] to minimise the scan time penalty. This method has shown fast and accurate results in the abdomen and is possible to perform within a breath-hold, even with a 32-transmit channel RF body array [16]. It is a promising solution to the B_1^+ mapping problem in the body at UHF, however implementing this technique will require future work and coding the TIAMO MR pulse sequence into the MR system.

4.2.4 Summary

An overview of current B_1^+ mapping techniques used on both conventional (VFA, AFI and DREAM) and pTx (linear combination approach, relative B_1^+ mapping and B1TIAMO) systems has been presented. The remainder of this chapter covers work carried out to investigate and validate the concepts related to each of these methods. The research and development of further B_1^+ mapping techniques for 7 T body imaging are also put forward for future implementation.

4.3 Methods

An overview of the development of B_1^+ mapping for abdominal application on a 7 T system is now presented. Concepts covering multiple aspects of B_1^+ mapping methods were explored using the NOVA head coil on the classic Philips Achieva 7 T system, and the NOVA 8TX/32RX head coil and MRCoils 8TX/32RX body array on the 7 T pTx system.

4.3.1 AFI

4.3.1.1 Error Propagation

The random error in the full analytical AFI solution (Equation 4.4) due to Gaussian noise in the underlying signals was derived. The full derivation is presented in Appendix A. The dependence of the random error in the final results on actual flip angle α, the ratio of TR's n, and T_1 was investigated. The constant variables used were $n = 5$, flip angle $= 60°$,$T_1 = 1000$ ms, $T_2^* = 50$ ms, $M_0 = 1$ and SNR $= 10$.

4.3.1.2 AFI Reconstruction Comparisons

To confirm a full understanding of the MR scanner AFI calculation, B_1^+ maps were collected on a spherical phantom using the NOVA head coil on the conventional 7 T system. B_1^+ magnitude and phase distributions were calculated

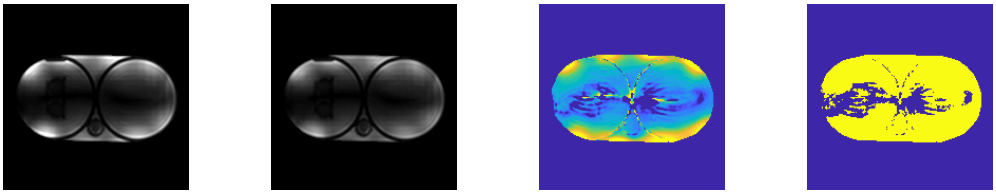
off-line using the raw images and compared to the data output from the scanner. The full analytical AFI equation (Equation 4.4) was used in the off-line reconstruction with $T_1 = 1500$ ms and $T_2 = 100$ ms.

4.3.1.3 AFI Spoiling

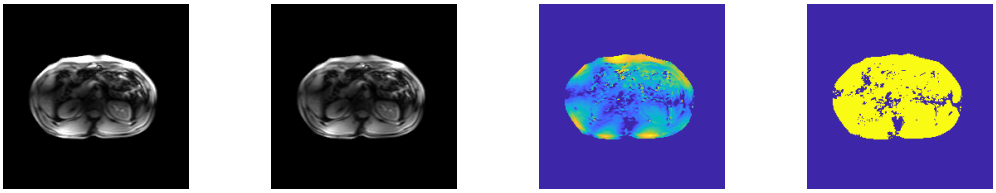
The effect of increasing the spoiler gradients at the end of each TR in the AFI sequence was investigated using a 8 TX/32RX body array on the 7 T pTx system. B_1^+ maps calculated by the scanner software often have masked regions indicating that no useful B_1^+ information exists. Inspection of the data revealed that regions where the signal intensity in the underlying gradient echo images is such that $S_1 > S_2$ are where the AFI reconstruction is valid and are included in the mask; regions where $S_2 < S_1$ are masked out. This can occur when there is inadequate spoiling of the transverse magnetisation between gradient echo acquisitions.

Masking also occurs in the regions furthest from the transmit arrays (in the middle of the phantom or subject) where the signal intensity is low and close to the noise floor in both S_1 and S_2 images. Examples of this masking in the body phantom and in vivo are shown in Figure 4.11. The images highlighting where $S_1 > S_2$ (Figures 4.11 (d) and (h)) correspond to the masked regions in the B_1^+ maps (Figures 4.11 (c) and (g)).

Spoiler gradients were adjusted to investigate the effect this would have on the masking and low signal areas of the B_1^+ maps. The default spoiler gradient in the AFI sequence had a magnitude of 20 mT and a duration of 50 ms. AFI acquisitions were repeated with spoiler gradients of 50 mT/50ms and 50 mT/60 ms. All other AFI parameters were kept constant over the three scans; $\alpha = 40°$, $TR_1/TR_2 = 40/200$ ms. A comparison of the B_1^+ values along a line of interest (bottom left to top right of phantom) was made.



(a) Image 1 (b) Image 2 (c) B_1^+ Map (d) $S_1 > S_2$



(e) Image 1 (f) Image 2 (g) B_1^+ Map (h) $S_1 > S_2$

Figure 4.11: AFI data acquired in body phantom and in vivo; (a,b) and (e,f) show the underlying gradient echo images, (c,g) the calculated B_1^+ distribution and (d,h) highlights the voxels where $S_1 > S_2$.

4.3.2 DREAM

4.3.2.1 Error Propagation

The random error propagation in the determination of α due to noise using the DREAM method [15] was investigated to study its dependence on STEAM flip angle, α, according to different values of imaging flip angle, β. The constant variables used were $I_{STE} = 0.87$, $I_{FID} = 0.8$, $\alpha = 1$ - 90°, $\beta = 5$, 10 and 15°, and SNR = 2. The values of I_{STE}, I_{FID} and SNR were measured from the underlying raw images of acquired DREAM data.

4.3.2.2 DREAM Reconstruction Comparison

To confirm a full understanding of the scanner DREAM reconstruction, B_1^+ maps were calculated off-line using Equation 4.5 and compared to those output from the scanner.

DREAM B_1^+ maps were collected on a spherical phantom on the classic 7 T system. The underlying images were used to calculate B_1^+ distributions with both

the approximate and full analytical approaches outlined in Equations 4.5 and 4.6. The agreement between the two different reconstructions was investigated for the following different T_1 values; 250 ms, 500 ms, 1000 ms, 1500 ms, 3000 ms.

4.3.3 Comparing VFA, AFI and DREAM

Ideally, VFA, AFI and DREAM B_1^+ mapping methods should return identical B_1^+ distributions. An experiment was performed on the conventional 7 T system with the NOVA 32-channel head coil, and a spherical phantom to investigate this. It was important to ensure that the same drive scale (see Chapter 3, Section 5) was used for each acquisition in order to directly compare between the distributions obtained using each method. The voxel size in each acquisition was 3 x 3 x 7 mm^3, other scan parameters used are listed in Table 4.1.

Table 4.1: Scan parameters used for comparison of VFA, AFI and DREAM methods.

Scan	Drive Scale	α (°)	β (°)	TR_1 (ms)	TR_2 (ms)	Duration (mins:secs)
AFI	0.1411	40	-	40	200	5:26
DREAM	0.1411	40	7	-	-	0:10
VFA	0.1411	10 - 180	-	-	-	10:12 (0:34/scan)

Lines of interest were drawn across each resultant B_1^+ magnitude distribution and the B_1^+ values along the lines were compared across all methods. The correlation between AFI and DREAM produced B_1^+ values across the full FOV was also studied.

4.3.4 Linearity of B_1^+ Response

The linear relationship between B_1^+ mapping methods and RF power supply was investigated in order to prove that B_1^+ information could be inferred directly from the measured image intensity; this is the basis of the B_1^+ mapping techniques presented for pTx applications.

B_1^+ maps were acquired in the body phantom using the body array on the 7 T pTx system at the following drive scales; 0.1, 0.2, 0.3, 0.4 and 0.5 using both AFI ($\alpha = 40°$, $TR_1 = 30$ ms, $TR_2 = 150$ ms) and DREAM ($\alpha = 40°$, $\beta = 7°$) acquisition methods. The mean B_1^+ magnitude was measured in three ROIs in each distribution and plotted against the drive scale to check for a linear repsonse.

4.3.5 Single Channel versus Linear Combination B_1^+ Maps

Single channel B_1^+ maps were calculated from a set of acquired AFI "All-But-One" maps (see Figure 4.9) using the inverse of the transformation matrix outlined in Equation 4.10. These were then compared to acquired single channel B_1^+ maps also using the same AFI method (see Figure 4.8 for this dataset).

Both sets of B_1^+ maps were scaled so that the total power demand was equivalent. B_1^+ magnitude values were compared along lines of interest across the diameter of the phantom originating from the maximum signal region produced adjacent to each transmit element, as shown in Figure 4.12.

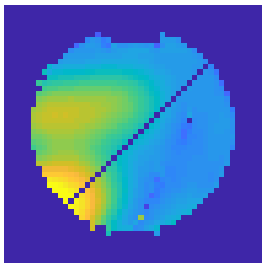


Figure 4.12: Line of interest across diameter of phantom originating from the maximum signal region adjacent to each transmit element. Lines of interest were repeated in this manner for each transmit element.

4.3.6 Adapting B_1^+ Mapping for Body Imaging

The following section was performed using the body phantom and 8TX/32RX body array on the 7 T pTx system. A simple approach was proposed to improve the relative B_1^+ maps for body imaging applications. This involved masking

final single channel B_1^+ distributions according to the areas where the linear response between the reconstructed B_1^+ values and signal in the FFE images is no longer valid. Examples of the original and masked relative B_1^+ magnitude maps calculated in the body phantom are shown alongside the associated phase maps.

4.3.6.1 Combining Different Transmit Phases

A method for combining two B_1^+ maps acquired with different transmit RF phase settings in an approach similar to B1TIAMO was developed. The resulting B_1^+ map was optimised in terms of signal coverage across the FOV with reduced B_1^+ drop outs. The optimised B_1^+ map was then used in the relative B_1^+ mapping calculation to produce absolute flip angle values for individual channel B_1^+ distributions.

Two sets of AFI B_1^+ maps ($B1^+_{mode1}$ and $B1^+_{mode2}$) were acquired in the body phantom at a drive scale of 0.4. The implemented transmit phase settings were linear mode and 45° quadrature mode (see Chapter 4). The weightings used to combine the B_1^+ maps, w_{mode_1} and w_{mode_2}, were calculated on a voxel-by-voxel basis based on the random error in the AFI underlying GRE signals that was calculated previously, σ_α^2, for both of the B_1^+ maps:

$$w_{mode} = \sqrt{\frac{1}{\sigma_\alpha^2}} \tag{4.16}$$

The optimum absolute B_1^+ map ($B^+_{1,optimum}$) was calculated as follows:

$$B1^+_{optimum} = \frac{\left(w_{mode_1} \times B1^+_{mode1}\right) + \left(w_{mode2} \times B1^+_{mode2}\right)}{w_{mode1} + w_{mode2}} \tag{4.17}$$

4.3.6.2 Combining Different RF Powers

Another method for generating an optimised B_1^+ map was developed. This time individual B_1^+ maps were acquired using the AFI method at different drive scales (see Figure 4.13). The drive scales applied for each separate scan were 0.1, 0.2, 0.3 and 0.4 respectively.

In the lower drive scale data B_1^+ values are in the linear regime near the transmit elements, not in the centre of the phantom as the signal is low. In the higher drive scale maps, the B_1^+ values that are in the linear regime are more likely to be towards the centre of the phantom due to the increase in transmit efficiency. Near the elements the signal is very high resulting in large flip angles which are outwith the linear regime. By using a weighted average of these different distributions, a resultant B_1^+ distribution should be considered valid in the linear regime across the full extent of the phantom.

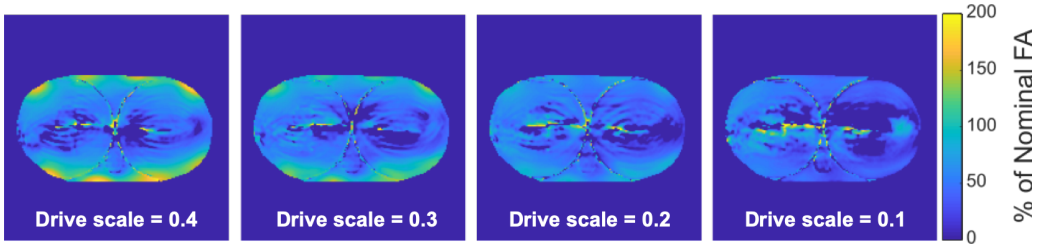


Figure 4.13: AFI B_1^+ maps acquired at four different drive scales; displayed in order of decreasing drive scale.

All B_1^+ maps were scaled to the maximum applied drive scale, 0.4 (e.g. the 0.1 drive scale B_1^+ map was multiplied by a factor of 4). This approach could be taken due to the linearity of B_1^+ mapping techniques with drive scale. A weighted average of the scaled B_1^+ maps then results in an optimised, combined B_1^+ map. The weights are calculated from the signal in the underlying AFI images at different drive scales using the same method outlined in the previous section. Theoretically, the calculated B_1^+ map represents the B_1^+ distribution at a drive scale of 0.4.

4.4 Results

4.4.1 AFI

4.4.1.1 Error Propagation

Figure 4.14 presents the random error propagation in the full analytical solution for AFI with respect to actual flip angle α, the ratio of TR's n, and T_1. The propagated error approaches 10° at values of α below 30°; approaches 6° at values of n less than 2 and increases as the T_1 of a given material decreases.

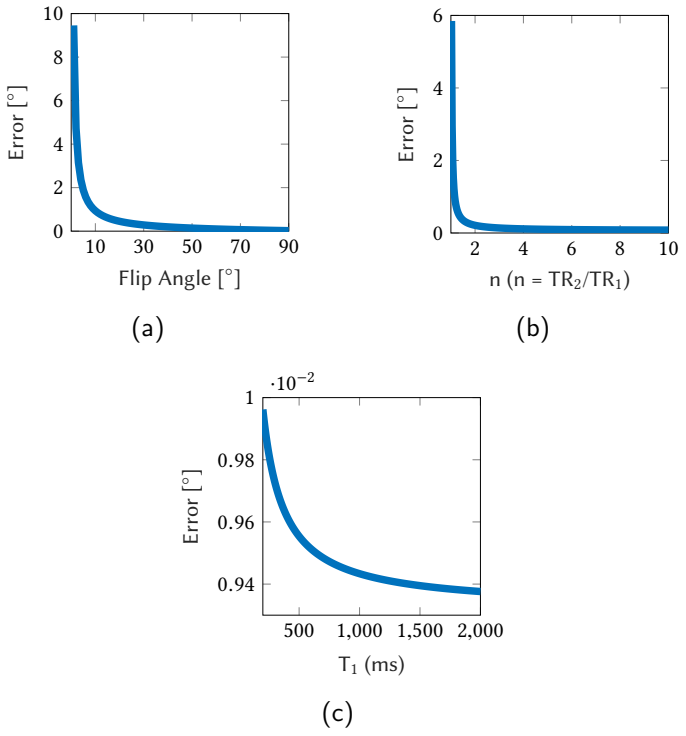
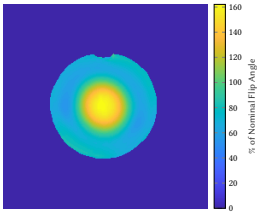


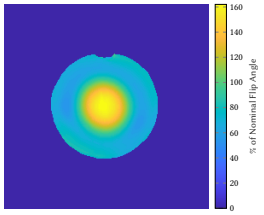
Figure 4.14: Random error propagation in the full analytical AFI solution as a function of (a) actual flip angle α, (b) ratio of TR's n, and (c) T_1 relaxation time.

4.4.1.2 AFI Reconstruction Comparison

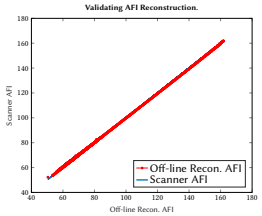
The off-line reconstructions closely matched those calculated by the scanner software; scanner B_1^+ magnitude and phase maps are presented in Figures 4.15 (a) and 4.15 (d), and the off-line reconstructed B_1^+ magnitude and phase maps are presented in Figures 4.15 (b) and 4.15 (e). Figures 4.15 (c) and (f) present the correlation between scanner and off-line data for magnitude and phase data respectively and show that the off-line reconstructions match those output from the scanner directly indicating that the scanner AFI reconstruction was as expected.



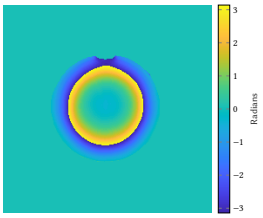
(a) Scanner AFI B_1^+ magnitude map



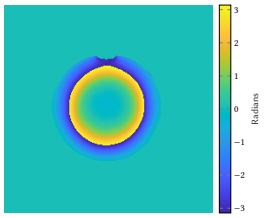
(b) Off-line recon. AFI B_1^+ magnitude map



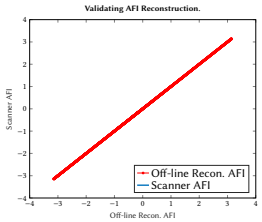
(c) Magnitude maps correlation



(d) Scanner AFI B_1^+ phase map



(e) Off-line recon. AFI B_1^+ phase map



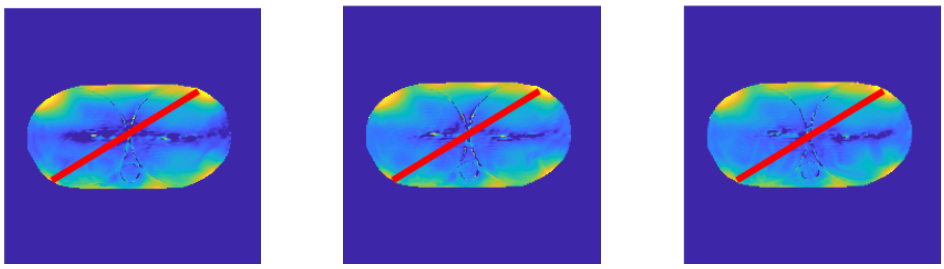
(f) Phase maps correlation

Figure 4.15: Examples of scanner and off-line reconstructed AFI B_1^+ maps; magnitude and phase data shown for comparison. Note air bubble at the top of the phantom.

4.4.1.3 AFI Spoiling

Figure 4.16 (a) shows an AFI B_1^+ map acquired with default spoiler gradients (20 mT, 50 ms), (b) shows a B_1^+ map acquired with spoiler gradients increased

to 50mT and (c) shows a B_1^+ map acquired with a 50 mT spoiler gradient of 60 ms duration. There is less masking of the area in the centre of the phantom, where signal is low, in (b) and (c) compared with (a).



(a) Default Gradients: 20mT, 50 ms

(b) Adjusted Gradients: 50mT, 50 ms

(c) Adjusted Gradients: 50mT, 60 ms

Figure 4.16: Examples of AFI B_1^+ maps acquired with default and adjusted spoiler gradients. Red line shows line of interest taken for Figure 4.17.

Figure 4.17 shows the comparison of the B_1^+ values along a line of interest across each magnitude map. In voxels numbered 1 - 40 there was no significant change to the B_1^+ values. In voxels numbered > 40 the calculated B_1^+ is greater in the maps acquired with increased spoiler gradients indicating that the signal in the second gradient echo image is lower (compared to the default image) and any residual transverse coherence has been removed.

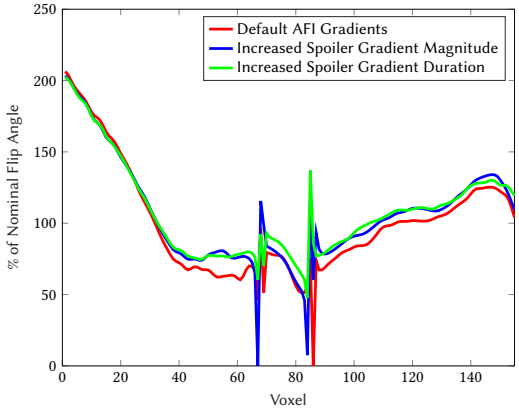


Figure 4.17: Comparison of AFI B_1^+ values acquired with default and adjusted spoiler gradients along line of interest (top, right to bottom, left of phantom).

4.4.2 DREAM

4.4.2.1 Error Propagation

Figure 4.18 shows the random error propagation with respect to STEAM angle, α. Random error is high at α's below 30° and greater than 70°. Increasing the excitation pulse, β, decreases the error in the predicted value of α.

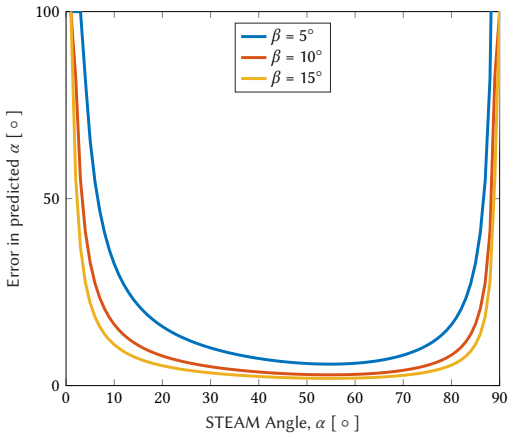
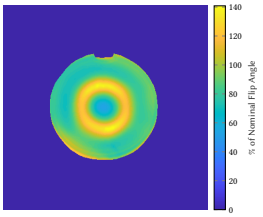


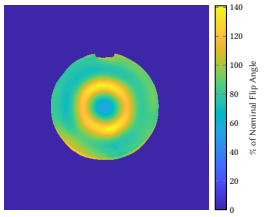
Figure 4.18: Random error in estimated STEAM angle with respect to actual STEAM angle, α [15].

4.4.2.2 DREAM Reconstruction Comparison

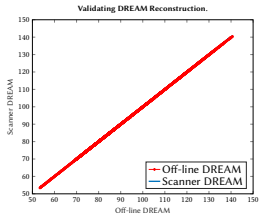
Scanner B_1^+ magnitude and phase maps are presented in Figures 4.19(a) and 4.19(b), the off-line reconstructed B_1^+ magnitude and phase maps are presented in Figures 4.19(c) and 4.19(d). Figures 4.19 (c) and (f) display the correlation between the two B_1^+ magnitude and phase distributions respectively. The off-line reconstructions are identical to the B_1^+ distributions output directly from the scanner.



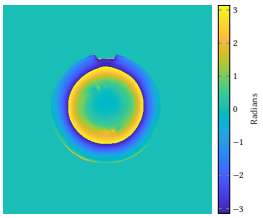
(a) Scanner DREAM B_1^+ magnitude map



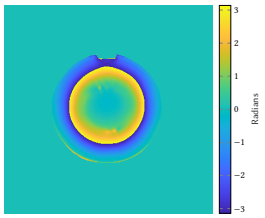
(b) Off-line recon. DREAM B_1^+ magnitude map



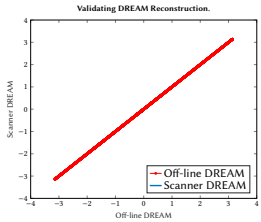
(c) Magnitude map correlation



(d) Scanner DREAM B_1^+ phase map



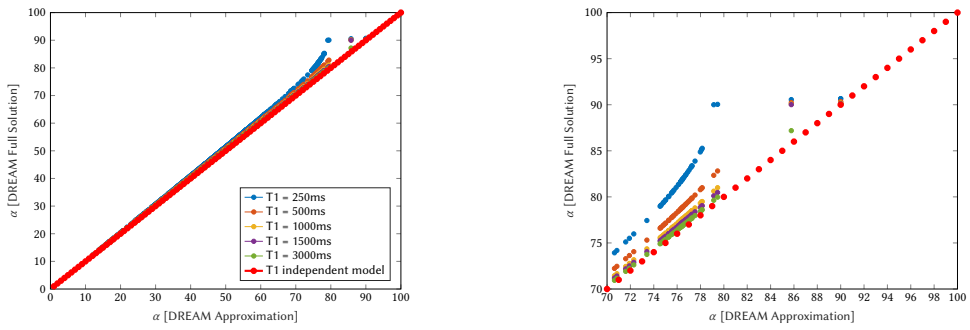
(e) Off-line recon. DREAM B_1^+ phase map



(f) Phase map correlation

Figure 4.19: Examples of scanner and off-line reconstructed DREAM B_1^+ maps; magnitude and phase data shown for comparison.

DREAM data reconstructed with the full analytical solution with different T_1 values correlated with data reconstructed with the approximate solution (independent of T_1) is displayed in Figure 4.20 (a). Solutions for α start to deviate at around 70°. Figure 4.20 (b) highlights the flip angle region from 70° - 100° where the deviation between the calculated values of α can be seen to increase at lower values of T_1.

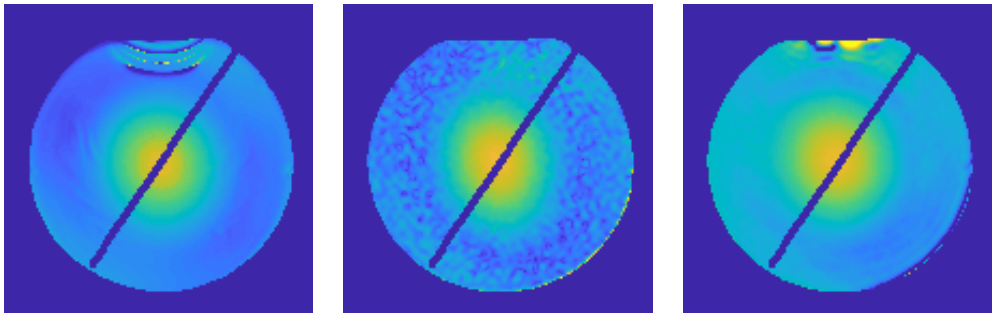


(a) (b)

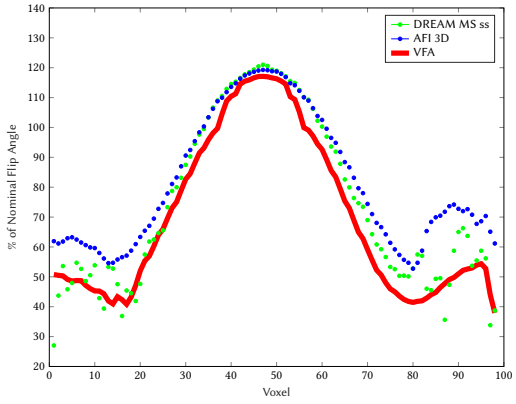
Figure 4.20: Correlation plot of DREAM B_1^+ maps calculated with approximation and T_1/T_2 dependent equations. Units are % of STEAM angle, α.

4.4.3 Comparing VFA, AFI and DREAM

Figure 4.21 displays the three B_1^+ maps acquired with (a) VFA, (b) DREAM and (c) AFI techniques. All methods were acquired using a 3D acquisition and so slice profile effects did not have to be considered. The line of interest along which B_1^+ values were compared is highlighted. All profiles reflect a peak B_1^+ of 120 % of nominal flip angle in the middle of the phantom; this corresponds to 48°. The profiles start to deviate between 70 and 110 % of nominal flip angle (28 - 44°). The VFA profile for B_1^+ values less than 60 % of nominal flip angle ($<$ 24°) corresponding to the outer layer of the phantom is matched by the DREAM profile (although it is considerably more noisy). In this region, the AFI overestimates the B_1^+ by about 10 % ($\sim$ 4°). Deviation of both DREAM and AFI from the VFA results is expected due to the higher random error propagation at low flip angles present in the respective reconstruction methods as shown in Figures 4.14 (a) and 4.18. The VFA has lower error propagation due to the multiple data points involved in calculating the measured flip angles.



(a) VFA (b) DREAM (c) AFI



(d) Comparing B_1^+ Profiles

Figure 4.21: B_1^+ maps showing line of interest drawn for comparing magnitude profiles.(a) resulting B_1^+ distribution calculated from VFA method, (b) B_1^+ distribution obtained using DREAM and (c) B_1^+ distribution obtained using AFI, (d) shows the comparison of B_1^+ values along the line of interest. AFI and DREAM closely resemble the VFA B_1^+ distribution in the middle of the phantom and less so around the periphery of the phantom where the B_1^+ is lower.

Figure 4.22 displays the correlation between AFI and DREAM B_1^+ values across the whole FOV. There is a high correlation above 110 % of nominal flip angle ($>$ 44°). Between 80 - 110 % (32 - 44°), AFI and DREAM results begin to deviate from each other, and below 80 % of nominal flip angle ($<$ 32°) the correlation is low due to the noisy DREAM distribution and random error propagation in both methods at low flip angles.

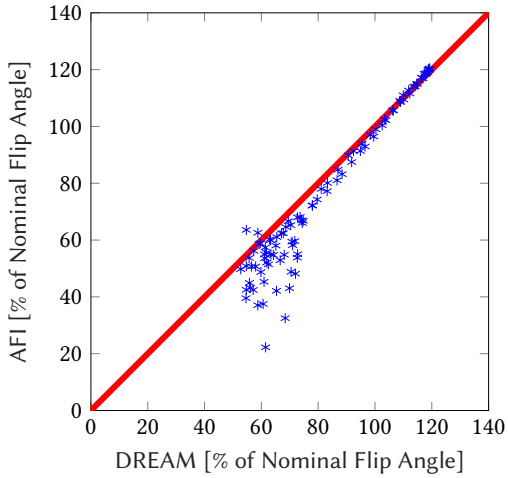
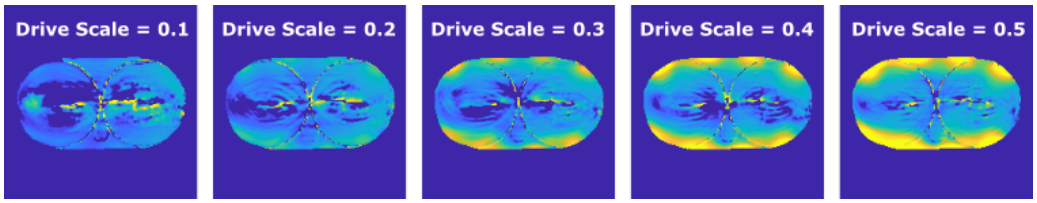


Figure 4.22: Correlation of B_1^+ values from distributions generated using the AFI and DREAM methods. Values correlate well at high B_1^+ values (> 90 % of nominal flip angle corresponds to $\sim 35°$), and there is a low correlation at low flip angles.

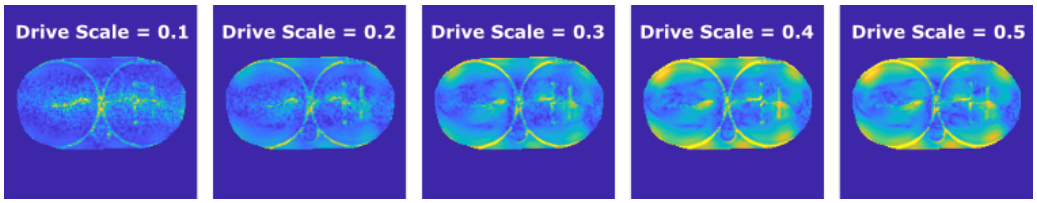
4.4.4 Linearity of B_1^+ Response

Figure 4.23 shows the B_1^+ maps acquired using (a) AFI and (b) DREAM acquisition methods at varying drive scales. The ROIs 1-3 are shown in Figure 4.24 (a) and include examples in the (1) centre right, (2) upper left and (3) top right of the phantom. The mean B_1^+ value in each ROI obtained from AFI and DREAM distributions were plotted against drive scale and are presented in Figures 4.24 (b), (c) and (d) for ROI 1, ROI 2 and ROI 3 respectively. From observation of all three plots it is clear that the linear characteristics of the of B_1^+ mapping methods depend on the location of the ROI in the FOV.

In ROI 1 (centre right of phantom) the mean B_1^+ is unstable, particularly in the DREAM data where low B_1^+ has been incorrectly reconstructed as high B_1^+. In addition to this, the effect of severely decreasing B_1^+ towards the centre of the phantom that results in low B_1^+ values with noise characteristics is shown. In ROI 2 (upper left) there is evidence of linearity within the range of drive scale 0.2 - 0.4. In ROI 3 (top right) the B_1^+ transmit efficiency is high and the linear



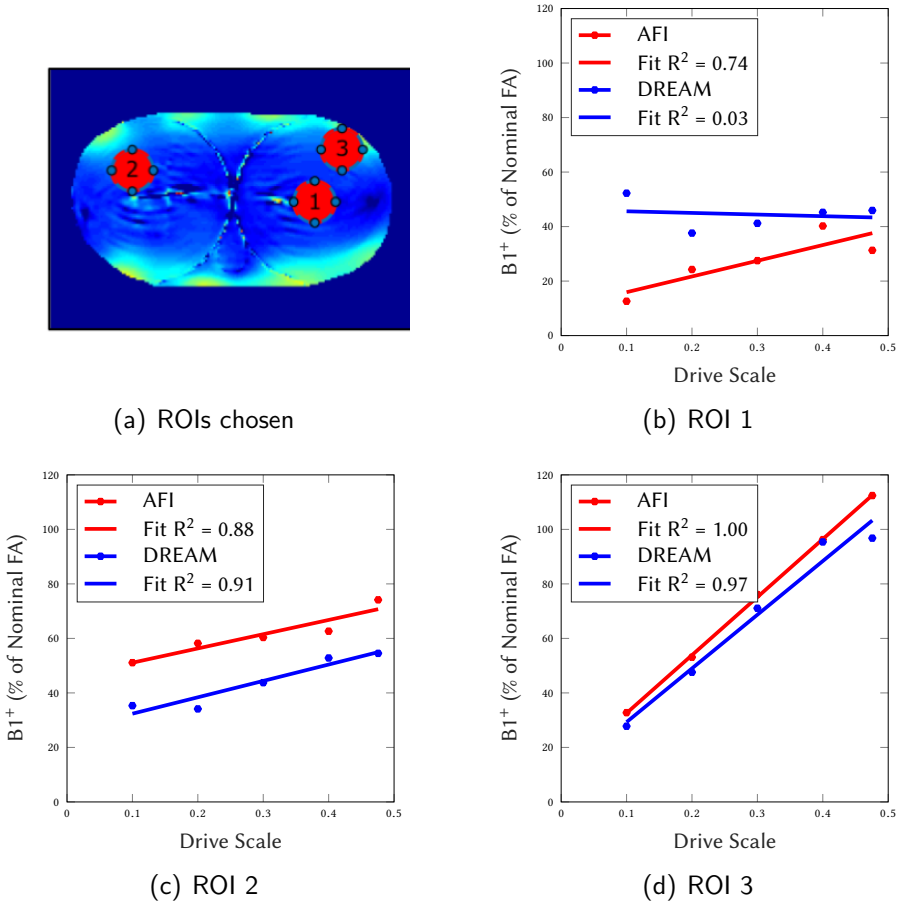
(a)



(b)

Figure 4.23: (a) AFI and (b) DREAM B_1^+ Maps acquired at different drive scales.

behaviour is very clear. Similar to ROI 2 results the linearity changes below drive scale $= 0.2$ and above drive scale $= 0.4$. The large dynamic range of B_1^+ values experienced in the body phantom can be seen by comparing results across each plot.



(a) ROIs chosen

(b) ROI 1

(c) ROI 2

(d) ROI 3

Figure 4.24: Plots of measured B_1^+ vs. drive scale in different regions of interest in the body phantom demonstrates how linearity of B_1^+ mapping is not consistent across different ROIs and over the full range of RF power available.

4.4.5 Single Channel versus Linear Combination B_1^+ Maps

Figure 4.25 displays single channel B_1^+ maps calculated from the "All-But-One" channel AFI B_1^+ maps shown in Figure 4.9. The comparison of B_1^+ values between a directly acquired single channel AFI B_1^+ map and a calculated single channel B_1^+ map for transmit element number 3 is displayed in Figure 4.26.

The inverted All-But-One and acquired single channel maps do not have identical B_1^+ values. In the transmit element 3 example, the inverted All-But-One values

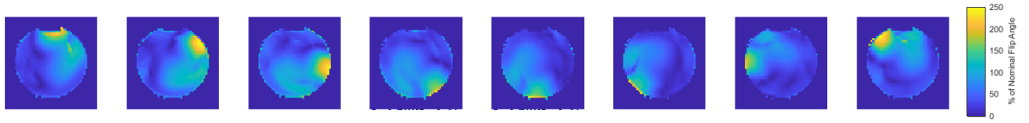


Figure 4.25: Single channel AFI Maps calculated by multiplying 'All-But-One' AFI maps by the inverse of matrix, A.

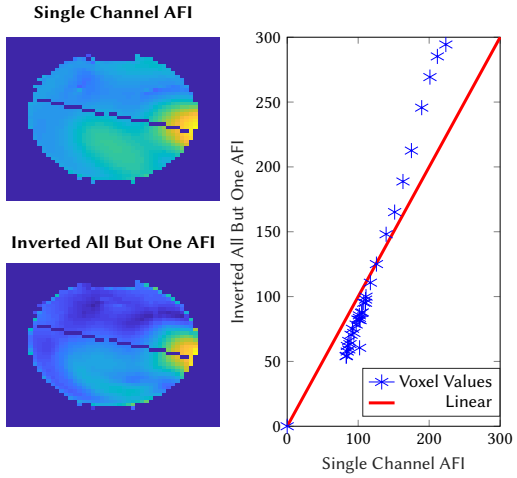


Figure 4.26: Plots show B_1^+ values (in % of Nominal Flip Angle) from single channel and inverted All-But-One AFI maps. Values are taken along lines of interest originating from the maximum signal region of each transmit element. Example from transmit element 3 is shown.

cover a greater range of flip angles demonstrating the wider dynamic range of the All-But-One method. This highlights the advantage of this method for capturing more information about the full distribution of B_1^+ values generated close to and further away from each transmit element.

4.4.6 Adapting B_1^+ Mapping for Body Imaging

Relative B_1^+ maps calculated by voxel-by-voxel multiplication are shown in Figure 4.27. High B_1^+ values in middle of phantom are not physical but arise due to low signal noise and incorrect B_1^+ reconstruction based on the underlying AFI (or DREAM) method.

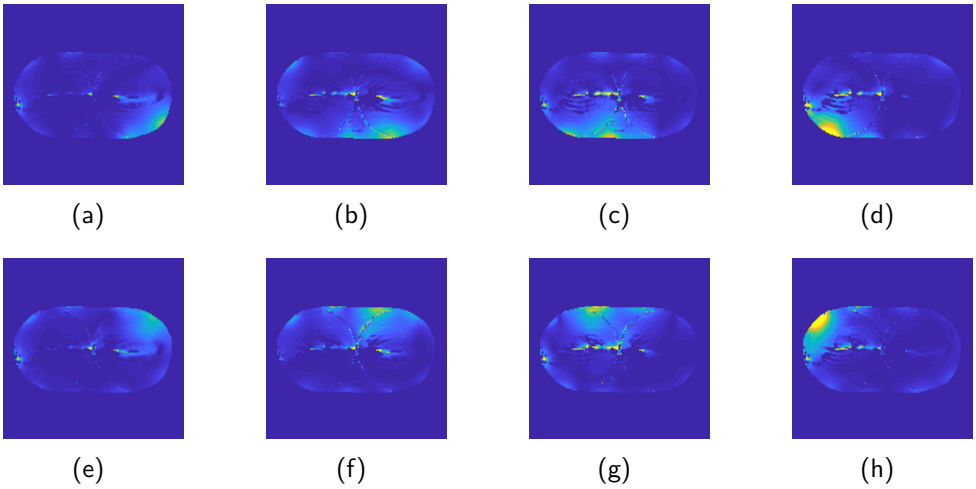


Figure 4.27: Conventional relative B_1^+ maps; non-physical high B_1^+ values in the centre of the phantom correspond to low signal areas in LFA-SPGR images and where linear response of B_1^+ is not valid.

A plot of normalised signal intensity from one of the single channel LFA-SPGR images against the corresponding channel relative B_1^+ map is shown in Figure 4.28. A positive linear trend can be seen across all of the voxels, and outlier values are more severe at lower signal. For this reason, the relative B_1^+ map threshold was set to a normlaised signal intensity of 0.1.

Figure 4.29 shows the relative B_1^+ maps after they have been masked according to signal intensity values less than 0.1 where the linear behaviour of the reconstructed B_1^+ values was no longer valid. The associated relative B_1^+ phase maps are presented in Figure 4.30. These are calculated from the single channel LFA-SPGR images and are relevant in the unmasked areas in Figure 4.29.

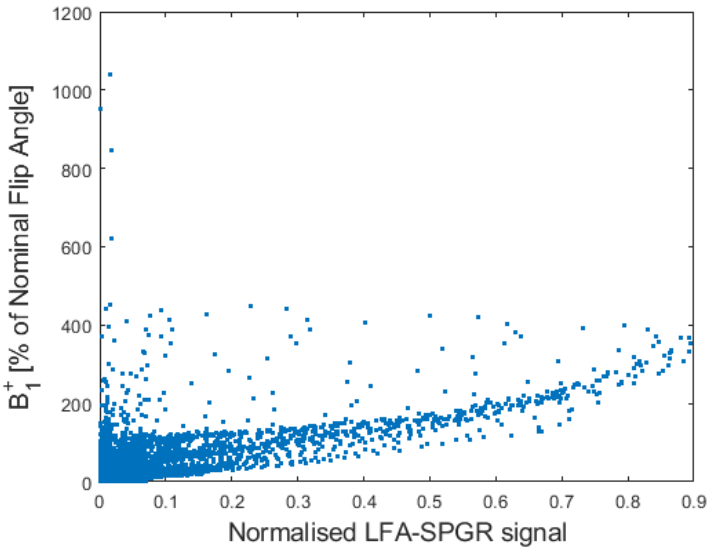


Figure 4.28: Example of a plot of signal from a single channel LFA-SPGR image versus B_1^+ values in the equivalent voxels.

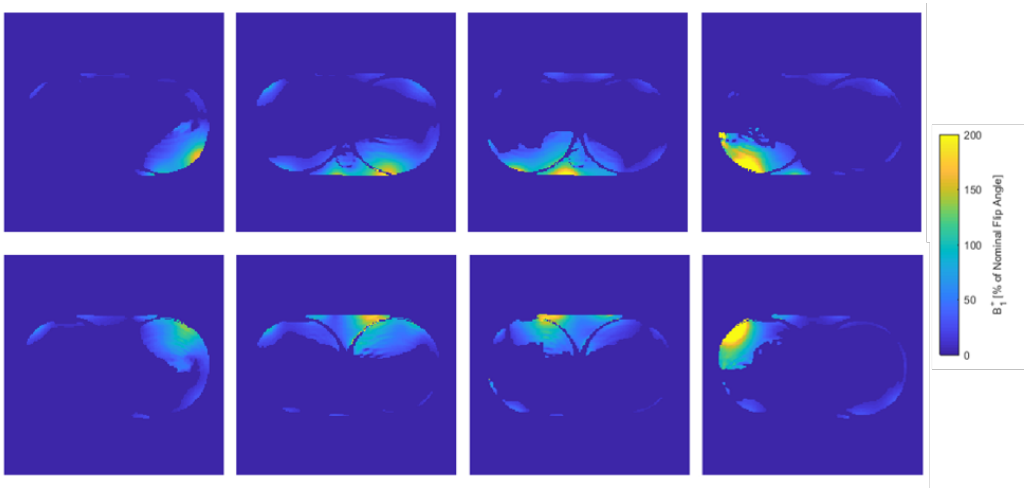


Figure 4.29: Relative B_1^+ maps masked according to areas where the linear response of the reconstructed B_1^+ values is no longer valid.

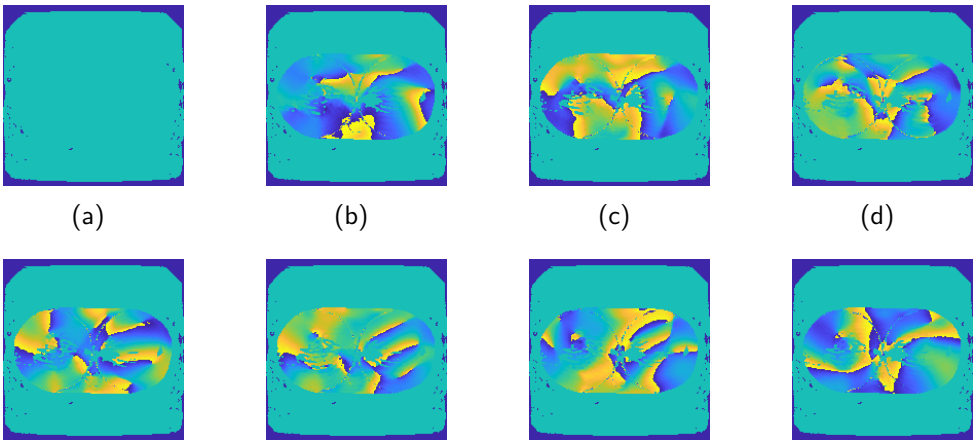


Figure 4.30: Relative B_1^+ phase maps calculated from the low angle FFE images.

4.4.6.1 Combining Different Transmit Phases

The calculated voxel weights based on underlying images acquired using the AFI method are illustrated (using a logarithmic scale) in Figure 4.31 and demonstrate that higher weighting was given to higher signal areas. Figure 4.32 displays each acquired B_1^+ map acquired with linear and quadrature transmit phase settings, and the final combined, optimised B_1^+ map which contains increased B_1^+ information in areas where there is no B_1^+ data in the acquired distributions.

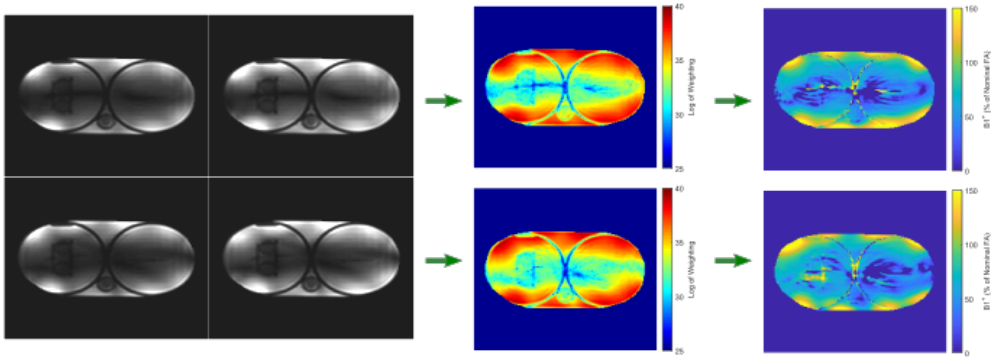
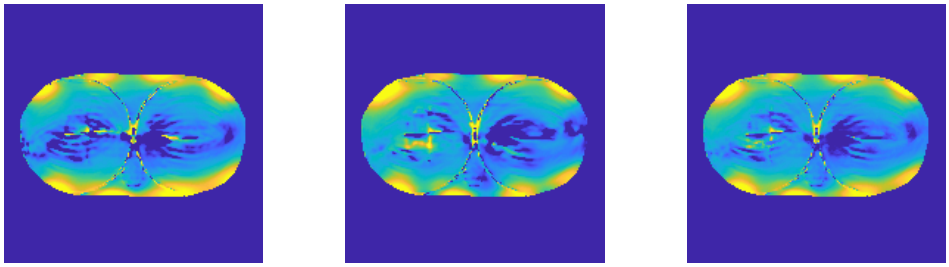


Figure 4.31: Weights are calculated for each voxel based on the underlying images acquired with the AFI sequence. This is repeated for data acquired in multiple different transmit RF phase settings. These weights are then applied to the respective AFI maps which are combined to produce an optimised B_1^+ map. Image data acquired in the body phantom is shown.



(a) Linear transmit phase setting

(b) Quadrature transmit phase setting

(c) Combined B_1^+ map

Figure 4.32: Combining B_1^+ maps acquired with different transmit phase setting. (a) displays a B_1^+ map acquired with linear transmit phase settings, (b) displays a B_1^+ map acquired with quadrature transmit phase settings and (c) displays the combined B_1^+ map calculated from a weighted average of maps shown in (a) and (b). The weights are calculated based on the underlying signal intensity in the images acquired using the AFI method.

4.4.6.2 Combining Different RF Powers

The B_1^+ maps all scaled to the maximum acquired drive scale are displayed in Figure 4.33. Figure 4.34 displays the combined B_1^+ map calculated from the weighted average of the scaled maps shown in the previous figure that represented the 0.4 drive scale distributions.

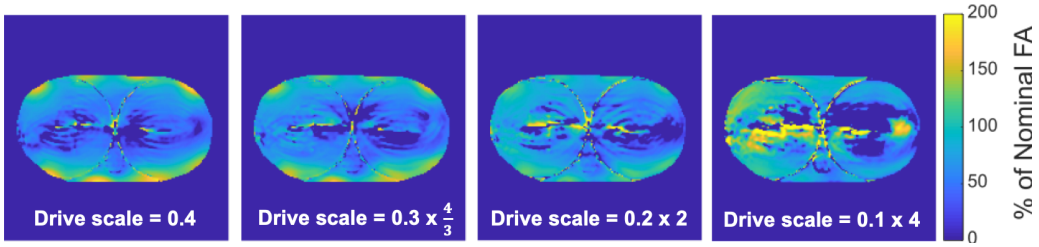


Figure 4.33: AFI B_1^+ maps (acquired at drive scales 0.1, 0.2, 0.3 and 0.4) all scaled to the maximum drive scale.

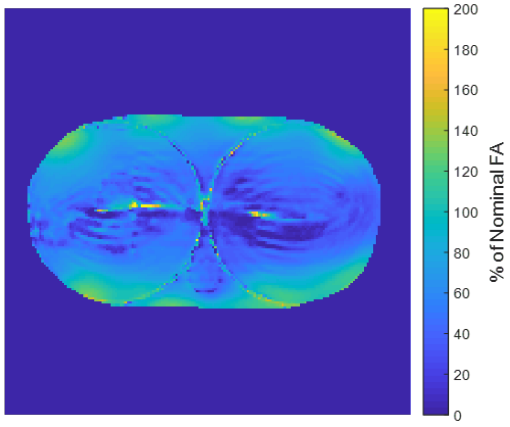


Figure 4.34: B_1^+ map reconstructed from a weighted average of four individual AFI B_1^+ maps acquired at different drive scales. Weights were calculated based on the signal in the underlying images which varied with drive scale.

4.5 Discussion

4.5.1 AFI

The random error propagation in the AFI reconstruction confirmed that there is high error in the determination of actual flip angles at low flip angles ($<$ 20°). This is an issue for large FOVs where signal can be low at distances far from the transmit elements in the centre of either the body phantom or subject. Calculated B_1^+ in this region can result in noisy results returning high B_1^+ values that are not physical, or the signal in this area can be masked out where $S_2 > S_1$; however, this can be improved marginally by increasing the spoiler gradients in the AFI sequence.

4.5.2 DREAM

DREAM has high random error propagation in the determination of the STEAM angle α at low flip angles ($<$ 20°), similar to AFI. Additionally, the random error propagation increases as flip angles approach 90°. For shorter T_1 values (which is not as problematic at UHF) it is recommended that the full analytical solution

is used due to the deviation of results compared to those obtained with the approximate solution.

4.5.3 Comparing VFA, AFI and DREAM

AFI and DREAM methods produced similar B_1^+ values to those calculated with the VFA technique. However, they do not accurately map the low B_1^+ values corresponding to low flip angles that are prone to random error in the signal fof the underlying images of each method. This leads to systematic errors in the reconstruction of final B_1^+ values. The correlation between AFI and DREAM demonstrated the robustness of both methods at higher flip angles, but both are unreliable at determining low B_1^+ values at low flip angles. In terms of practical considerations, AFI was found to be more robust to use as conflicts often arose with DREAM when during scanning sessions.

4.5.4 Linearity of B_1^+ Response

The plots of B_1^+ versus drive scale (Figure 4.24) confirm that B_1^+ mapping methods are not proportional to RF power with the same scale factor in different ROIs in large FOVs due to the large dynamic range. Therefore, methods that produce B_1^+ fields that are linear with RF power, across the typical FOVs experienced in body imaging, are essential for accurate B_1^+ mapping in the body.

4.5.5 Single Channel versus Linear Combination B_1^+ Maps

Acquired single channel B_1^+ maps and calculated single channel B_1^+ maps (obtained by inverting All-But-One data) did not reproduce identical B_1^+ values. This was expected as the calculated B_1^+ data from the All-But-One maps should exhibit a larger dynamic range, more representative of the B_1^+ values generated close to and far from each transmit element. The gradient of the relationship between the acquired and calculated data is not equal to that of a linear relationship. This is likely due to different B_1^+ power calibrations used for each of the underlying acquisitions. For the single channel maps, one transmit channel

was activated; for the calculated maps, seven transmit channels were activated. The power calibrations were unable to be controlled by the scanner user with the NOVA head coil as the hardware restrictions limited the choice of drive scale during scanning. Although the linear combination method could be advantageous for its wider dynamic range, it still requires iterative acquisition of B_1^+ maps on each transmit channel which can be time consuming compared to the relative B_1^+ mapping method where only a single B_1^+ map with all-channels-on is required.

4.5.6 Adapting B_1^+ Mapping for Body Imaging

The methods put forward for improving the quality and validity of relative B_1^+ maps for body applications are now discussed. Masking the relative B_1^+ maps according to where the linear response of the reconstructed B_1^+ values is no longer valid improves the quality of the data and would solve issues surrounding magnitude-based RF shimming with non-physical values in the centre of the body phantom or subject where low signal is a challenge. The B_1^+ phase maps can be calculated quickly from the LFA-SPGR data, applying the same masking to this data improves the validity of the relative B_1^+ phase distributions for each transmit channel. This is important as these maps are the basis for phase-only RF shimming calculations that are employed throughout this thesis.

4.5.6.1 Approaches for Combining B_1^+ Maps

An optimised B_1^+ map was produced by combining two separate B_1^+ maps acquired with different transmit phase settings. The optimised map has improved the existing B_1^+ information in the middle of the phantom. Combining B_1^+ maps that were required at different drive scales also produces a final optimised B_1^+ map with improved coverage and B_1^+ information in the centre of the phantom.

Both methods for producing optimised B_1^+ maps (acquisition with different transmit phase settings and drive scales) are promising approaches for B_1^+ mapping for

7 T body applications. However, changing the transmit phase settings and drive scales before each acquisition is time consuming. Further work should include exploring these methods more in depth and programming the scanner so that these parameters can be changed conveniently during scanning sessions.

4.6 Conclusion

B_1^+ mapping is important for B_1^+ calibration and RF shimming during in vivo scans on pTx systems. B_1^+ mapping methods need to be time efficient and accurately reflect the underlying flip angle distribution across the whole FOV. Although the AFI method has a longer acquisition time than DREAM, it was a more robust sequence during initial body imaging work. Sufficient coverage with coarse resolution could still be achieved within a single breath hold. Linear combination and relative B_1^+ mapping techniques were described. Both of these methods address the problem of increased dynamic range sufficiently in smaller FOV imaging applications. Relative B_1^+ mapping using DREAM to acquire the necessary B_1^+ map is the most time efficient method considered.

The problems associated with using these methods for body imaging were explained. This includes the lack of a consistent linear regime across the large FOVs experienced in the body. Examples of methods that can be used to improve B_1^+ mapping for UHF abdominal imaging were described. Relative B_1^+ maps where information was non-linear in low signal areas was eliminated and optimised B_1^+ maps based on combinations of different transmit phases or powers were calculated. These are promising approaches for B_1^+ mapping in the body at 7 T but requires future work in investigating the best way to extrapolate to low and high areas of B_1^+ in order to be used as part of the imaging work flow.

References

[1] Francesco Padormo, Arian Beqiri, Joseph V. Hajnal, and Shaihan J. Malik. Parallel transmission for ultrahigh-field imaging. *NMR in Biomedicine*, 2015.

[2] Rudolf Stollberger and Paul Wach. Imaging of the active B1 field in vivo. *Magnetic Resonance in Medicine*, 35(2):245–251, 1996.

[3] Kay Nehrke. On the steady-state properties of actual flip angle imaging (AFI). *Magnetic Resonance in Medicine*, 61(1):84–92, 2009.

[4] Ulrich Katscher, Christian Findeklee, Peter Vernickel, Kay Nehrke, Tobias Voigt, and Olaf Dössel. Determination of Electric Conductivity and Local SAR Via B1 Mapping. *IEEE Transactions on Medical Imaging*, 28(9):1365–1374, 2009.

[5] Tobias Voigt, Kay Nehrke, Olaf Doessel, and Ulrich Katscher. T1 corrected B1 mapping using multi-TR gradient echo sequences. *Magnetic Resonance in Medicine*, 64(3):725–733, 2010.

[6] Korea Jhy, Korea Jml, Philips Healthcare Korea, Philips Healthcare Japan, Jeong Hee Yoon, Jeong Min Lee, Eunju Kim, Tomoyuki Okuaki, and Joon Koo Han. Quantitative liver Function analysis: Volumetric T1 Mapping with Fast Multisection B 1 Inhomogeneity Correction in Hepatocyte-specific Contrast-enhanced Liver MR Imaging 1. *radiology.rsna.org n Radiology*, 282(2), 2017.

[7] Roy A M Haast, Dimo Ivanov, and Kâmil Uludağ. The impact of B1+ correction on MP2RAGE cortical T1 and apparent cortical thickness at 7T. *Human brain mapping*, 39(6):2412–2425, 2018.

[8] Valentina Hartwig, Nicola Vanello, Giulio Giovannetti, Daniele De Marchi, Massimo Lombardi, Luigi Landini, and Maria Filomena Santarelli.

B1+/actual flip angle and reception sensitivity mapping methods: Simulation and comparison. *Magnetic Resonance Imaging*, 29(5):717–722, 2011.

[9] Fabien Balezeau, Pierre-Antoine Eliat, Alejandro Bordelois Cayamo, and Herve Saint-Jalmes. Mapping of low flip angles in magnetic resonance. *Phys. Med. Biol*, 56:6635, 2011.

[10] Vasily L. Yarnykh. Actual flip-angle imaging in the pulsed steady state: A method for rapid three-dimensional mapping of the transmitted radiofrequency field. *Magnetic Resonance in Medicine*, 57(1):192–200, 2007.

[11] Alois M. Sprinkart, Kay Nehrke, Frank Traber, Wolfgang Block, Jurgen Gieseke, Georg Schmitz, Winfried A. Willinek, Hans Schild, and Peter Bornert. Ultrafast volumetric B1+ mapping for improved radiofrequency shimming in 3 tesla body MRI. *Journal of Magnetic Resonance Imaging*, 40(4):857–863, 2013.

[12] Shaihan J. Malik, Gavin D. Kenny, and Joseph V. Hajnal. Slice profile correction for transmit sensitivity mapping using actual flip angle imaging. *Magnetic Resonance in Medicine*, 65(5):1393–1399, 2011.

[13] Y Zur and S Stokar. A Phase-Cycling Technique for Canceling Spurious Echoes in NMR Imaging. *Journal of Magnetic Resonance*, 71:212–228, 1987.

[14] Kay Nehrke, Maarten J. Versluis, Andrew Webb, and Peter Börnert. Volumetric B1+ mapping of the brain at 7T using DREAM. *Magnetic Resonance in Medicine*, 71(1):246–256, 2014.

[15] Kay Nehrke and Peter Bornert. DREAM — A Novel Approach for Robust, Ultrafast, Multislice B1 Mapping. *Magnetic Resonance in Medicine*, 68:1517–1526, 2012.

[16] Sascha Brunheim, Marcel Gratz, Sören Johst, Andreas K. Bitz, Thomas M. Fiedler, Mark E. Ladd, Harald H. Quick, and Stephan Orzada. Fast and

Accurate Multi-channel B1+ Mapping Based on the TIAMO Technique for 7T UHF Body MRI. *Magnetic Resonance in Medicine*, in press(February):1–13, 2017.

[17] Glen R Morrell and Matthias C Schabel. An analysis of the accuracy of magnetic resonance flip angle measurement methods. *Physics in Medicine and Biology*, 55(20):6157–6174, 2010.

[18] Daniel J Park, Neal K Bangerter, Ahsan Javed, Joshua Kaggie, Mohammad Mehdi Khalighi, and Glen R Morrell. A statistical analysis of the Bloch–Siegert B1 mapping technique. *Physics in Medicine and Biology*, 58(16):5673–5691, 2013.

[19] D Brunner and K Pruessmann. A matrix approach for mapping array transmit fields in under a minute. *Proceedings 16th Scientific Meeting, International Society for Magnetic Resonance in Medicine*, Toronto:354, 2008.

[20] Kay Nehrke and Peter Bornert. Eigenmode analysis of transmit coil array for tailored B1 mapping. *Magnetic Resonance in Medicine*, 63(3):754–764, 2010.

[21] K. Nehrke and P. Bornert. Improved B1-Mapping for Multi RF Transmit Systems. *Proc Intl Soc Mag Reson Med*, 16:353, 2008.

[22] Shaihan J. Malik, David J. Larkman, and Joseph V. Hajnal. Optimal linear combinations of array elements for B1 mapping. *Magnetic Resonance in Medicine*, 62(4):902–909, 2009.

[23] Kawin Setsompop, Vijayanand Alagappan, Borjan Gagoski, Thomas Witzel, Jonathan Polimeni, Andreas Potthast, Franz Hebrank, Ulrich Fontius, Franz Schmitt, Lawrence L. Wald, and Elfar Adalsteinsson. Slice-Selective RF pulses for In-vivo B1+ Inhomogeneity Mitigation at 7 Tesla using Parallel RF Excitation with a 16-Element Coil. *Magnetic Resonance in Medicine*, 60(6):1422–1432, 2008.

[24] Pierre-Francois Van De Moortele, Snyder Carl, Lance Delabarre, Gregor Adriany, Tommy Vaughan, and Kamil Ugurbil. Calibration Tools for RF Shim at Very High Field with Multiple Element RF Coils: From Ultra Fast Local Relative Phase to Absolute Magnitude B1+ Mapping. *Ismrm*, 15:1, 2007.

[25] Francesco Padormo, Aaron T. Hess, Paul Aljabar, Shaihan J. Malik, Peter Jezzard, Matthew D. Robson, Joseph V. Hajnal, and Peter J. Koopmans. Large dynamic range relative B1+ mapping. *Magnetic Resonance in Medicine*, 76(2):490–499, 2016.

[26] H-P. Fautz, M. Vogel, P. Gross, A. Kerr, and Y. Zhu. B1 mapping of coil arrays for parallel transmission. Technical Report 1, 2005.

[27] Stephan Orzada, Stefan Maderwald, Benedikt Andreas Poser, Andreas K. Bitz, Harald H. Quick, and Mark E. Ladd. RF excitation using Time Interleaved Acquisition of Modes (TIAMO) to address B1 inhomogeneity in high-field MRI. *Magnetic Resonance in Medicine*, 2010.

[28] Sascha Brunheim, Stephan Orzada, Soeren Johst, Marcel Gratz, Maximilian N Voelker, Oliver Kraff, Martina Floeser, Andreas K Bitz, Mark E Ladd, and Harald H Quick. Combining B1 mapping with TIAMO for fast and accurate multi-channel RF shimming in 7 Tesla body MRI. *Proc. Intl. Soc. MRM 24*, (Figure 3):3186, 2016.

[29] Mark A. Griswold, Peter M. Jakob, Robin M. Heidemann, Mathias Nittka, Vladimir Jellus, Jianmin Wang, Berthold Kiefer, and Axel Haase. Generalized Autocalibrating Partially Parallel Acquisitions (GRAPPA). *Magnetic Resonance in Medicine*, 47(6):1202–1210, 2002.

5 Robust RF Modelling for Evaluation of 7 T Body Imaging

Parallel Transmission Technology (pTx) at 7 T poses a particular MR safety challenge due to the potential for local SAR hotspots that can arise from constructive interference of electric fields generated from individual transmit RF channels. SAR distributions cannot be predicted a priori and so electromagnetic (EM) simulations are essential for full local SAR assessment. The overall goal of this chapter is to outline a method for efficient local SAR estimations of subject-specific models for abdominal imaging at 7 T. The sensitivity of the estimates of local SAR and B_1^+ in relation to coil displacement, intra-subject variability due to respiration, and inter-subject variability within a library of subject-specific models is also explored.

This chapter contains methods and results that were published as abstracts in the proceedings of the 26th and 27th Annual Meetings of the International Society for Magnetic Resonance in Medicine (ISMRM):

- Repeatability of FDTD simulations for determining local SAR and B_1^+ distributions for UHF abdominal imaging, **2019**, *In Proc. ISMRM (Montreal)*, #4157
- Simplified subject-based models for efficient electromagnetic simulations and evaluation of local SAR for 7 T abdominal MRI, **2019**, *In Proc. ISMRM (Montreal)*, #4156
- Effects of Respiration on B_1^+ and SAR in Whole-Body Imaging at 7 T, **2018**, *In Proc. ISMRM (Paris)*, #4179

5.1 Introduction

Abdominal MR imaging at 7 T shows great promise due to the increase in signal-to-noise (SNR) [1]. However, when imaging at UHF it is important to ensure subject safety and limit the tissue heating effects that can be caused by the increased RF energy deposition introduced in Chapter 3. The Specific Absorption Rate (SAR) is used as a measure for this energy deposition and is a concern at all field strengths but even more so at 7 T due to the increase in frequency of the RF fields used for excitation [2].

Estimations of SAR must be made prior to scanning to ensure restrictions set by the International Electrotechnical Commission (IEC) and The Food and Drug Administration (FDA) are met [3, 4]. It is difficult to measure SAR in vivo and so numerical simulations are used to evaluate the expected global and local SAR distributions [5]. Global SAR is easier to estimate and can be controlled by restricting power during scanning. However, there is a lack of reliable techniques for monitoring and measuring local SAR in vivo. Due to the use of local transmit coils and the shorter wavelengths of the RF radiation at 7 T there is a danger of reaching peak local SAR values whilst still being within global SAR safety limits. The complicated behaviour of local SAR is due to the unique electromagnetic interactions of the RF fields within heterogeneous tissues with different dielectric properties that are present in the human body [6].

Therefore, local SAR simulations must contain realistic representations of the RF transmit system and subject anatomy. Work has been performed with highly detailed generic human body models in a small population of body compositions to characterise the inter-subject variability [7–10]. These results provided conservative safety factors so that 7 T scanning could be performed. However, working within these conservative regimes can be detrimental to image quality, and this has motivated further development of methods for investigating local SAR in the body at 7 T on an individual subject basis.

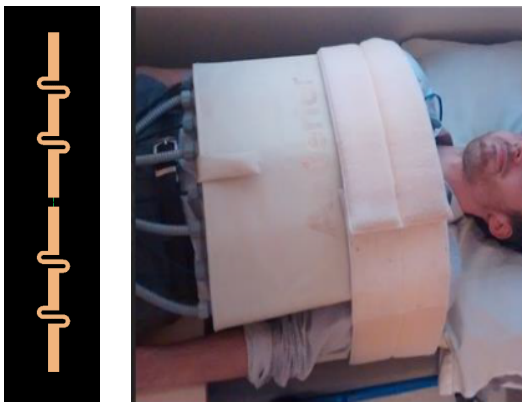
This chapter aims to develop a robust modelling pipeline for investigating local

SAR in the abdomen at 7 T. This includes performing FDTD simulations with an efficient RF coil model and subject-specific body models to provide measures of intra- and inter-subject variability in a population of healthy volunteers.

As described in Chapter 3, local SAR can be estimated using the FDTD method for EM simulations to model RF behaviour [11]. When simulating pTx systems, if all transmit RF channels are simulated simultaneously with a specific amplitude and relative phase setting, only this single RF configuration can be investigated. However, simulating each transmit channel independently enables unique RF settings to be applied off-line during local SAR computation. This means that fully characterising a pTx system can take significant amounts of time as the number of full simulations required is equal to the number of transmit channels.

Each transmit RF channel in the coil model needs to be tuned to resonant frequency in the simulation to ensure realistic representation of the RF transmit system. The tuning process can also take considerable lengths of time as it requires a broadband frequency sweep (0 - 1 GHz). Therefore, a coil model that is capable of accurate and rapid tuning is desirable.

Initial EM simulations were performed with a model of the body array (MRCoils 8TX/32RX fractionated dipole body array [12]) with transmit dipoles modelled as thin blocks of perfectly conducting material as displayed in Figure 5.1 (a). This model only tuned to resonant frequency (300 MHz) when dipoles were orientated along Cartesian mesh edges. This did not represent how the body array is wrapped around the subject in real life situations, as shown in Figure 5.1 (b).



(a) (b)

Figure 5.1: (a) Example of one of the fractionated dipoles used in the coil model in initial simulations. Dipoles were modelled as thin blocks of perfectly conducting material. (b) Demonstration of body array wrapped around subject.

The Cartesian gridding used in the FDTD simulation poses a problem for the curved meanders of the fractionated dipoles (see Figure 5.2). There are techniques developed in EM simulation packages to improve the accuracy of the mesh generated for geometrical features such as complex curved surfaces or small gaps in material [13] however, these are not always available in every software version. When the dipoles were tilted to mimic how they are wrapped around a subject in the scanner, they would not tune to resonance as the curved meanders were no longer sufficiently meshed. Accurate determination of coupling ratios and dipoles tuned to resonance are necessary for accurate SAR predictions. Therefore, this configuration could not be used to produce accurate results.

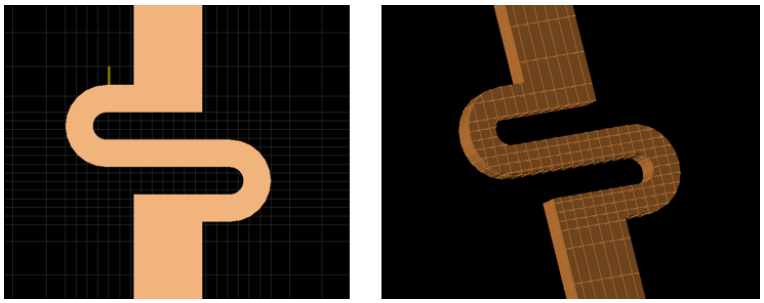


Figure 5.2: Example of a curved meander of the dipole and a meshed block model.

In order to allow for variations in the dipole orientation during scanning the block dipole model was replaced by a wire dipole model. In this model straight perfectly conducting wires and multiple inductors were used to represent each transmit dipole. By using this model, developed by Bawden et al. [14], individual transmit elements could effectively be rotated in the xy-plane whilst still maintaining resonant tuning at 300 MHz. Additionally, comparing simulations where the target cell sizes were equivalent, the wire model tuning converged 2.2 times faster than the block dipole with the meanders.

Complex human models based on highly detailed, high resolution segmentations of 3D image data can be constructed of millions of voxels. Simulations with these models require similar numbers of Yee cells (see Section 3.9) in order to fully capture information about the dielectric properties for different tissue types and the boundaries between them, contributes to significant simulation time.

Furthermore, these complex human models only represent a small fraction of the human population. Scaling models up or down to match other human geometries is not sufficient as retaining information about exact internal tissue distributions is vital for accurate SAR modelling. The modelling of male and female body types of all ages, Body Mass Index (BMI) values and realistic positions based on subject-specific models would allow local SAR distributions to be assessed in a general population [8, 15].

Typically, simulations with generic human models are performed and to compensate for differences in different body types additional safety factors are applied to results when investigating worst case local SAR conditions [16, 17]. These safety factors can potentially be highly conservative severely limiting the power available for scanning [18]. Alternatively, individual subjects can be modelled to allow more accurate local SAR predictions, but construction of these models can be very time consuming, requiring skilled user intervention for tissue segmentation [19, 20].

Existing literature has shown that using truncated whole-body models with reduced tissue complexity can be used to simulate local SAR in the head without compromising the results [2, 18, 21]. This finding is incredibly useful as it means that less tissue types require segmentation when constructing subject-specific body models for simulations speeding up the process. The work in this chapter is based on the hypothesis that the same approach can be taken in the body by using truncated whole-body models with reduced tissue complexity to simulate local SAR in the abdomen.

5.1.1 Outline

This chapter addresses the challenges discussed in the previous section and covers the following pieces of work:

- Verification of FDTD simulations through comparison of simulated B_1^+ fields and acquired B_1^+ maps in a body phantom.
- Simulations with the developed wire dipole model are performed, local SAR and B_1^+ distributions are calculated and compared to results obtained with the original full block dipole model.
- A method for creating subject-specific, simplified body models was developed. The use of simplified models to reproduce accurate results was assessed by looking at the truncation of generic whole-body models and the reduced tissue complexity of subject-specific models.

- Efficient simulations combined with simplified models offer a robust approach for RF modelling and evaluating body imaging at 7 T. This is used to study the following three concepts.
  - The sensitivity of local SAR results to small displacements of the coil model was also determined. In reality the body array (and subject) do not always remain in the same position throughout the scan session due to movement. Investigating the sensitivity of RF modelling results to realistic displacements will give insight into the variability in maximum local SAR evaluations and increase confidence in values used to form final power limits.
  - Respiration induced variations in both local SAR and B_1^+ [22, 23] provide a measure of intra-subject variability. This is important information for assessing the robustness of RF shimming and RF pulse design at 7 T in the body [24]. The developed subject-specific models are used to evaluate the effect of respiration on calculated local SAR and B_1^+ fields. The results are verified by comparing B_1^+ maps acquired in the same subjects in vivo.
  - Inter-subject variability of peak local SAR results in a library of models was also investigated. This is extremely important as it characterises the worst case scenario peak local SAR values. The correlation of these results with body composition of the subjects and different RF phase settings generated using a Monte Carlo method were evaluated.

5.2 Methods

5.2.1 Simulations

EM simulations were performed using Remcom XFdtd 7.7.1 (Remcom, State College, PA, USA) and were executed on an NVIDIA Titan Xp GPU. Each transmit dipole was driven by feeding a port located halfway along each dipole with 0° phase shift and tuned ideally at 300 MHz (each dipole was tuned to a slightly different frequency due to the interaction with the body model placed in the coil). An example of a tuned dipole is shown in Figure 5.3. Open boundary conditions were defined in all directions and calculations were terminated after simulation of a system energy decay of -30 dB.

An optimised gridding algorithm (PrOGrid, Remcom) was applied in all simulations. The minimum feature size was defined as 5 cells for good conductors and 2 cells for poor conductors. This resulted in minimum cell edge lengths of 3.6 x 1.5 x 0.4 mm^3 around the dipole feeds and maximum edge lengths of 7.8 x 7.7 x 29.2 mm^3 towards the periphery of the simulation space. On average there were on the order of 5 million cells across each simulation. The average runtime for each simulation was approximately 30 minutes depending on the extent of the body model. EM fields, scattering (S-) parameters (see Section 3.4.2) and input powers for each transmit element were exported once each simulation had terminated along with biological tissue density and electrical conductivity data associated with the body model in each simulation.

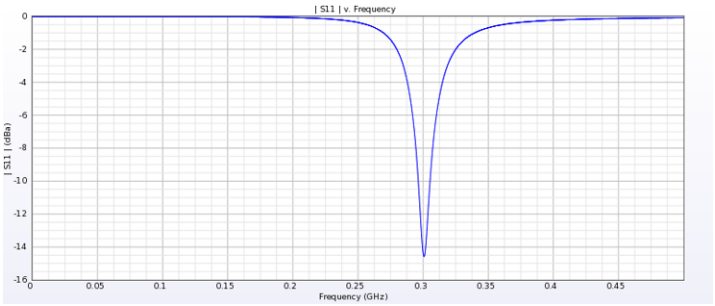


Figure 5.3: S-parameter [S_{11}] vs. frequency plot for a wire dipole: inductors were tuned such that each transmit dipole had a resonance frequency of 300 MHz.

5.2.2 Data Processing

The post-processing and analysis of the exported data was carried out in Matlab R2018b (The MathWorks Inc, Natick, MA, USA) using in-house scripts. Electric and magnetic fields were normalised to 1 W incident power for each transmit element before calculating SAR distributions and B_1^+ fields.

These were projected onto a 2 mm isotropic Cartesian grid for the mass averaging method used (described in Section 3.9.3). S-parameters were used to construct the S-matrices (discussed in Section 3.4.2) for the coil model in each simulation. A SAR per $\sqrt{(B_1^+)^2}$ value for each simulation was calculated from the peak local SAR value after scaling the local SAR distribution by the same factor required to normalise the B_1^+ distribution to a maximum value of 1 μT.

5.2.3 Comparing Simulated and Experimental B_1^+ Distributions

To provide a test of the validity of the EM simulations and wire based body array model, the B_1^+ distribution generated from a simulation with a model of the body phantom (described in Section 3.7) was compared to a B_1^+ map collected on the same phantom on the 7 T Philips Achieva multi-transmit system.

The model of the phantom, shown in Figure 5.4, was constructed with the

following dielectric properties for each simulated material [25]:

Table 5.1: Conductivity and density values of the simulated materials included in the body phantom model.

Material	Conductivity, σ [Sm^{-1}]	Density, ρ [kgm^{-3}]
Copper Sulphate Solution	10.7	988.2
Plastic Casing	1e^{-15}	1180
Vegetable Oil	1e^{-10}	900

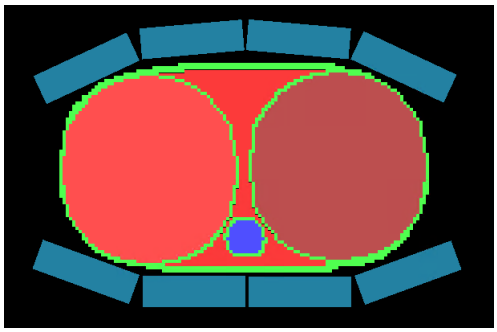


Figure 5.4: Body array and phantom models used in the EM simulations.

The B_1^+ mapping acquisition method used was DREAM [26]; transverse orientation, FOV = 304 x 480 x 400 mm^3 , voxel size = 3.125 x 3.125 x 4 mm^3, STEAM flip angle $\alpha = 40°$, imaging flip angle $\beta = 7°$, imaging sequence repetition time TR = 5.3 ms, echo times = 3.6/4.05 ms, echo order: STE first.

In order to directly compare the B_1^+ distributions the simulated data was scaled to 3 W average power per transmit channel (to match the power limits set on the scanner) and the experimental data was converted from $\%$ of nominal flip angle to units of micro-Tesla (μT). This was achieved using details of the RF excitation pulses used for the STEAM sequence ($B_{1\,max}^+ = 1.6\ \mu$T) which dictate the nominal flip angle for the DREAM B_1^+ mapping method.

5.2.4 Simplified Dipole Model Verification

The agreement between the wire dipole model [14] and the full block dipole model was investigated. In the block based model each radiative fractionated

dipole antenna consisted of two copper strips which were centrally fed by a voltage feed with a load of 50 Ω. This framework was created using CAD software to represent the exact geometry and imported into simulation software.

The wire based model replaced the fractionated dipole antennas with straight perfectly conducting wires. These wires were also centrally fed by a voltage feed with a load of 50 Ω and included four inductors placed along each wire to represent the dipole meanders. Values for the inductors were adjusted to tune each dipole to 300 MHz and ranged from 70 - 95 nH. The element casing and fibreglass circuit board upon which each dipole was placed was modelled as a plastic substrate. The dimensions of each transmit element was 100 mm x 30 mm x 400 mm and the length of each wire dipole was 310 mm; this is demonstrated in Figure 5.5.

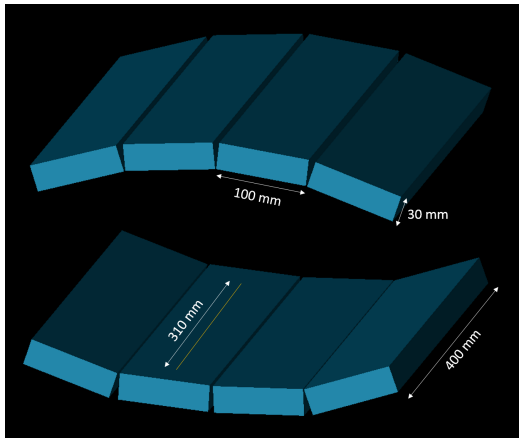
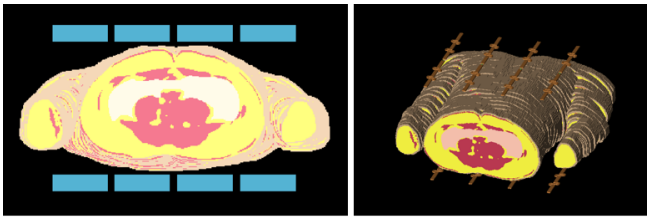


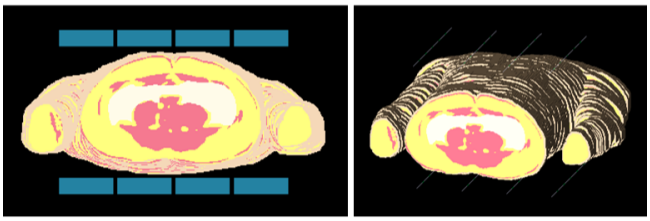
Figure 5.5: Body array model; dimensions of transmit element casings [400 x 100 x 30 mm^3] and dipole elements [310 mm in length] shown.

In reality, receive loops are contained within the plastic substrates along the length of each dipole. However, these were not included in the simulation model as they are detuned and have negligible effect in normal operations. Both wire and block dipole body array models included the ability to move individual elements so they could accommodate the human models, just as the body array would adapt to individual subject's body contours.

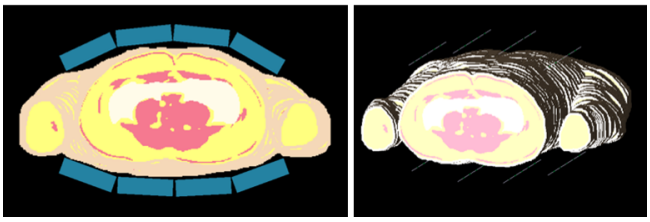
Three simulations were run according to the methods outlined in Section 5.2.1 with a male body model (examples are shown in Figure 5.6). The first simulation (*Block Model*) used the block dipole model with each element placed straight along the Cartesian grid lines. The second simulation (*Wire Model (straight configuration)*) replaced the block dipole model with the wire dipole model elements in the same locations and orientation. The third simulation (*Wire Model (tilted configuration)*) was run with wire dipole elements tilted in the x, y plane such that each element was positioned in accordance with the contours of the body model.



(a) Block dipole model with straight elements.



(b) Wire dipole model with straight elements.



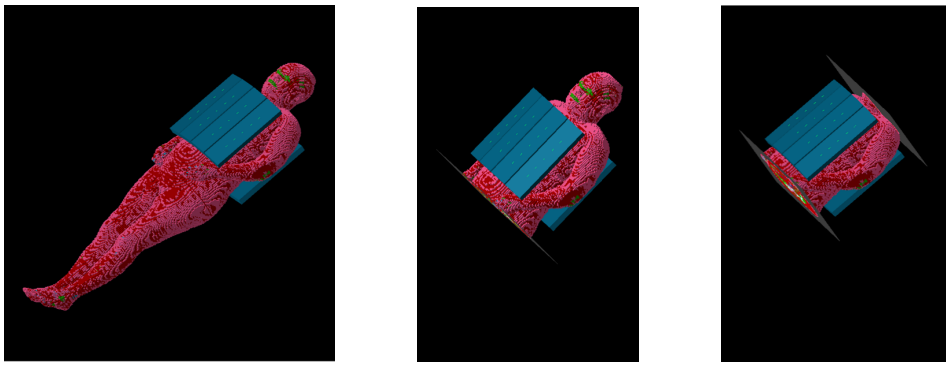
(c) Wire dipole model with rotated elements in xy-plane.

Figure 5.6: Examples of the coil geometries used in each simulation (with a male body model) performed for wire dipole model verification.

5.2.5 Development of Simplified Body Models

5.2.5.1 Truncation

A generic, whole-body, male human model based on data from the National Library of Medicine's Visible Human Project [27] was available as part of the simulation software. This body model was used to study the effects of replacing whole-body models with torso-only models. Three separate simulations were performed with a whole-body, upper-body and torso-only model as shown in Figure 5.7. Upper-body and torso-only models were obtained by restricting the computational space to the target anatomy. A perfectly matched layer (PML) boundary was used (layers = 7) to avoid any problems with open boundaries in the truncated simulations (see Chapter 3, Section 3.9.1).



(a) Whole-body. (b) Upper-body. (c) Torso-only.

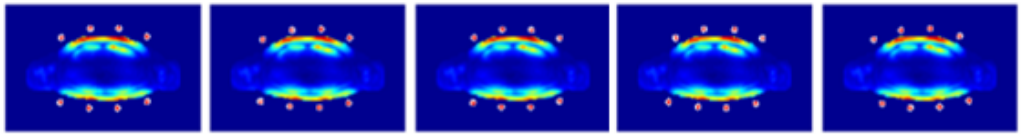
Figure 5.7: Whole-body and truncated versions of the generic male human model used in simulations.

5.2.5.2 Repeatability and Coil Model Position

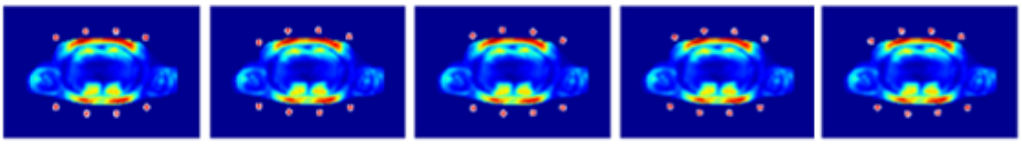
Two subject-specific models (male and female) were created based on data acquired on a 3T Philips Ingenia MR system. The mDixon sequence with TR = 5.0 ms, $TE_1/\Delta TE$ = 1.19/1.18 ms and flip angle = 3° was used. The FOV was fixed to 560 x 300 x 560 (AP x FH x RL) mm^3 and the voxel resolution was 1.3 x 1.3 x 5 mm^3 resulting in a total scan duration of 10.1 s.

Image outputs were used to manually segment 12 different abdominal tissue types using Analyze software. These regions were labelled according to the Remcom tissue library and constructed into 3D body models (resolution 1.5 x 1.5 x 5 mm^3) encompassing the torso and arms of each subject in Matlab. The body models were then imported into the EM software for simulation.

Five separate simulations were performed with each model to generate EM fields from individual elements. The body array model was displaced in $\pm$x directions (corresponding to the RL direction) by 10 mm and then reconformed around the body at the new position in each simulation. Figure 5.8 highlights how the positions of the coil elements were subtly changed in each simulation.



(a) Male model simulations.



(b) Female model simulations.

Figure 5.8: Body array positions in each of the five separate simulations for the (a) male model and (b) female model investigations. Note the subtle movement and overall small displacements of each transmit coil element between each of the columns.

The variation of local SAR between positions for each model was calculated and used to compute an expected error for final local SAR values in subsequent simulations. The local SAR variability result was also used to determine when simplified simulations started to deviate significantly from validated simulations.

5.2.5.3 Reduced Tissue Complexity

Six versions of each manually segmented model were created with increasingly reduced tissue complexity to represent successive stages of simplified tissue segmentation. The different tissue assignments are outlined in Table 5.2, and the conductivity and density values of the different tissues used in the simplified models, generated by the Remcom tissue library, are listed in Table 5.3. Full simulations were repeated with each of these models with the coil and human models in the same geometry.

Table 5.2: Tissue types included in each of the simplified models. A male and female of each model type was constructed.

	Tissue Types					
Model Type	Abdominal Organs	Muscle	Fat	Skin	Lung	Bone
Full	Organ specific	Muscle	Fat	Skin	Lung	Bone
MFSLB	Muscle	Muscle	Fat	Skin	Lung	Bone
MFSLBa	Muscle	Muscle	Fat	Skin	Lung	Fat
MFSLBb	Muscle	Muscle	Fat	Skin	Lung	Muscle
MFLBa	Muscle	Muscle	Fat	Muscle	Lung	Bone
MFLBb	Muscle	Muscle	Fat	Fat	Lung	Bone
MFL	Muscle	Muscle	Fat	Fat	Lung	Fat

Table 5.3: Conductivity and density values of reduced complexity tissue types.

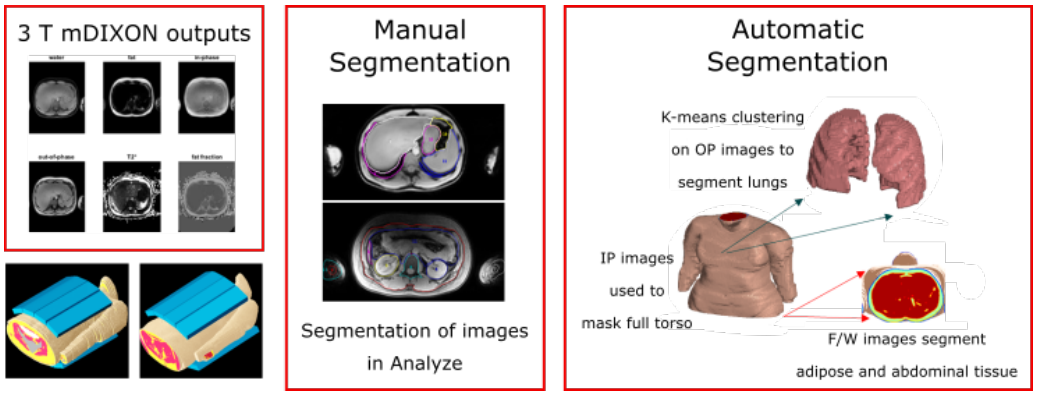
Tissue	Conductivity [Sm^{-1}]	Density [kgm^{-3}]
Muscle	0.8	1090
Fat	0.035	911
Skin	0.0002	1109
Lung	0.03	394
Bone	0.07	1178

5.2.5.4 Automatic Segmentation

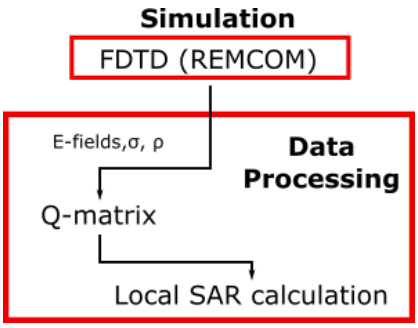
The most simplified model that returned accurate results was used to develop an automatic segmentation method for generating subject-specific torso-only body models from 3 T mDixon data. The input images for the automatic

segmentation were the same 3T mDixon data used previously. The in-phase mDixon images were used to segment the subject from the image background using the Otsu method; this is an automatic clustering based image thresholding technique [28]. Fat and water images were used to segment fat and water-based tissues for each model. Adaptive k-means clustering [29] was implemented on the out-of-phase images to segment the lungs. Finally, a 2 mm^3 layer of skin tissue, corresponding to a single voxel layer, was added to each subject model and all tissue types were labelled according the Remcom tissue library.

Simulations were run according to Section 5.2.1 with the male and female automatically segmented simplified models. Results from these simulations were then compared to those obtained from the manually constructed models in order to confirm if the automatically segmented models could replace the manually segmented models in simulations to investigate local SAR. The automatic segmentation process is illustrated in Figure 5.9.



(a)



(b)

Figure 5.9: Overview of (a) subject-specific model construction; manual and automatic segmentation of 3 T mDixon images were used to construct body models for EM simulations, and (b) local SAR analysis pipeline; simulated electric fields, conductivity and density data were exported from the FDTD simulation and processed using the Q-matrix formulism to calculate local SAR for a given human body model.

5.2.6 Intra-subject Variability: Respiration Study

Seven healthy subjects (three female, four male) were scanned on a Philips 3 T Ingenia. mDixon scans (described in Section 5.2.5.2) were repeated at exhale and inhale breath hold positions. A mock 7 T body array with vials of copper sulphate solution attached on top of each anterior element was placed under the 3 T 32-channel receive body array during scanning permitting the location of the vials to be indicated in the segmentation process and used as markers for

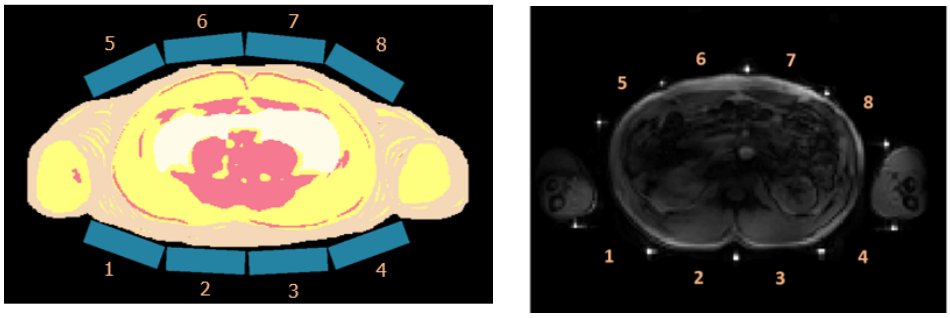
the transmit element locations in subsequent EM simulations as shown in Figure 5.10 (a). Subject-specific body models were constructed from the mDixon data in the method outlined in Section 5.2.5.2.

The subjects also underwent scans on a Philips 7 T Achieva 8-channel pTx system (Best, Netherlands) with the MRCoils 8 TX/32 RX fractionated dipole array coil (Utrecht, Netherlands). Abdominal B_1^+ maps were acquired at exhale and inhale. In all of the subjects, individual transmit element B_1^+ maps were acquired using the AFI technique (voxel size = 3 x 3 x 10 mm^3, FOV = 450 x 450 x 10 mm^3, TE = 2.05 ms, TR1 = 40 ms, TR2 = 200 ms, flip angle $\alpha = 40^\circ$, breath-hold duration per element = 20 s) [30].

Repeatability was assessed in one subject by acquiring another set of single channel B_1^+ maps in a separate scanning session. B_1^+ maps were also acquired with all channels on using the same AFI parameters in three of the subjects. These were used to examine the change in the B_1^+ magnitude induced by respiration in the liver and kidneys. Fiducial markers that contained copper sulphate solution were attached inbetween the transmit elements of the 7 T body array and allowed assessment of the position of the coil during each respiratory phase (see Figure 5.10 (b)).

EM simulations were run with the exhale and inhale body models with the coordinates of the body models matching between separate simulations. The coil model was adjusted between the exhale and inhale simulations according to the contours of each body model, mock array element location markers from the 3 T mDixon data and the placement of the fiducial markers from the 7 T in vivo images. Local SAR, B_1^+ distributions and S-matrices were evaluated in order to study the changes induced by respiration effects. In order to compare simulated and in vivo B_1^+ distributions the simulated data was scaled to 3 W incident power per transmit channel as this was used for the 7 T scans.

Simulated and in vivo individual transmit channel B_1^+ data from all seven subjects was analysed to calculate the change in the magnitude of the B_1^+ field due to respiration using the following approach. The mean B_1^+ magnitude and standard



(a) Body model in the EM simulation showing the numbered transmit elements that directly correspond to the in vivo scans.

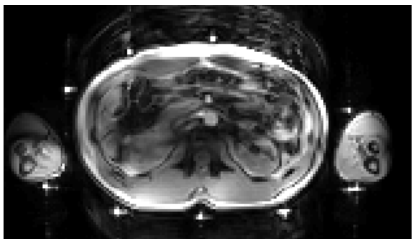
(b) 7 T in vivo image showing fiducial markers attached to the transmit elements of the body array.

Figure 5.10: Fiducial markers attached to the transmit elements of the body array during in vivo scanning allowed direct comparison between in vivo and simulated positioning of the transmit elements.

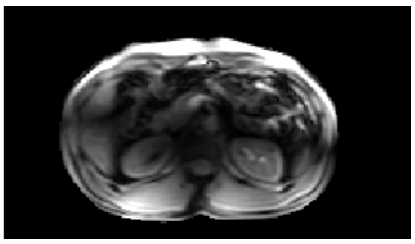
deviation was measured in ROIs of 4 x 4 voxels under each transmit element for each respiration phase. The same ROI was applied to the exhale and inhale data.

In vivo all channels on B_1^+ data was analysed for the subset of three subjects. The mean B_1^+ magnitude and standard deviation was measured in three ROIs within the liver and kidneys. The underlying gradient echo images from the AFI data were used to select the ROI within the organ of interest. An average value calculated from the three mean B_1^+ values in each organ was then quoted for the final result.

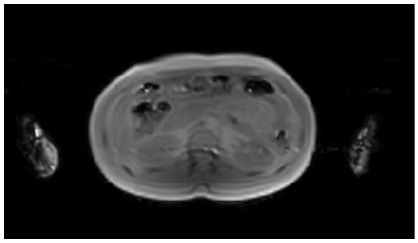
Equivalent anatomical slices were assessed in the in vivo and simulated data sets. The image slices were matched manually between the 7 T images (see Figures 5.11 (a) and (b)), 3 T mDixon images (see Figure 5.11 (c)), and constructed body model (see Figure 5.11 (d)). The same position in the abdomen was then found in the simulated body models and relevant data for all subjects. Figure 5.12 shows density and conductivity maps in a simulated body model that corresponds to the slices shown in Figure 5.11.



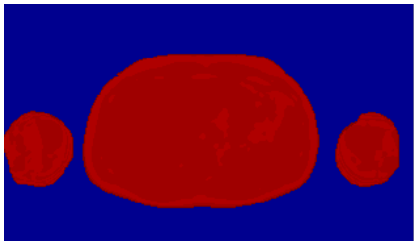
(a) Underlying image of B_0 Map



(b) Underlying image of B_1^+ Map

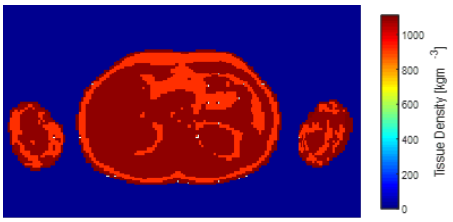


(c) 3 T mDixon slice

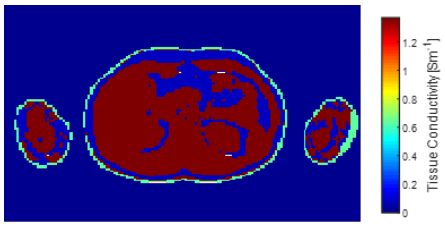


(d) Body model constructed from the 3 T data

Figure 5.11: Demonstration of the corresponding anatomical slices between different data sets acquired on different scanners. Images presented are; (a) an underlying image from a 7 T B_0 map, (b) an underlying image from a 7 T B_1^+ map, (c) corresponding 3 T mDixon image, (d) a slice from the simplified subject-specific model constructed from the 3 T mDixon images. Slice shown here for one subject encompasses the bottom of the liver and kidneys.



(a) Simulation.



(b) Simulation.

Figure 5.12: Examples of (a) density and (b) conductivity tissue maps exported for a simulated body model. Slice presented is equivalent to the in vivo slices outlined in Figure 5.11.

5.2.7 Inter-subject Variability

Ten healthy subjects (four females and six males, BMI range 19.7-36.7) were scanned at 3 T with the mock 7 T body array and mDixon data was acquired according to Section 5.2.5.2 to generate a small library of subject-specific models. Simulations were performed and data was processed according to Sections 5.2.1 and 5.2.2 respectively.

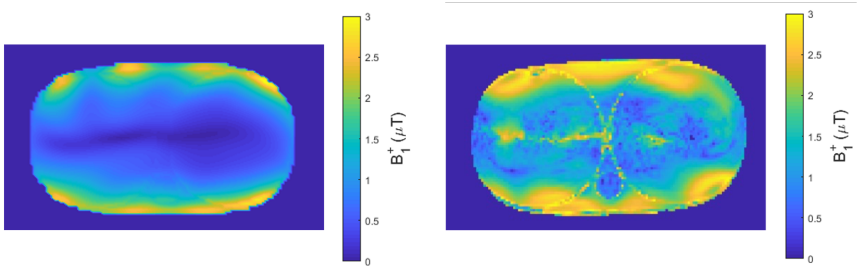
A Monte Carlo simulation [31] was performed on a high performance computing (HPC) cluster with each generated subject-specific dataset. A total of 10^3 static RF configurations were simulated by generating eight random phases (in the range 0° - 360°) while keeping the RF amplitude of each channel equal to 1. The corresponding 10^3 maximum local SAR values, maximum B_1^+ values and RF phase settings were used to assess inter-subject variability. An inter-subject safety factor was determined in relation to the current average 3 W power supply per channel applied to the 7 T MR system.

Fat images from the mDixon data were analysed for visceral and subcutaneous fat volumes in an external software program. Measures for the total number of voxels in each fat image that corresponded to visceral or subcutaneous fat were correlated with the local SAR values obtained in each subject.

5.3 Results

5.3.1 Comparing Simulated and Experimental B_1^+ Distributions

Figure 5.13 (a) shows a simulated B_1^+ distribution in a model of the body phantom and Figure 5.13 (b) displays the acquired B_1^+ map in the body phantom. Both distributions are similar providing confidence that the EM simulations reproduce experimental conditions. Notably, the dark band of destructive interference in the middle of the simulated B_1^+ distribution matches the noisy central region in the acquired B_1^+ map. This central line corresponds to where the B_1^+ magnitude and therefore signal is low, and the DREAM reconstruction is prone to errors (see Chapter 4).

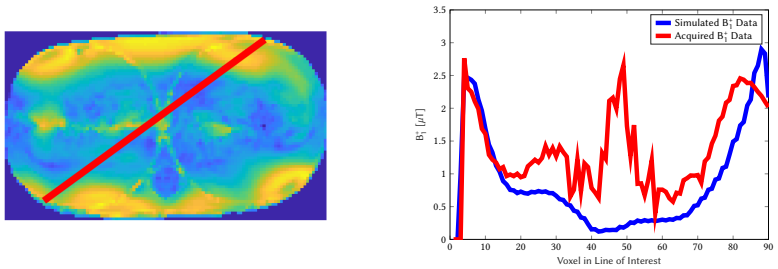


(a) Simulated B_1^+ distribution. (b) Acquired B_1^+ distribution.

Figure 5.13: EM simulations are validated by comparing (a) simulated and (b) acquired B_1^+ distributions in the body phantom. Experimental B_1^+ distributions were acquired using the DREAM method.

Magnitude B_1^+ values from both distributions were compared along a line of interest starting from the posterior of the phantom to the anterior surface on a diagonal line through the centre of the phantom (this line is shown in Figure 5.14 (a)). The B_1^+ drop-off from the phantom surface towards the central region is steeper in the simulated data compared to the experimental B_1^+ map. This is likely due to greater localisation of deposited RF energy at the surface of a given sample in the wire dipole coil model compared to the fractionated dipoles

in the body array. The B_1^+ values from the central region of the acquired B_1^+ map reflect the noisy estimates of B_1^+ values reconstructed from low signal in the underlying images.



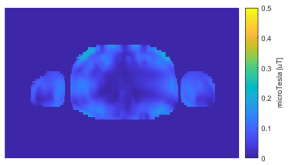
(a) (b)

Figure 5.14: Magnitude B_1^+ profiles were compared between the simulated and acquired data. The line of interest drawn for the profile is displayed in (a) and (b) shows the comparison of simulated and acquired B_1^+ values measured along the line of interest in the phantom.

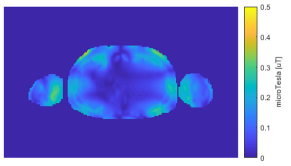
5.3.2 Simplified Dipole Model Verification

Figure 5.15 shows B_1^+ distributions in the central slice of the body model in *Block Model*, *Wire Model (straight configuration)* and *Wire Model (tilted configuration)* simulations respectively. In general, B_1^+ distributions are consistent between the simulations. The magnitude of B_1^+ increases between *Block Model* and *Wire Model (straight configuration)* simulations, and again in the *Wire Model (tilted configuration)*. This is expected as the dipole elements are successively brought closer to the body model and are more realistically adapted to the contours of the simulated biological tissue, which would result in greater transmit efficiency and energy deposition.

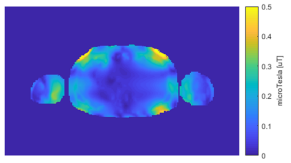
Local SAR maximum intensity projections (MIPs) are shown in Figure 5.16 with the location of local SAR hotspots highlighted. Maximum local SAR and SAR/$\sqrt{(B_1^+)^2}$ values for each simulation are listed in Table 5.4. Figure 5.17 shows the position of the transmit dipoles in each of the simulations.



(a) Block dipole model.



(b) Wire dipole model (straight configuration).

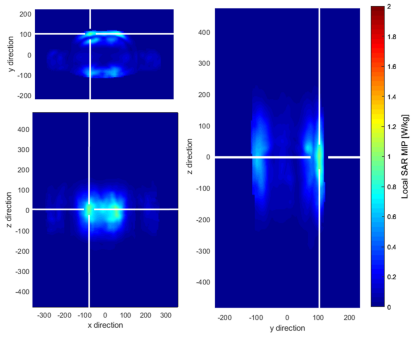


(c) Wire dipole model (tilted configuration).

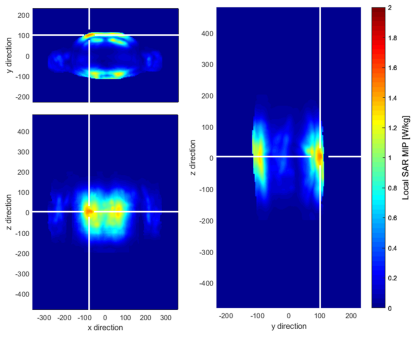
Figure 5.15: B_1^+ field generated in central slice of body model for (a) block dipole, (b) wire dipole (straight configuration) and (c) wire dipole (tilted configuration) simulations.

Table 5.4: Maximum Local SAR Results in Wire Dipole Model Development Simulations

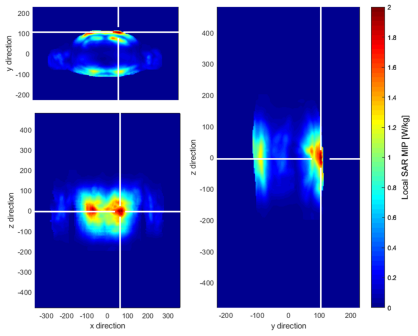
Simulation	Max. Local SAR [Wkg^{-1}]	SAR/$\sqrt{(B_1^+)^2}$ [Wkg$^{-1}\mu$T^{-1}]
Block Model	0.98	3.97
Wire Model (straight)	1.47	3.89
Wire Model (tilted)	2.01	3.20



(a) Block dipole model.



(b) Wire dipole model (straight configuration).



(c) Wire dipole model (tilted configuration).

Figure 5.16: Local SAR MIPs shown in transverse, coronal and sagittal views for (a) block dipole, (b) wire dipole (straight configuration) and (c) wire dipole (tilted configuration) simulations.

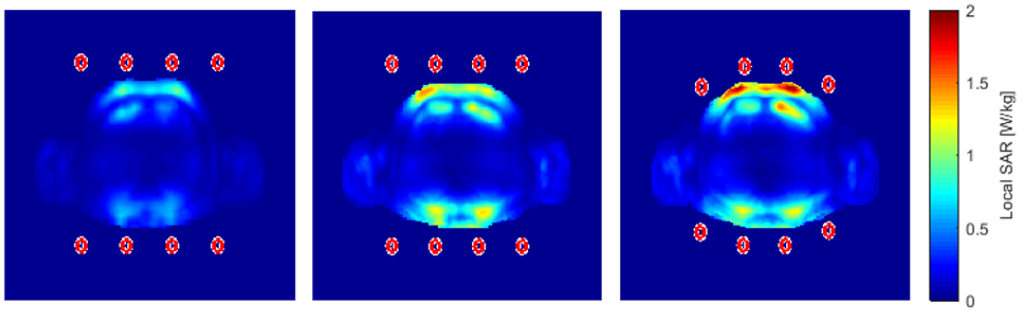
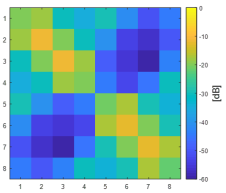


Figure 5.17: Location of dipole elements in each simulation highlighted by the red circles on the anterior and posterior of body model for block dipole, wire dipole (straight configuration) and wire dipole (tilted configuration) simulations respectively.

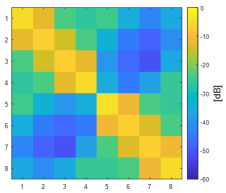
The resonant frequencies of the tuned dipoles are listed in Table 5.5. In both simulations the wire model dipoles have higher resonant frequencies than the block model. S-matrices for each coil model are displayed in Figure 5.18. The wire dipole simulation demonstrates higher coupling between nearest neighbour elements and between anterior and posterior elements compared to the block dipole model results.

Table 5.5: Resonant Frequencies for each element in Wire Dipole Model Development Simulations

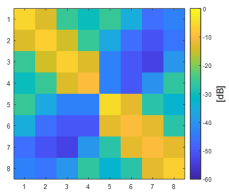
	Transmit Dipole Resonant Frequency [MHz]							
Simulation ↓ Dipole →	1	2	3	4	5	6	7	8
Block Model	299	280	279	297	302	281	283	301
Wire Model (straight)	308	305	305	307	308	306	306	308
Wire Model (tilted)	307	306	306	304	310	304	297	307



(a) Block dipole model.



(b) Wire dipole model (straight configuration).



(c) Wire dipole model (tilted configuration).

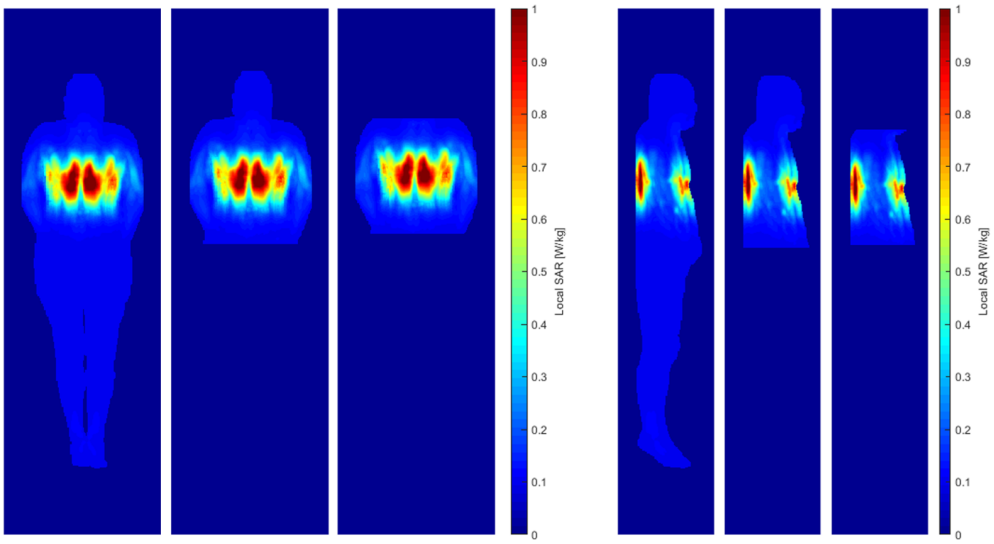
Figure 5.18: S-matrices for the coil model in (a) block dipole, (b) wire dipole (straight configuration) and (c) wire dipole (tilted configuration) simulations.

5.3.3 Development of Simplified Body Models

5.3.3.1 Truncation

Figure 5.19 shows coronal and sagittal local SAR MIPs from the successively truncated male generic body model simulations. The location of the peak local SAR hotspot did not change as the body model was truncated. Table 5.6 lists the maximum local SAR and SAR/$\sqrt{(B_1^+)^2}$ values for each simulation. B_1^+

distributions in a posterior coronal slice are shown in Figure 5.20. Resonant frequencies of each tuned dipole did not change between each simulation and the S-matrices showed no significant differences indicating that the results were unchanged by the use of truncated models.

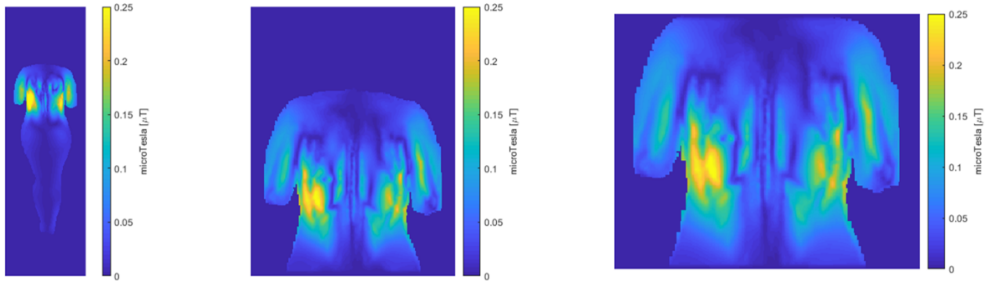


(a) Coronal Local SAR MIPs. (b) Sagittal Local SAR MIPs.

Figure 5.19: Local SAR MIPs from simulations with successively truncated generic body models.

Table 5.6: Maximum Local SAR Results in Truncated Model Simulations

Simulation	Max. Local SAR [Wkg^{-1}]	SAR/$\sqrt{B_1^{+2}}$ [Wkg$^{-1}\mu$T^{-1}]
Whole Body Model	1.04	2.53
Upper Body Model	1.03	2.50
Torso Only Model	1.02	2.51



(a) Whole body. (b) Upper body. (c) Torso only.

Figure 5.20: B_1^+ distribution in a posterior coronal slice of each truncated model.

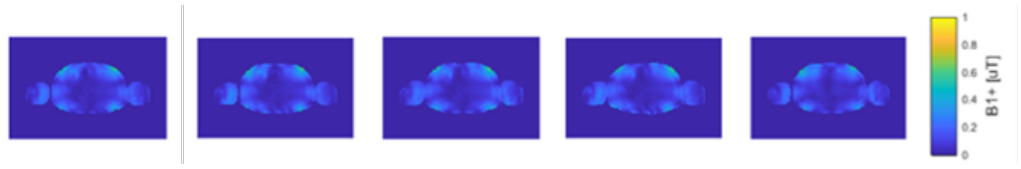
5.3.3.2 Repeatability and Coil Model Position

Transmit dipoles were moved in the xy-plane relative to an initial simulation. In the x direction (R-L) the maximum displacements were 19 and 11 mm and this corresponded to maximum displacements in the y direction (A-P) of 3 and 5 mm (for simulations with male and female models respectively).

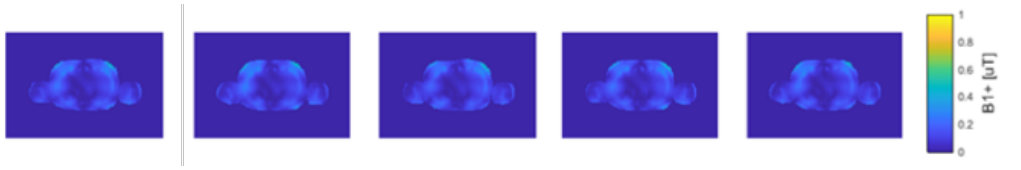
Figure 5.21 presents B_1^+ magnitude distributions from each of the five simulations in the male and female models. The slice shown is that containing the maximum local SAR value in the initial simulation. No significant changes were observed between the different simulated B_1^+ data.

Figures 5.22 and 5.23 display the local SAR MIPs from each of the simulations with the maximum local SAR location indicated for the male and female model respectively. The mean maximum local SAR value was 2.0 $\pm$ 0.4 Wkg^{-1} (20% variation) and 1.3 $\pm$ 0.1 Wkg^{-1} (4% variation) for male and female simulations respectively. The 95^{th} percentile values for the male were 0.62 $\pm$ 0.03 Wkg^{-1} and for the female were 0.45 $\pm$ 0.01 Wkg^{-1}. A SAR Variation Factor (calculated as maximum peak local SAR value/minimum peak local SAR value) and Safety Factor (calculated as 10 Wkg^{-1}/maximum peak local SAR value) were calculated. All of the listed results are presented in Table 5.7.

Local SAR values in the location of the maximum value in each simulation were compared across all simulations. Local SAR values at these points were all within



(a) Male model.



(b) Female model.

Figure 5.21: B_1^+ distributions for the five simulations where the coil elements have been displaced relative to the placement in the initial simulation.

20% of the maximum local SAR value for the simulation under consideration. Figures 5.22 and 5.23 demonstrate the movement of the maximum local SAR locations between simulations which are indicated by the intersection of the white lines. From the simulations with the male model, the maximum displacement of the local SAR hotspot in the x- direction was 18.6 mm and in the y- direction 3 mm. For the simulation with the female model this was 11.3 mm and 5.2 mm for x and y directions respectively.

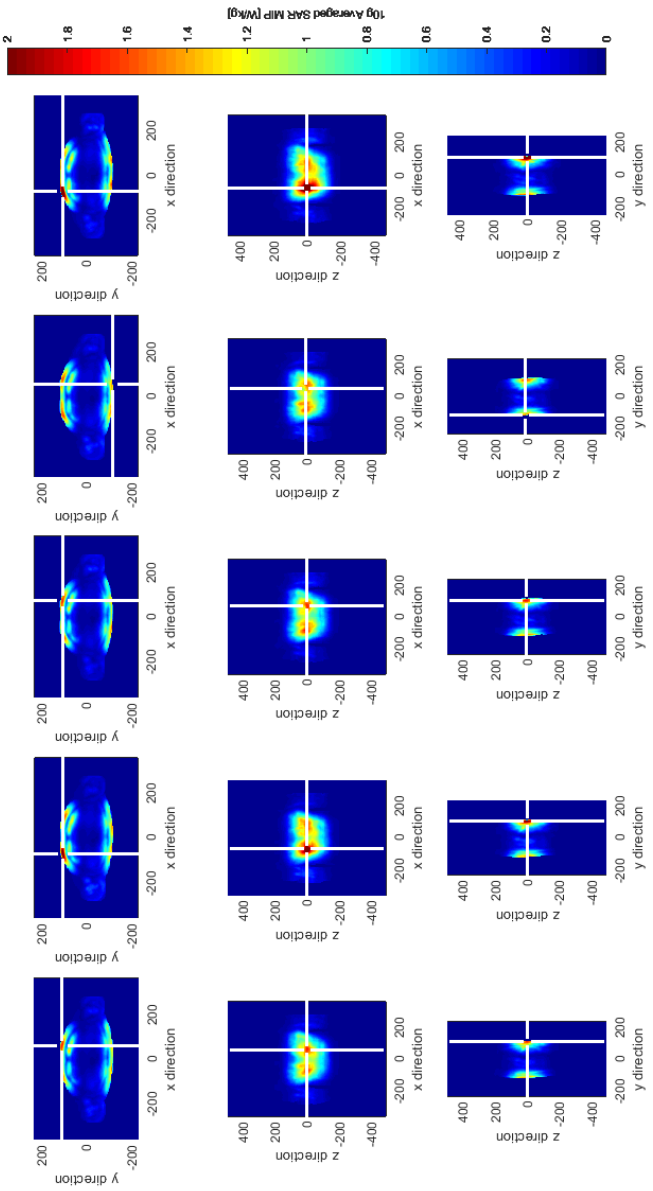


Figure 5.22: Local SAR MIPs for different locations of coil elements in the male body model; maximum local SAR value location marked by intersection of white lines.

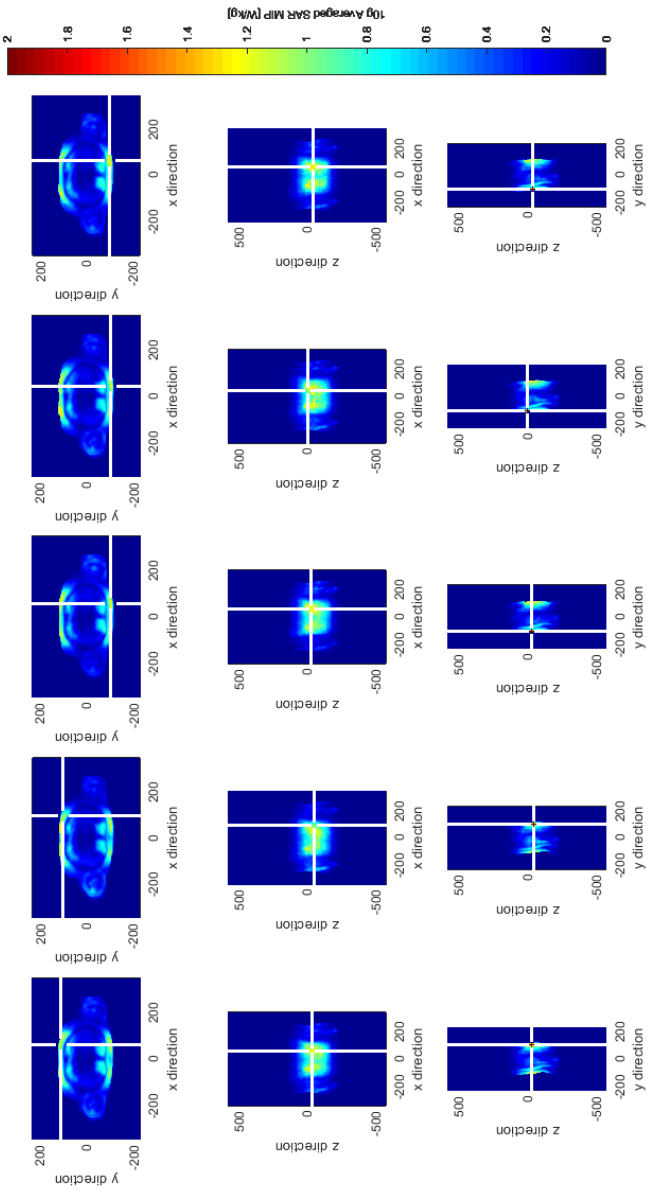


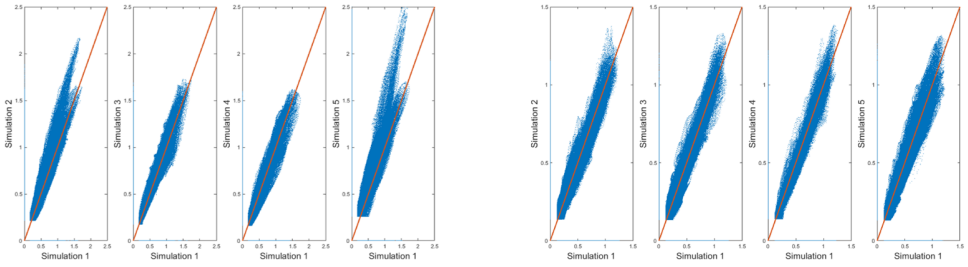
Figure 5.23: Local SAR MIPs for different locations of coil elements in the female body model; maximum local SAR value location marked by intersection of white lines.

Table 5.7: Results from repeatability simulations.

Simulation	Max. Local SAR [Wkg^{-1}]	SAR/$\sqrt{(B_1^+)^2}$ [Wkg$^{-1}\mu$T^{-1}]	SAR Variation Factor [SVF]	Safety Factor [SF]
Male	2.0 $\pm$ 0.4	3.0 $\pm$ 0.7	1.6	3.9
Female	1.34 $\pm$ 0.1	2.6 $\pm$ 0.2	1.1	7.2

S-matrices from each simulation with the coil model displaced were not significantly different to that from the initial simulations. The maximum standard deviation of the S-matrix calculated over all simulations was 7.5% and 5.6% and the maximum change in individual S-parameters was 8.3 and 6.1 dB for male and female simulations respectively. This corresponds to a variation of less than 10% in the forward and reflected power measured in each transmit element.

Scatter plots showing the correlation between local SAR distributions from initial and succeeding simulations in every voxel of the body models are displayed in Figure 5.24 (local SAR values less than 10% of the maximum local SAR result in each simulation were not shown in the scatter plots to improve visualisation). The correlation coefficients were above 0.9 in each plot.



(a) Male simulation data.

(b) Female simulation data.

Figure 5.24: Voxel-wise local SAR correlation between initial and succeeding simulations with different coil model placements.

5.3.3.3 Reduced Tissue Complexity

Local SAR and B_1^+ distributions from full, MFSLB, MFSLBa and MFSLBb body models are shown in Figures 5.25 and 5.26 for male and female models respectively. The slice displayed corresponds to that in which the maximum local SAR value was located in the fully segmented model simulation. The difference in local SAR between each of the models with respect to the fully segmented model in the same slice is shown in Figure 5.27. Results are only shown for full, MFSLB, MFSLBa and MFSLBb models where the skin tissue was retained. Once the skin tissue was reassigned (in models MFLBa, MFLBb and MFL) distributions changed significantly and therefore were eliminated from further analysis.

Quantitative results including maximum local SAR and SAR/$\sqrt{(B_1^+)^2}$ values are outlined in Table 5.8. As the tissue types were gradually reassigned, the maximum change in S-parameters calculated for the MFSLB simulation was 6.6/4.9 dB, for MFSLBa was 6.8/5.0 dB and for MFSLBb was 6.0/5.0 dB with regard to male/female model simulations respectively.

Table 5.8: Maximum local SAR and SAR/$\sqrt{(B_1^+)^2}$ values listed for each model type. Greyed out results were excluded from rest of analysis.

Model	Model Type	Max. Local SAR [Wkg^{-1}]	SAR/$\sqrt{(B_1^+)^2}$ [Wkg$^{-1}\mu$T^{-1}]
Male	Full	1.74	2.77
	MFSLB	1.87	3.19
	MFSLBa	1.77	2.99
	MFSLBb	1.76	2.97
	MFLBa	2.65	4.01
	MFLBb	1.57	3.22
	MFL	1.65	3.37
Female	Full	1.22	2.40
	MFSLB	1.20	2.38
	MFSLBa	1.19	2.37
	MFSLBb	1.19	2.38
	MFLBa	2.23	3.77
	MFLBb	1.04	2.78
	MFL	1.07	2.86

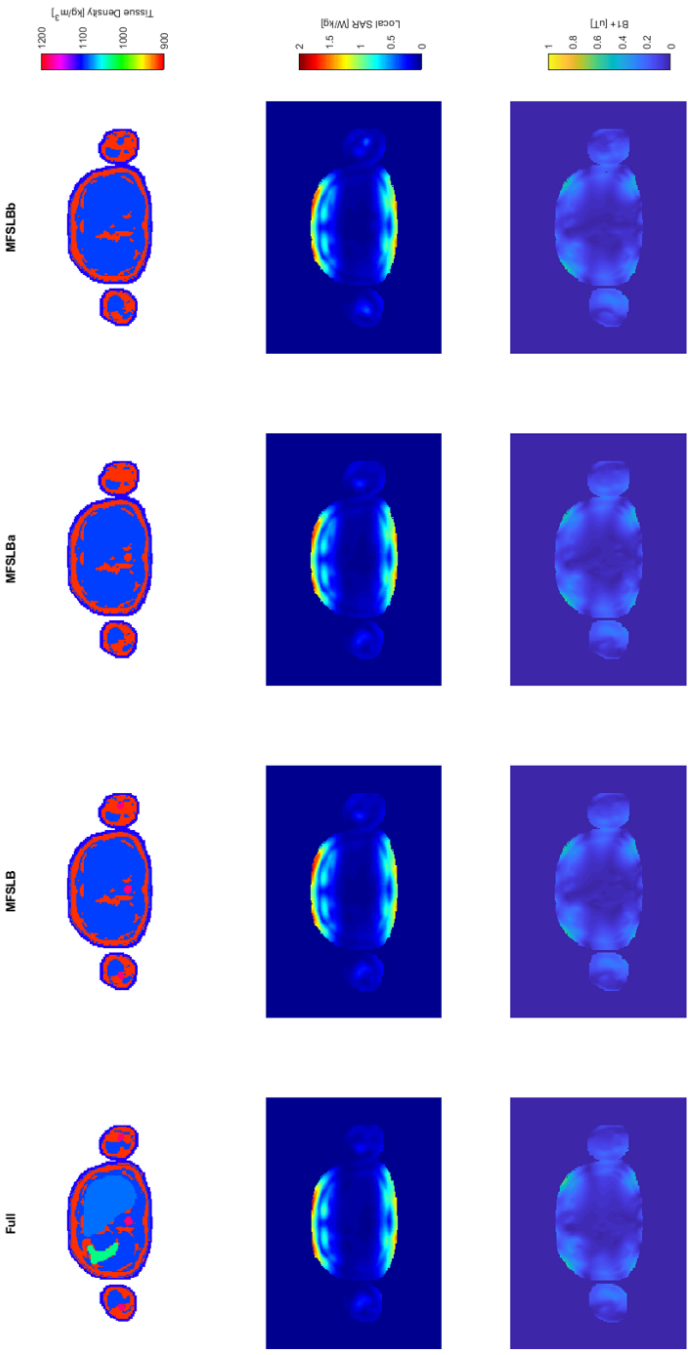


Figure 5.25: Local SAR and B_1^+ distributions in male full, MFSLB, MFSLBa and MFSLBb models.

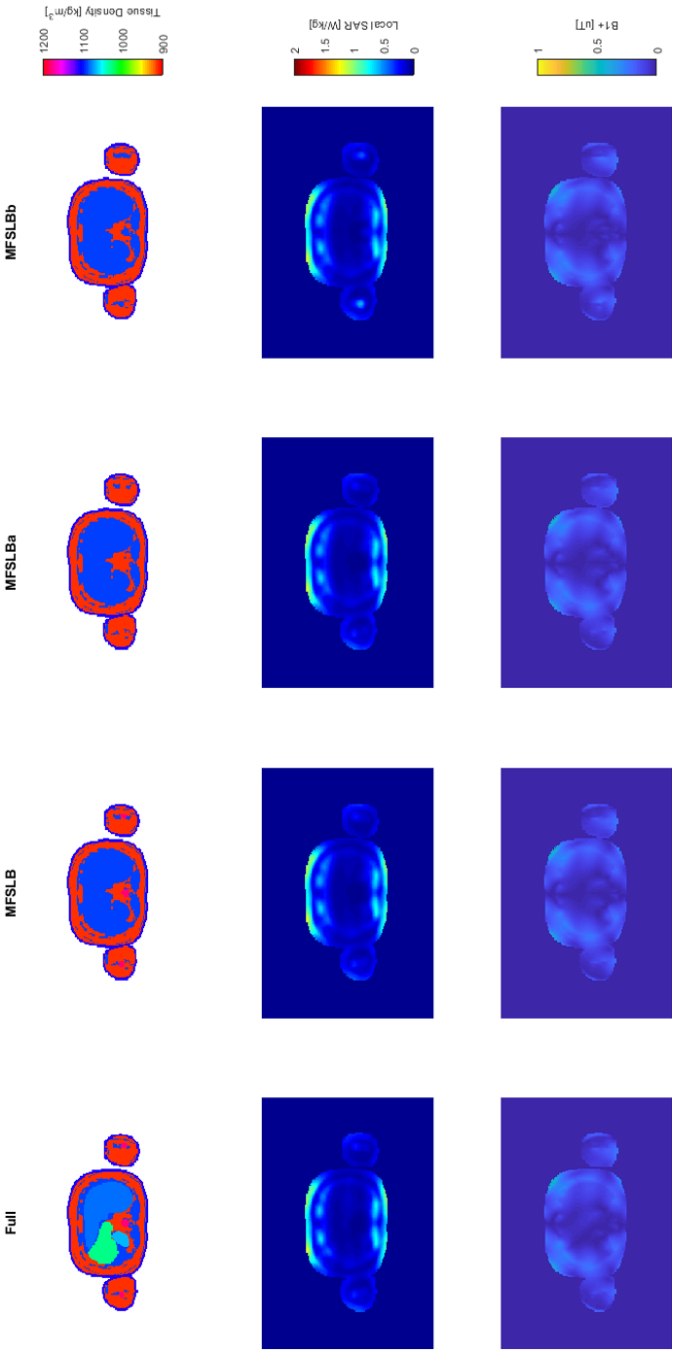
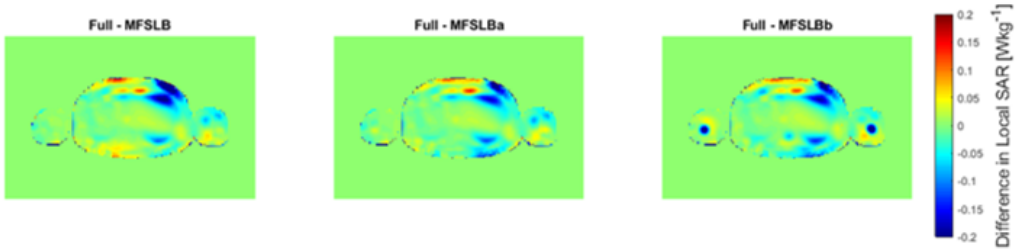
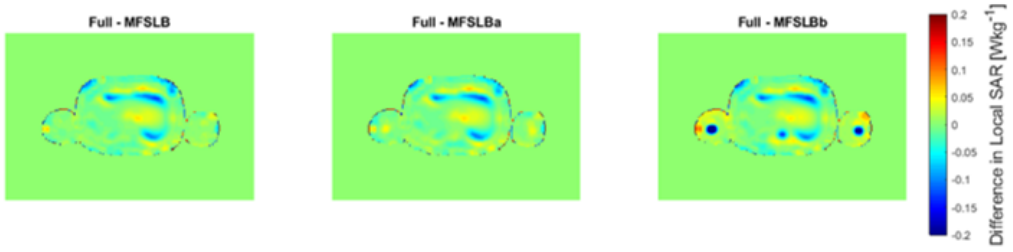


Figure 5.26: Local SAR and B_1^+ distributions in female full, MFSLB, MFSLBa and MFSLBb models.



(a) Male model results.

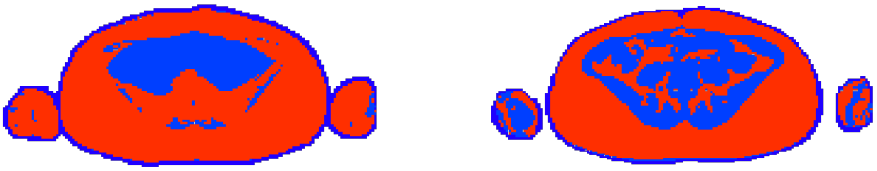


(b) Female model results.

Figure 5.27: Differences in local SAR distributions between full segmented model results and models with reducing levels of tissue complexity (*MFSLB, MFSLBa and MFSLBb respectively*).

5.3.3.4 Automatic Segmentation

Examples of a manual and automatic segmentation in the lower abdomen of the female model are shown in Figure 5.28. In the automatically segmented model the delineation of the fat, muscle and pelvic bone are superior to the manual segmentation. Figure 5.29 shows tissue density maps, local SAR and B_1^+ distributions from both manual and automatic segmentations used to construct the male and female models. The slice shown corresponds to the maximum local SAR value in each separate simulation.



(a) Manually segmented female model.

(b) Automatically segmented female model.

Figure 5.28: Example of the effect of the different tissue segmentation approaches in the female model obtained with the (a) manual and (b) automatic segmentation process.

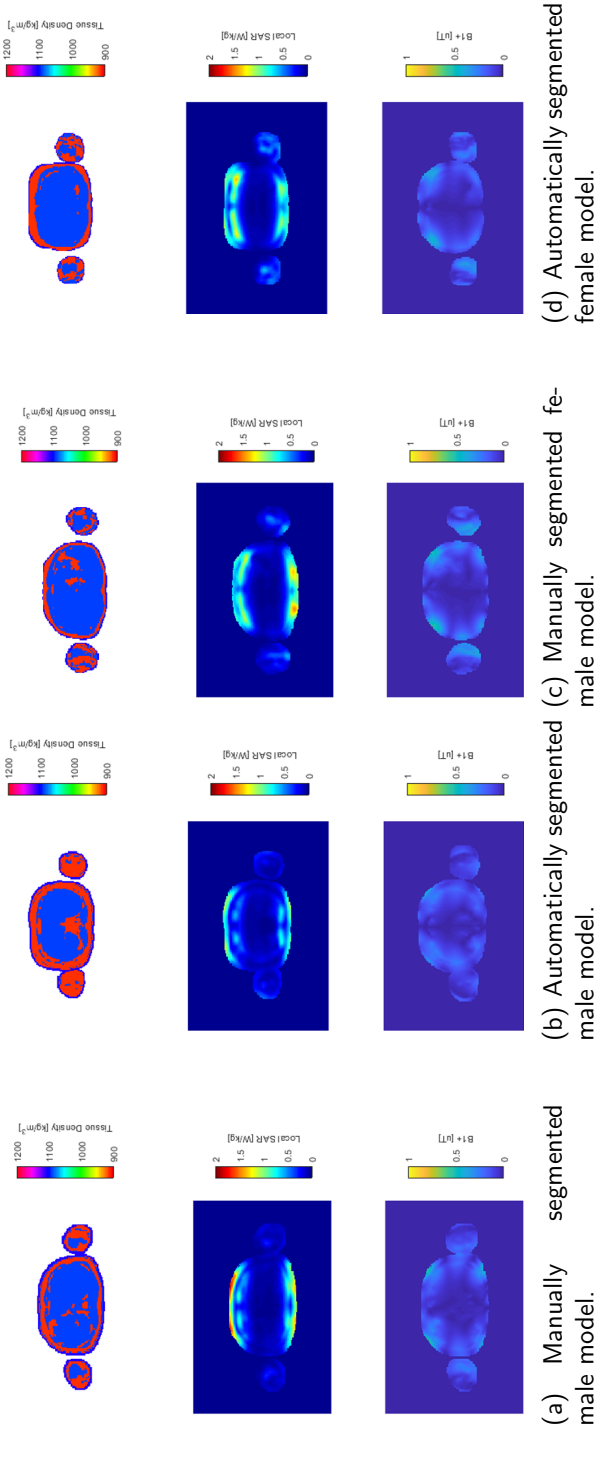
Figure 5.30 highlights the locations of the maximum local SAR values in each local SAR MIP generated from each of the four simulations. In the male model, the hotspot moves from the anterior to the posterior of the model. In the female model, the hotspot remains on the anterior surface of the model but moves to the right of the model's torso.

Quantitative results are outlined in Table 5.9. The male model showed a 16% decrease in the maximum local SAR value and the female model showed an increase of 13% when comparing results from the automatically segmented models to manually segmented versions. The SAR/$\sqrt{(B_1^+)^2}$ values decreased by 14% and 12% and the 95^{th} percentile local SAR values both increased by 8% and 27% for male and female results respectively.

Table 5.9: Quantitative results from automatically and manually segmented model simulations.

Model	Segmentation Method	Max. Local SAR [Wkg^{-1}]	SAR/$\sqrt{(B_1^+)^2}$ [Wkg^{-1} μ T $^{-1}$]
Male	Manual	1.77	2.99
	Automatic	1.48	2.58
Female	Manual	1.19	2.37
	Automatic	1.35	2.08

The maximum absolute differences between the individual S-parameters obtained with manually and automatically segmented models was 8.3 dB for the male models and 8.2 dB for the female models. This corresponds to a small change in coupling (a maximum of 10 dB variation relates to $1/10^{th}$ variation in reflected power) which does not affect the performance of the coil model in the simulation.



(a) Manually segmented male model.

(b) Automatically segmented male model.

(c) Manually segmented female model.

(d) Automatically segmented female model.

Figure 5.29: Tissue density maps and local SAR and B_1^+ distributions comparing manually and automatically segmented models.

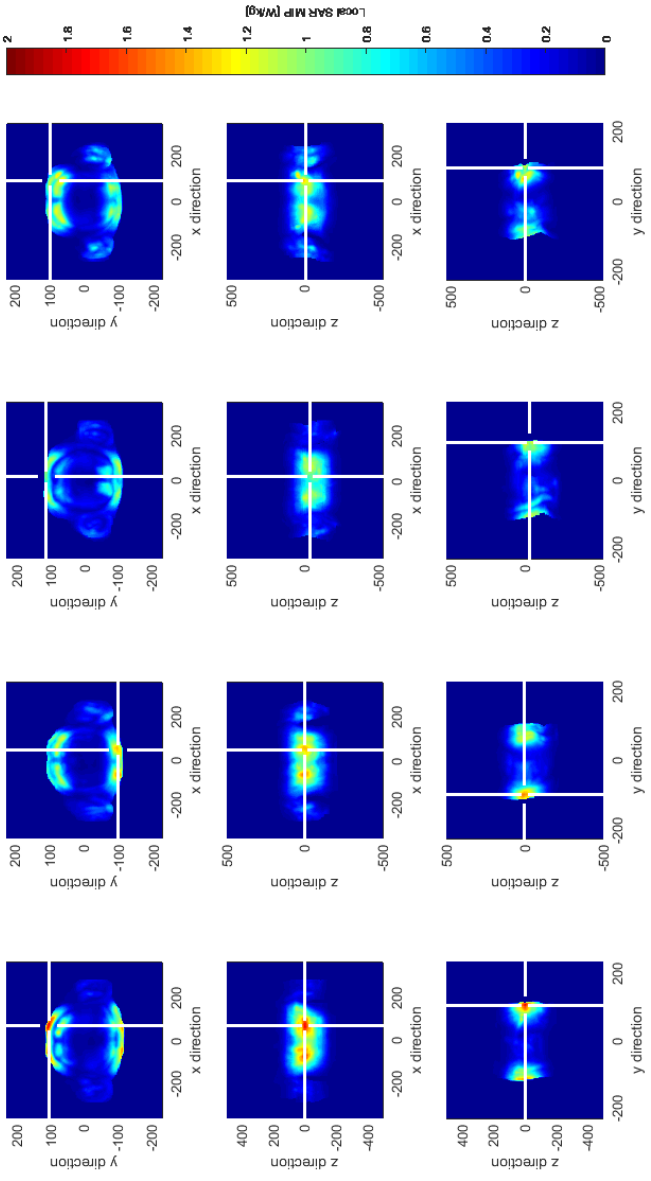


Figure 5.30: Local SAR hotspots in manually and automatically segmented models.

5.3.4 Intra-subject Variability: Respiration Study

Figure 5.31 shows the maximum local SAR values calculated at exhale and inhale for each of the seven simulated body models. There was a general trend showing increased local SAR on the inhale breath hold, however this increase was not significant. An increase of local SAR could be expected at inhale due to the higher volume of air in the lungs and an increase in the surface boundaries between lung tissue and air which both have different dielectric properties and can contribute to discontinuities in the SAR distributions.

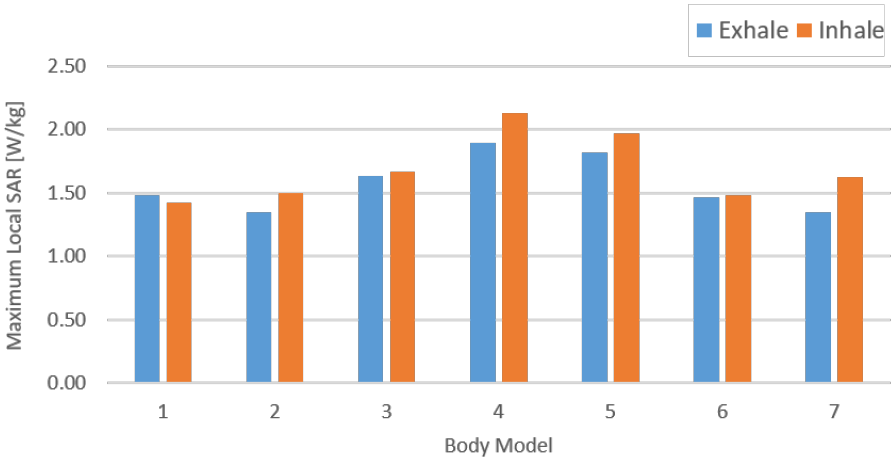
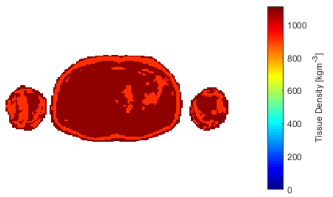


Figure 5.31: Maximum local SAR values at exhale and inhale for each simulated body model.

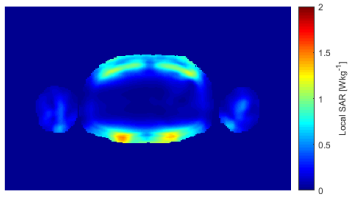
Tissue density maps, local SAR and B_1^+ distributions in a simulated model at exhale and inhale are displayed in the slice which contained the maximum local SAR value in Figure 5.32. The displacement of internal organs between breath-hold positions is clear in the tissue density maps (Figures 5.32 (a) and (b)). Local SAR distributions are similar between the slices and the position of the peak local SAR values did not vary beyond the results presented in the repeatability investigation (see Section 5.3.3.2 and Figures 5.32 (c) and (d)) across all of the simulated subject-specific models. In addition, the general pattern of the B_1^+ distributions did not change due to respiration (Figures 5.32 (e) and (f)).



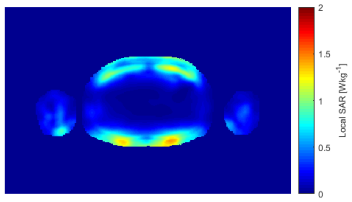
(a) Exhale tissue density map



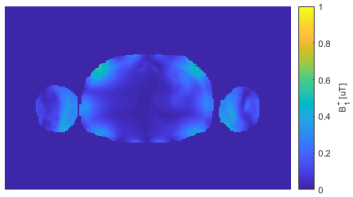
(b) Inhale tissue density map



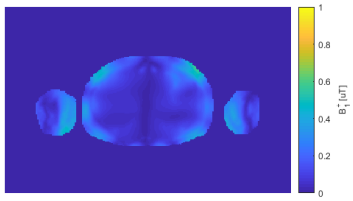
(c) Exhale local SAR distribution



(d) Inhale local SAR distribution



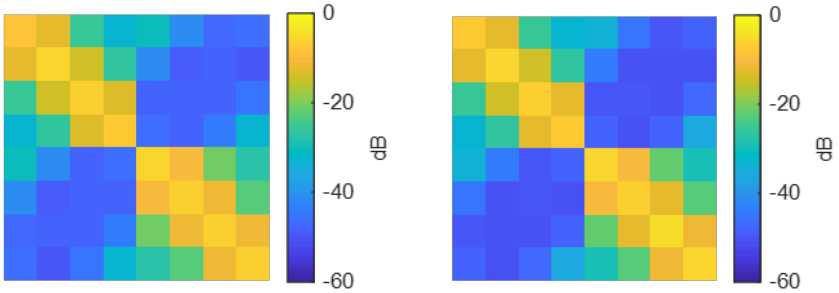
(e) Exhale B_1^+ distribution



(f) Inhale B_1^+ distribution

Figure 5.32: Comparison of exhale and inhale simulation data: (a) and (b) show tissue density maps in an exhale and inhale model respectively; (c) and (d) are the local SAR distributions calculated in the same slices and models as presented above; (e) and (f) are the respective simulated B_1^+ distributions. The displayed slice corresponded to that containing the maximum local SAR value in each exhale and inhale simulation.)

An example of the S-matrices calculated from an exhale and inhale simulation in the same subject model is shown in Figure 5.33. No changes to the overall coupling behaviour between elements was observed although small variations, less than 10dB, in individual S-parameters did occur in each subject.



(a) Exhale S-Matrix (b) Exhale S-Matrix

Figure 5.33: Simulated S-matrices from an (a) exhale and (b) inhale simulation performed with body models corresponding to the same subject. No significant changes to the individual S-parameters are observed.

Figure 5.34 shows in vivo and simulated individual transmit channel B_1^+ distributions for one subject and associated body model. Figure 5.35 shows the mean magnitude B_1^+ in ROIs under each transmit element at exhale and inhale averaged over all subjects in both in vivo and simulated data. Error bars correspond to the standard deviation of mean B_1^+ values at each transmit element across all subjects. The in vivo results show a greater change in the B_1^+ values under transmit elements 5 - 8. These correspond to the anterior elements and so this greater change in B_1^+ is expected due to the anterior movement of the body during respiration (Figure 5.35 (a)). These results were not reproduced in the simulated data (Figure 5.35 (b)).

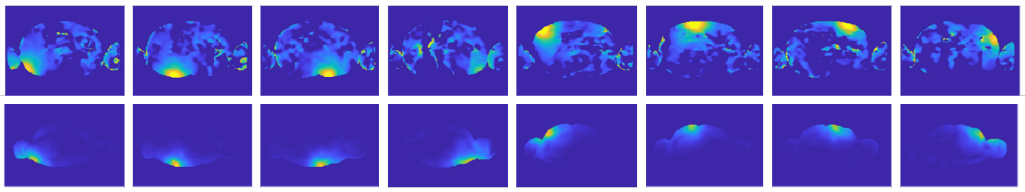
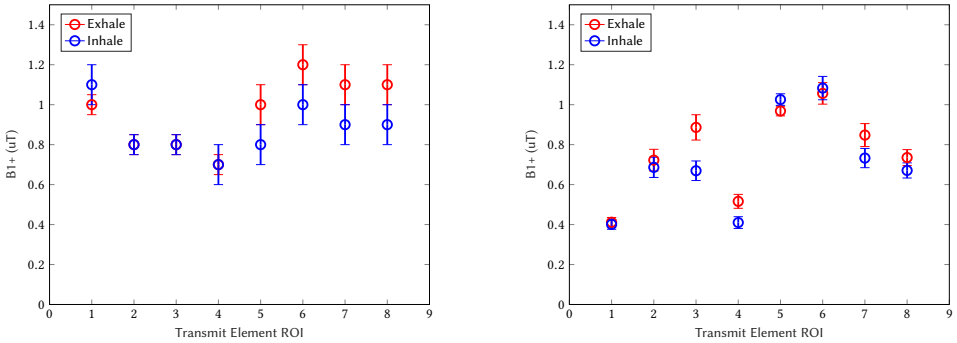


Figure 5.34: In vivo (*top row*) and simulated (*bottom row*) B_1^+ maps for the eight individual transmit channels.



(a) In vivo results.

(b) Simulation results.

Figure 5.35: Mean B_1^+ in a ROI over each transmit element. Measured from individual channel B_1^+ maps from (a) in vivo data and (b) simulated data.

The discrepancy between the measured in vivo and simulated changes in B_1^+ could be due to the nature of the subject's breath-hold technique at 7 T compared to 3 T (on which the simulated data is based on). Figure 5.36 presents measures of the breath-hold displacement in each subject measured from 7 T images (yellow bars) and 3 T body model images (green bars). The breath hold displacement is mismatched in each case with subjects 3, 4 and 7 having particularly pronounced differences.

Figure 5.37 shows in vivo B_1^+ maps acquired with all channels on at exhale, inhale with the difference between these two distributions are displayed. It is observed that the greatest change in B_1^+ (corresponding to the red regions) is on the anterior of the subject, as expected. The B_1^+ distribution, with particular reference to the interference patterns in the body, does not change significantly. This was also the case for the simulated B_1^+ distributions shown in Figure 5.32.

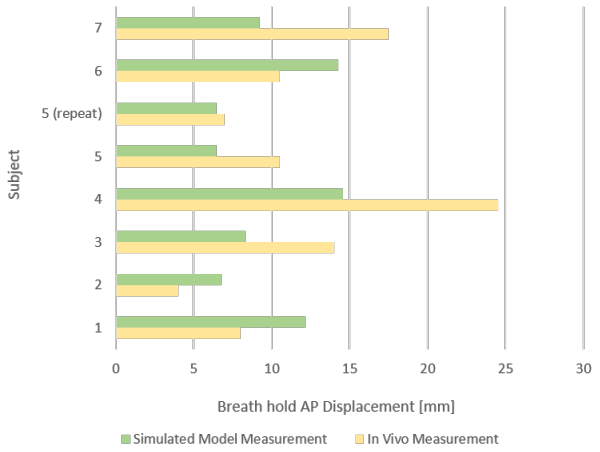


Figure 5.36: Breath hold displacement in each subject measured in AP direction on 3 and 7 T images. Mismatch between breath holds could explain the difference between in vivo and simulated results.

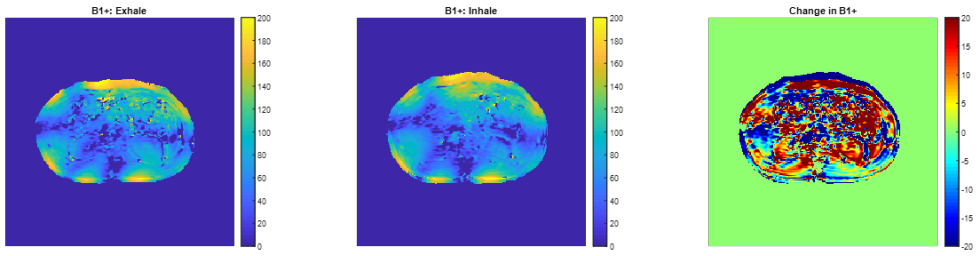
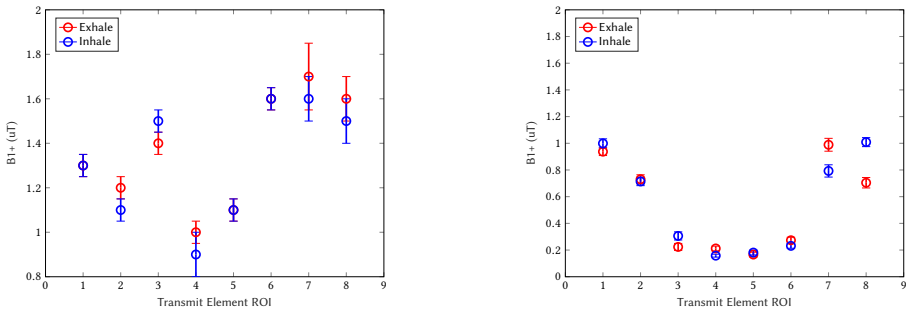


Figure 5.37: In vivo all channels on B_1^+ maps acquired at exhale and inhale positions. The difference between these two distributions is also presented to show the greatest change in B_1^+ is on the anterior of the subject.

Figure 5.38 shows the mean B_1^+ in ROIs under each transmit element in the all channels on B_1^+ maps at exhale and inhale in both in vivo and simulated data in three of the subjects. As was the case for the individual channel B_1^+ maps, the in vivo data captures the change in B_1^+ on the anterior of the body whereas the change in the simulated B_1^+ data presented is less pronounced.



(a) In vivo results. (b) Simulation.

Figure 5.38: Mean B_1^+ in a ROI over each transmit element. Measured from all channels on B_1^+ maps.

Figure 5.39 presents the mean B_1^+ calculated across three ROIs in each of the following abdominal organs; liver, right kidney and left kidney. The change in B_1^+ due to respiration in each organ was less than 5% of the nominal flip angle (which in this case was 40 °).

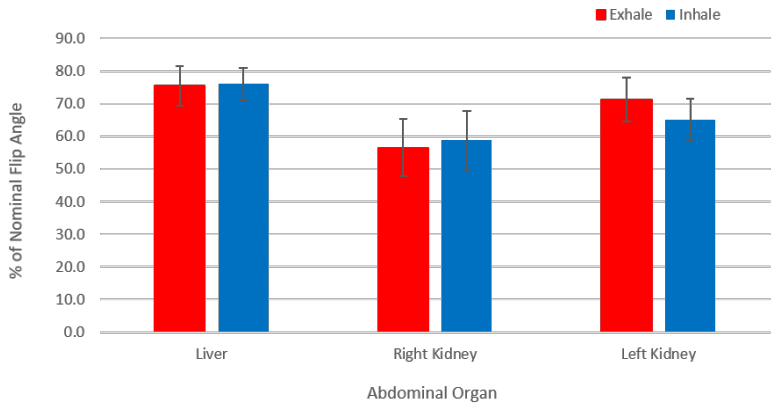


Figure 5.39: Mean B_1^+ calculated from the three ROIs in abdominal organs; liver and the kidneys. Measured from in vivo all channels on AFI B_1^+ maps.

Repeatability was assessed in one of the subjects by measuring the change in mean B_1^+ in ROIs under each transmit element in two image data sets acquired in separate scanning sessions. In Figure 5.40, the exhale data (red line = scan 1, grey line = scan 2) shows similar characteristics between separate scans, as does

the inhale data (blue line = scan 1, yellow line = scan 2). However, in terms of quantitative results the repeatability is poor. Again, this is probably due to inconsistent breath-holding technique between the separate scan sessions.

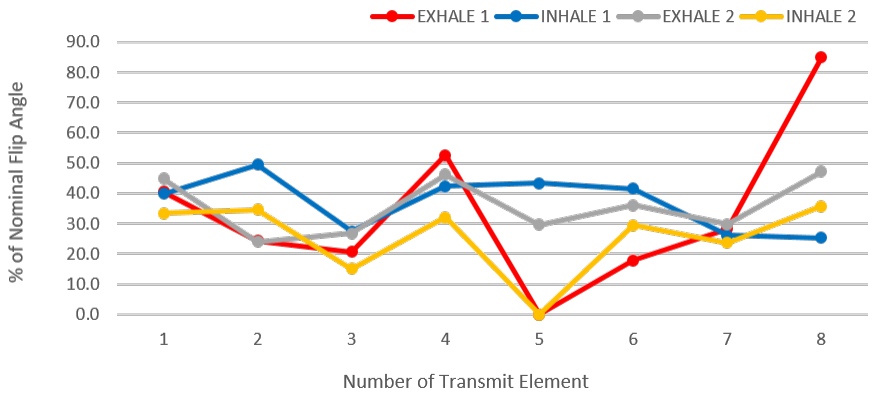


Figure 5.40: Repeated B_1^+ measurements in one subject.

5.3.5 Inter-subject Variability

The resulting 10^4 maximum local SAR values from 10 subjects were in the range 0.89 to 3.99 Wkg^{-1} and are approximated by the gamma distribution $\Gamma(18.7,0.11)$. The inter-subject peak local SAR variability range corresponding to 8 $\times$ 1 W input power was 2.06 Wkg^{-1} $\pm$ 24%. This result indicates that operating at 3 W per channel corresponds to a 1.6 inter-subject variability safety factor. This is sufficient in reducing the risk of exceeding local SAR limits across a population.

The transmit RF settings corresponding to the lowest, mid-range and highest 100 local SAR values were analysed. The phase difference between neighbouring transmit elements was calculated for each unique RF setting; these were then summed together over the 100 RF settings of interest. There was no correlation between this measure of phase difference and each specified local SAR range indicating that subject composition had a greater influence on the local SAR generated than the transmit RF phases employed.

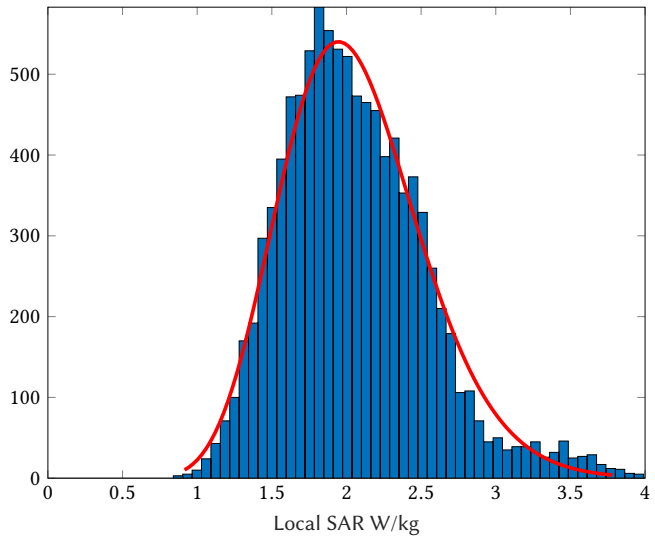


Figure 5.41: Histogram of the maximum local SAR values for all 10 subjects x 1000 random transmit RF phase settings. Distribution follows Gamma function shown by red line.

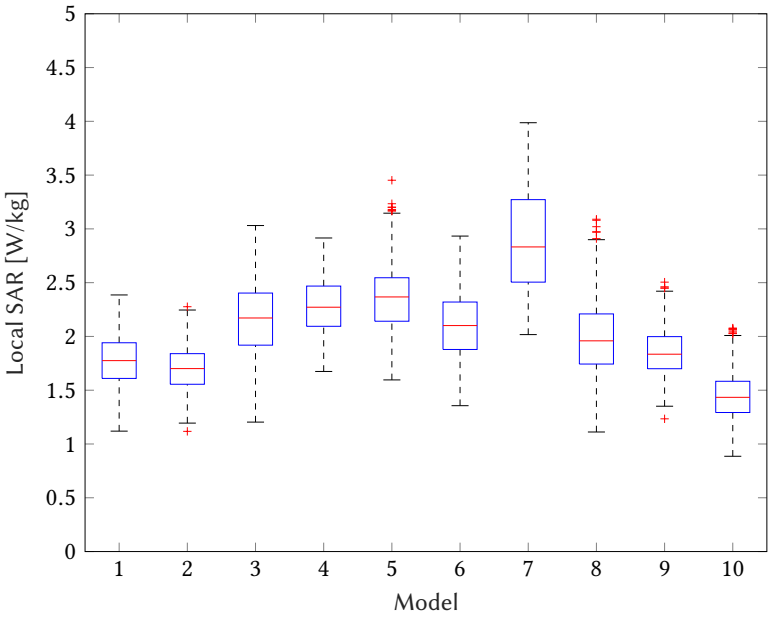


Figure 5.42: Boxplot of the maximum local SAR values generated for each model with 8 x 1 W input power and 1000 random transmit RF phase settings.

Figure 5.43 shows an example of the visceral and subcutaneous fat segmented in one subject. The visceral fat measures showed no correlation with the maximum local SAR across all subjects. However, the combined visceral and subcutaneous fat (total fat volume detected) demonstrated a slight positive correlation ($R = 0.16$) with maximum local SAR (see Figure 5.44 (a)). In particular, the subject with the highest total fat measure corresponded to the highest maximum local SAR simulated out of all the subjects. The BMI of each subject had the greatest correlation with the maximum local SAR values ($R = 0.38$) and is displayed in Figure 5.44 (b). Figure 5.44 (c) shows the correlation between subject BMI and the measure of detected fat tissue ($R = 0.51$). These do not directly correlate highlighting that subjects with higher BMI's are also likely to have more higher levels of muscle tissue.

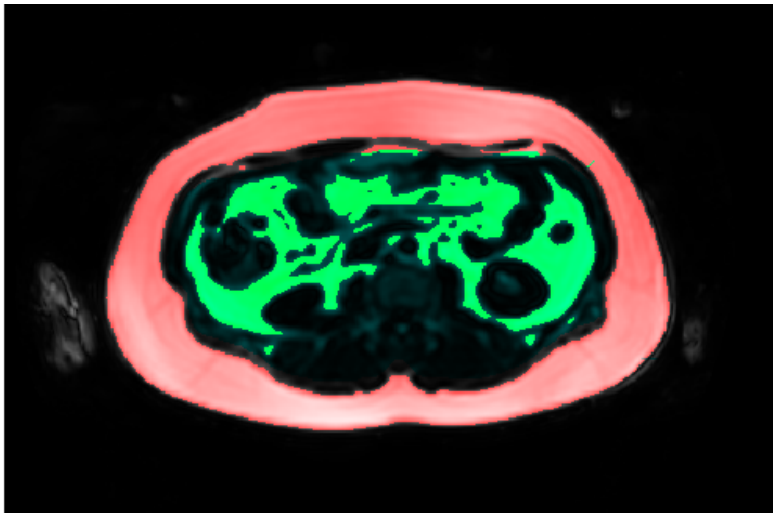
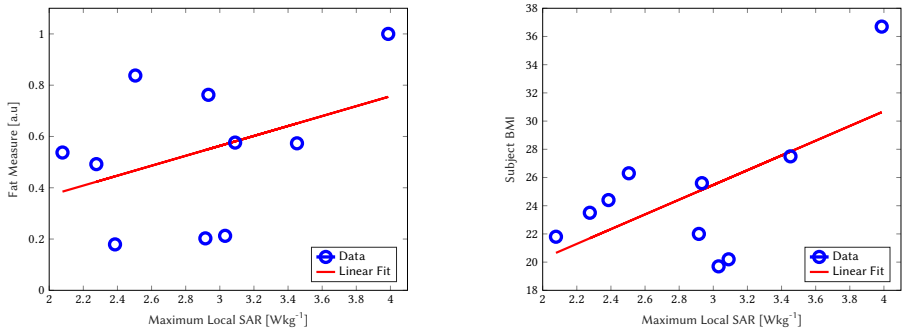
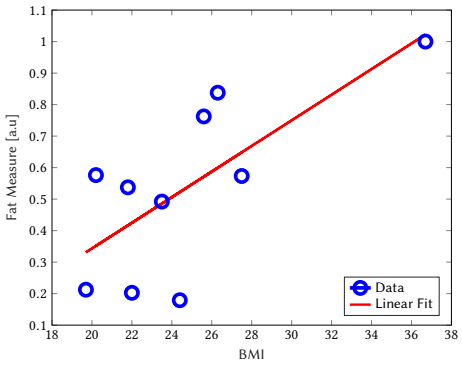


Figure 5.43: Example of the visceral (area shaded in green) and subcutaneous (area shaded in red) fat tissue segmentation in one subject based on analysis of 3 T mDixon images.



(a) Fat Correlation

(b) BMI Correlation



(c) BMI Correlation

Figure 5.44: Correlation plots comparing (a) peak local SAR values with measure of fat content, (b) peak local SAR values with BMI, and (c) BMI with measure of fat content across all subjects.

5.4 Discussion

A method for performing EM simulations with a modified wire dipole coil model and simplified, subject-specific body models for assessing local SAR in the abdomen at 7 T has been presented. The main results of the work in this chapter cover an analysis of the sensitivity and variation of local SAR and B_1^+ distributions in the abdomen at 7 T with respect to small coil displacements, respiration and inter-subject variability.

Comparing Simulated and Experimental B_1^+ Distributions

B_1^+ distributions that were both simulated and acquired experimentally in a body phantom (shown in Figure 5.13) showed some similar characteristics. As it is only the B_1^+ magnitude that is of interest in the context of MR safety, the fact that the interference patterns present in the distributions were similar indicates that the relative transmit phases between simulated dipoles match those used experimentally; thus adding confidence to the validity of the EM simulations.

The B_1^+ was more localised at the surface of the phantom in the simulated data. It is thought that this could be due to the RF energy being deposited over a relatively long, thin area by the wire model compared to the fractionated block dipoles in the RF coil. Future work to investigate the disagreement between simulated and experimental B_1^+ distributions should include a study of the concentration of deposited RF energy at the phantom model surface and how this changes when a single wire is split into two wires separated by the width of the fractionated dipole. The results from this study may provide some insight into adaptations that can be made to the existing wire model. In addition to this, a revision of the body phantom model dielectric properties should be made. Over time the body phantom contents may have degraded and so the analytical solutions for the expected conductivity and density of the phantom materials may not exactly match. This may be a contributing factor to the difference between the experimental data and the simulated B_1^+ distributions.

Simplified Dipole Model Verification

B_1^+ interference patterns were consistent between the *Block Model*, *Wire Model (straight configuration)* and *Wire Model (tilted configuration)* simulations. The increase in B_1^+ magnitude between *Block Model* and *Wire Model (straight configuration)* simulations can be attributed to the increase in the resonance frequencies of the individual wire dipoles (listed in Table 5.5). In the block model, dipoles did not all tune to the same resonant frequency, however, with the wire

model achieving a resonant frequency of approximate 300 MHz for all dipoles was possible due to the nature of the tuning. The increase in B_1^+ magnitude between *Wire Model (straight configuration)* and *Wire Model (tilted configuration)* simulations, as shown in Figure 5.6, was expected as the outermost dipoles were brought closer to the body model improving the transmit efficiency of the coil in these areas.

On moving from the *Block Model* to *Wire Model (tilted configuration)* simulation, the maximum local SAR value doubled. Simulating the transmit dipoles as wires overestimates local SAR compared to the original block dipole model. However, using the wire model method allows for more realistic positioning of the coil elements around the contours of the body allowing for better RF modelling of the local power deposited by each dipole in biological tissue.

Development of Simplified Body Models

Truncation

Local SAR MIPs calculated for the whole, upper and torso only body models were similar across all models. This was also the case for the listed maximum local SAR and SAR/$\sqrt{(B1^+)^2}$ values. The location of the maximum local SAR values did not change between the models. B_1^+ distributions in each model did not present any noticeable differences. The tuning of the dipoles remained at resonance even when the models were truncated, and the S-matrices did not present any significant changes to the performance of the coil model.

The torso only model reproduced whole-body model results which confirmed that the torso only models can be used without affecting overall simulation results. It also means that the runtime of the simulation is significantly shortened due to the reduced grid size required to encompass the body model. The field-of-view required for the acquisition of mDixon images used to create the subject-specific models is also reduced meaning shorter scan times at 3 T.

Repeatability with Respect to Coil Model Position

Local SAR distributions showed good repeatability between simulations with different coil models displacements (shown in Figures 5.22 and 5.23), although the location of the maximum local SAR values did change significantly in some simulations. A change in the location of peak local SAR was expected as the coil model was reoriented around the contours of each human model and RF deposition in the body would change accordingly. The location of maximum local SAR was not always linked to the distance of the dipole away from the human model. The 20% variation in maximum local SAR values over all simulations performed (in the male model) suggests that repeatability should be taken into account as an additional safety factor when performing local SAR evaluations based on FDTD simulations. The lower 4% variation in the female model is attributed to the limited movement of each dipole element due to the more pronounced contours of the female model.

B_1^+ distributions did not vary significantly between each simulation (shown in Figure 5.21). The similarity of B_1^+ interference patterns provides confidence that RF shimming calculations should be robust against small movements.

The differences induced in the S-parameters implies there are changes to the coupling between dipole elements as the body array model is moved. However, the loading of the body array continues to be sufficient and the dipoles remain tuned to resonant frequency. The changes in the S-parameters due to movement of the body array are considerably larger than those reported to be induced by physiological motion measured by Hess et al, and Jaeschke et al [32, 33].

Reduced Tissue Complexity

Local SAR distributions were similar for the full, MFSLB, MFSLBa and MFSLBb models. The maximum local SAR values from the simplified model simulations were all within 10% of the full model value. When bone was reassigned as muscle (MFSLBb) there were elevated local SAR values in the arms of the model, therefore this tissue type assignment could not be used to replicate the

full model results. The maximum local SAR values from the MFSLB models differed by +7.3% and -2.0% and from the MFSLBa models varied by +1.8% and -2.7% for male and female models respectively.

Peak local SAR values were overestimated in the reduced complexity male model results, and underestimated in the female model results, however all were within 10% of the value from the full model versions. Ideally, future investigations into reduced tissue complexity of body models would be performed with more than two simplified models of different genders to validate if the over- and under-estimations were genuine effects based on the gender of the model or due to inherent uncertainties within the simulated data.

MFSLBa models reproduced results that best matched the results from the fully segmented models. The tissue complexity of these models differentiated between lung, fat, muscle and skin tissue (bone was assigned to fat tissue). This level of tissue assignment was used to construct the simplified body models used in the remainder of the work in this chapter for assessing subject-specific local SAR for 7 T abdominal MRI.

Automatic Segmentation

The respective decrease and increase in maximum local SAR values for male and female models when moving to the automatic segmentation method for constructing body models was less than the expected variation of 20% calculated from the repeatability simulations. Therefore, local SAR values produced by the automatically segmented models were still within an acceptable range. The changes were likely due to the effects of the different approaches to the segmentations of fat and muscle tissues in each subject.

The common decrease in SAR/$\sqrt{(B_1^+)^2}$ by a factor of 0.8 suggests that the simulated B_1^+ fields consistently decrease and increase with local SAR distributions for male and female automatically segmented models. This value is used for local SAR monitoring and in RF pulse design and so power limits based on simulations with the automatically segmented models should be conservative to

account for this.

The common increase in the 95th percentile local SAR values reflects that the local SAR distributions generated in the automatically constructed models were skewed consistently; again, it is anticipated that this was due to increased accuracy in the automatic segmentation of fat and muscle tissues.

The general patterns of the local SAR distributions were similar, especially at the boundaries between fat and muscle tissues. This is known to be the area in which local SAR is increased and indicates the acute sensitivity of the simulation results to the exact distributions of fat and muscle tissues [34–37]. Elevated local SAR values on the surface on the manual model simulations were not present in the automatically segmented model simulations. This is because the local SAR distributions in the automatically segmented models more accurately represent the exact fat and muscle tissue compositions in each subject as the segmentations were based on a direct image threshold method compared to a user-based manual segmentation.

In the male model the maximum local SAR location moved from anterior to posterior (shown in Figure 5.30). This was within an acceptable range as this was also shown in the repeatability simulations where the locations of the maximum local SAR moved with coil displacement. In the female model the displacement in maximum local SAR along the torso of the model could also be due to superior segmentation of fat and muscle tissues within the breast region in the automatically segmented model.

These models were based on preliminary data acquired at 3 T in which an inadequate shutter size was used. This caused some signal drop out in the arms throughout the mDixon images. It was easy to work around this artefact in the manual segmentation by inferring where the outline of the arms would be between slices, however, in the automatic segmentation these regions were included as areas of background noise causing errors in the segmentation of fat and muscles tissue in the arms. In subsequent 3 T acquisitions care was taken to ensure subjects arms were captured during the mDixon scans to improve the

images used as input for the automatic segmentation. This was important as the arms are a key feature for simulating the true geometry of a subject within the body array.

To summarise, a method of segmentation based on signal thresholding and k-means clustering of 3 T mDixon images was used to automatically segment fat, muscle and lung tissues. This information was then used to construct simplified human models found to be suitable for use in EM simulations to assess local SAR for 7 T abdominal applications.

Intra-subject Variability: Respiration Study

The simulated change in peak local SAR value at exhale and inhale was not significant (Figure 5.31). This increases the confidence that local SAR estimations are robust against respiration and a respiration safety factor does not need to be taken into account when considering an overall safety factor for local SAR estimations.

The B_1^+ fields did vary significantly due to respiration in the anterior areas of the body in vivo (Figure 5.35). This could lead to errors in quantitative imaging that rely on knowledge of the exact flip angle distribution and confirms the need for breath-held scans with short durations for a particular RF shim set. The change in B_1^+ between exhale and inhale is lower in the posterior side of the subjects. Therefore, changes in B_1^+ during respiration are less of a concern for organs such as the kidneys and posterior sections of the liver. However, in whole liver studies, as the organ extends across most of the anterior and posterior of the subject, the changes in B_1^+ in the liver could be detrimental to the RF shim that is applied.

The simulated changes in B_1^+ were lower than the results reported from the in vivo data. The discrepancy between acquired and simulated distributions was attributed to inconsistent breath-hold technique across scans performed on the 3 T and 7 T scanners. S-matrices showed no significant changes in the coupling behaviour, confirming that the loading of the coil was not affected by respiration.

However, small fluctuations did occur and have possible future application as a method for detecting respiration induced movements [32, 33].

Inter-subject Variability

The inter-subject variability calculated for random RF shim settings in a population of ten subjects was reported. Peak local SAR values obtained corresponded to a 1.6 safety factor currently in place for in vivo scanning. This means that current power limits are conservative with respect to inter-subject variability and with additional simulations to increase the statistical power of these findings, the power per channel could potentially be increased as long as additional safety factors are not compromised.

No obvious link between peak local SAR values and specific RF shim settings was found. However, future work is planned to study the phase difference between pairs of neighbouring transmit elements and observe how these relate to the exact positions of the local SAR hotspots generated in the body models. In addition to this, there was no strong correlation between peak local SAR values and subject composition. Other work investigating inter-subject variability has reported lower peak local SAR values in subjects with higher BMI [38]. Extending this work in a larger library of models with more varied body compositions might reflect these findings.

5.5 Conclusion

Simplified subject-specific models and a wire dipole-based body array model were used to investigate local SAR on realistic geometries as opposed to performing simulations with generic human models and restricted coil geometries. Studying intra- and inter- subject variability in a database of human models, has increased the confidence in current local SAR predictions that inform power limits set at the scanner for 7 T body imaging.

References

[1] Anja Laader, Karsten Beiderwellen, Oliver Kraff, Stefan Maderwald, Karsten Wrede, Mark E. Ladd, Thomas C. Lauenstein, Michael Forsting, Harald H. Quick, Kai Nassenstein, and Lale Umutlu. 1.5 versus 3 versus 7 Tesla in abdominal MRI: A comparative study. *PLoS ONE*, 12(11):1–18, 2017.

[2] S. Wolf, D. Diehl, M. Gebhardt, J. Mallow, and O. Speck. SAR simulations for high-field MRI: How much detail, effort, and accuracy is needed? *Magnetic Resonance in Medicine*, 69(4):1157–1168, 2013.

[3] International Electrotechnical Commission. SAR Compliance Guidance Document 2010 60601-2-33. Technical report.

[4] Jana Delfino Ph.D. Criteria for Significant Risk Investigations of Magnetic Resonance Diagnostic Devices Guidance for Industry and Food and Drug Administration Staff. 2014.

[5] Tao Su, Raj Mittra, Wenhua Yu, Joe Wiart, and France Telecom. Calculation of SAR using FDTD sub-domain approach. *IEEE/ACES International Conference on Wireless Communications and Applied Computational Electromagnetics, 2005.*, pages 20–23, 2005.

[6] Esra Neufeld, Marie Christine Gosselin, Manuel Murbach, Andreas Christ, Eugenia Cabot, and Niels Kuster. Analysis of the local worst-case SAR exposure caused by an MRI multi-transmit body coil in anatomical models of the human body. *Physics in Medicine and Biology*, 56(15):4649–4659, 2011.

[7] Matthew Restivo, Alexander Raaijmakers, Cornelis van den Berg, Peter Luijten, and Hans Hoogduin. Improving peak local SAR prediction in parallel transmit using in situ S-matrix measurements. *Magnetic Resonance in Medicine*, 77(5):2040–2047, 2017.

[8] Morgane Le Garrec, Vincent Gras, Marie-France Hang, Guillaume Ferrand, Michel Luong, and Nicolas Boulant. Probabilistic analysis of the specific absorption rate intersubject variability safety factor in parallel transmission MRI. *Magnetic Resonance in Medicine*, 78(3):1217–1223, 2017.

[9] Özlem Ipek, Alexander J. Raaijmakers, Jan J. Lagendijk, Peter R. Luijten, and Cornelis A T Van Den Berg. Intersubject local SAR variation for 7T prostate MR imaging with an eight-channel single-side adapted dipole antenna array. *Magnetic Resonance in Medicine*, 71(4):1559–1567, 2014.

[10] E.F. Meliado, A.J.E Raaijmakers, M.H.F. Savenije, A. Sbrizzi, M. Maspero, P.R. Luijten, and C.A.T. van den Berg. On-line Subject-Specific Local SAR Assessment by Deep Learning. *In Proc. ISMRM (Paris)*, 293, 2018.

[11] Karl S. Kunz and Raymond J. Luebbers. *The finite difference time domain method for electromagnetics*. CRC Press, 1993.

[12] Alexander J.E. Raaijmakers, Michel Italiaander, Ingmar J. Voogt, Peter R. Luijten, Johannes M. Hoogduin, Dennis W.J. Klomp, and Cornelis A.T. van den Berg. The fractionated dipole antenna: A new antenna for body imaging at 7 Tesla. *Magnetic Resonance in Medicine*, 75(3):1366–1374, 2016.

[13] Miguel R Cabello, Luis D Angulo, J Alvarez, A Rubio Bretones, and Salvador G Garcia. A New Conformal FDTD for lossy thin panels. *IEEE Transactions on Antennas and Propagation*, PP(c):1–1, 2019.

[14] Stephen Bawden. Electrical lengthening to improve electromagnetic simulations and SAR calculations of meandered body dipole elements at 7T. *In Proc. ISMRM (Paris)*, 639, 2018.

[15] Martijn de Greef, Ozlem Ipek, Alexander J. E. Raaijmakers, Johannes Crezee, and Cornelis A. T. van den Berg. Specific absorption rate intersubject variability in 7T parallel transmit MRI of the head. *Magnetic Resonance in Medicine*, 69(5):1476–1485, 2013.

[16] Martijn De Greef, Ozlem Ipek, Alexander J.E. Raaijmakers, Johannes Crezee, and Cornelis A.T. Van Den Berg. Specific absorption rate intersubject variability in 7T parallel transmit MRI of the head. *Magnetic Resonance in Medicine*, 69(5):1476–1485, 2013.

[17] Shaihan J Malik, Arian Beqiri, Anthony N Price, Jose Nuno Teixeira, Jeffrey W Hand, and Joseph V Hajnal. Specific absorption rate in neonates undergoing magnetic resonance procedures at 1.5T and 3T. *NMR in biomedicine*, 28(3):344–52, 2015.

[18] Thomas M. Fiedler, Mark E. Ladd, and Andreas K. Bitz. SAR Simulations & Safety. *NeuroImage*, 168:33–58, 2018.

[19] H. Homann, P. Börnert, H. Eggers, K. Nehrke, O. Dössel, and I. Graesslin. Toward individualized SAR models and in vivo validation. *Magnetic Resonance in Medicine*, 66(6):1767–1776, 2011.

[20] Thomas M. Fiedler, Mark E. Ladd, and Andreas K. Bitz. RF safety assessment of a bilateral four-channel transmit/receive 7 Tesla breast coil: SAR versus tissue temperature limits: SAR. *Medical Physics*, 44(1):143–157, jan 2017.

[21] Jin Jin, Feng Liu, Ewald Weber, and Stuart Crozier. Improving SAR estimations in MRI using subject-specific models. *Physics in Medicine and Biology*, 57(24):8153–8171, 2012.

[22] F Padormo, S Malik, J Hajnal, and D Larkman. Assessing and Correcting Respiration Induced Variation of B1 in the Liver. *Proceedings 17th Scientific Meeting, International Society for Magnetic Resonance in Medicine*, Honolulu:753, 2009.

[23] Glover Paul. Doran Emma, Bawden Stephen, Bowtell Richard, Gowland Penny. Effects of Respiration on B1+ and SAR in Whole-Body Imaging at 7 Tesla. In *In Proc. ISMRM (Paris).*, 2018.

[24] Sebastian Schmitter, Xiaoping Wu, Kâmil Uurbil, and Pierre François Van De Moortele. Design of parallel transmission radiofrequency pulses robust against respiration in cardiac MRI at 7 Tesla. *Magnetic Resonance in Medicine*, 74(5):1291–1305, 2015.

[25] Marija Bešter-Rogač. Electrical Conductivity of Concentrated Aqueous Solutions of Divalent Metal Sulfates.

[26] Kay Nehrke and Peter Bornert. DREAM — A Novel Approach for Robust, Ultrafast, Multislice B1 Mapping. *Magnetic Resonance in Medicine*, 68:1517–1526, 2012.

[27] M.J. Ackerman. The Visible Human Project. *Proceedings of the IEEE*, 86(3):504–511, 1998.

[28] Nobuyuki Otsu. Threshold Selection Method From Gray-Level Histograms. *IEEE Trans Syst Man Cybern*, SMC-9(1):62–66, 1979.

[29] C. Chinrungrueng and C.H. Sequin. Optimal adaptive k-means algorithm with dynamic adjustment of learning rate. *IEEE Transactions on Neural Networks*, 6(1):157–169, 1995.

[30] Vasily L. Yarnykh. Actual flip-angle imaging in the pulsed steady state: A method for rapid three-dimensional mapping of the transmitted radiofrequency field. *Magnetic Resonance in Medicine*, 57(1):192–200, 2007.

[31] Robert L Harrison. Introduction To Monte Carlo Simulation.

[32] Aaron T. Hess, Elizabeth M Tunnicliffe, Christopher T. Rodgers, and Matthew D. Robson. Diaphragm position can be accurately estimated from the scattering of a parallel transmit RF coil at 7 T. *Magnetic Resonance in Medicine*, 79(4):2164–2169, 2018.

[33] Sven H.F. Jaeschke, Matthew D. Robson, and Aaron T. Hess. Cardiac gating using scattering of an 8-channel parallel transmit coil at 7T. *Magnetic Resonance in Medicine*, 80(2):633–640, 2018.

[34] Zhangwei Wang, James C. Lin, Weihua Mao, Wanzhan Liu, Michael B. Smith, and Christopher M. Collins. SAR and temperature: Simulations and comparison to regulatory limits for MRI. *Journal of Magnetic Resonance Imaging*, 26(2):437–441, 2007.

[35] Hanno Homann. *SAR Prediction and SAR Management for Parallel Transmit MRI*. Technische Informationsbibliothek u. Universitatsbibliothek, 2012.

[36] Fatemeh Adibzadeh, Margarethus M. Paulides, and Gerard C. van Rhoon. SAR thresholds for electromagnetic exposure using functional thermal dose limits. *International Journal of Hyperthermia*, 34(8):1248–1254, 2018.

[37] Wenli Liu, Hongkai Wang, Pu Zhang, Chengwei Li, Jie Sun, Zhaofeng Chen, Shengkui Xing, Ping Liang, and Tongning Wu. Statistical evaluation of radiofrequency exposure during magnetic resonant imaging: Application of whole-body individual human model and body motion in the coil. *International Journal of Environmental Research and Public Health*, 16(6), 2019.

[38] Ettore F. Meliadò, Cornelis A.T. van den Berg, Peter R. Luijten, and Alexander J.E. Raaijmakers. Intersubject specific absorption rate variability analysis through construction of 23 realistic body models for prostate imaging at 7T. *Magnetic Resonance in Medicine*, 2018.

6 High Resolution MR Angiography for Imaging Small Vessels

The work in this chapter was presented during an oral session at the Society for Magnetic Resonance Angiography 31st Annual International Conference (2019). The preliminary research was presented as an electronic poster at the 26th Annual Meeting of the International Society for Magnetic Resonance in Medicine (2018) [1].

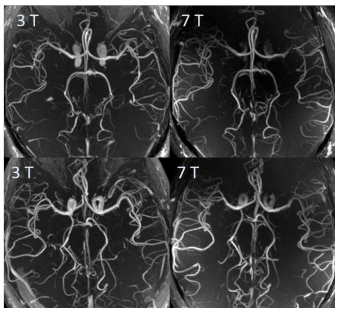
6.1 Introduction

Magnetic Resonance Angiography (MRA) is an imaging technique that exploits the sensitivity of MRI to moving nuclei and is used to visualise blood vessels and assess vascular conditions non-invasively [2]. MRA was first implemented as a clinical technique in 1985 [3] and was used by Edelman et al. to successfully acquire angiograms of the coronary arteries [4]. Since then there have been multiple advancements made in imaging techniques and hardware that have made MRA a routine clinical method. Diagnosis of vascular diseases across the whole body is possible using tailored coils designed to fit specific body parts such as the head or extremities.

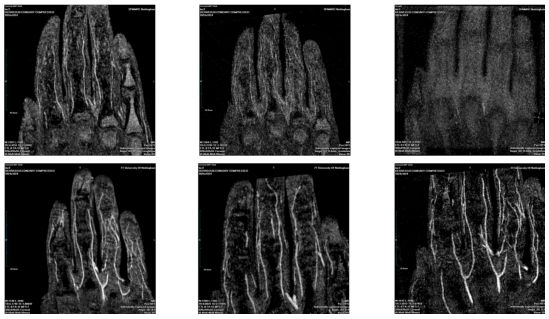
MRA can be applied to gain information about vascular kinetics and haemodynamics [5, 6]. MR techniques that have been developed to accelerate image acquisitions, such as parallel imaging, undersampled radial k-space trajectories and compressed sensing [7] have contributed to the improved diagnostic accuracy of MRA such that it competes with CT angiography (CTA) and digital subtraction angiography [8, 9].

High resolution MRA has been developed at 7 T for imaging microvasculature and has been shown to provide superior detail compared to clinical images obtained at 1.5 and 3 T. An example of this is the increased delineation of small peripheral vessels in the brain at 7 T compared to 3 T [10] as displayed in

Figure 6.1 (a). Another example includes contrast enhanced musculoskeletal images that demonstrate the benefits of both using contrast to enhance vasculature detail in the hand and the higher resolution that is possible due to the inherent increase in SNR available at 7 T [11] is shown in Figure 6.1 (b).



(a) Brain MRA at 3 and 7 T: spatial resolution of 0.63 x 0.80 x 1 mm^3 [10]



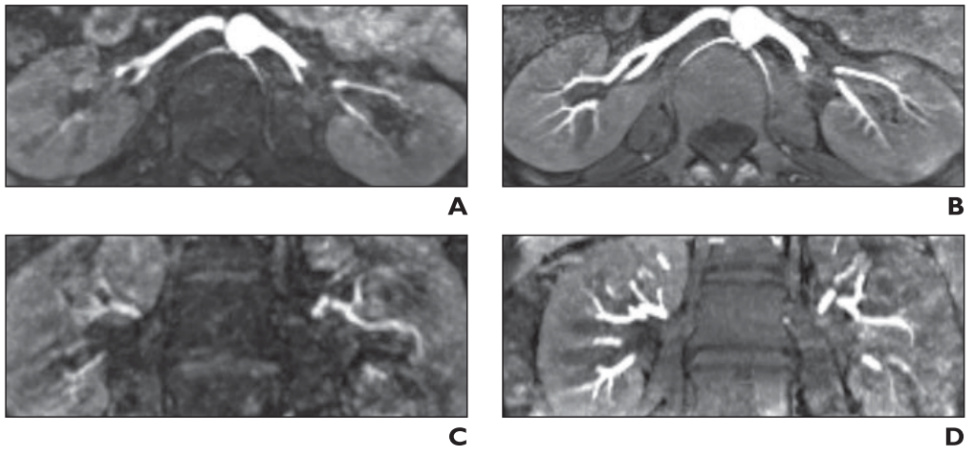
(b) Hand CE-MRA at 3 and 7 T: spatial resolutions are 0.5, 0.4 and 0.3 mm isotropic [11]

Figure 6.1: Examples of neuro and hand MRA at 3 and 7 T.

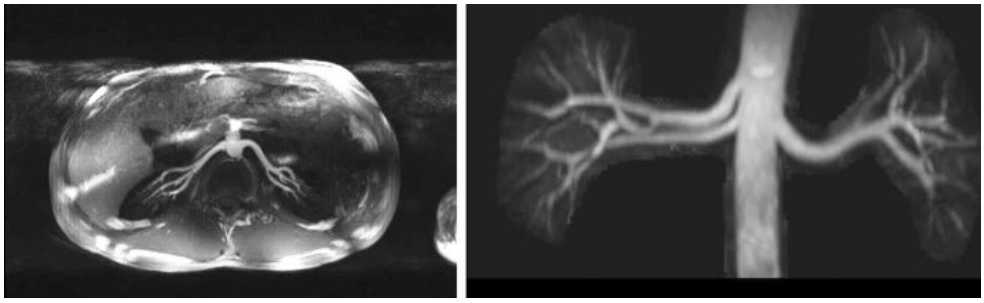
As 7 T becomes increasingly used for abdominal MRI due to advancements made in pTx [12] and novel coil design [13], the potential for enhanced imaging of vascular networks in abdominal organs can be researched. The kidneys are an ideal choice of organ in which to develop 7 T abdominal MRA due to their size and placement in the abdomen. As the kidneys are relatively small organs, the severe B_1^+ inhomogeneity experienced at 7 T should not be a problem for static pTx applications (see 3.2).

Similar to the way in which clinical images at 3 T have significantly improved the visualisation of peripheral renal arteries when compared to 1.5 T (Figure 6.2 (a)) [14], it is anticipated that results at 7 T will enhance the detail with which blood vessels can be resolved. Several groups have worked on 7 T renal angiography and current published work includes preliminary contrast [15], and non-contrast enhanced [16, 17] results demonstrating concepts such as dynamic B_1^+ shimming [18] that were implemented to obtain successful renal angiograms within local SAR constraints (see 3.8). An example of non-contrast enhanced

renal MRA data adapted from the 7 T renal MRI review paper by de Boer et al. [19] is presented in Figure 6.2 (b).



(a) SSFP MRA in the kidneys at 1.5 and 3 T. Transverse (A, B) and coronal (C, D) MIPs at 1.5 T (A, C) and 3 T (B, D) [14].



(b) Low flip angle GRE renal MRA and associated MIP at 7 T. Figure adapted from: [18]

Figure 6.2: Examples renal MRA collected at different field strengths.

This chapter outlines the development of high resolution 2D TOF-MRA combined with a multi-echo acquisition for imaging small vessels in the kidneys at 7 T. This protocol was then applied to the liver and Deep Inferior Epigastric Perforator (DIEP) vessels to demonstrate its potential use in other body MRA applications.

6.2 Clinical Applications

This section outlines the anatomy and basic physiology of the organs to which MRA will be applied in this chapter.

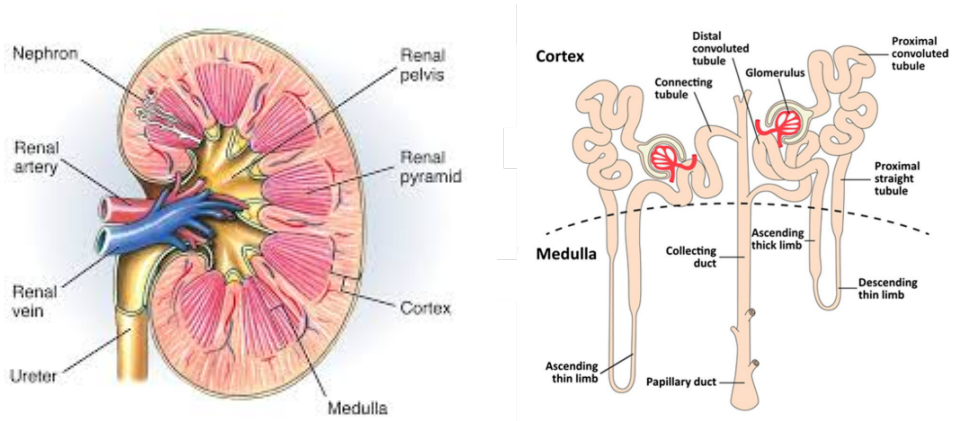
6.2.0.1 Kidney Function and Vasculature

The kidneys make up less than 1% of total body mass but demand 20 - 25% of cardiac output [20]. Their function is to process and filter the total blood volume, reabsorb electrolytes and secrete unwanted waste metabolites whilst controlling the body's fluid balance. Regulation mechanisms in the kidney balance filtration rates and urine production of which up to 1.5 L can be produced daily.

The microscopic structural and functional component of the kidney is the nephron (see Figure 6.3). There are approximately one million nephrons in each kidney and together they filter the blood through multiple reabsorption and secretion processes to produce urine which drains into the renal pelvis and out through the ureter to the bladder. The filtering component of the nephron is called the renal corpuscle and the reabsorption and secretion component is the renal tubule. The renal corpuscle filters solutes from the blood and transfers water and small solutes to the renal tubules in each of the nephrons.

The kidney itself (renal parenchyma) can be divided into the renal cortex and the renal medulla. The renal medulla makes up the inner region of the kidney and contains the renal pyramids and collecting ducts. The medulla is hypertonic compared to the filtrate in the nephrons and so assists with the reabsorption of water.

The cortex is the outer region of the kidney that contains the renal corpuscles, renal tubules and blood vessels. Ultrafiltration occurs in the cortex which is where large molecules such as proteins and blood cells are kept in the blood. Smaller molecules, such as sodium, are passed through to the renal tubule which delivers fluid that has been filtered to the medullary collecting duct system [21].



(a) Renal parenchyma. (b) Nephron.

Figure 6.3: Basic renal anatomy: (a) schematic diagram showing the renal cortex and medulla regions, the main renal artery and vein entering and leaving the kidney, renal pyramids and renal pelvis in the medulla and ureter leading to the bladder. (b) detailed diagram of the nephron showing how the components span both sides of the cortico-medullary border [19].

The kidneys receive blood via the renal artery which branches from the abdominal aorta and venous drainage is via the renal vein into the inferior vena cava (IVC). Most of the total Renal Blood Flow (RBF) to the kidneys perfuses the cortex (90 %), whilst only 10 % is delivered to the more metabolically active medulla. Oxygen extraction is high in the medulla and so it is extremely sensitive to hypoxia and changes in renal blood flow. Intralayer perfusion is heterogeneous and the intrarenal vasculature enables diffusion of O_2 from arteries to veins in the cortex as well as from cortex to medulla. Vascular architecture promotes plasma distribution at vessel branches resulting in different blood O_2 contents in the perfusing daughter vessels.

Each renal artery branches into segmental arteries, which then divide further into interlobar arteries, which penetrate the renal capsule and extend through the renal columns between the renal pyramids. The interlobar arteries then supply blood to the arcuate arteries that run through the boundary of the cortex and the medulla. Peritubular capillaries run alongside the nephrons and penetrate

the renal medulla to combine and form veins that eventually form the renal vein. This then exits the kidney and joins the Inferior Vena Cava (IVC) that transports deoxygenated blood back to the heart [22].

In renal imaging, small distal vessels at the cortico-medullary border and small intrarenal arteries are of interest in Chronic Kidney Disease (CKD) patients as a potential marker of early end-organ damage in hypertension. CKD is a progressive disorder causing scarring of the renal tissues that leads to End Stage Kidney Disease (ESKD) [23]. This scarring is thought to be related to chronic ischaemia created by the loss of the peritubular capillaries [24].

Renal Artery Disease (RAD) is also associated with high blood pressure and hypertension and can lead to renal failure due to stenosis (Renal Artery Stenosis (RAS)) and reduction of the arterial diameters. MRA can be used to image the affected intrarenal and accessory arteries vital for diagnostic information. Computed Tomography Angiography (CTA) is more widely available than MRA but requires iodinated contrast which is not ideal in patients with impaired renal function. There is a need to monitor the progression of RAD and response to hypertension treatments. After imaging it can be decided whether intervention with revascularisation strategies is required [25].

Atherosclerotic Renovascular Disease (ARVD) is another progressive condition that disturbs normal renal function due to inadequate blood supply and damage caused by hypertension. It accounts for 90 % of RAS in the Western population. ARVD can lead to CKD and ESKD and provides another example of how vascular imaging is crucial for informing intervention and preventing further renal impairment [26].

Using non-invasive imaging is also beneficial in the case of screening for donors where angiography is used to map transplant vasculature [27]. Angiography is also a valuable tool for evaluating graft vessels. CTA with iodinated contrast is used for this or MRA with gadolinium based contrast. Development of MRA techniques that do not require contrast enhancement with improved image quality and diagnostic accuracy have made substantial progress [28].

MRA can be added to a multi-parametric protocol to provide additional vascular information that compliments functional measures such as Glomerular Filtration Rate (GFR) which is considered the reference standard for evaluating renal function [29]. This is vital for accurately diagnosing Acute Kidney Injury (AKI) [30], CKD and renal masses [31].

6.2.0.2 Liver Function and Hepatic Vasculature

The liver's main function is to control metabolic processes such as glycogen storage, red blood cell decomposition and hormone production. It can also be considered as an accessory digestive organ producing bile which aids the breakdown of fats in the small intestine. It is located in the right upper quadrant of the abdomen below the diaphragm.

Blood supply to the liver is via the right and left Hepatic Arteries (HA) and the Portal Vein (PV) (see Figure 6.4). The PV carries deoxygenated blood from the spleen and Gastrointestinal (GI) tract delivering 75 % of the liver's blood supply, whilst the remaining blood flow comes from the oxygenated blood through the hepatic arteries. Blood travels through the liver and flows out through the Hepatic Veins (HV) that drain into the IVC [32].

Using MRA to image the vascular network of the liver is a valuable, non-invasive diagnostic method for use in patients with suspected liver vascular disease [33]. For example, in patients with suspected portal hypertension identifying blocked vessels is important for treatment planning. Angiography can also provide more information regarding smaller intrahepatic lesions in patients with liver scarring conditions such as fibrosis and cirrhosis [34].

These conditions can alter the vasculature within the liver, causing disarrangements of circulation which can worsen liver disease progression, cause the onset of portal hypertension and reduce liver perfusion which can lead to liver failure. The potential to include microvasculature detail in the computation of hepatic network connectivity is desirable for assessing the structural progression of liver disease [35].

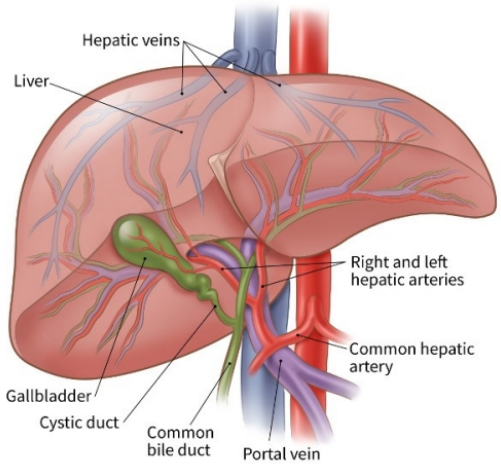


Figure 6.4: Basic liver anatomy: portal vein (PV) and hepatic arteries (HA) deliver oxygenated blood to the liver. Vascular network throughout the liver is tortuous. Blood flows through central veins to the hepatic veins (HV) that each drain into the inferior vena cava (IVC).

6.2.0.3 Blood Supply to the Lower Abdominal Wall

The Deep Inferior Epigastric Artery (DIEA) has perforating branches that supply blood to the lower abdominal wall. These Deep Inferior Epigastric Perforator (DIEP) vessels pass through the rectus muscle and fascia to reach the subcutaneous fat and skin (Figure 6.5). This provides a connection to the Superficial Inferior Epigastric Artery (SIEA) and Superficial Inferior Epigastric Vein (SIEV) [36, 37].

DIEP flap surgery for breast reconstruction involves transferring patient's skin and subcutaneous tissues from the lower abdominal wall to the chest to form a breast mound (Figure 6.6). Only the perforating vessels are removed and the rectus muscle is spared resulting in fewer complications compared to other breast reconstruction surgeries [37–39]. Identification of viable donor sites for the DIEP flap is based on the location, shape and size of perforating vessels.

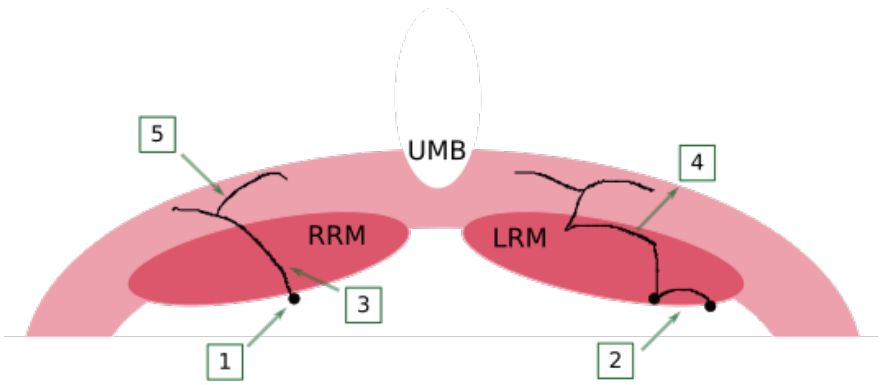


Figure 6.5: Lower abdominal wall arterial supply: [1] deep inferior epigastric artery (DIEA) under the rectus muscle (RM), [2] DIEA within the RM, [3] Perforating artery, [4] Subfascial perforator, [5] Subcutaneous perforator. UMB marks the umbilicus.

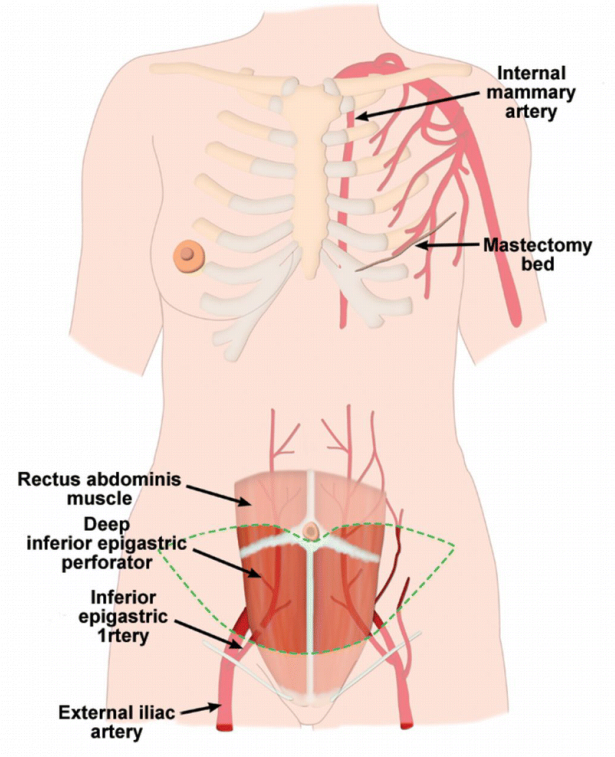


Figure 6.6: Schematic of DIEP surgery [38]

Abdominal vasculature is very individual and so pre-operative imaging on a case-by-case basis to inform surgical planning and dissection is essential to ensure reliable arterial supply. CTA with iodinated contrast agents is commonly used to image the DIEP vessels. MRA with gadolinium based contrast agents is becoming increasingly used as it uses non-ionising radiation which is preferred in cancer patients [40] and can locate perforating vessel branches easily [41]. An example of perforating vessels imaged at 1.5 T with contrast enhancement is shown in Figure 6.7 [42]. 3 T contrast enhanced coronal images that highlight the DIEA and SIEA are shown Figure 6.8 [41].

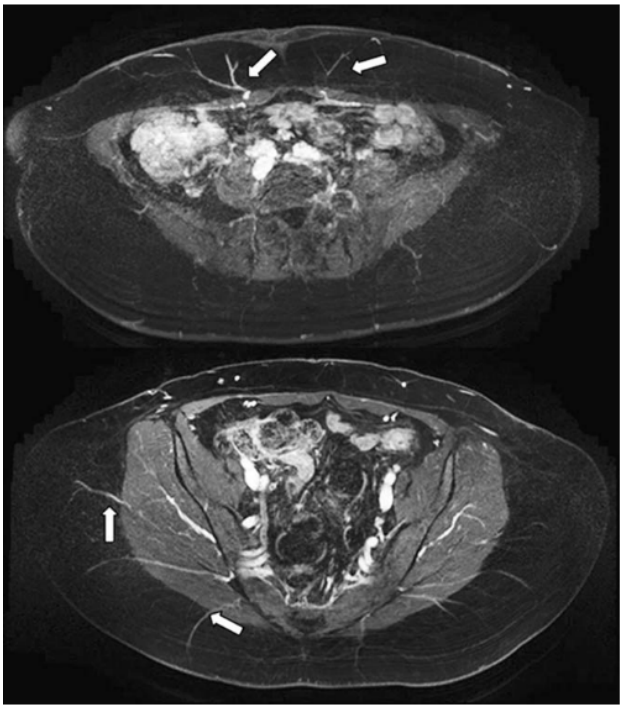


Figure 6.7: 1.5 T images of perforator arteries (highlighted by the arrows). Figure taken from [42].



Figure 6.8: 3 T contrast enhanced images of deep and superior inferior epigastric vessels demonstrating different types of branching patterns in separate subjects. Figure taken from [41].

6.3 Magnetic Resonance Angiography

6.3.1 Contrast vs. Non-Contrast Enhancement

MRA can be performed with (contrast enhanced, CE) or without (non-CE) exogenous contrast agents. In CE-MRA, gadolinium (Gd) is usually injected into the blood which causes a shortening of its T_1 due to its paramagnetic properties. This leads to blood vessels appearing bright in T_1-weighted images. Functional information can be gained from CE-MRA; the average time it takes for a contrast agent to pass through a region of interest in a tissue is the mean transmit time (MTT). This can be measured in dynamic studies to describe tissue perfusion [43, 44].

Gd based contrast agents (GBCA) have been linked to nephrogenic systemic fibrosis (NSF) in patients with renal failure. Therefore, preventing the use of GBCA's in patients with renal impairment is highly desirable [45–50]. Gd has also been found to accumulate in the brain in healthy volunteers [51]. The long term effects of this are unknown.

In non-CE MRA, contrast is obtained from the velocity or movement of the blood. Unenhanced techniques tend to have lengthy acquisition times, particularly for peripheral arteries, and common image artefacts (such as ghosting which can be caused by the pulsatile nature of blood flow [52]) have made CE

MRA more favourable. However, non-CE techniques have been developed that are comparable to CE MRA results even at lower field strengths.

Removing the need for contrast administration can also lighten the workload for MRI radiologists or radiographers who are required to dispense the contrast agents, non-CE scans can be easily repeated without disrupting clinical workflow and the potential risks associated with GBCA can be avoided. There are two main non-CE MRA techniques; phase contrast angiography (PCA) and time-of-flight MRA (TOF-MRA). These are both outlined in the following sections.

6.3.2 Phase Contrast Angiography

Phase Contrast Angiography (PCA) uses bipolar gradients to manipulate the phase of moving spins relative to stationary spins depending on the velocity of the flow. This generates phase contrast between stationary tissue and flowing blood as the stationary spins experience no net phase shift, and moving spins accrue a net phase shift linearly proportional to their velocity (Figure 6.9). If two spins are flowing at the same constant velocity but in opposite directions then they will have equal but opposite phase shifts. Velocity can be calculated by measuring the change in phase.

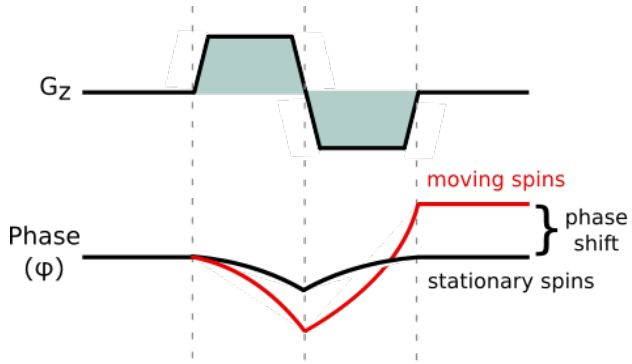


Figure 6.9: PCA phase shift induced by the application of bipolar gradients.

To eliminate other contributing phase shifts, for example from B_0 inhomogeneity, in PCA two sets of image data are acquired with imaging parameters held

fixed except for the first moment of the bipolar gradient. Phases of the two resulting images are subtracted on a pixel-by-pixel basis. This highlights the flow information and suppresses the unwanted phase variation in the background tissue.

The bipolar gradients can be applied prior to the readout along each of the axes either one at a time or simultaneously to provide flow sensitivity in each relative direction. The amplitude, duration and spacing of the bipolar gradients determine the sensitivity to slow or fast flows. These variables are controlled by the velocity encoding (VENC) parameter and are predetermined prior to the PCA acquisition to optimise performance of the study.

Velocity components of flow along each direction (v_x, v_y, v_z) can be calculated by measuring the phase shifts along each direction in which the bipolar gradients are applied (x-, y-, and z-). The total acquired phase shift can be found by integrating over the precession frequency, ω, of spins at each spatial location, $\mathbf{r}$, and is proportional to its velocity, $\mathbf{v}(t)$, the strength of the applied gradient, $\mathbf{G}(t)$, and the length of time it moves within that gradient, t:

$$\phi(\mathbf{r},t) = \int \omega(\mathbf{r},t)dt = \gamma \int \mathbf{r}(t)\mathbf{G}(t)dt = \gamma \int \mathbf{v}(t)\mathbf{G}(t)tdt \tag{6.1}$$

PCA can generate 1D, 2D, 3D or 4D flow data which can be displayed in directionally-insensitive magnitude images or in a cine format. It is useful in 2D to create quick vascular scout images prior to performing non-PC MRA techniques and in cine mode to quantify blood flow and velocities within vessels. 3D-PC-MRA is generally not used due to its long acquisition times and the invention of sequences that perform the same function with shorter acquisition times such as Time-of-Flight (TOF).

6.3.3 Time-of-Flight (TOF) Angiography

Partial saturation of longitudinal magnetisation occurs when signal is attenuated and forced into a steady state due to incomplete T_1 relaxation between RF pulses if the $T_1 << TR$. Time-of-Flight (TOF) angiography uses spoiled gradient echo pulse sequences to partially suppress static tissue signal. A typical 2D TOF-MRA sequence is outlined in Figure 6.10. Flow compensation gradients are applied before the readout and after slice selection during phase encoding gradients. These reduce the intravoxel phase dispersion effects from moving spins by eliminating the phase shift using the method outlined in Figure 6.9.

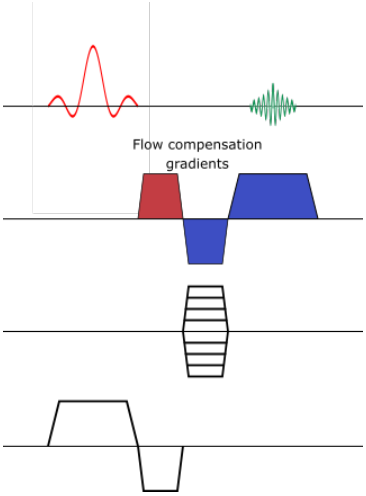


Figure 6.10: 2D TOF-MRA Sequence

The equation describing the relationship between signal S, T_1, TR, flip angle θ, equilibrium longitudinal magnetisation M_0, TE and T_2^* is:

$$S = \frac{M_0 sin\theta(1 - e^{-TR/T_1})}{(1 - cos\theta e^{-TR/T_1})} e^{-TE/T_2^*} \tag{6.2}$$

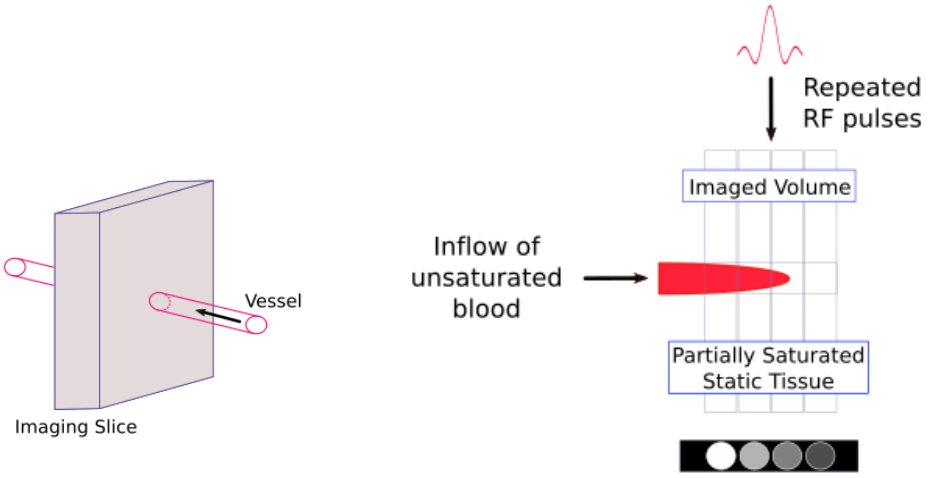
The signal S decreases as the ratio TR/T_1 decreases, therefore saturation increases if TR is shortened or the T_1 is longer. The maximum signal occurs when the flip angle is equal to the Ernst angle:

$$\theta_E = arccos(e^{-TR/T_1}) \tag{6.3}$$

Flow Related Enhancement (FRE) is a phenomenon that restores signal intensity lost to partial saturation from the inflow of magnetised blood that has not been exposed to the series of RF pulses into the imaging slice (Figure 6.11 (a)). FRE increases with flow velocity and as the flow becomes more perpendicular to the imaging slice. Additionally, FRE is increased if slice thickness, Δz, is reduced. There is complete inflow replacement of magnetisation in the imaging slice during each TR interval, and no further increase of FRE if the perpendicular component of the velocity surpasses:

$$v_{max} = \frac{\Delta z}{TR} \tag{6.4}$$

Figure 6.11 (b) further demonstrates FRE and how the signal from inflowing blood generates contrast against the partially saturated background tissue. Fast flowing blood takes less time to travel through an imaging volume and is therefore exposed to less RF pulses resulting in high blood signal. Slower flowing blood is exposed to more RF pulses and appears with relatively lower signal.



(a) (b)

Figure 6.11: Time-of-flight angiography: (a) Schematic representation of inflowing blood entering an imaging slice. This is the effect that gives rise to flow related enhancement. (b) Fully magnetised blood flows into imaging volume. Signal from blood is enhanced relative to the stationary tissue background which experiences partial saturation from exposure to repeated RF pulses.

In 3D TOF there is more FRE in the slices where flowing blood enters the slab, and less FRE in the slices where the vessel exits (see Figure 6.11 (b)). However, in reality this is complicated by vessels that have twisted trajectories and variable blood velocities.

2D TOF involves splitting the imaging volume into sequentially acquired slices. The number of slices is solely limited by the imaging time and field-of-view. The imaging plane is chosen to be perpendicular to the flow to maximise the FRE signal. Motion artefacts are less likely in 2D TOF and if they do occur they arise on a slice-by-slice basis as opposed to corrupting the entire acquisition as would be the case in 3D TOF.

Arteries and veins often overlap which can be detrimental to the imaging of particular arteries of interest. Spatial saturation pulses can be applied parallel

to the imaging slice to suppress the venous signal, but this approach assumes that the arteries and veins have different directions of flow within the vessels [53]. This can be difficult in organs such as the liver; where the vasculature is tortuous and further complicated with a dual blood supply from both portal vein and hepatic artery, or in the kidney; where the renal artery and renal vein run parallel [54].

Artefacts can arise in 2D TOF Maximum Intensity Projection (MIP) images due to moving vessels and pulsatile flow caused by respiration and cardiac motion. This causes irregular, frequency modulated patterns close to the vessels. Flow compensation gradients can be used to counteract these artefacts and reduce accumulated phase errors. Alternatively, cardiac triggering can overcome the pulsatile flow, however movement from respiration and other patient movement still can contribute to this artefact, particularly in body imaging.

6.3.4 Benefits of 7 T

At 7 T, the longer T_1 relaxation time of different tissues leads to improved suppression of the background signal at lower flip angles. The signal intensity in the vessels remains constant and when combined with the higher SNR readily available at 7 T, a higher Contrast-to-Noise Ratio (CNR) between the vessels and background can be reached. Therefore, it should be possible to obtain higher spatial resolution angiograms at 7 T without loss of contrast compared to 3 T. This has been already exploited in the brain for visualising the small cerebral vessels [55].

The increase in endogenous contrast has the potential to remove the need for contrast administration currently required at lower field strength abdominal studies, removing the complications associated with GBCAs that were mentioned previously in Section 6.3.1.

6.3.5 Challenges at 7 T

Performing MRA in the abdomen at 7 T comes with unique imaging challenges. The B_1^+ inhomogeneity is greatly increased and this can result in varying suppression of the background signal across the FOV. To account for increased SAR at 7 T, there are additional power constraints and to compensate, for a given flip angle, the TR in the angiography sequence is lengthened. Consequently, in order to perform high resolution angiography scans within the time frame of a breath-hold ($\approx$ 25 seconds) parallel acceleration (e.g. SENSE) must be implemented.

Both the long TR and implementation of SENSE result in lower SNR, however, the long TR can be exploited to acquire multiple gradient refocused echoes within a single TR. This is already an established method and involves combining the angiograms obtained from each echo to provide more information than exists in an individual angiogram [56]. The resultant combined angiograms have enhanced SNR which can outweigh most of the reduction in SNR associated with the use of SENSE.

6.3.6 Outline

This chapter outlines the development of a high resolution 2D multi-echo TOF-MRA protocol in the kidneys at 7 T, qualitative assessment of the angiograms produced and quantitative analysis of SNR, CNR and renal vessel radii in healthy subjects. Preliminary results from the application of this protocol in the liver and lower abdominal wall are also presented, alongside results from PCA of the large vessels in the liver. The 2D TOF-MRA gradient echo sequence was implemented as a starting point for developing abdominal imaging at 7 T. The benefits of imaging at 7 T compared to 3 T are demonstrated and the challenges of UHF body imaging are discussed.

6.4 Materials and Methods

6.4.1 Study Population

Eight healthy volunteers (6 female, 2 male; average age 40 $\pm$ 16 years) were enrolled for a 7 T renal MRA study. Data acquisition was conducted in accordance with the institutional review board and approved and informed consent was obtained before each examination. Data was collected in four of these subjects on the 3 T Achieva and 3 T Ingenia wide bore scanner for comparison (2 female, 2 male; average age 25 $\pm$ 1 years).

6.4.2 MRI and Coil System

All examinations were performed in the feet-first, supine position on a 7 T Philips Achieva pTx system equipped with a high-performance gradient system providing a strength of 40 mT/m and a maximum slew rate of 200 mT/m/ms. For RF transmission, 8 x 1 kW amplifiers were used to drive an 8 TX/32 RX body array (MRCoils).

The two transceiver array plates were positioned such that the centre line of the coil coincided with the region between the bottom of the ribs and the hips of each subject. This ensured maximum signal in the area where the kidneys were likely to be located and minimised the need for repositioning subjects once scanning had started.

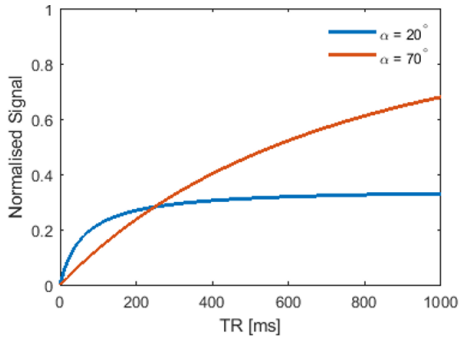
The forward and reflected RF power in each transmit channel was monitored throughout the examination using the Philips standard software power monitoring unit (SPMU). Average power per channel was set to 3 W which is the limit set from local SAR calculations performed in-house. A Philips 3 T Achieva and Philips 3 T Ingenia with dual-RF transmit, both with 32-channel receive coils were also used to produce comparison data.

6.4.3 Sequence Optimisation and Imaging

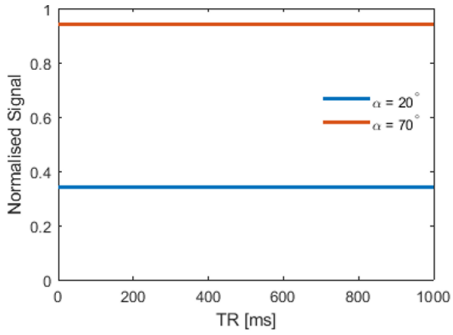
6.4.3.1 Development

A 2D TOF-MRA sequence was optimised at 7 T during pilot tests in healthy volunteers to satisfy local SAR constraints and increased T_1 relaxation times. This involved addressing the longer TRs and limited high flip angle pulses required to generate sufficient image contrast. A high flip angle and short TR are required to sufficiently suppress the background tissue (see Figure 6.12 (a)). The flip angle also needs to be large enough to give reasonable signal from the inflowing blood (see Figure 6.12 (b)) and, the TR needs to be long enough to allow the inflowing blood to enter the imaging slice.

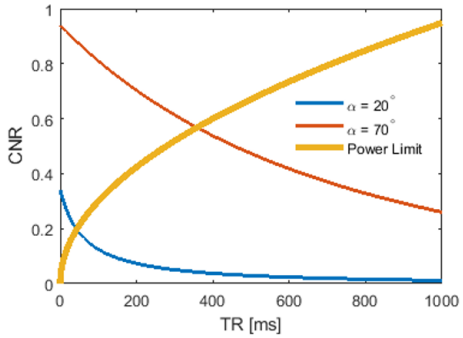
The power limit (corresponding to the local SAR limit) for a particular flip angle is proportional to $\sqrt{TR}$. An arbitrary power limit curve is plotted on top of contrast curves which were calculated as the difference between the signal curves for blood and background tissue ($T_1 = 1000$ ms) in Figure 6.12 (c). Levels of available contrast above the power limit curve can not be achieved during scanning, therefore, a high flip angle at the minimum allowed TR is desired. The TR also needs to be short enough so that high resolution imaging can be performed within a breath hold.



(a) Tissue signal.



(b) Inflowing blood signal.



(c) Demonstration of the power limitations of achievable contrast (difference between blood and tissue signals).

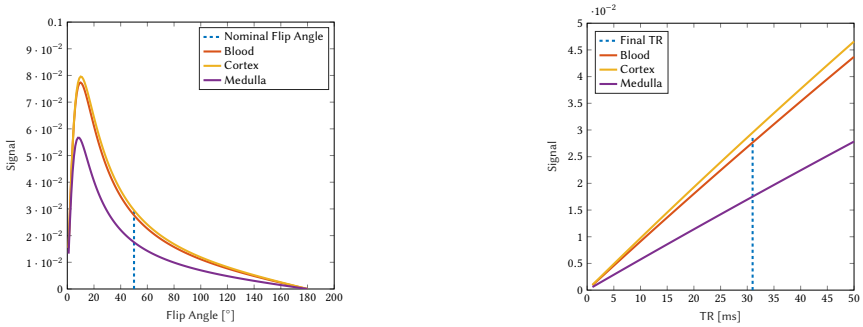
Figure 6.12: Associated concepts for sequence development: (a) normalised signal curves for flip angles 20° and 70° that correspond to background tissue with a T_1 = 1000 ms. (b) Normalised signal curves generated with 20° and 70° that correspond to inflowing blood. The signal is proportional to sinθ and is constant with TR. (c) The difference between the inflowing blood and tissue signals for each simulated flip angle (this is the contrast between the inflowing blood and static tissue). The curve corresponding to the arbitrary power limit, which is proportional is $\sqrt{TR}$, is also displayed. Contrast generated above the power limit curve can not be achieved during scanning.

On consideration of these concepts, imaging parameters were set with the shortest TE available, and the TR and flip angle were determined from simulations of the FLASH signal for blood and renal tissues.

The T_1 values used to simulate the FLASH signal are listed in Table 6.1. $T_{1,blood}$ was taken from current literature [57], and the $T_{1,cortex}$ and $T_{1,medulla}$ values were obtained during preliminary T_1 measurements at 7 T. Figure 6.13 (a) displays the signals simulated for a TR of 31 ms across the flip angle range 0° - 180°, and Figure 6.13 (b) displays the signals simulated for a flip angle of 50° across the TR range 1 - 50 ms. The dashed lines in each plot highlight the final values selected for flip angle and TR parameters which were shown to achieve high saturation of the background tissue, high signal in the vessels and thus superior contrast within local SAR limits.

Table 6.1: T_1 values used to plot FLASH signal curves at 7 T

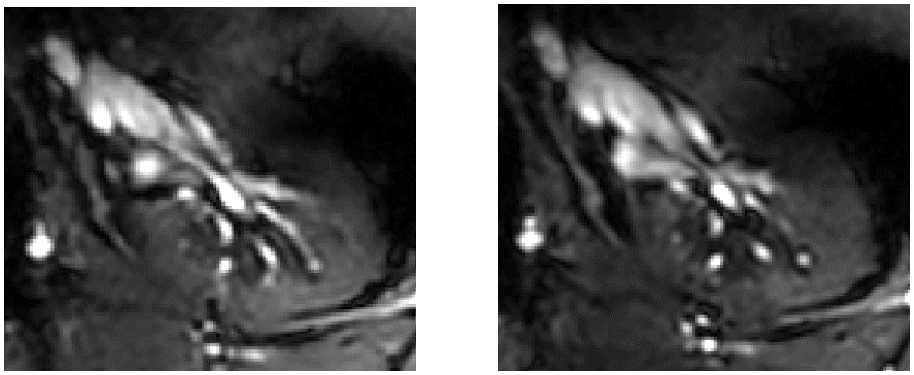
Tissue	T_1 value (ms)
Blood	2087
Renal cortex	1930
Renal medulla	2849



(a) (b)

Figure 6.13: FLASH signal curves aid development of renal angiography protocol: (a) simulated signal for blood and renal tissues for a TR of 31 ms, (b) simulated signals for a flip angle of 50°. Dashed lines mark the values used as final imaging parameters.

A demonstration of the importance of optimising the TR for the transit time of renal blood flow is shown in Figure 6.14. The sensitivity to signal in the peripheral vessels is greater in the image acquired with (a) TR = 25 ms compared to the image obtained with the (b) TR = 20 ms.



(a) TR = 25 ms (b) TR = 20 ms

Figure 6.14: Demonstration of sensitivity of signal in the peripheral vessels to choice of TR parameter. Signal in the peripheral vessels is greater in the image with the longer TR.

Initially, the TOF-MRA sequence was applied in the transverse orientation in concatenated scans to cover the full length of the kidney. 7 T images and final mip were compared to those produced at 3 T in order to assess the possibility of 2D TOF at 7 T (see Figure 6.15 for comparison of 3 and 7 T renal angiograms). From this preliminary work increased detail in the small vasculature in the peripheral regions of the kidney motivated further development of this approach. Imaging acquisition parameters used at this stage at 3 and 7 T were: TR = 20 ms, TE_1 = 5.4 ms, field-of-view = 230 x 230 x 12 mm^3, water fat shift = 298 Hz/pixel, requested flip angle = 70°, voxel size = 1.5 x 1.5 mm^2 with a slice thickness of 2 mm, and a reconstructed in-plane resolution of 0.65 x 0.65 mm^2. No parallel imaging was implemented.

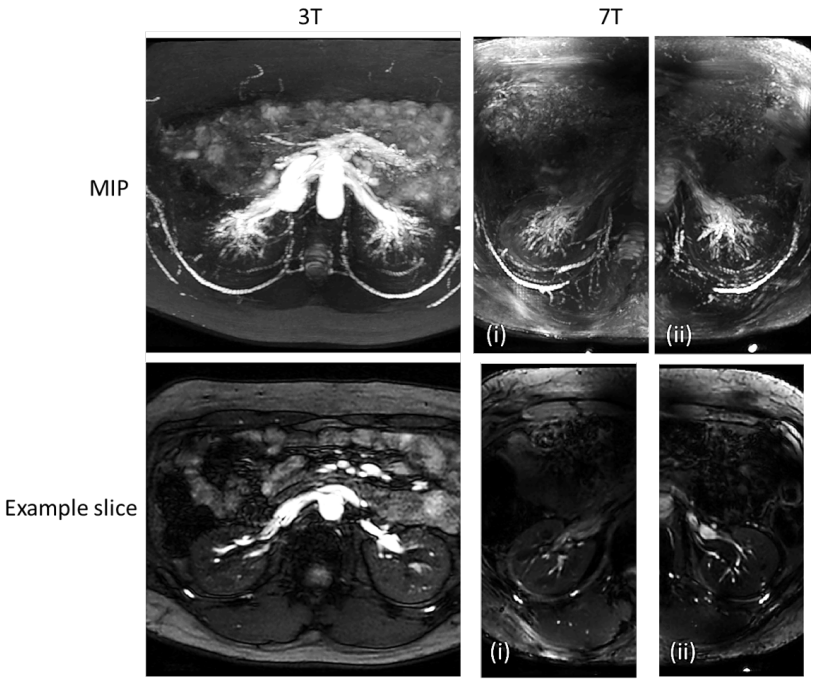


Figure 6.15: Preliminary work comparing renal angiograms collected at 3 and 7 T in the transverse orientation.

The 7 T protocol was then optimised to increase the spatial resolution of the images and to implement parallel imaging. The longer TR in the TOF-MRA sequence derived from the FLASH signal simulations (TR extended from 20 to 31 ms) was exploited to acquire multiple echoes. By summing over these echoes for each image slice it was possible to recover SNR lost due to the use of longer TR's (which are required at 7 T because of the longer T_1 values and local SAR constraints) and parallel imaging to improve the quality of the final MIP's.

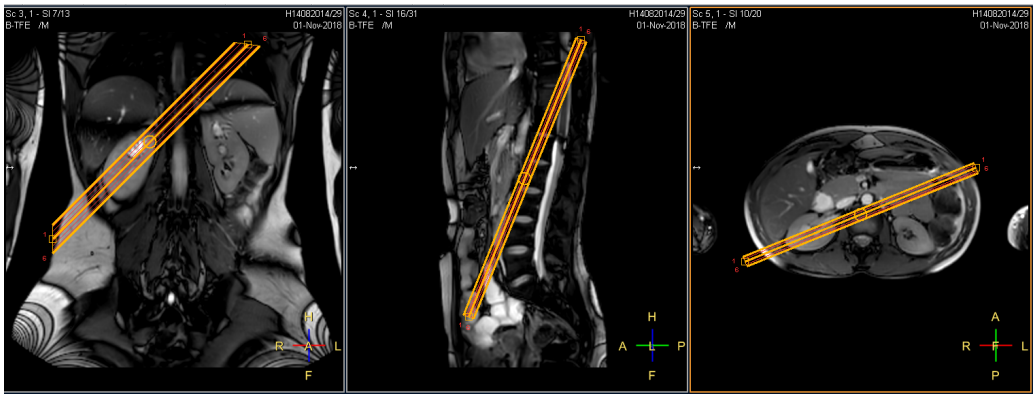
To maximise coverage and allow the images to be acquired within a single breath hold the image acquisition was altered to a coronal oblique orientation. Furthermore, it was decided to focus on only one kidney as B_1^+ shimming over both kidneys simultaneously proved difficult. The right kidney is located under the liver and more centrally in the abdomen when compared to the left kidney. Therefore, the right kidney was considered to be more challenging to image and

the best choice for optimising a renal protocol. Again, the 7 T renal images were compared to those acquired at 3 T, using the same imaging sequence, in a subset of volunteers to assess the quality of vascular detail in the angiograms.

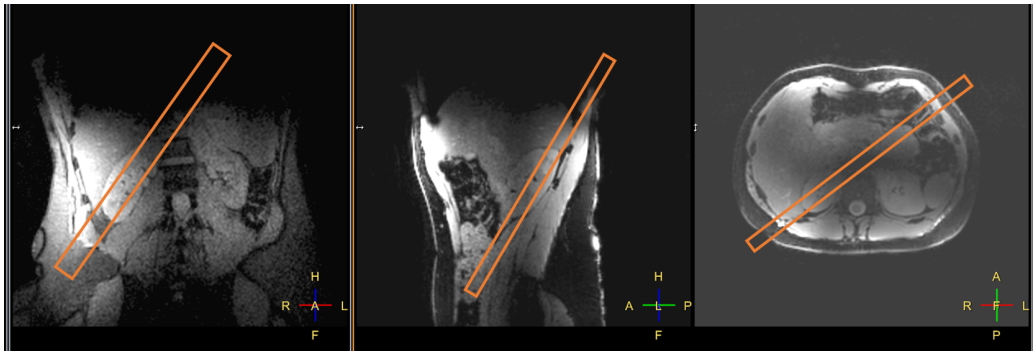
The large range of flip angles achieved in the abdomen was challenging. A target flip angle of 50° in the kidney region with a TR = 31 ms, was selected from the preliminary results and this produced consistent contrast between renal tissues and the small peripheral vessels. Actual flip angles were determined in vivo by collecting a DREAM B_1^+ map immediately prior to the angiography scan in the same geometry and measuring the actual flip angle in a ROI encompassing the kidney. The target flip angle was then achieved by increasing or decreasing the flip angle parameter.

6.4.3.2 Localiser Scans

Quadrature mode transmit B_1^+ phases (45° relative phase set on each channel) were used at the beginning of each imaging session. Survey images were initially run to ensure the subject was at the correct placement within the body coil; this comprised of 12 slices in the three perpendicular orientations. If subjects were not placed such that there was high signal in the region of interest they were repositioned accordingly. A SENSE reference scan was then run to collect coil sensitivity information. Three mDIXON localiser scans were performed in transverse, coronal and sagittal orientations; these were used for planning the coronal oblique geometry for each angiography scan. Examples of the planning stage in one subject at 3 T and another subject at 7 T are shown in Figures 6.16 (a) and (b) respectively. Similar geometries were used between 3 and 7 T scanners; however, this was difficult to match exactly due to the different positioning of subjects between the scanners. The 3 T Ingenia is a wide bore scanner and so subjects could lie with padding under the knees for comfort in a more relaxed position compared to that in the narrower 3 T Achieva bore. On the 7 T Achieva the bore is again narrower, and the body array set-up does not allow any room for subjects to lie with padding under the knees. Therefore, the overall spinal alignment of the subject differs between the scanners.



(a) Planning the coronal oblique acquisition on 3 T mDixon images.



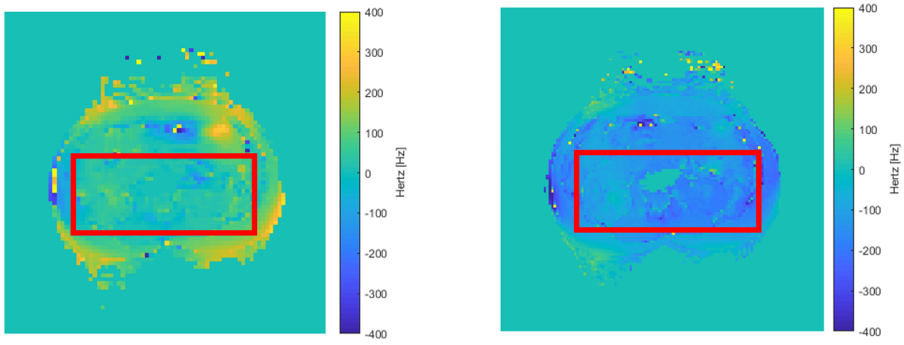
(b) Planning the coronal oblique acquisition on 7 T mDixon images.

Figure 6.16: Coronal oblique geometry planning; examples shown in (a) one subject at 3 T and (b) another subject at 7 T.

6.4.3.3 B_0 and B_1^+ Mapping

The same quadrature setting was to collect a B_0 map (TE = 1.6 ms, TR = 7 ms, FA = 8°), DREAM B_1^+ map on all transmit channels (STEAM flip angle α = 40°, imaging flip angle β = 7°, TR = 5.4 ms, TE_{STE} = 3.8 ms, FE_{FID} = 4.21 ms, scan duration = 3.8 s) and single channel gradient echo images (flip angle α = 1°, TR = 8 ms, TE = 6.7 ms, scan duration = 22.4 ms). These scans were all acquired with the voxel resolutions of 5 x 5 x 5 mm^3 and matrix dimensions 80 x 80. B_0 shimming was implemented with Philips volume B_0 shimming; for the renal angiography the volume of interest was selected over the posterior of

the subject to ensure a homogenous B_0 in the area encompassing both kidneys. This is demonstrated in Figure 6.17.



(a) B_0 map acquired with default shim parameters before shimming.

(b) B_0 map acquired with Philips volume B_0 shim.

Figure 6.17: In vivo B_0 maps demonstrating application of Philips volume B_0 shimming used for the renal angiography; volume of interest was selected over the posterior of the subject encompassing both kidneys.

Relative B_1^+ maps (see Chapter 4) were calculated for each individual channel using an in-house RF shimming program. An RF shim was calculated for a volume of interest drawn around the right kidney. Phase-only RF shimming was performed to optimise constructive interference and increase the homogeneity of the B_1^+ field in the ROI.

6.4.3.4 B_1^+ Optimisation

Once the desired coronal, oblique geometry was achieved an RF shimmed DREAM B_1^+ map was then acquired in order to measure the actual flip angle that was achieved in the kidney; an example of this is shown in Figure 6.18. The flip angle parameter for the angiography scan was then adjusted so that the actual flip angle was 50°. In the majority of subjects this meant increasing the nominal flip angle to 100° for an actual flip angle of 50° in the kidney.

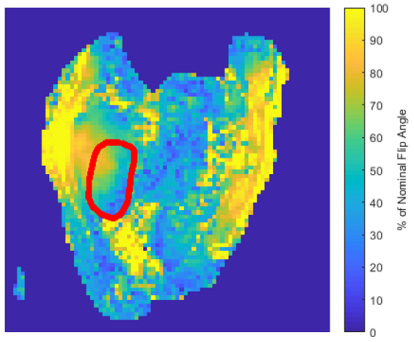


Figure 6.18: In vivo, coronal, oblique, DREAM B_1^+ map; % of nominal flip angle calculated in kidney ROI. Flip angle used in MRA scan adjusted such that the actual flip angle achieved is 50°.

6.4.3.5 Final Imaging Parameters

The final high resolution, multi-echo, TOF MRA scanning parameters were as follows: TR = 31 ms, TE_1 = 5.9 ms, ΔTE = 7.0 ms, number of echoes/TR = 4, field-of-view = 12 (A-P) x 348 (F-H) x 292 (R-L) mm^3, water fat shift = 2.37 pixels, target flip angle = 50°, and in-plane resolution of 0.726 x 0.726 mm^2 with a slice thickness of 2 mm. To achieve the target flip angle in most subjects, the flip angle parameter was set at 100°. This generated RF excitation pulses with a B_1 magnitude of 1.025 μT and duration τ of 1.7 ms on each transmit channel; using an average B_1 excitation across the FoV of 8.200 μT.

Parallel imaging was performed with the sensitivity encoding algorithm (SENSE). A factor of 2.5 was chosen to produce sufficient SNR and allow for satisfactory coverage of the kidney within a breath hold. Flyback gradients with flow compensation were also enabled to ensure all acquired echoes had the same read-out polarity. This prevented fat-shift directions alternating with echo number and minimised phase accumulation errors from moving spins.

Lower resolution angiography data was also acquired with the same scan parameters in each subject, within a single breath-hold, to demonstrate the anatomical detail gained with the high-resolution scanning. In one subject, the SENSE factor was decreased in order to demonstrate the effect of SENSE on the SNR of

the final images. Image acquisition was repeated in another subject in order to assess repeatability. All TOF-MRA scans that were performed in the protocol are outlined in Table 6.2.

Table 6.2: MR Angiography: additional scans

Scan Resolution	Voxel Size [mm^3]	No. of Slices	SENSE Factor	Scan Time [s]
High	0.75 x 0.75 x 2	6	2.5	29
Medium high	1 x 1 x 2	6	2.5	21
Medium	1.5 x 1.5 x 2	6	2.5	14
Medium (more slices)	1.5 x 1.5 x 2	12	2.5	27
Medium (low SENSE)	1.5 x 1.5 x 2	6	2.0	28
Low	2 x 2 x 2	6	2.5	11

6.4.4 Qualitative and Quantitative Image Analysis

MRA images and maximum intensity projections (MIPs) were assessed for physiological content in 3 and 7 T data. SNR and CNR ratios were calculated according to $SNR_{vessel} = \frac{signal_{vessel}}{noise}$ and $CNR = \frac{signal_{vessel} - signal_{surrounding\ tissue}}{noise}$. Noise was defined as the standard deviation of signal in the background and was measured in an extracorpeal ROI (this method was possible as the quadrature body coil (QBC) background mask was disabled).

Both ratios were calculated for the first echo alone and the summed multi-echo image data, and were measured in voxels containing signal from the peripheral renal vessels located at the cortico-medulluary border in each image slice. Surrounding tissue signal, $signal_{surrounding\ tissue}$ for the CNR measurements was obtained from voxels in the medulla. The mean and standard deviation of SNR and CNR values were computed across slices. Mean values were compared at 3 T in a subset of subjects and at 7 T in all subjects. SNR and CNR were also compared in one subject in which two scans were acquired with different SENSE factors. Repeatability of SNR and CNR was investigated in two subjects at 7 T.

6.4.5 Assessment of Vessel Radii

High resolution (0.75 x 0.75 x 2 mm^3) 7 T TOF-MRA data was used to assess the distribution of vessel radii in healthy volunteers. The methods implemented were based on previous work relating to the assessment of vessel radii in the brain between a patient cohort and healthy controls [58]. All analysis was performed in Matlab R2019a and is outlined in Figure 6.19. Summed multi-echo images of the kidney, excluding the main renal artery and vein, were passed through a wavelet denoising algorithm. A spatially adaptive thresholding method was written to overcome the variation in vessel intensities between central and peripheral regions of the kidney and was used to calculate a binary vessel mask for each image slice. Additionally, the spatially adaptive thresholding helped overcome some of the signal variation caused by B_1^+ inhomogeneity which was generally present in the images despite the use of RF shimming.

The spatially adaptive threshold assessed the intensity of each voxel and its neighbouring voxels (within a 5 x 5 x 5 neighbourhood). If the central voxel value was greater than the mean of the neighbourhood, it was classed as a vessel and labelled with a 1. The vessel mask was applied to each image and a MIP was calculated before undergoing a second wavelet denoising stage as shown as part of Figure 6.19. A MIP of the binary vessel masks was used to calculate a 2D Euclidean Distance Transform (EDT) which was multiplied by the voxel resolution (0.75 x 0.75 mm^2) to convert voxel number to millimetres. The binary vessel mask MIP also underwent a skeletonisation process to detect the centre lines of the vessels. The vessel centre lines and EDT were multiplied together to obtain a vessel radius map for each subject.

Vessel radii less than 0.375 mm were eliminated from analysis as these values should not be reliably resolved, however, vessels between 0.375 - 0.75 mm could theoretically be detected due to partial volume effects. Radii less than 0.375 mm were most likely due to inaccurate segmentation of low CNR regions in the cortex tissue around the edge of the kidney.

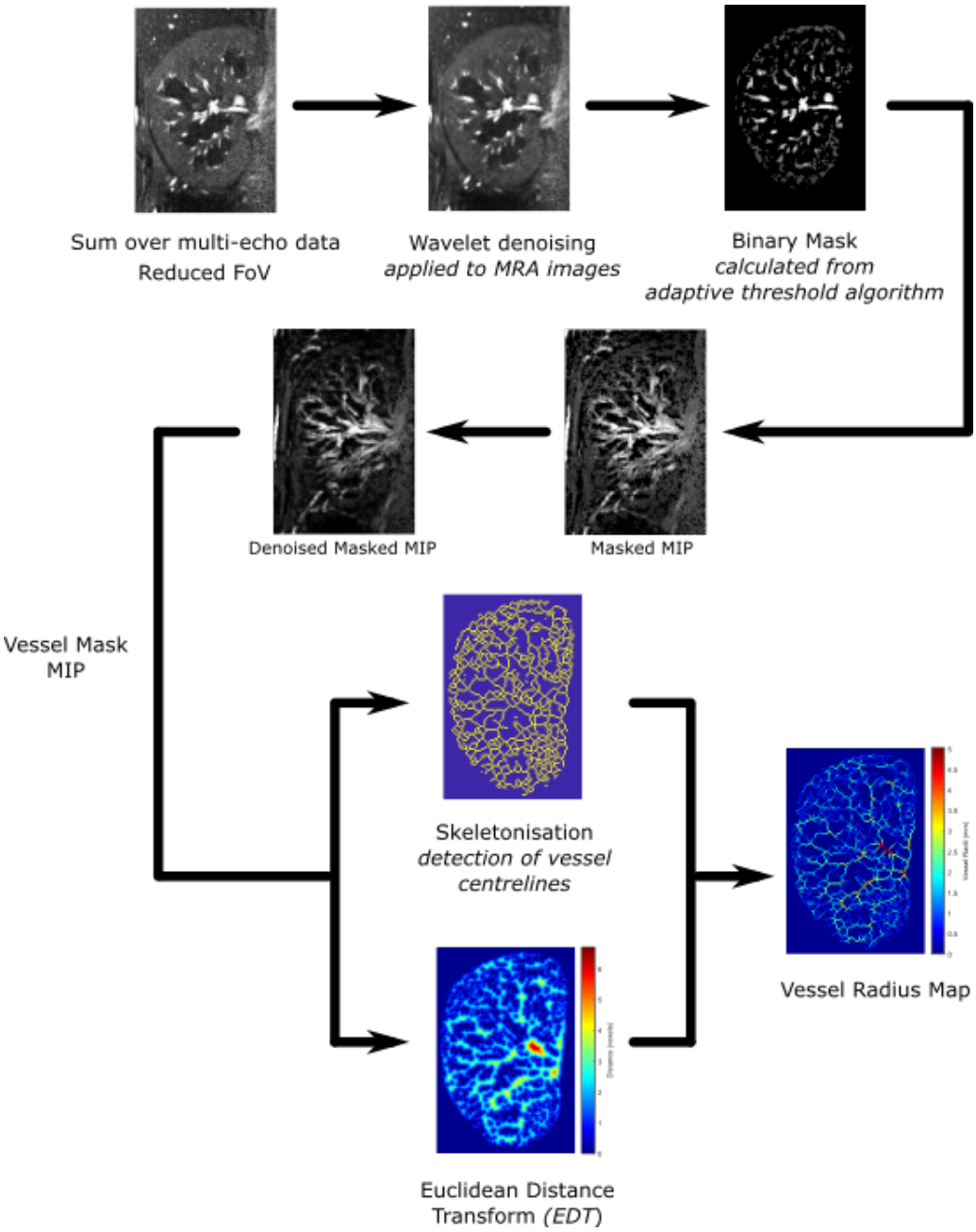


Figure 6.19: Processing pipeline used to assess vessel radii from 2D TOF-MRA data.

The resulting vessel radii were counted and binned into small (0.375 - 1.0 mm), medium (1.0 - 2.0 mm) and large ($>$ 2.0 mm). The counts in each category were divided by the total number of vessel radii values to determine the relative frequency (% of Detected Vessels). The mean and standard deviation of the % of Detected Vessels in each category was determined across all subjects. The same analysis was performed on the 3 T data acquired in a subset of the volunteers.

6.4.6 Liver Angiography

The 2D TOF-MRA protocol with voxel resolution 1.5 x 1.5 x 2 mm^3 was also implemented in a healthy volunteer to collect preliminary liver angiography data and to demonstrate the benefits of multi-echo acquisition for increased vasculature detail. A lower resolution was used in order to cover a larger FOV within a breath hold. For these scans the transceiver array plates were positioned such that the centre line of the coil coincided with the bottom of the ribs to ensure maximum signal generation over the liver region. A phase null RF shim was also used to improve the B_1^+ homogeneity within the field-of-view. The final geometry was transverse through the right superior subsegments of the liver, avoiding the large hepatic artery and portal vein that tend to dominate the image in liver MRA.

Phase contrast angiography (PCA) scans were added to the TOF-MRA sequence with the aim of investigating the potential for monitoring haemodynamic changes to liver tissue at 7 T. Survey images were acquired in 3 orthogonal planes to locate the liver and the main feeding vessels (portal vein (PV) and hepatic artery (HA)). The imaging parameters used are outlined in Table 6.3. PCA on the PV and HA was performed using a single slice TFE technique with the imaging slice placed perpendicular to the vessels. PCA data was analysed using the Philips Q-flow software. ROIs were drawn over the vessels of interest and the mean flux and mean velocity (over the cardiac cycle) were calculated.

Table 6.3: PCA Imaging Parameters

Parameter	Value
Time resolution (ms)	53
TR (ms)	8.8
TE (ms)	4.1
Flip Angle (°)	5
FOV (mm^2)	143 x 280
Acquisition Matrix	188 x 185
Acquired Voxel Size (mm^2)	1.17 x 1.17
Slice thickness (mm)	6
Cardiac Frequency (bpm)	80
Velocity Encoding (cms^{-1})	100
Number of cardiac phases	15
SENSE factor	2.5
Acquisition time (s)	12.4

6.4.7 Lower Abdominal Wall Angiography

The TOF-MRA protocol was adapted for imaging the DIEP vessels in the abdominal wall. This was developed in 7 female healthy volunteers. Placement on the bed was such that the centre line of the coil was aligned with the umbilicus of each subject. The adapted MRA protocol was as follows:

- Initial survey scan.
- Transverse, coronal and sagittal mDixon localiser scans.
- Coronal, free-breathing, 2D TOF-MRA (0.75 x 0.75 x 2 mm^3). This consisted of 40 slices and served as a roadmap for identifying the DIEP vessels.
- Transverse, breath-held, 2D TOF-MRA (0.75 x 0.75 x 2 mm^3). A series of 6 stacks were acquired that each consisted of 6 slices.

RF shimming was not implemented as the default transmit phase setting of the body array was sufficient to produce a homogeneous B_1^+ field close to the anterior transceiver array where the DIEP vessels are located. A 3D multi-planar

reconstruction tool (RadiAnt DICOM Viewer) was used to identify and track the perforating vessels in the transverse image data set. This was then used to display the optimal view of the vessel track through the abdominal wall.

6.5 Results

All examinations were performed successfully and no side effects associated with imaging at 7 T were reported. The average examination time was 45 minutes which included positioning of the subject, B_0 and B_1^+ shimming and acquisition of multiple MRA scans.

6.5.1 Localiser Scans

Figure 6.20 shows coronal, transverse and sagittal images used to plan the B_1^+ calibration scans and coronal oblique geometry for the angiography at 7 T. These images demonstrate the type of destructive interferences that were commonplace during scanning sessions. This is particularly noticeable in the middle of the transverse and sagittal images. The coronal image is taken from a slice nearer the posterior transmit array and so the low signal is not as problematic.

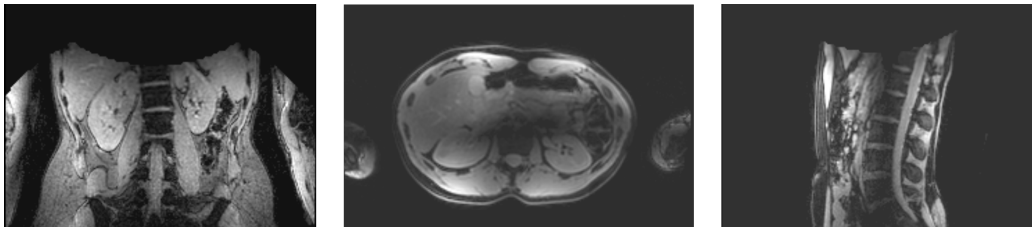
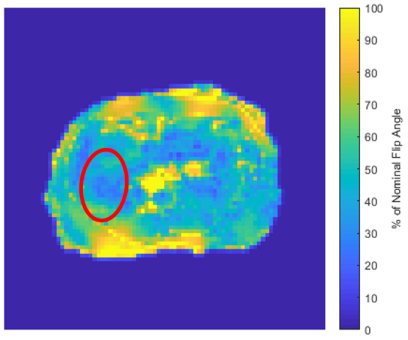


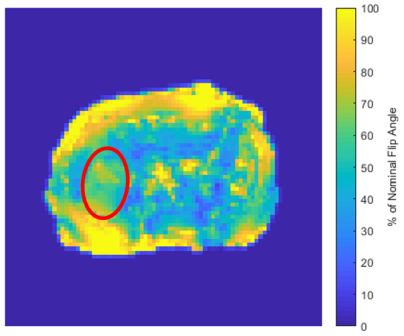
Figure 6.20: Example of 7 T localiser scans.

6.5.2 B_1^+ Optimisation

Figure 6.21 displays DREAM B_1^+ maps before and after phase-only RF shimming was performed and demonstrates an increase of B_1^+ in the right kidney. Figure 6.22 displays pre- and post-RF shim mean B_1^+ values (in % of nominal flip angle) measured within an ROI encompassing the kidney for each individual subject. The figure displays the mean $\pm$ the standard deviation σ.



(a) B_1^+ map acquired with default quad setting.



(b) B_1^+ map acquired after phase-only RF shim.

Figure 6.21: In vivo DREAM B_1^+ maps demonstrating effect of RF shimming; volume of interest was selected over the right kidney.

The group mean result pre-RF shim was 46 $\pm$ 8 % and post-RF shim was 57 $\pm$ 7 %. In each subject implementing the phase-nulling method for RF shimming to the region over the right kidney increased transmit efficiency and the magnitude of the B_1^+ field in this area. Standard deviations increased in each subject after RF shimming reflecting the large heterogeneity of the B_1^+ field within the kidney ROI even after local RF shimming had been applied.

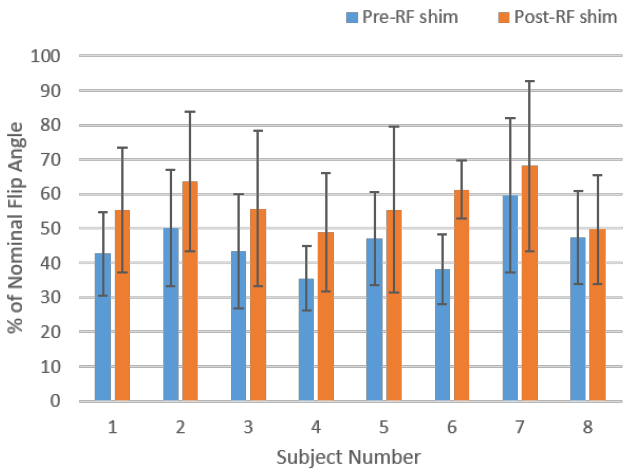


Figure 6.22: Mean B_1^+ measured in kidney ROI before and after phase-null RF shimming is implemented. Error on the mean is $\pm\ \sigma$.

6.5.3 Qualitative image analysis

Different spatial resolutions of the same image slice within a subject are shown in Figure 6.23 demonstrating the advantage of imaging at higher spatial resolution in the kidney. As the spatial resolution is increased from 2 x 2 x 2 mm^3 to 0.75 x 0.75 x 2 mm^3 the vascular detail at the cortico-medullary boundary increases.

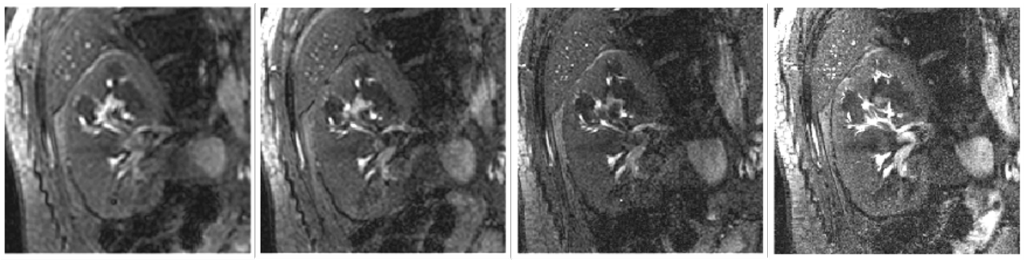


Figure 6.23: Image slice at different resolutions; demonstrates additional vasculature detail gained in high resolution imaging at 7 T. Voxel resolutions left-right: 2 x 2 x 2 mm^3, 1.5 x 1.5 x 2 mm^3, 1 x 1 x 2 mm^3 and 0.75 x 0.75 x 2 mm^3.

Figure 6.24 shows the images acquired at 5.9, 12.9, 19.9, 26.9 ms within a single TR for in one slice. The decrease in signal intensity is characteristic of T_2^* decay with the signal from venous blood decaying faster than the signal from arterial blood [59–61]. Two examples of comparing first echo and summed multi-echo images are shown in Figure 6.25. In both cases there is an increase in SNR and the enhanced detail of smaller vessels in the summed multi-echo data. This confirms the capability for multi-echo acquisition to improve the visualisation of renal vasculature.

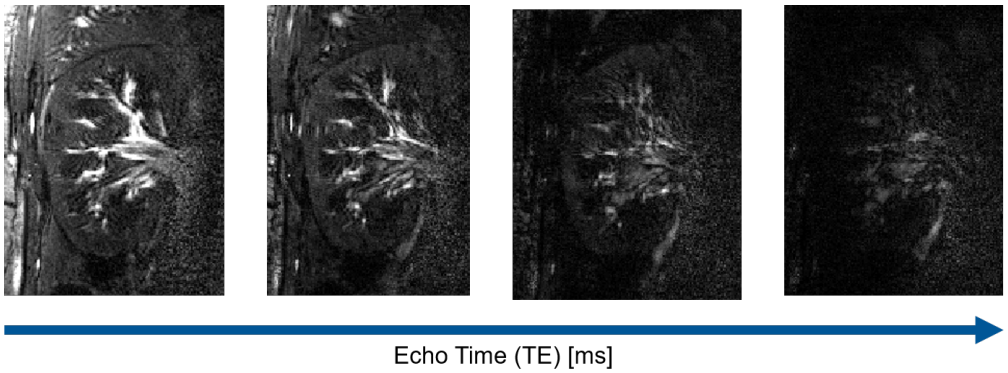
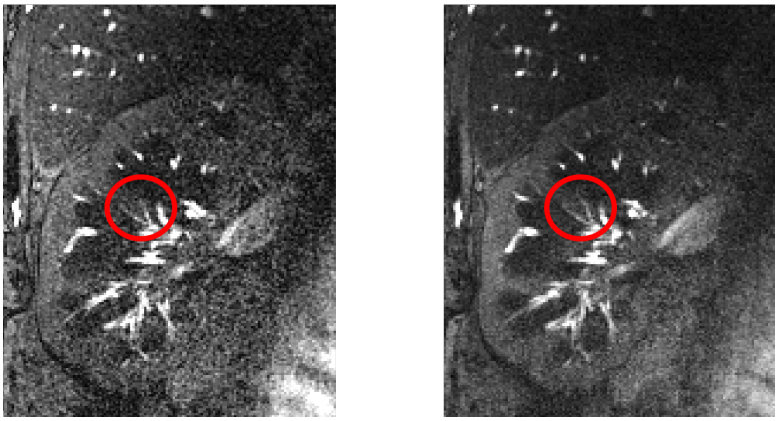


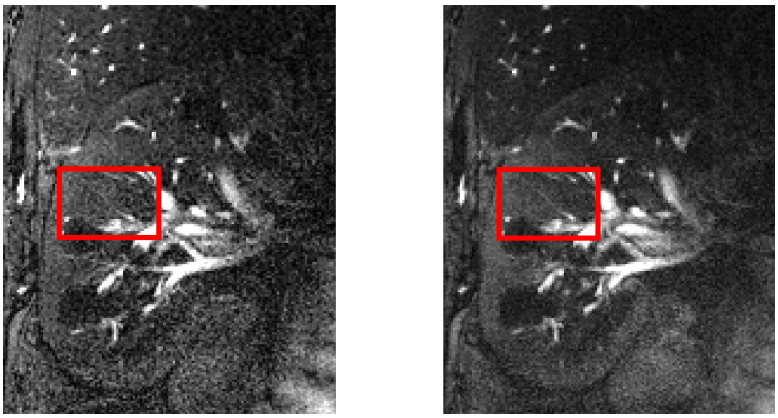
Figure 6.24: Multiple echo images acquired at 5.9, 12.9, 19.9, 26.9 ms in a single slice; decrease in signal intensity is characteristic of T_2^* decay.

MIP's calculated from first echo and summed multi-echo images separately are compared in Figure 6.26. In the multi-echo MIP there is higher SNR in the distal vessels at the cortico-medullary boundary.

An example MIP from another subject is shown in Figure 6.27 where multiple vessels that come from the division of the renal artery and vein are more resolved. The highlighted vessel is an intra-renal artery which is now resolvable due to the contribution of the arterial blood signal in the later echoes. Figure 6.28 presents MIP's calculated from summed multi-echo data in each of the eight subjects.



(a)



(b)

Figure 6.25: Examples from two different image slices comparing first echo [*left*] and summed multi-echo data [*right*].

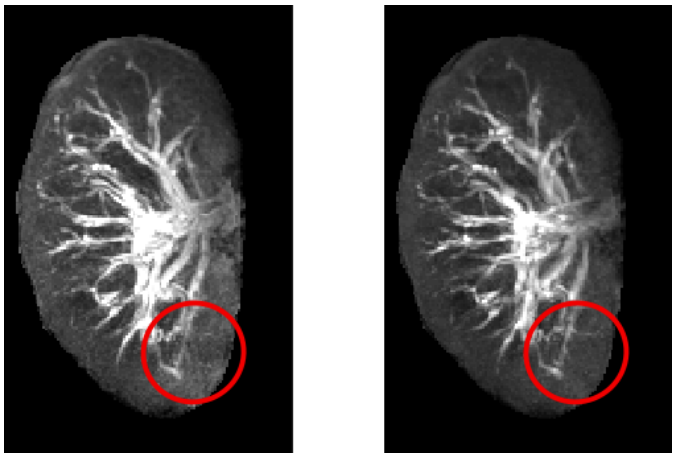


Figure 6.26: Maximum intensity projections from [*left*] first echo MRA images [*right*] summed multi-echo MRA images. Higher SNR in distal vessels of kidney achieved in summed data.

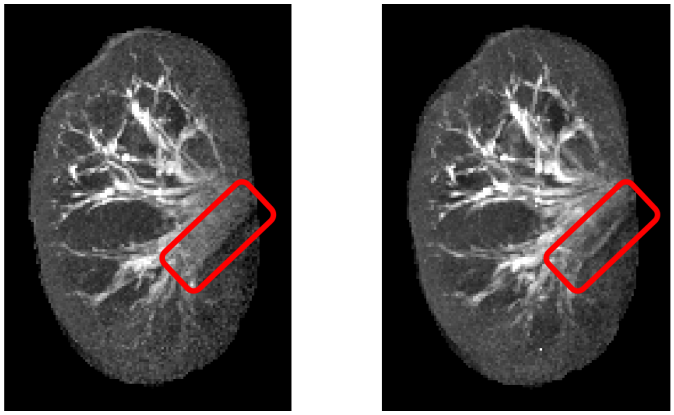


Figure 6.27: Comparison of first echo and summed multi-echo MIPs; red box highlights improved detail in the summed angio.

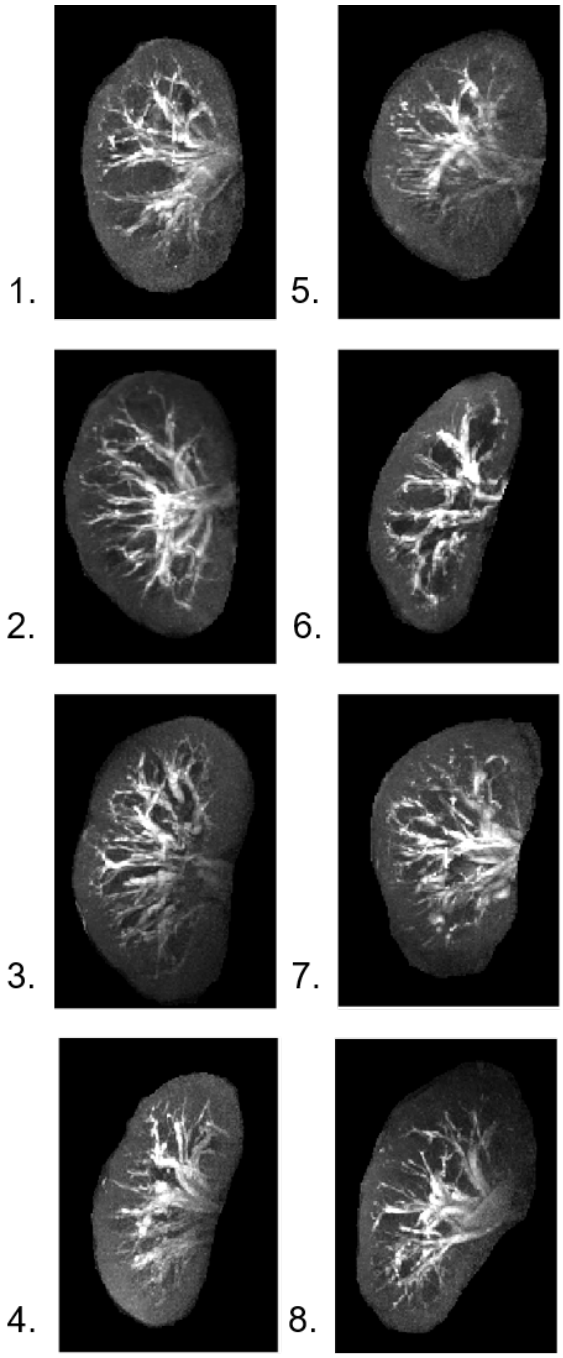


Figure 6.28: Summed multi-echo renal MRA MIPs showing data collected in each of the eight healthy subjects (*subject numbers next to respective MIP*).

6.5.4 Quantitative image analysis

The distance between the posterior of the subject and the centre of the right kidney was measured from the image data from the B_0 maps (see Figure 6.29). The distance for each subject is presented in Table 6.4.

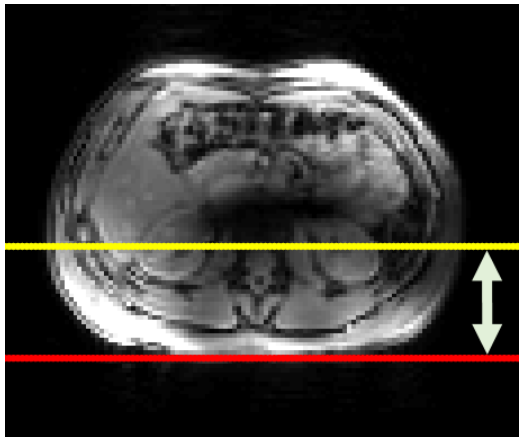


Figure 6.29: Distance from subject posterior to centre of right kidney.

Table 6.4: Results from measuring the distance from posterior of each subject to the centre of the right kidney. Measurements were obtained from images of B_0 map.

Subject	1	2	3	4	5	6	7	8
Distance [cm]	6.9	6.3	6.4	6.6	6.8	7.5	5.9	8.0

The SNR measured in the peripheral renal vessels in subjects that were scanned at both 3 T on the Achieva and Ingenia (which has digital architecture), and the 7 T is presented in Figure 6.30. Consistently at each field strength, the summed multi-echo images demonstrate higher SNR in the vessels. There is a clear increase in SNR between 3 and 7 T data for subjects 1 -3, although Subject 4 shows 7 T SNR values comparable with the 3 T data. There were no relevant factors concerning Subject 4 that might have explained this (for example, large BMI) and so the lower 7 T results are most likely due to poor coil placement over the kidneys during the 7 T scanning session.

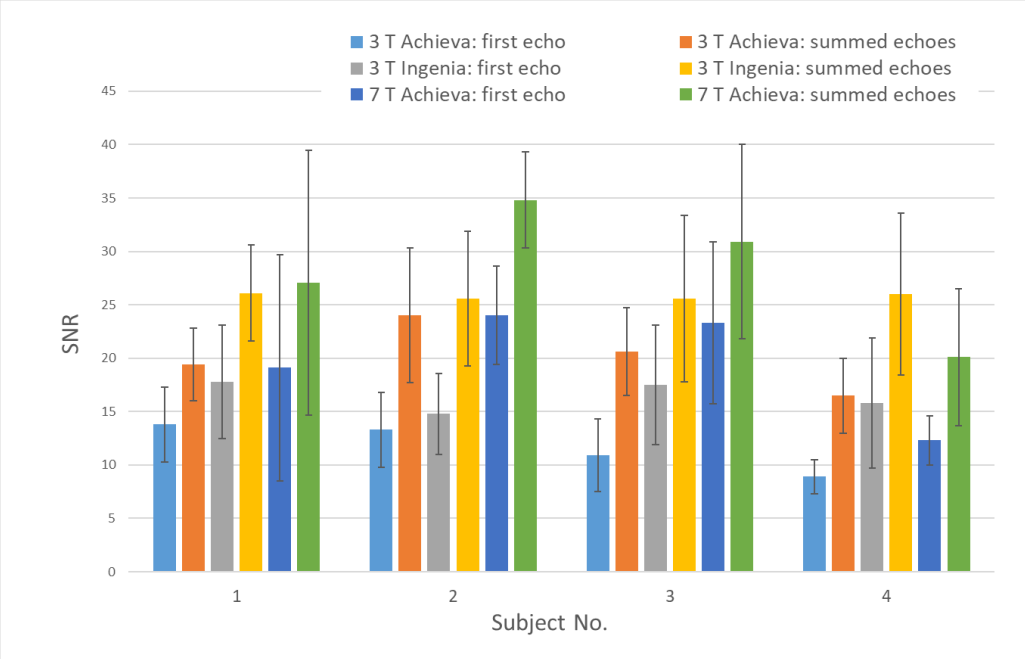


Figure 6.30: SNR measured in peripheral renal vessels in subset of volunteers that were scanned at 3 T and 7 T. First echo only and summed multi-echo image data are compared.

These measures were repeated in the remainder of the subjects at 7 T and results are presented in Figure 6.31. The increase in vessel SNR in the summed multi-echo data is observed across all subjects. Subjects 4 and 5 have noticeably lower SNR than the rest of the subjects and this is reflected in the final MIPs displayed in Figure 6.28. Again, this could be due to sub-optimal placement of the body array within these specific scanning sessions.

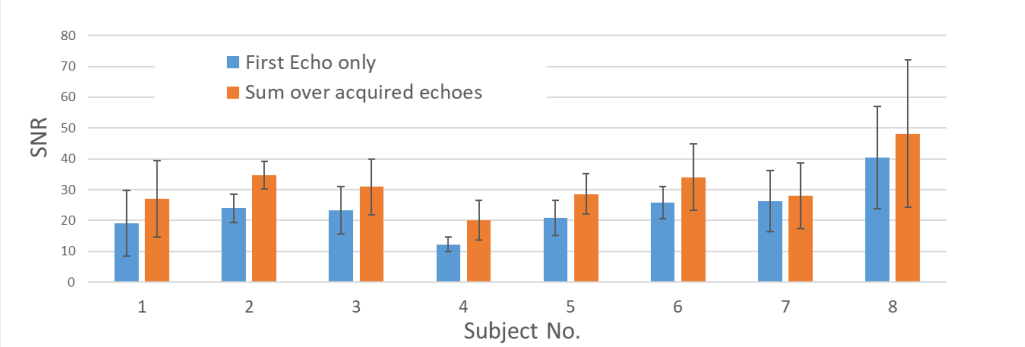


Figure 6.31: SNR measured in peripheral renal vessels in each subject. First echo only and summed multi-echo image data are compared.

Table 6.5 presents additional SNR results. SNR measures were compared between two datasets acquired with different SENSE factors (2 versus 2.5) on subject 4. SNR was higher in the images acquired with the lower SENSE factor as expected. The repeatability of SNR measures in subjects 3 and 6 showed consistent gain of SNR in summed multi-echo images within the same scanning session.

Table 6.5: Results demonstrating effect of reducing SENSE factor and repeatability on SNR.

Subject	**Scan**	**SNR** (1^{st} Echo)	**SNR** (All Echoes)
4	SENSE 2.5	14.0 ± 4.3	22.4 ± 4.8
	SENSE 2.0	19.3 ± 2.3	28.8 ± 9.5
3	Repeat 1	23.3 ± 7.6	30.9 ± 9.1
	Repeat 2	24.4 ± 10.5	36.0 ± 10.8
6	Repeat	25.8 ± 5.2	34.1 ± 10.7
	Repeat 2	29.6 ± 5.5	32.7 ± 7.1

The CNR was measured in peripheral renal vessels against the background tissue in subjects scanned at 3 and 7 T, and results are presented in Figure 6.32. CNR is highest in the 7 T summed multi-echo image data for each subject. In subjects 1 and 4 the 7 T CNR is not significantly higher than that obtained at 3 T. CNR was then calculated for all subjects scanned at 7 T and are presented in Figure 6.33. CNR is higher in the summed multi-echo images across all subjects. Subject 7 shows no significant increase in CNR between first echo and summed echo images, however, the quality of the MIP displayed in Figure 6.28 does not appear to be affected.

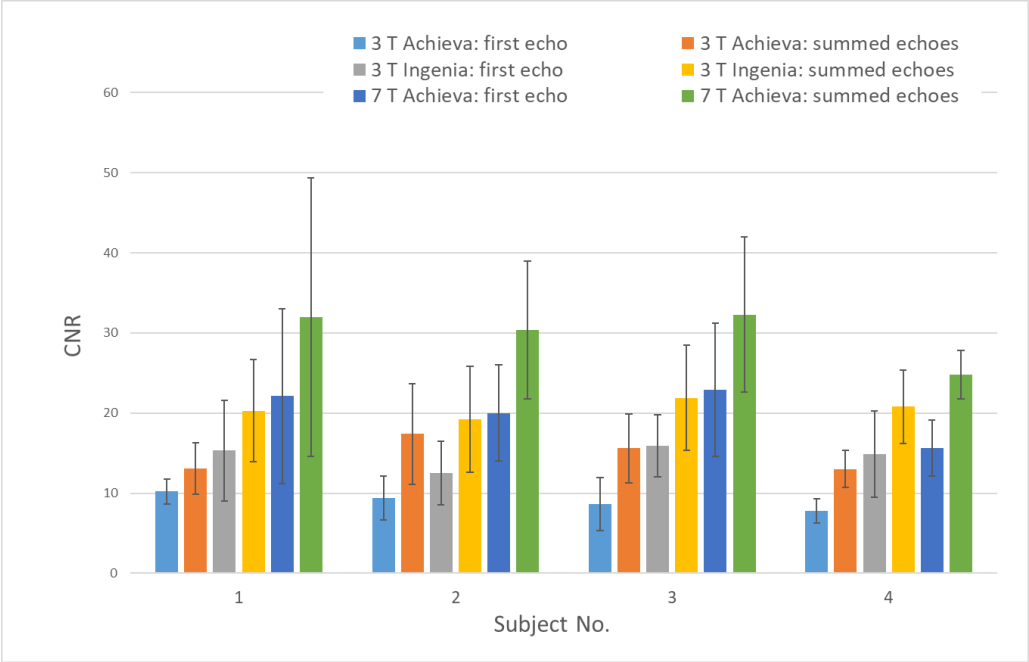


Figure 6.32: CNR in subset of volunteers scanned at 3 and 7 T. First echo only and summed multi-echo image data are compared.

Table 6.6 outlines results for the additional SENSE and repeatability scans. The CNR increased in both first echo and summed multi-echo images in the dataset acquired with a lower SENSE factor. The repeatability of the CNR measures in subjects 3 and 6 showed consistent increases in CNR values of the summed multi-echo images.

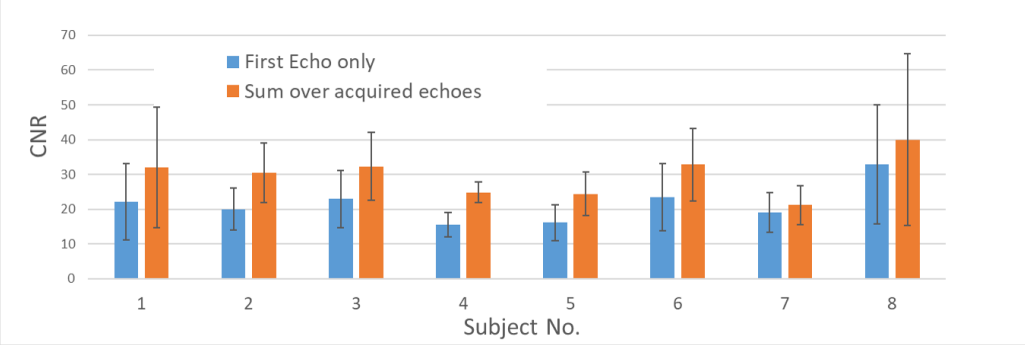


Figure 6.33: CNR measured in peripheral renal vessels in each subject. First echo only and summed multi-echo image data are compared.

Table 6.6: Results demonstrating effect of reducing SENSE factor and repeatability on CNR.

Subject	**Scan**	**CNR** (1^{st} Echo)	**CNR** (All Echoes)
4	SENSE 2.5	20.9 ± 4.4	31.4 ± 5.5
	SENSE 2.0	25.2 ± 6.8	40.8 ± 7.4
3	Repeat 1	22.9 ± 8.3	32.3 ± 9.7
	Repeat 2	22.3 ± 11.8	32.1 ± 15.6
6	Repeat 1	23.5 ± 9.7	32.8 ± 10.4
	Repeat 2	16.4 ± 8.8	20.7 ± 10.1

No correlation was found between the posterior to kidney distances (presented in Table 6.4) and the outlying SNR and CNR results across the subjects. The average % increase in SNR and CNR values between the multi-echo data compared to first echo data calculated across all subjects scanned at 7 T was 7 % for both measures.

6.5.5 Assessment of Vessel Radii

A vessel radii map overlaid onto the underlying renal anatomy is shown in Figure 6.34. The vessel radii are estimated across the vessel centrelines in millimetres.

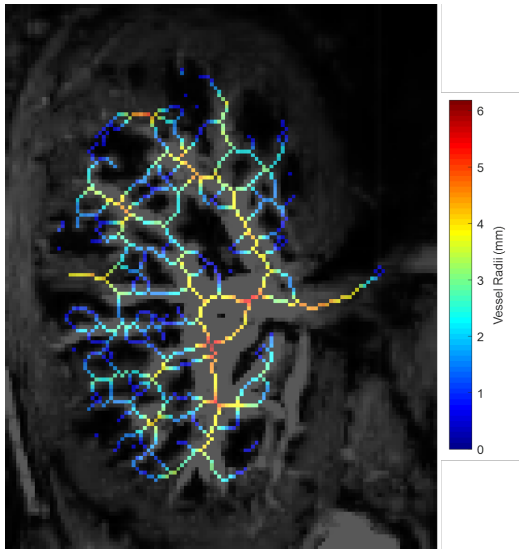
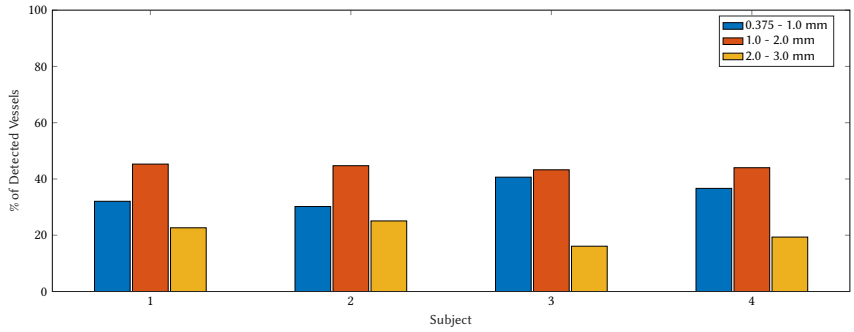
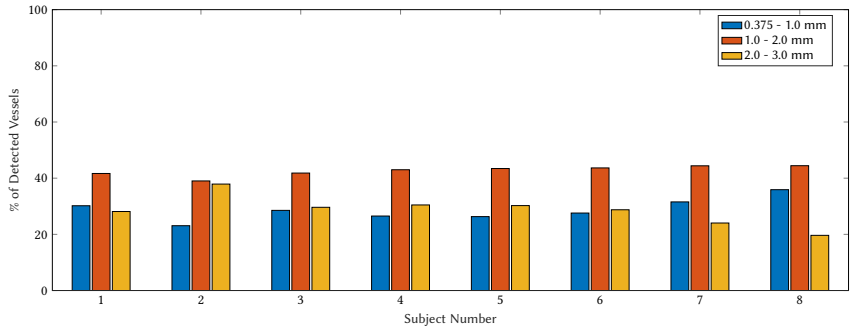


Figure 6.34: Vessel radii map following EDT and skeletonisation of renal vessel mask.

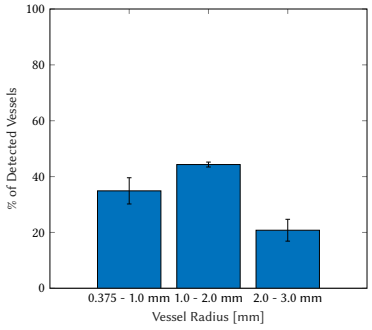
The vessel radii frequencies were calculated from 3 and 7 T angiograms corresponding to the categories of vessel thickness outlined in the methods section for each subject and are presented in Figures 6.35 (a) and (b) respectively. The highest fraction of vessels detected had medium radii (1 - 2 mm) in each subject. Large radii (2 - 3 mm) had lower counts in every subject, which is expected as analysis excluded the main renal artery entering and renal vein draining the kidney. The average frequency of vessel radii across all subjects is shown in Figures 6.35 (c) and (d) for the 3 and 7 T data respectively. The average radii results were similar between the two field strengths, and the standard deviation of the vessel radii in each category was larger for the 7 T data.



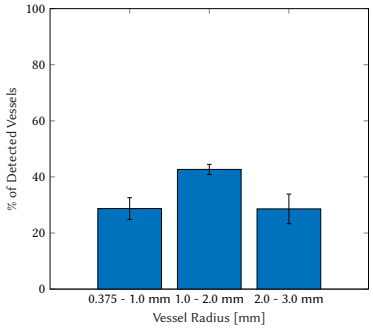
(a) 3 T results



(b) 7 T results



(c) 3 T results



(d) 7 T results

Figure 6.35: Frequency of vessel radii for small, medium and large vessel categories. Counts shown for each subject separately at (a) 3 T and (b) 7 T. Average frequency across all relevant subjects of different vessel radii at (c) 3 T and (d) 7 T.

6.5.6 Liver Angiography

Figure 6.36 shows multi-echo data acquired in one image slice and demonstrates the expected T_2^* decay in the liver. Cardiac, respiratory and SENSE induced artefacts are severe in this geometry highlighting the need for further development of the TOF-MRA protocol for application to the liver.

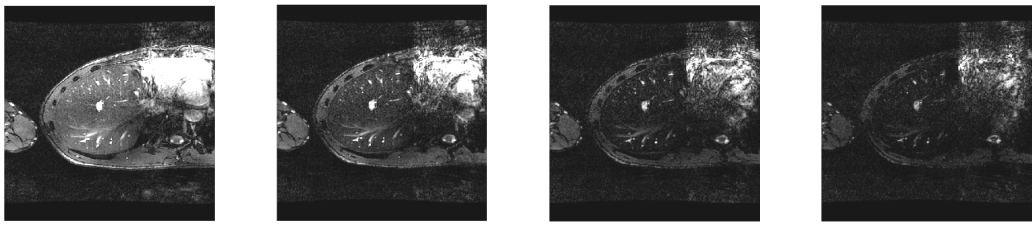
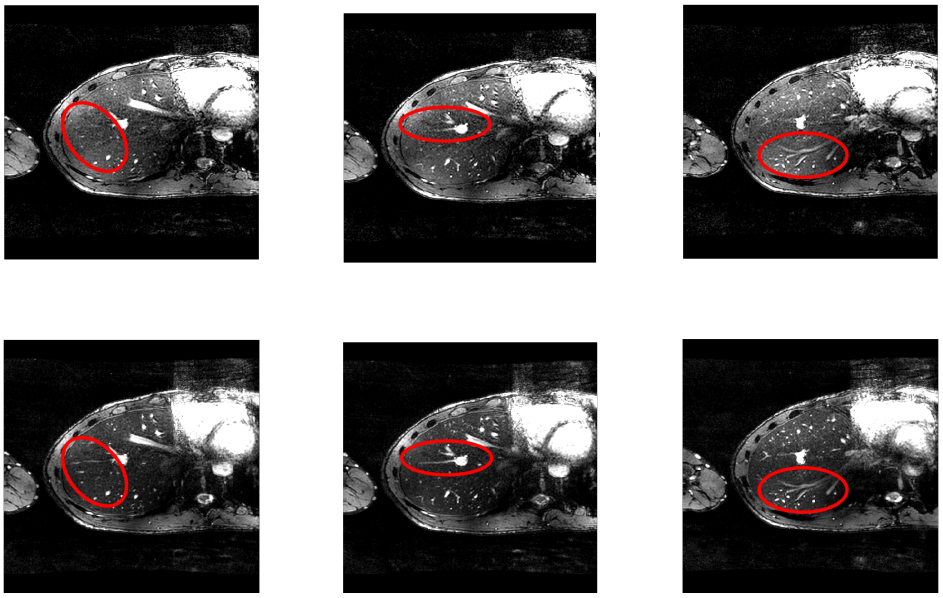


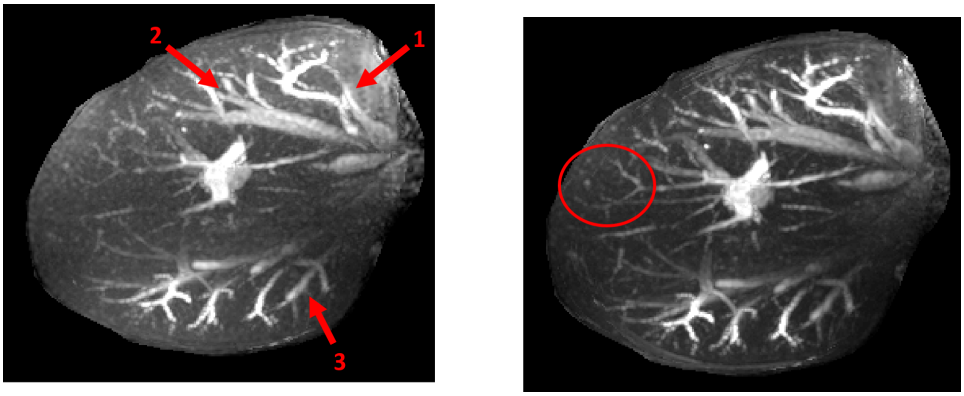
Figure 6.36: Liver multi-echo images.

The first echo only and summed multi-echo images are displayed in Figure 6.37 for comparison. The increase in SNR for the multi-echo images is apparent in each case. Detail of the branching vessels originating from the portal vein and hepatic arteries which lead to the peripheral microvasculature are enhanced. This translates through to the MIP's computed from first echo and summed multi-echo images separately (see Figure 6.38). Hepatic vasculature including the left hepatic artery, the portal vein and the right hepatic artery are identified in the first echo image. In the summed multi-echo image there is an overall increase in image contrast and an area of superior visualisation of peripheral branching vessels is highlighted.



(a) (b) (c)

Figure 6.37: Liver first echo [*top*] and summed multi-echo [*bottom*] images.



(a) (b)

Figure 6.38: (a) First echo and (b) summed multi-echo MIP's in the liver. The red circle highlights an area of better visualisation of branching vessels. Arrows identify territories of hepatic vasculature from (1) the left hepatic artery, (2) the portal vein and (3) the right hepatic artery.

Figure 6.39 shows an example of sagittal survey images acquired for PCA showing the portal vein and hepatic artery in the same imaging slice. Examples of the magnitude and phase images (for cardiac cycles 1 and 15) are shown in Figure 6.40. The mean flux for the PV was 13.65 mls^{-1} and 5.52 mls^{-1} for the HA and Figure 6.41 shows a graph of mean velocity versus trigger delay time for the PV and HA.

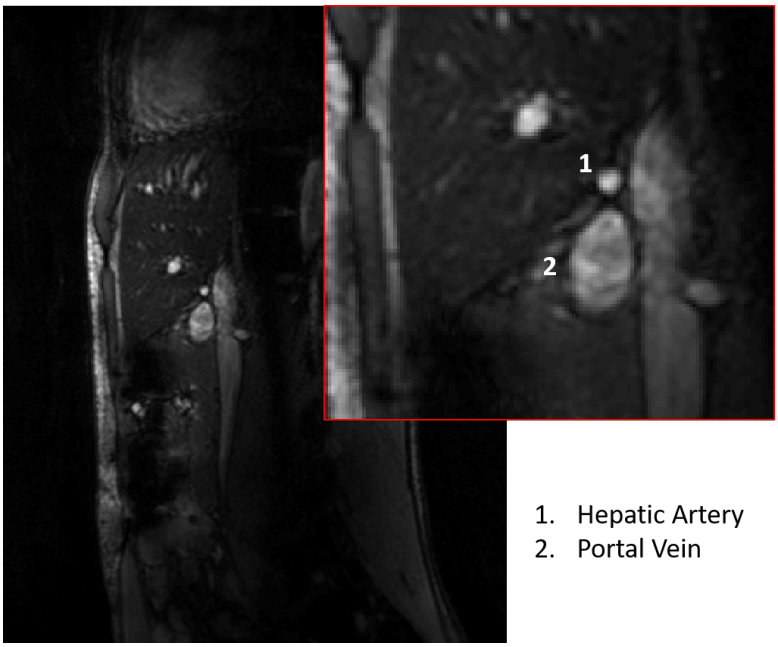


Figure 6.39: TOF-MRA survey image for planning PCA: sagittal orientation shows clear delineation of the (1) hepatic artery above the (2) portal vein.

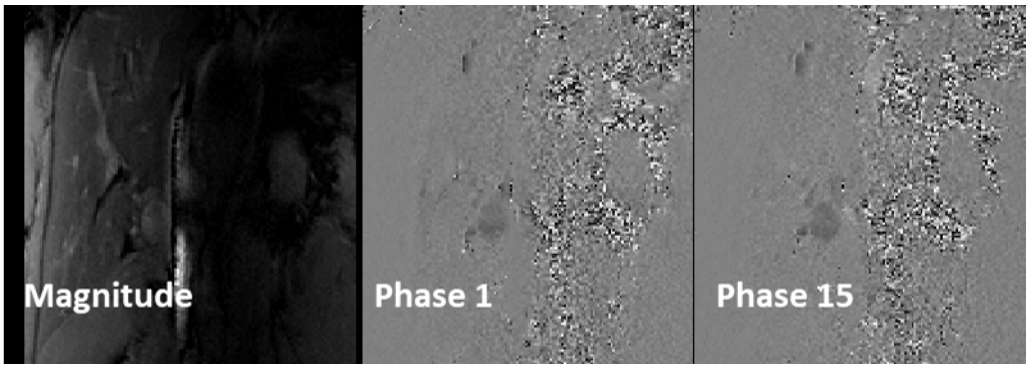


Figure 6.40: Visualisation of liver blood flow through the portal vein and hepatic artery; source magnitude and velocity images (sagittal plane) are shown at different time points in the cardiac phase.

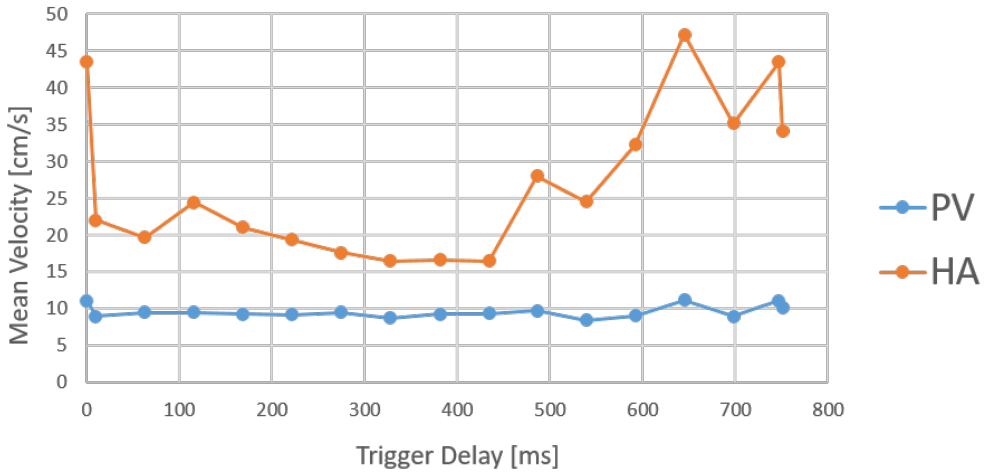
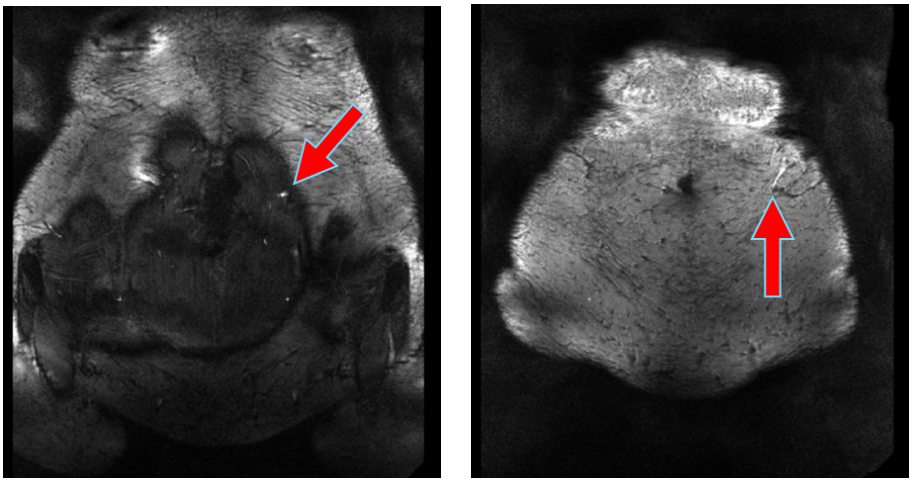


Figure 6.41: QFlow analysis of mean velocity versus trigger delay time in portal vein and hepatic artery ROIs.

6.5.7 Lower Abdominal Wall Angiography

Figure 6.42 (a) shows an example of a 2D TOF-MRA perforator vessel detected through the rectus abdominis muscle, which when followed through the image slices (posterior to anterior) forms a branching point for the widely separated vessel branches of the SIEA, this is shown in Figure 6.42 (b).



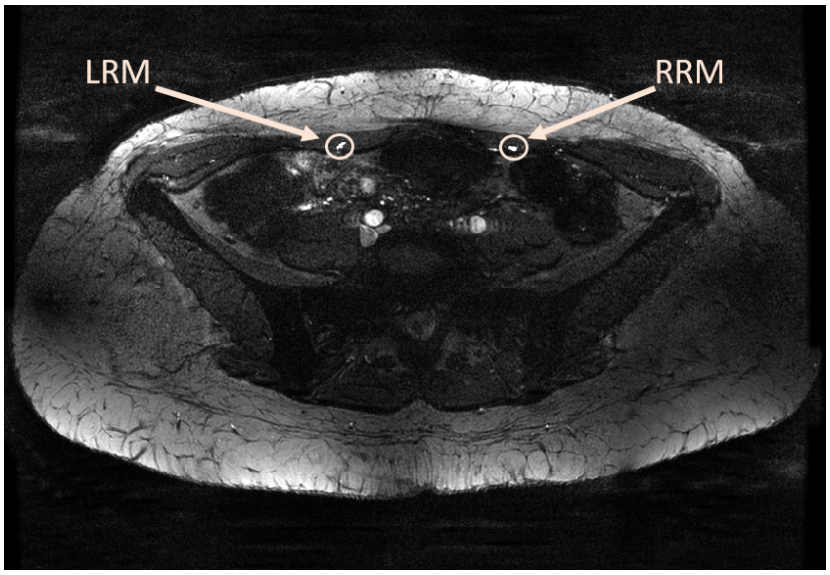
(a) (b)

Figure 6.42: Coronal 2D TOF-MRA roadmap for localising DIEP vessels.

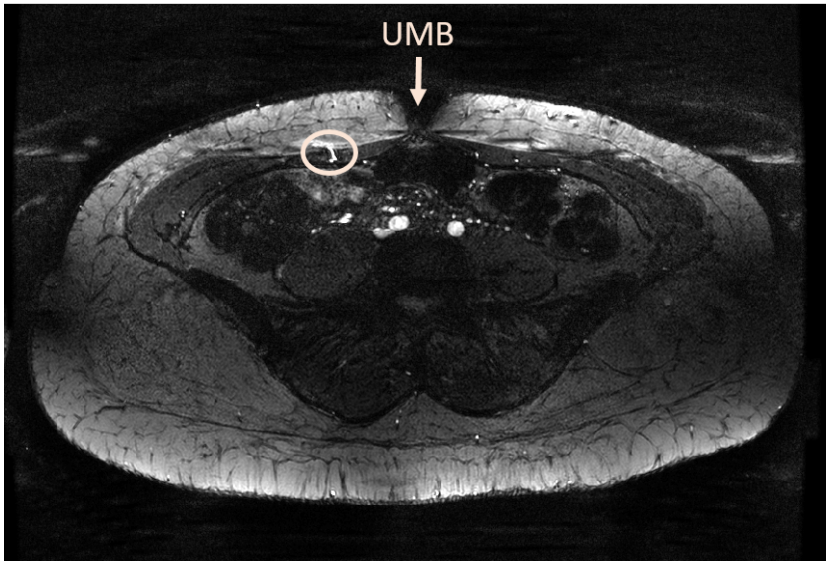
A transverse 2D TOF-MRA image is shown in Figure 6.43 (a), where the arrows point to the right and left rectus abdominis muscles and the circles highlight the right and left DIEA. Figure 6.43 (b) shows an image slice from the same dataset through the umbilicus (UMB) and highlights a DIEP vessel coming up through the right rectus muscle and penetrating the subcutaneous tissue.

An example of the views generated with the 3D multi-planar reconstruction tool using the coronal MRA data is displayed in Figure 6.44. The images show how the perforator in the coronal image could be projected into the sagittal, transverse and oblique planes. A perforator is this data set can be seen at the fascial layer that lies between the rectus muscle and subcutaneous tissue.

Figure 6.45 shows clinical contrast-enhanced (CE) 1.5 T angiograms that were received from a collaborating radiologist. These images were used for informing a pre-operative DIEP surgery plan. The 7 T images are higher resolution and the contrast between the perforating vessel and background tissue is greater aiding the delineation of the abdominal vessels compared to the CE 1.5 T data. This is a demonstration of how lower field contrast enhanced scans can benefit from the increase in intrinsic contrast at 7 T.

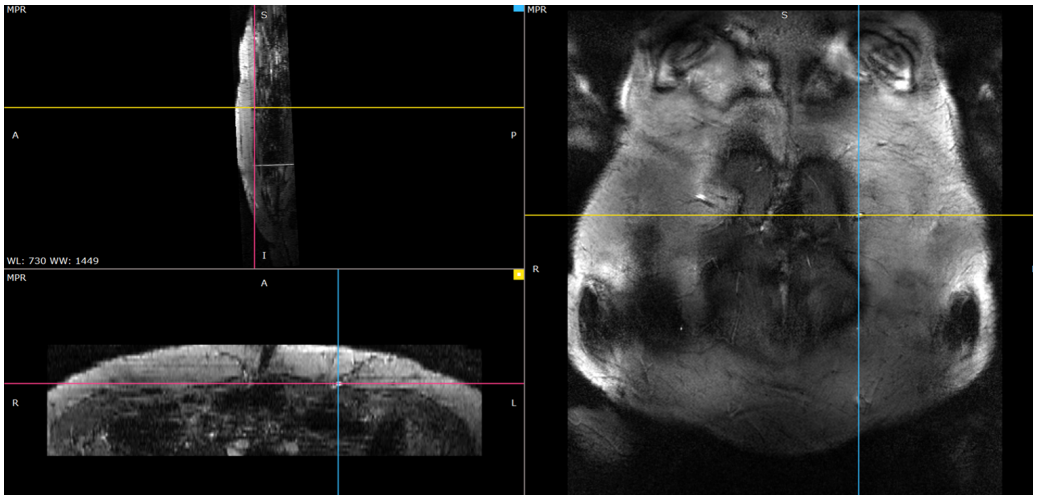


(a)

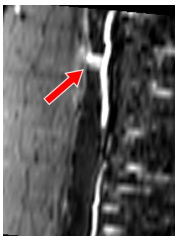


(b)

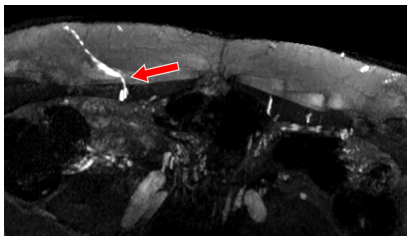
Figure 6.43: Transverse 2D TOF MRA images demonstrating (a) the right (RRM) and left (LRM) rectus muscles [*arrows*] and the right and left deep inferior epigastric arteries located deep in the rectus abdominus [*circles*] (b) the umbilicus (UMB) [*arrow*] and a perforating branch artery [*circle*].



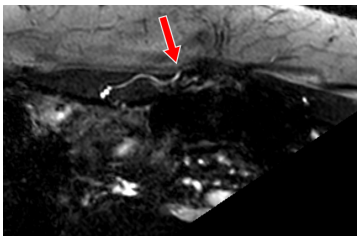
(a)



(b)



(c)



(d)

Figure 6.44: 3D multi-planar reconstruction of coronal TOF-MRA data. Demonstrates projection of perforating vessels in the different image planes.

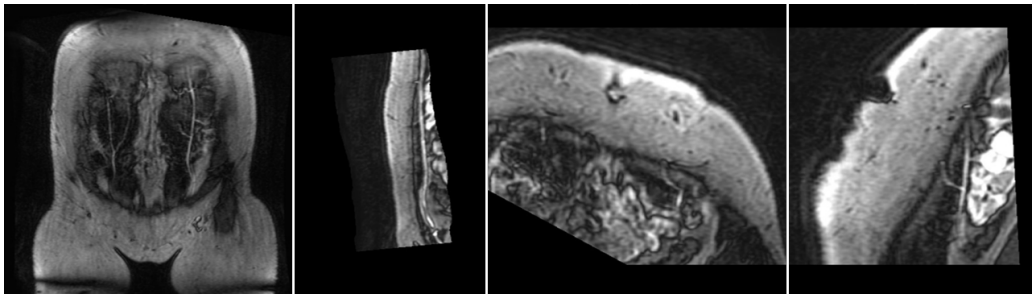


Figure 6.45: Clinical 1.5 T DIEP images

6.6 Discussion

Renal Angiography

Multi-echo 2D TOF-MRA images acquired at 7 T showed higher SNR and CNR compared to images acquired at 3 T, excellent differentiation of anatomical structures and more detailed renal vasculature without the need for contrast enhancement. However, image quality is compromised in some subjects due to the severe B_1^+ inhomogeneity at UHF and limited RF power available.

With phase-only RF shimming it was possible to increase the B_1^+ achieved within the kidney, however the excitation across the field of view was still highly variable which is reflected in the large standard deviations in Figure 6.18. Alternative RF shimming optimisation algorithms might resolve this issue. In the quantitative results where SNR and CNR were measured, the low SNR of Subjects 4 and 5 highlights the subject-dependent nature of body imaging at 7 T. Subject body composition and size has some influence on the ability to achieve the target flip angles due to power limitations and subject position, and transmit coil placement need to be carefully arranged in order to ensure successful imaging. If any of these factors are amiss then results can be sub-optimal. Methods to avoid this might include placing fiducial markers inside the coil so that they can be checked during initial survey scans, or referring to someone who is clinically trained in anatomy when placing the coil on subjects before scanning takes place, and should be employed in future studies to ensure consistent results.

Analysis of vessel radii across all subjects scanned at 3 and 7 T demonstrated that vessels with a radii of 1 - 2 mm were of the highest frequency, which is in line with renal vessel measurements found in the literature [62, 63]. Variable SNR and CNR across the FOV meant that a thresh-hold based segmentation of the vessels was not trivial. Smoothing the images with the wavelet denoising algorithm was necessary, however, this obscured the increased vascular detail within the 7 T images and limited the effective resolution. This reduced the potential for detecting more microvasculature in the 7 T images when compared

to the 3 T images. The contrast in the renal cortex between the bright blood vessels and background tissue was not as good as the contrast in the renal medulla tissue which reduced the sensitivity of the developed algorithm to the small vessels in the cortical tissue in images from both field strengths. The increased standard deviation of the % of detected vessels in each radii category in the 7 T data reflects these difficulties in the analysis and the variation of radii frequencies across the subjects.

Liver Angiography

TOF-MRA is known to be difficult in liver due to tortuous nature of vascular network. However, vessels in the proximal branching arteries can theoretically be assessed [64]. Therefore, despite using a lower resolution TOF-MRA scan to image the liver, the detail of vasculature achieved in both the summed multi-echo images and MIP's allows visualisation of the portal vein and right and left HA all the way to the periphery of the liver.

Liver angiography at 7 T requires further development in healthy volunteers, particularly in optimising the geometry for imaging the liver in order to reduce SENSE artefacts and respiratory and cardiac motion. However, 7 T liver MRA shows potential for improved visualisation of the branching in the liver and the smaller peripheral vessels with the high resolution TOF-MRA scan.

The PCA results show that measures of haemodynamic flow are possible in the liver at 7 T in both the PV and HA. The mean flux and velocity values were lower than is reported elsewhere in the literature [65] suggesting that further optimisation of the PCA parameters is required to accurately reflect the flow characteristics. It is hard to resolve the HA at 3 T and so using 7 T could be a real advantage for assessing hepatic haemodynamic changes which are relevant in clinical questions surrounding patients with chronic liver disease.

Lower Abdominal Wall Angiography

Applying the 2D TOF-MRA protocol to the lower abdominal wall to image the DIEP vessels was successful in regard to visualisation of the perforator vessels from below the rectus abdominis muscles to the subcutaneous fat layer. Images obtained in healthy volunteers were used to identify the perforator vessels which are essential landmarks included in pre-operative reports produced for planning DIEP surgery.

After discussion with a consultant radiologist, it was acknowledged that the 7 T images gave no additional anatomical or vascular detail compared to DIEP images obtained at 1.5 T, however, the 1.5 T DIEP images require contrast enhancement. Therefore, performing this protocol at 7 T removes the need for gadolinium based contrast agent administration. This is an example of the benefit of imaging patients with poor renal function at 7 T where administration of Gd is not advised, but the patients still require a diagnostic scan that will benefit them. Another benefit of 7 T is its potential to offer more information regarding arterial and venous vasculature (due to the different T_2^* values associated with oxygenated and deoxygenated blood) within the abdomen which would give extra knowledge about the perforator and how viable it is for dissection in surgery.

RF shimming was essential for the renal and liver angiography, whilst the DIEP angiography did not benefit significantly from RF shimming as the ROI is near the surface transmit coil. The 45$\circ$ quadrature coil phase setting was sufficient for imaging near the anterior elements of the body array. This implies that complications and drawbacks associated with long calibration times associated with 7 T body imaging for B_1^+ mapping and RF shimming would not be a problem in this case. Therefore, this approach has potential as a quick, robust, non-CE method for pre-operative DIEP surgery planning. Future work should include evaluation against non-contrast 3 T angiography and producing quantitative measurements of the location of the vessels in the abdomen.

Future Directions

It is recognised that B_1^+ inhomogeneity needs to be better addressed. This might include replacing current RF shimming algorithms with different figures of merit and employing more sophisticated concepts such as 3D tailored RF pulses (see Chapter 3). These methods have been shown to decrease flip angle heterogeneity and improve contrast achieved with TOF-MRA on a 7 T pTx system in the brain periphery [66] however, these approaches might be more unstable when applied to the body. Moreover, other dynamic pTx applications could be applied to avoid exciting the in-flowing arteries.

Applying the developed angiography protocol to patient groups discussed throughout this chapter will be integral to demonstrating the full potential for 7 T body MRA. This includes increased information relating to the delineation of small microvasculature features and exploiting contrast mechanisms that could add details about venous integrity.

6.7 Conclusion

The work in this chapter has covered the development of a high resolution, multi-echo 2D TOF-MRA protocol for imaging small vessels in the abdomen at 7 T. It has been demonstrated that it is possible to achieve superior renal vasculature information at 7 T compared with 3 T data and that clinically useful applications in the liver and lower abdominal wall are also feasible.

References

[1] Emma Doran, Stephen Bawden, Christopher Mirfin, Paul Glover, Richard Bowtell, Penny Gowland, and Susan Francis. A comparison of 7 and 3 Tesla time-of-flight renal MR angiography for detection of intrarenal vessels. *Proceedings of the International Society for Magnetic Resonance in Medicine*, 26(4602):4602, 2018.

[2] David Saloner. An Introduction to MR Angiography. *RadioGraphics*, (15):453–465, 1993.

[3] VJ Wedeen, RA Meuli, RR Edelman, SC Geller, LR Frank, TJ Brady, and BR Rosen. Projective Imaging of Pulsatile Flow with Magnetic Resonance. *Science*, 230(4728):946–948, 1983.

[4] W J Manning, W Li, and R Edelman. A Preliminary Report Comparing Magnetic Resonance Coronary Angiography with Conventional Angiography. *The New England Journal of Medicine*, 328(12):828–832, 1993.

[5] Frank R. Korosec, Richard Frayne, Thomas M. Grist, and Charles A. Mistretta. Time-resolved contrast-enhanced 3D MR angiography. *Magnetic Resonance in Medicine*, 36(3):345–351, 1996.

[6] M. Markl, S. Schnell, C. Wu, E. Bollache, K. Jarvis, A. J. Barker, J. D. Robinson, and C. K. Rigsby. Advanced flow MRI: emerging techniques and applications. *Clinical Radiology*, 71(8):779–795, 2016.

[7] Joshua D. Trzasko, Clifton R. Haider, Eric A. Borisch, Norbert G. Campeau, James F. Glockner, Stephen J. Riederer, and Armando Manduca. Sparse-CAPR: Highly accelerated 4D CE-MRA with parallel imaging and nonconvex compressive sensing. *Magnetic Resonance in Medicine*, 66(4):1019–1032, 2011.

[8] Hale Ersoy, HongLei Zhang, and Martin Prince. Peripheral MR Angiography. *Journal of Cardiovascular Magnetic Resonance*, 8(3):517–528, 2006.

[9] Ingitha Borisch, Markus Horn, Bernhard Butz, Niels Zorger, Bogdan Draganski, Thilo Hoelscher, Ulrich Bogdahn, and Johann Link. Preoperative Evaluation of Carotid Artery Stenosis: Comparison of Contrast-Enhanced MR Angiography and Duplex Sonography with Digital Subtraction Angiography. Technical report.

[10] Cornelius Von Morze, Duan Xu, Derk D. Purcell, Christopher P. Hess, Pratik Mukherjee, David Saloner, Douglas A.C. Kelley, and Daniel B. Vigneron. Intracranial time-of-flight MR angiography at 7T with comparison to 3T. *Journal of Magnetic Resonance Imaging*, 26(4):900–904, 2007.

[11] CN Ludman, P Morgan, A Peters, L Jiang, M Clemence, and PA Gowland. Contrast Enhanced MR angiography at 7 Tesla: Challenging the limits of spatial resolution. *In Proc. ISMRM (Seattle, Washington, USA)*, 2006.

[12] Francesco Padormo, Arian Beqiri, Joseph V. Hajnal, and Shaihan J. Malik. Parallel transmission for ultrahigh-field imaging. *NMR in Biomedicine*, 2015.

[13] Stephan Orzada, Andreas K. Bitz, Sören Johst, Marcel Gratz, Maximilian N. Völker, Oliver Kraff, Ashraf Abuelhaija, Thomas M. Fiedler, Klaus Solbach, Harald H. Quick, and Mark E. Ladd. Analysis of an Integrated 8-Channel Tx/Rx Body Array for Use as a Body Coil in 7-Tesla MRI. *Frontiers in Physics*, 5:17, 2017.

[14] Rotem Shlomo Lanzman, Patric Kröpil, Peter Schmitt, Sonja Marie Freitag, Adrian Ringelstein, Hans Jörg Wittsack, and Dirk Blondin. Nonenhanced free-breathing ECG-gated steady-state free precession 3D MR angiography of the renal arteries: Comparison between 1.5 T and 3 T. *American Journal of Roentgenology*, 194(3):794–798, 2010.

[15] L. Umutlu, S. Maderwald, S. Kinner, O. Kraff, A. K. Bitz, S. Orzada, S. Johst, K. Wrede, M. Forsting, M. E. Ladd, T. C. Lauenstein, and H. H. Quick. First-pass contrast-enhanced renal MRA at 7 Tesla: initial results. *European Radiology*, 23(4):1059–1066, 2013.

[16] Lale Umutlu, Stephan Orzada, Sonja Kinner, Stefan Maderwald, Irina Brote, Andreas K. Bitz, Oliver Kraff, Susanne C. Ladd, Gerald Antoch, Mark E. Ladd, Harald H. Quick, and Thomas C. Lauenstein. Renal imaging at 7 Tesla: Preliminary results. *European Radiology*, 21(4):841–849, 2011.

[17] L. Umutlu, S. Maderwald, O. Kraff, S. Kinner, L. C. Schaefer, K. Wrede, G. Antoch, M. Forsting, M. E. Ladd, T. C. Lauenstein, and H. H. Quick. New look at renal vasculature: 7 tesla nonenhanced T1-weighted FLASH imaging. *Journal of Magnetic Resonance Imaging*, 36(3):714–721, 2012.

[18] Gregory J. Metzger, Edward J. Auerbach, Can Akgun, Josh Simonson, Xiaoming Bi, Kâmil Uğurbil, and Pierre François Van De Moortele. Dynamically applied B1+ shimming solutions for non-contrast enhanced renal angiography at 7.0 tesla. *Magnetic Resonance in Medicine*, 69(1):114–126, 2013.

[19] Anneloes de Boer, Johannes M. Hoogduin, Peter J. Blankestijn, Xiufeng Li, Peter R. Luijten, Gregory J. Metzger, Alexander J.E. Raaijmakers, Lale Umutlu, Fredy Visser, and Tim Leiner. 7 T renal MRI: challenges and promises. *Magnetic Resonance Materials in Physics, Biology and Medicine*, 29(3):417–433, 2016.

[20] Daniel P. Kaufman, Hajira Basit, and Stephen J. Knohl. *Physiology, Glomerular Filtration Rate (GFR)*. StatPearls Publishing, 2019.

[21] Rizk E.S. El-Galley and Thomas E. Keane. Embryology, anatomy, and surgical applications of the kidney and ureter. *Surgical Clinics of North America*, 80(1):381–401, 2000.

[22] Tahagod Mohamed and Maria Luisa S. Sequeira-Lopez. Development of the renal vasculature. *Seminars in Cell & Developmental Biology*, 91:132–146, 2019.

[23] Eva E. Vink, Rosa L. de Jager, and Peter J. Blankestijn. Sympathetic Hyperactivity in Chronic Kidney Disease: Pathophysiology and (New) Treatment Options. *Current Hypertension Reports*, 15(2):95–101, 2013.

[24] Pottumarthi V. Prasad, Jon Thacker, Lu-Ping Li, Muhammad Haque, Wei Li, Heather Koenigs, Ying Zhou, and Stuart M. Sprague. Multi-Parametric Evaluation of Chronic Kidney Disease by MRI: A Preliminary Cross-Sectional Study. *PLOS ONE*, 10(10):e0139661, 2015.

[25] M. et al. Tendera. ESC Guidelines on the diagnosis and treatment of peripheral artery diseases: Document covering atherosclerotic disease of extracranial carotid and vertebral, mesenteric, renal, upper and lower extremity arteries * The Task Force on the Diagnosis and Treat. *European Heart Journal*, 32(22):2851–2906, 2011.

[26] Su Wei Lim, Constantina Chrysochou, David L. Buckley, Philip A. Kalra, and Steven P. Sourbron. Prediction and assessment of responses to renal artery revascularization with dynamic contrast-enhanced magnetic resonance imaging: a pilot study. *American Journal of Physiology-Renal Physiology*, 305(5):F672–F678, 2013.

[27] Soumeya Brachemi and Guillaume Bollée. Renal biopsy practice: What is the gold standard? *World journal of nephrology*, 3(4):287–94, 2014.

[28] Yu-Ting Wang, Ying-Chun Li, Long-Lin Yin, Hong Pu, and Jia-Yuan Chen. Functional assessment of transplanted kidneys with magnetic resonance imaging. *World journal of radiology*, 7(10):343–9, 2015.

[29] Meiying Zeng, Yingsheng Cheng, and Binghui Zhao. Measurement of single-kidney glomerular filtration function from magnetic resonance perfusion renography. *European Journal of Radiology*, 84(8):1419–1423, 2015.

[30] Dong Jian, Yang Li, Su Tao, Yang XueDong, Chen Bin, Zhang Jue, Wang XiaoYing, and Jiang XueXiang. SCIENCE CHINA Quantitative assessment

of acute kidney injury by noninvasive arterial spin labeling perfusion MRI: a pilot study. 56(8):745–750, 2013.

[31] N.K. Ramamurthy, B. Moosavi, M.D.F. McInnes, T.A. Flood, and N. Schieda. Multiparametric MRI of solid renal masses: pearls and pitfalls. *Clinical Radiology*, 70(3):304–316, 2015.

[32] Dushyant Sahani, Aparna Mehta, Michael Blake, Srinivasa Prasad, Gordan Harris, and Sanjay Saini. Preoperative Hepatic Vascular Evaluation with CT and MR Angiography: Implica-tions for Surgery 1. *RadioGraphics*, 24:1367–1380, 2004.

[33] Peter L Choyke, Peter Yim, Hani Marcos, Vincent B Ho, Rakesh Mullick, Ronald M Summers, and P L Choyke. Hepatic MR Angiography: A Multiobserver Comparison of Visualization Methods M. Technical report, 2001.

[34] Plinio Rossi and Howard R. Gould. Angiography and Scanning in Liver Disease. *Radiology*, 96(3):553–562, 1970.

[35] Ivan Amat-Roldan, Annalisa Berzigotti, Rosa Gilabert, and Jaime Bosch. Assessment of hepatic vascular network connectivity with automated graph analysis of dynamic contrast-enhanced us to evaluate portal hypertension in patients with cirrhosis: A pilot study1. *Radiology*, 277(1):268–276, 2015.

[36] Christopher R. Davis, Lyn Jones, Rachel L. Tillett, Helen Richards, and Sherif M. Wilson. Predicting venous congestion before DIEP breast reconstruction by identifying atypical venous connections on preoperative CTA imaging. *Microsurgery*, 39(1):24–31, 2019.

[37] D. L. Lam, Lee M. Mitsumori, P. C. Neligan, B. H. Warren, W. P. Shuman, and T. J. Dubinsky. Pre-operative CT angiography and three-dimensional image post processing for deep inferior epigastric perforator flap breast reconstructive surgery. *British Journal of Radiology*, 85(1020), 2012.

[38] Wade Hedegard, Bethany Niell, Michelle Specht, Jonathan Winograd, and Elizabeth Rafferty. Breast reconstruction with a deep inferior epigastric perforator flap: Imaging appearances of the normal flap and common complications, 2013.

[39] Anabel M. Scaranelo, Bridgette Lord, Riham Eiada, and Stefan O. Hofer. Imaging approaches and findings in the reconstructed breast: A pictorial essay. *Canadian Association of Radiologists Journal*, 62(1):60–72, 2011.

[40] David Greenspun, Julie Vasile, Joshua L Levine, Heather Erhard, Rebecca Studinger, Victoria Chernyak, Tiffany Newman, Martin Prince, and Robert J Allen. Anatomic Imaging of Abdominal Perforator Flaps without Ionizing Radiation: Seeing Is Believing with Magnetic Resonance Imaging Angiography.

[41] Julie V Vasile and Joshua L Levine. Magnetic resonance angiography in perforator flap breast reconstruction. *Gland surgery*, 5(2):197–211, 2016.

[42] Tiffany M. Newman, Julie Vasile, Joshua L. Levine, David T. Greenspun, Robert J. Allen, Minh-Tam Chao, Priscilla A. Winchester, and Martin R. Prince. Perforator flap magnetic resonance angiography for reconstructive breast surgery: A review of 25 deep inferior epigastric and gluteal perforator artery flap patients. *Journal of Magnetic Resonance Imaging*, 31(5):1176–1184, 2010.

[43] Hyun J Jeong, Parmede Vakil, John J Sheehan, Sanjiv J Shah, Michael Cuttica, James C Carr, Timothy J Carroll, and Amir Davarpanah. Time Resolved MRA: Evaluation of Intrapulmonary Circulation Parameters in Pulmonary Arterial Hypertension.

[44] Parmede Vakil, James C Carr, and Timothy J Carroll. Combined Renal MRA and Perfusion with a Single Dose of Contrast. 2012.

[45] Aurang Z Khawaja, Deirdre B Cassidy, Julien Al Shakarchi, Damian G McGrogan, Nicholas G Inston, and Robert G Jones. Revisiting the risks

of MRI with Gadolinium based contrast agents—review of literature and guidelines. *Insights into Imaging*, 6(5):553–558, 2015.

[46] Jeffrey D Schlaudecker and Christopher R Bernheisel. Gadolinium-associated nephrogenic systemic fibrosis, 2009.

[47] Nicola Schieda, Jason I Blaichman, Andreu F Costa, Rafael Glikstein, Casey Hurrell, Matthew James, Pejman Jabehdar Maralani, Wael Shabana, An Tang, Anne Tsampalieros, Christian B Van Der Pol, and Swapnil Hiremath. Gadolinium-Based Contrast Agents in Kidney Disease: A Comprehensive Review and Clinical Practice Guideline Issued by the Canadian Association of Radiologists. *Canadian Journal of Kidney Health and Disease*, 5:1–17.

[48] Moshe Rogosnitzky and Stacy Branch. Gadolinium-based contrast agent toxicity: a review of known and proposed mechanisms, 2016.

[49] Constantina Chrysochou, David L. Buckley, Paul Dark, Alistair Cowie, and Philip A. Kalra. Gadolinium-enhanced magnetic resonance imaging for renovascular disease and nephrogenic systemic fibrosis: Critical review of the literature and UK experience. *Journal of Magnetic Resonance Imaging*, 29(4):887–894, 2009.

[50] Theresa Reiter, Oliver Ritter, Martin R Prince, Peter Nordbeck, Christoph Wanner, Eike Nagel, and Wolfgang Rudolf Bauer. Minimizing Risk of Nephrogenic systemic fibrosis in Cardiovascular Magnetic Resonance, 2012.

[51] Tomonori Kanda, Toshio Fukusato, Megumi Matsuda, Keiko Toyoda, Hiroshi Oba, Jun'ichi Kotoku, Takahiro Haruyama, Kazuhiro Kitajima, and Shigeru Furui. Gadolinium-based contrast agent accumulates in the brain even in subjects without severe renal dysfunction: Evaluation of autopsy brain specimens with inductively coupled plasma mass spectroscopy. *Radiology*, 276(1):228–232, 2015.

[52] J A Kaufman, D McCarter, S C Geller, and A C Waltman. Two-Dimensional Time-of-Flight Angiography of the Lower Extremities: Artifacts and Pitfalls. *AJR*, 171:129–135, 1998.

[53] Y. Wang, Y. Yu, D. Li, K. T. Bae, J. J. Brown, W. Lin, and E. M. Haacke. Artery and vein separation using susceptibility-dependent phase in contrast-enhanced MRA. *Journal of Magnetic Resonance Imaging*, 12(5):661–670, 2000.

[54] Maha Torabi, Keyanoosh Hosseinzadeh, and Michael P Federle. CT of Nonneoplastic Hepatic Vascular and Perfusion Disorders. *RadioGraphics*, 28:1967–1982, 2008.

[55] Cezary Grochowski and Grzegorz Staśkiewicz. Ultra high field TOF-MRA: A method to visualize small cerebral vessels. 7 T TOF-MRA sequence parameters on different MRI scanners – Literature review. *Neurologia i Neurochirurgia Polska*, 51(5):411–418, 2017.

[56] C. L. Dumoulin, S. P. Souza, and H. Feng. Multiecho magnetic resonance angiography. *Magnetic Resonance in Medicine*, 5(1):47–57, 1987.

[57] X. Zhang, E. T. Petersen, E. Ghariq, J. B. De Vis, A. G. Webb, W. M. Teeuwisse, J. Hendrikse, and M. J. P. van Osch. In vivo blood T1 measurements at 1.5 T, 3 T, and 7 T. *Magnetic Resonance in Medicine*, 70(4):1082–1086, 2013.

[58] R.J. Dury. *Understanding haemodynamics in neurodegenerative disease*. PhD thesis, University of Nottingham, 2018.

[59] Swati D Rane and John C Gore. Measurement of T1 of human arterial and venous blood at 7T. *Magnetic resonance imaging*, 31(3):477–9, 2013.

[60] Hanzhang Lu and Yulin Ge. Quantitative evaluation of oxygenation in venous vessels using T2-Relaxation-Under-Spin-Tagging MRI. *Magnetic resonance in medicine*, 60(2):357–63, 2008.

[61] M J Silvennoinen, C S Clingman, X Golay, R A Kauppinen, and P C M Van Zijl. Comparison of the Dependence of Blood R 2 and R * 2 on Oxygen Saturation at 1.5 and 4.7 Tesla. 2003.

[62] Malin Andersson, Karl Jägervall, Per Eriksson, Anders Persson, Göran Granerus, Chunliang Wang, and Örjan Smedby. How to measure renal artery stenosis - a retrospective comparison of morphological measurement approaches in relation to hemodynamic significance. *BMC Medical Imaging*, 15(1):42, 2015.

[63] Sayf Al-Katib, Monisha Shetty, Syed Mohammad A. Jafri, and Syed Mohammed H. Jafri. Radiologic Assessment of Native Renal Vasculature: A Multimodality Review. *Genitourinary imaging: RSNA*, 37(1):136, 2017.

[64] Gunther Schneider, Luigi Graziolo, and Sanjay Saini. *MRI of the Liver, 2nd Edition*. 2006.

[65] Hadrien A Dyvorne, Ashley Knight-Greenfield, Cecilia Besa, Nancy Cooper, Julio Garcia-Flores, Thomas D Schiano, and Bachir Taouli. Quantification of Hepatic Blood Flow Using a High-Resolution Phase-Contrast MRI Sequence with Compressed Sensing Acceleration.

[66] Sebastian Schmitter, Xiaoping Wu, Edward J. Auerbach, Gregor Adriany, Josef Pfeuffer, Michael Hamm, Kamil Ugurbil, and Pierre-François Van de Moortele. Seven-tesla time-of-flight angiography using a 16-channel parallel transmit system with power-constrained 3-dimensional spoke radiofrequency pulse design. *Invest Radiol.*, 49(5):314–325, 2014.

7 T_2^*-Weighted Body MRI

Work outlined in this chapter was presented at the 25th and 27th Annual Meetings of the International Society for Magnetic Resonance in Medicine in 2017 and 2019 respectively [1, 2].

7.1 Introduction

T_2^*-weighted images are obtained by using a multi-echo gradient echo sequence and require high uniformity of the magnetic field [3]. Multiecho gradient echo scans can be used extensively in the development of abdominal imaging applications at UHF due to the low flip angles, short TR and low SAR burden associated with the sequence. Establishing abdominal imaging at 7 T will also require re-optimisation of pulse sequences and imaging protocols that are used at lower magnetic field strengths. This can only be done with accurate knowledge of the relaxation times of abdominal tissues at 7 T. In particular, information gained about the T_2^* relaxation times is fundamental to setting optimal echo times in gradient echo sequences and for choosing the echo time that maximises Blood Oxygen Level Dependent (BOLD) contrast in renal imaging protocols [4]. In addition to providing useful information for pulse sequences, there is also interest in using T_2^* relaxation time measurements to evaluate physiological changes associated with abdominal diseases.

Chronic Liver Disease (CLD) is an increasingly important problem caused by multiple etiological factors such as alcohol abuse and hepatitis [5] creating a need to be able to monitor degrees of inflammation, fibrosis, hepatic iron overload and liver fat content non-invasively. Currently liver biopsy is the clinical tool used to evaluate these factors [6], however a liver biopsy only samples $1/50{,}000^{th}$ of the total liver volume and so is susceptible to sampling errors, variability in results and can also be painful for the patient both during and after the procedure [7, 8].

T_2^* measurements can be made at conventional magnetic field strengths to assess hepatic iron overload and liver fat fraction which are the most common metabolic causes of chronic liver disease [9, 10]. These results can also be complimented with T_1 measurements that can provide additional information about degrees of necroinflammation and fibrosis [11].

Renal function can also be assessed non-invasively with T_2^* measurements to probe oxygenation using BOLD MR imaging [12–14]. This technique non-invasively assesses oxygen content by exploiting the paramagnetic nature of deoxygenated blood, which has a shorter T_2^* compared to oxygenated blood. Therefore, BOLD MRI can be used to identify renal hypoxia which has a direct link to the progression of chronic kidney disease (CKD) [15]. Differences between cortical and medullary tissues have been shown to increase in measurements made at 3 T compared with 1.5 T. This is due to a higher sensitivity to deoxyhemoglobin at higher magnetic fields [16].

It is anticipated that applying these measurements in similar patient groups at 7 T will provide additional information linked to the underlying physiological changes associated with CLD and CKD. The increased SNR and CNR at elevated field strengths should improve the specificity and sensitivity of the T_2^* measurements compared to results obtained at 3 T. However, performing quantitative measurements in vivo at 7 T is challenging due to the increased inhomogeneity of the B_1^+ field, chemical shift and susceptibility artefacts [17].

The following chapter shows preliminary T_2^*-weighted imaging results in the liver, uterus and colon. Fat and water images obtained using a Philips mDixon acquisition are also presented. A short study in which quantitative measures of T_2^* in abdominal tissues in healthy subjects at 3 and 7 T is outlined and proposes the use of T_2^* maps to reduce the bias field effects at 7 T.

7.2 Methods

Scanning was performed on a 7 T Philips Achieva 8-channel multi-transmit system with an 8-channel fractionated dipole transmit coil (MRcoils, Zaltbommel, Netherlands). Phase-only RF shimming was performed interactively over localised regions of the liver and kidney using in-house software [18]. Volume B_0 shimming was applied across both the liver and kidneys.

7.2.1 T_2^*-Weighted Imaging

Multi-gradient echo scans were performed in healthy subjects with the imaging parameters listed in Table 7.1. Resulting images across all echoes were assessed for interesting physiological and anatomical findings.

Table 7.1: T_2^*-Weighted Imaging Parameters

Scan Parameter	Transverse Scan	Sagittal Scan
TR [ms]	31	138
TE_1 [ms]	4.76	1.6
ΔTE [ms]	7	7
Number of echoes/TR	4	3
Water Fat Shift [pixels]	1.185	0.852
In-Plane Resolution [mm^2]	0.75 x 0.75	1 x 1
Slice Thickness [mm]	2	2
Target Flip Angle [$^\circ$]	100	25
Number of Slices	12	8

7.2.2 Fat-Water Imaging

mDixon scans were used to obtain anatomical images at the beginning of the 7 T body imaging protocol to aid the planning of geometries for specific scans. Imaging parameters for the mDixon scan included; TR = 49 ms, water-fat shift = 0.454 pixels, acquired voxel size = 1.8 x 1.8 x 2 mm^3, flip angle = 12°,

number of slices = 12, scan duration = 20 s. Outputs generated were water, fat, in-phase and out-of-phase images. These were assessed for the feasibility of using the mDixon data for preliminary fat imaging and future fat quantification research.

7.2.3 T_2^* measurements at 3 and 7 T

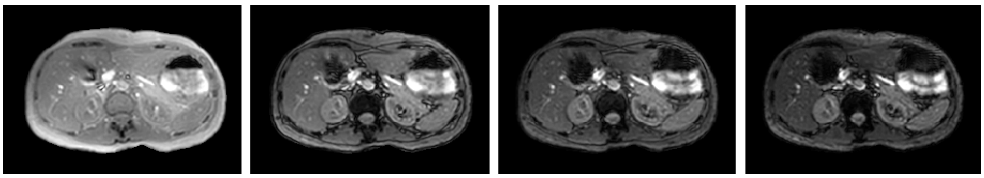
In this study, scanning was also performed on a 3 T Philips Ingenia system with dual transmit and both anterior and posterior receive coils. Volume B_0 shimming was also applied across both the liver and kidneys.

7.2.3.1 Image Acquisition

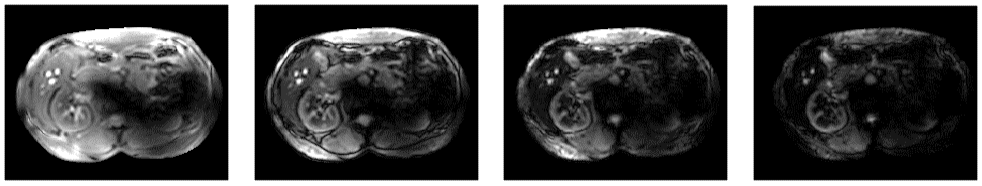
T_2^* values were measured in four healthy volunteers using a 2D multi-gradient echo imaging sequence with flyback gradients. Example images acquired at 3 and 7 T in one of the volunteers at different echo times are shown in Figure 7.1. Fat-water in-phase echo times were used to yield T_2^* values from a single transverse slice in the abdomen encompassing both the liver and kidneys in a single breath-hold. The scan was also repeated with out-of-phase echo times (see Table 7.2 for scan parameters used).

Table 7.2: Scan parameters for T_2^* measurements at both 3 and 7 T

Scan Parameters	3 T	7 T
Voxel volume [mm^3]	1.5 x 1.5 x 2	1.5 x 1.5 x 2
Water Fat Shift per voxel	0.174	0.357
TR (ms)	17.9	36.8
TE_1 (ms)	2.3	1.97
ΔTE (ms)	3/1.5 (IP/OP)	3/1.48 (IP/OP)
Flip Angle (°)	15	15
Field of View [mm^3]	450 x 450 x 2	450 x 450 x 2
No. of acquired echoes	12	12
Total scan time (s)	16.2	16.8



(a) 3 T



(b) 7 T

Figure 7.1: Multi-gradient echo images acquired at both field strengths: signal decay is faster at 7 T and the T_2^* contrast is greater - especially in the kidney where renal tissues (cortex and medulla) can be differentiated). However, B_1^+ inhomogeneity is severe in the 7 T images compared with the 3 T data.

7.2.3.2 Data Analysis

A pixel-wise weighted linear least squares regression was used to fit the log of the signal over multiple echoes to a function -$\frac{TE}{T_2^*}$ + log(S_0). A mono-exponential model was chosen as it was assumed that the fat fraction within the liver of the healthy subjects would be low. A correction for through-slice dephasing [19–21] was not possible as only a single slice was acquired.

To avoid noise bias, later echoes were eliminated that were above an empirical threshold value determined from using the signal in the final echo image as an estimate of the noise background. T_2^* voxel based maps were obtained and the mean and standard deviation in three different ROIs (5 x 5 voxels) within homogenous areas of the liver, kidney, and adipose and muscle tissues. T_2^* results for the liver were also compared for the different echo time acquisitions (in-phase versus out-of-phase). Lastly, the R_2^* relaxation rate for each abdominal tissue was calculated for each abdominal tissue at 3 and 7 T to best display the change between field strengths. All analysis was performed in Matlab R2018b.

7.3 Results and Discussion

7.3.1 T_2^*-Weighted Imaging

Figure 7.2 displays a T_2^*-weighted transverse image through the liver and left kidney. There is excellent contrast between the tissue and vessels in liver, as well as clear delineation of the renal cortex and medulla in the kidney. At this echo time, the signal from venous blood is heavily attenuated at 7 T, and so large veins appear as dark lines which can be seen in the posterior muscle tissue. There is a destructive B_1^+ band across the centre of the FOV, which was typical in each subject scanned at 7 T even after RF shimming had been applied (in this case in the region over the liver). Fixing the band of hypointensity will be crucial for engaging clinicians with 7 T body imaging. However, until sufficient advancements are made 7 T body images still have the potential to provide clinical insight in localised regions of interest.

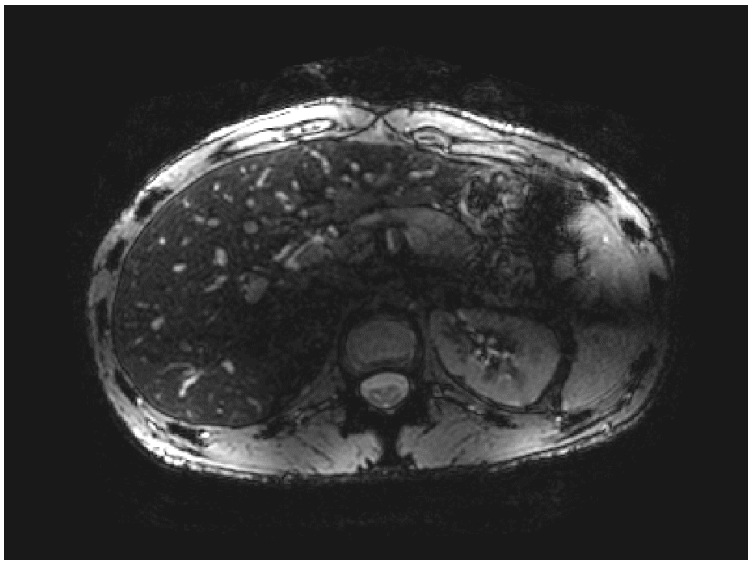
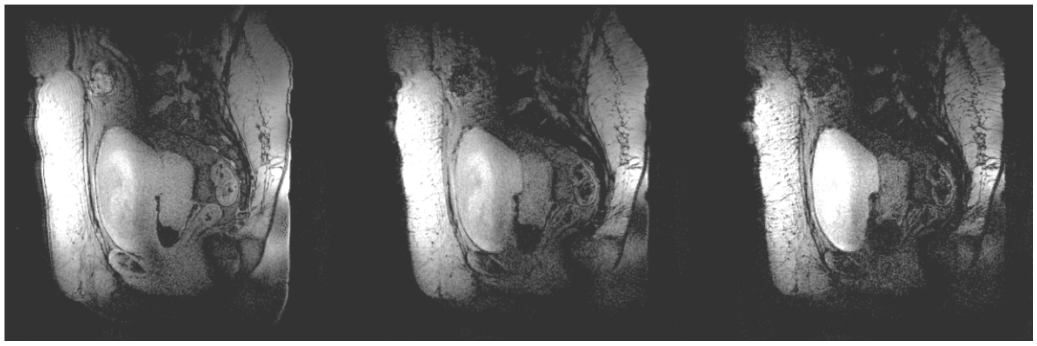


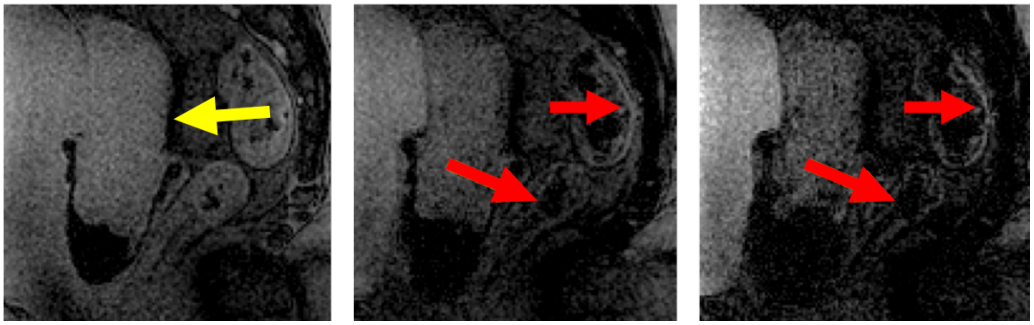
Figure 7.2: Example of T_2^*-weighted image of liver and left kidney.

Figure 7.3 displays sagittal T_2^*-weighted images acquired in a female volunteer. Figure 7.3 (a) demonstrates how the contrast between tissues changes with respect to echo time. Despite the relatively long ΔTE of 7 ms there is still

useful MR signal present in the later echoes. In this dataset there were two interesting findings which are presented in Figure 7.3 (b). The uterine cavity can be identified as well as colon wall. Determination of colon wall thickness can be used to diagnose irritable bowel syndrome and other colonic inflammation syndromes [22, 23]. Further high resolution imaging of the colon wall to resolve colon compartments relevant to the microbiome and structures visible in the contents of the colon are areas of interest [24].



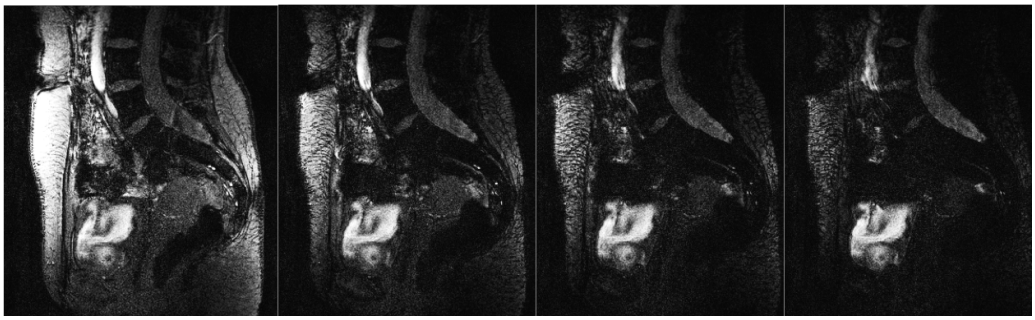
(a)



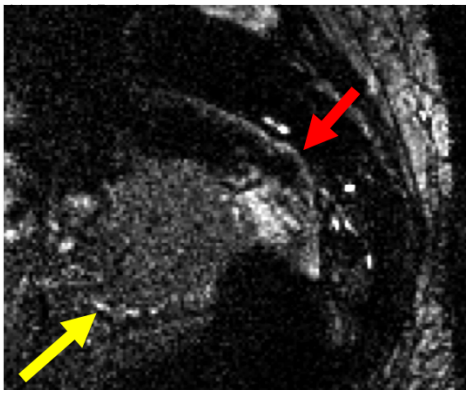
(b)

Figure 7.3: T_2^*-weighted images in first female volunteer: (a) varying the echo times adjusts the contrast, (b) at later echo times can successfully identify the uterine cavity (*yellow arrow*) and multiple sections of the colon wall (*red arrows*) on the 7 T images.

A second set of T_2^*-weighted images acquired in a second female volunteer are shown in Figure 7.4. This time, the contrast achieved is greater compared to the previous data and it is possible to resolve the vessels surrounding the uterine cavity as well as the colon wall.



(a)



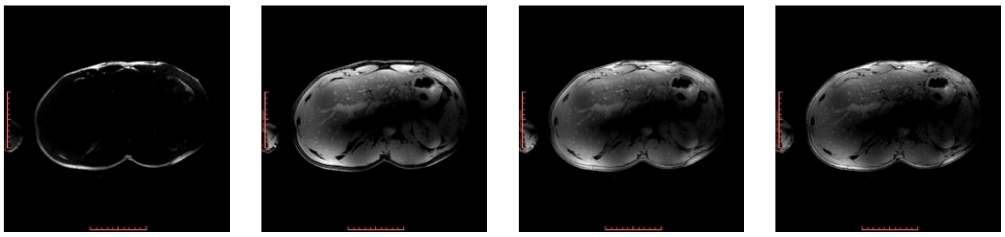
(b)

Figure 7.4: T_2^*-weighted images in second female volunteer: (a) varying the echo times adjusts the contrast, (b) vessels surrounding the uterine cavity (*yellow arrow*) and the colon wall (*red arrow*) were identified on 7 T images.

Bright signal from subcutaneous fat is problematic in all T_2^*-weighted images that are presented; this particularly affects the effectiveness of the windowing and presentation of the images. Future development of T_2^*-weighted imaging should include fat saturation methods that have been shown to be successful at 7 T such as; spectrally selective adiabatic inversion recovery (SPAIR) [25] and fat saturation [26].

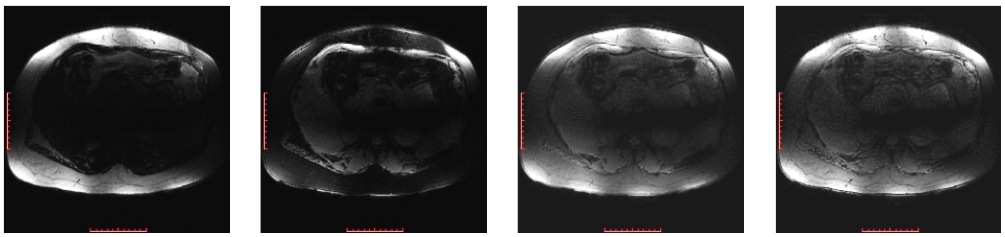
7.3.2 Fat-Water Imaging

Fat-water imaging using the Dixon technique (see Chapter 2) in the abdomen at 7 T has shown promising results. In Figure 7.5 fat, water, in-phase and out-of-phase images acquired in a male subject with a healthy weight BMI are shown in an axial slice through the liver. The quality of these images is not as high in larger subjects, as shown in Figure 7.6 where the same axial images are presented that were acquired in a female volunteer with BMI in the overweight range. Figure 7.6 (b) shows fat-water misregistration in the anterior subcutaneous fat. This misregistration normally corresponded to regions where there was phase wrapping in the B_0 maps and highlights the sensitivity of the Dixon technique to B_0 as well as B_1^+ inhomogeneities. Successful fat-water imaging in the abdomen at 7 T suggests that fat quantification measurements and the calculation of liver fat fraction maps is achievable.



(a) Fat (b) Water (c) In-Phase (d) Out-of-Phase

Figure 7.5: Fat-Water imaging: example 1. Subject with healthy weight BMI (in the range 18.5 - 24.9).

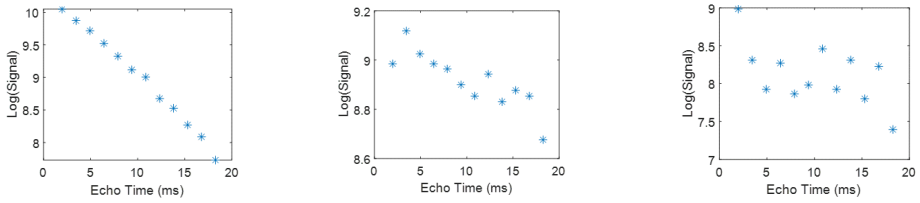


(a) Fat (b) Water (c) In-Phase (d) Out-of-Phase

Figure 7.6: Fat-Water imaging: example 2. Subject with BMI $>$ 25 in the overweight range.

7.3.3 T_2^* measurements at 3 and 7 T

Figure 7.7 demonstrates the stability of the decaying signal in different regions of the image with respect to the B_1^+ homogeneity. The signal behaviour from a voxel in a high intensity, homogenous area behaves linearly when the logarithm of the signal values is calculated. In a voxel where there is high B_1^+ inhomogeneity the linearity is not as obvious, and in a voxel from a low signal area (in the middle of the FOV in the centre of the body) the signal appears noisy and non-linear. The B_0 homogeneity in each of the voxels would also influence the linearity of the signal.

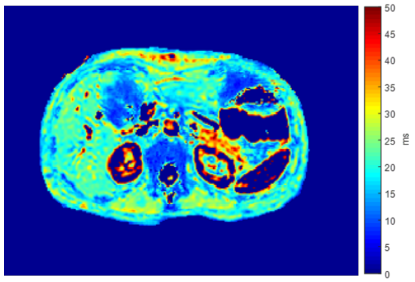


(a) Voxel from high, homogenous signal area. (b) Voxel from area with severe RF inhomogeneity. (c) Voxel from low signal area.

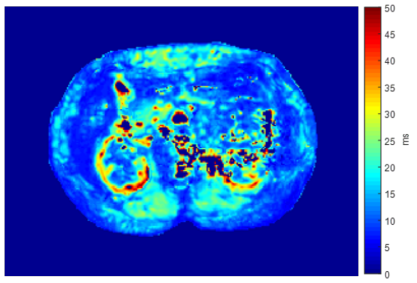
Figure 7.7: Logarithm plots of individual voxel signal versus echo time taken from regions of varying B_1^+ homogeneity.

Figure 7.8 shows T_2^* maps measured in approximately the same slice position in the same subject at (a) 3 T and (b) 7 T and show that the measured T_2^*

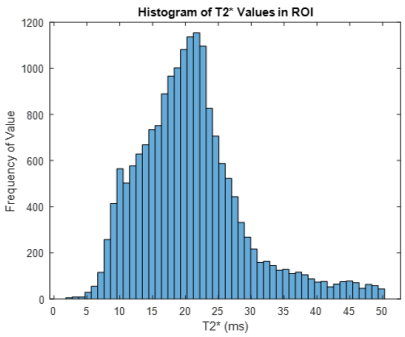
values decrease with increasing field strength. T_2^* values are shown to vary across the liver, cortical and medullary regions in the kidneys, fat and adipose tissues. Areas in the 7 T map were excluded due to low correlation between signal values over all echoes. This indicates that shorter echo times (ΔTE) may be required in future studies rather than restricting the echo times to produce in-phase fat and water signals. In the case of patients with high fat fractions a full bi-exponential fat-water signal model would be required for more accurate signal decay rates.



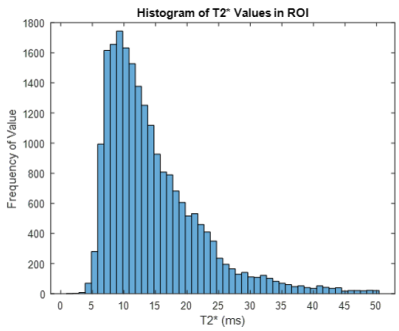
(a) T_2^* map based on 3 T image data.



(b) T_2^* map based on 7 T image data.



(c) Histogram of T_2^* values at 3 T.



(d) Histogram of T_2^* values at 7 T.

Figure 7.8: T_2^* maps (a) and (b) and associated histograms (c) and (d) of all T_2^* values in the FOV in one subject at 3 and 7 T respectively.

Results shown in Table 7.3 confirm the observations made from the T_2^* maps. Listed are T_2^* values at each field strength averaged over the four subjects, for each of the tissues of interest. The errors quoted are the standard deviations across all subjects. The standard deviations are greater in the 7 T data for

renal cortex, adipose and muscle tissues. The liver and renal medulla standard deviations are smaller in the 7 T data which is likely due to the better delineation of the liver tissue and vessels, and the renal medulla in the 7 T images when drawing the ROIs to measure T_2^*. 3 T results agreed with T_2^* values cited in the literature for cortical and medullary regions of the kidney [12], liver [27] and muscle [28]. However, values for adipose [29] did not match those previously found suggesting that the echo times might need to be adjusted to improve the characterisation of the adipose signal decay.

Table 7.3: Mean T_2^* values in abdominal tissues at 3 and 7 T

Field Strength (T)	**Liver**	**Kidney (Cortex)**	**Kidney (Medulla)**	**Adipose**	**Muscle**
3	21.5 $\pm$ 2.9	66.9 $\pm$ 4.3	35.4 $\pm$ 4.3	20.4 $\pm$ 2.9	26.8 $\pm$ 1.0
7	7.9 $\pm$ 0.5	31.3 $\pm$ 7.5	13.9 $\pm$ 2.9	15.6 $\pm$ 4.5	20.4 $\pm$ 1.7

Differences in mean T_2^* values between field strengths were statistically significant ($p<0.05$), apart for the adipose tissue. Some of the variance in the adipose results will be due to partial volume effects with vessels due to the coarse spatial resolution required to obtain this data in a breath hold at 7T. The average T_2^* in liver tissue at 7 T was 7.9 $\pm$ 0.5 ms and 8.6 $\pm$ 0.9 ms for in-phase and out-of-phase respectively which demonstrates the potential for fat quantification methods in the liver to measure fat fraction at 7 T.

Figure 7.9 shows the R_2^* relaxation rates for each abdominal tissue at 3 and 7 T. At 7 T there is an increased dispersion of R_2^* values across the different tissue types which is what generates the high T_2^* contrast in gradient echo sequences. Due to the higher relaxation rates at 7 T, there is potential to reduce the TE (and therefore the TR of the sequence) shortening the total acquisition time.

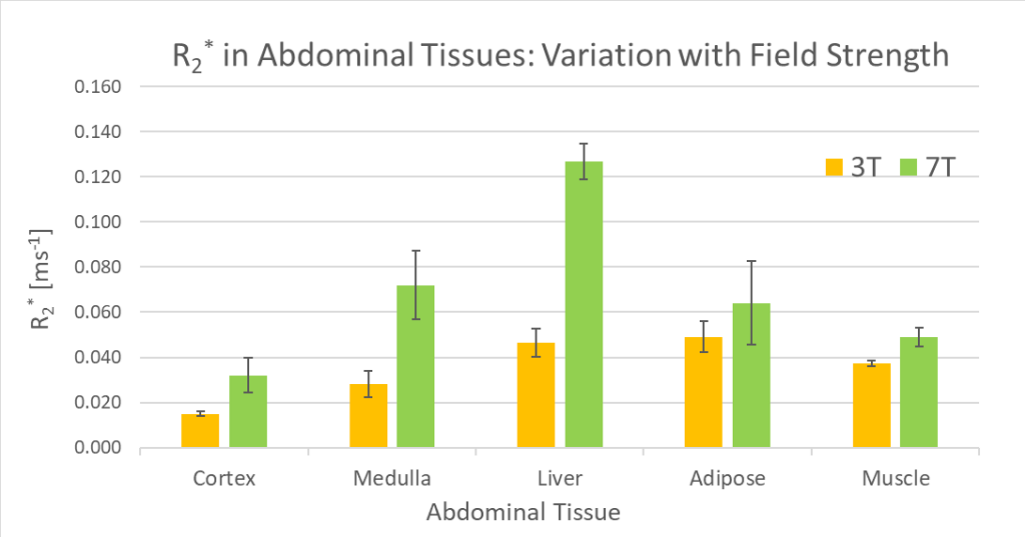
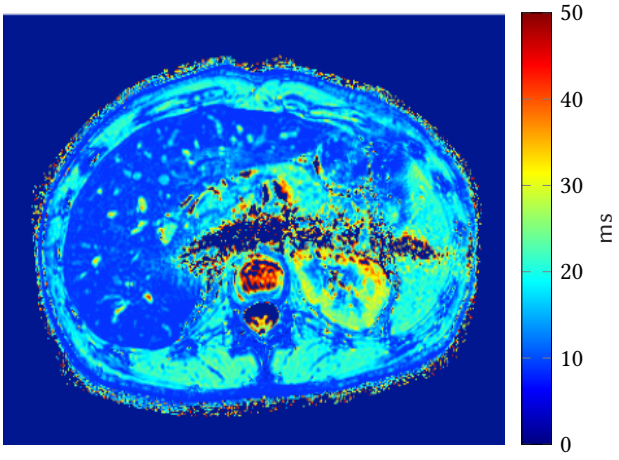


Figure 7.9: Variation of R_2^* relaxation rate with field strength in the liver, kidneys, adipose and muscle tissues.

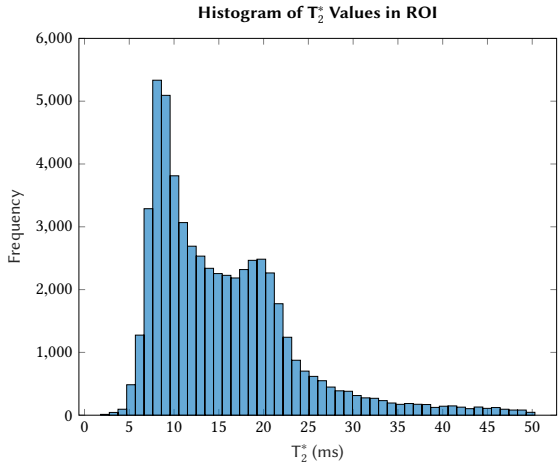
7.4 Conclusion

T_2^*-weighted images have been shown to provide excellent anatomical detail in vivo at 7 T and the adjustment of the echo time can improve the contrast between abdominal tissues, as observed in the colon wall in Figures 7.3 and 7.4. Measurements of T_2^* were made at 3 and 7 T in the liver, kidney, muscle and adipose tissues providing initial data for optimising pulse sequences in the body at UHF. Since this study was performed parallel imaging has been implemented on the 7 T system giving the potential to improve the resolution of the images acquired. A recently acquired dataset from which a T_2^* map was calculated is shown in Figure 7.10. The improved B_1^+ homogeneity in this dataset is also due to improvements made to the body coil, scanner and RF shimming software. The T_2^* map itself provides a bias field corrected T_2^*-weighted image and could provide robust, high contrast structural imaging information for 7 T body imaging applications, analogous to the MP2RAGE sequence which is used to produce bias field corrected T_1-weighted images routinely in the brain at UHF [30].

In conclusion, the results of this chapter present preliminary T_2^*-weighted images and quantitative measures. Further work will be required to confirm these findings in a larger group of subjects to assess intra- and inter- subject variability and to move from measures in healthy subjects to patient studies.



(a) T_2^* map.



(b) Histogram of T_2^* values across FOV.

Figure 7.10: Most recent quantitative T_2^* data at time of thesis submission.

References

[1] E. Doran, S. Bawden, P. Glover, A. Peters, S. Francis, R. Bowtell, and P. Gowland. T2* Measurements in Liver at 1.5, 3 and 7 T. *In Proc. ISMRM (Hawaii)*, (3193), 2017.

[2] Hannah G Williams, Emma Doran, Stephen Bawden, Christopher Mirfin, and Penny A Gowland. Liver mDixon at 7T. *In Proc. ISMRM (Montreal)*, (1801), 2019.

[3] Meng Yue Tang, Tian Wu Chen, Xiao Ming Zhang, and Xiao Hua Huang. GRE T2 *-Weighted MRI: Principles and Clinical Applications. 2014.

[4] Menno Pruijm, Iosif A Mendichovszky, Per Liss, Patricia Van der Niepen, Stephen C Textor, Lilach O Lerman, C T Paul Krediet, Anna Caroli, Michel Burnier, and Pottumarthi Vara Prasad. Renal blood oxygenation level-dependent magnetic resonance imaging to measure renal tissue oxygenation: a statement paper and systematic review. *Nephrology Dialysis Transplantation*, 33:ii22–ii28, 2018.

[5] Sam J. Thomson, Susan Westlake, Tony M. Rahman, Matthew L. Cowan, Azeem Majeed, J. Douglas Maxwell, and Jin Yong Kang. Chronic liver disease - An increasing problem: A study of hospital admission and mortality rates in England, 1979-2005, with particular reference to alcoholic liver disease. *Alcohol and Alcoholism*, 43(4):416–422, 2008.

[6] Don C. Rockey, Stephen H. Caldwell, Zachary D. Goodman, Rendon C. Nelson, and Alastair D. Smith. Liver biopsy. *Hepatology*, 49(3):1017–1044, 2009.

[7] Pierre Bedossa, Delphine Dargere, and Valerie Paradis. Sampling variability of liver fibrosis in chronic hepatitis C. *Hepatology*, 38(6):ajhep09022, 2003.

[8] Vlad Ratziu, Frédéric Charlotte, Agnès Heurtier, Sophie Gombert, Philippe Giral, Eric Bruckert, André Grimaldi, Frédérique Capron, and Thierry Poy-

nard. Sampling Variability of Liver Biopsy in Nonalcoholic Fatty Liver Disease. *Gastroenterology*, 128(7):1898–1906, 2005.

[9] Rajarshi Banerjee, Michael Pavlides, Elizabeth M. Tunnicliffe, Stefan K. Piechnik, Nikita Sarania, Rachel Philips, Jane D. Collier, Jonathan C. Booth, Jurgen E. Schneider, Lai Mun Wang, David W. Delaney, Ken A. Fleming, Matthew D. Robson, Eleanor Barnes, and Stefan Neubauer. Multiparametric magnetic resonance for the non-invasive diagnosis of liver disease. *Journal of Hepatology*, 60(1):69–77, 2014.

[10] Jens Peter Kühn, Diego Hernando, Alejandro Muñoz Del Rio, Matthias Evert, Stephan Kannengiesser, Henry Völzke, Birger Mensel, Ralf Puls, Norbert Hosten, and Scott B Reeder. Effect of multipeak spectral modeling of fat for liver iron and fat quantification: Correlation of biopsy with MR imaging results. *Radiology*, 265(1):133–142, 2012.

[11] B. Henninger, C. Kremser, S. Rauch, R. Eder, H. Zoller, A. Finkenstedt, H. J. Michaely, and M. Schocke. Evaluation of MR imaging with T1 and T2* mapping for the determination of hepatic iron overload. *European Radiology*, 22(11):2478–2486, 2012.

[12] Eleanor F. Cox, Charlotte E. Buchanan, Christopher R. Bradley, Benjamin Prestwich, Huda Mahmoud, Maarten Taal, Nicholas M. Selby, and Susan T. Francis. Multiparametric renal magnetic resonance imaging: Validation, interventions, and alterations in chronic kidney disease. *Frontiers in Physiology*, 8(SEP):1–15, 2017.

[13] Muhammad Haque, Tammy Franklin, and Pottumarthi Prasad. Renal oxygenation changes during water loading as evaluated by BOLD MRI: Effect of NOS inhibition. *Journal of Magnetic Resonance Imaging*, 33(4):898–901, 2011.

[14] S M Tumkur, A T Vu, L P Li, L Pierchala, and P V Prasad. Evaluation of intra-renal oxygenation during water diuresis: A time-resolved study using BOLD MRI. *Kidney Int*, 70(1):139–143, 2006.

[15] Qiangwei Fu, Sean P Colgan, and Carl Simon Shelley. Hypoxia: The force that drives chronic Kidney disease, 2016.

[16] Monika L. Gloviczki, Ahmed Saad, and Stephen C. Textor. Blood Oxygen Level Dependent Magnetic Resonance Imaging (BOLD MRI) analysis in Atherosclerotic Renal Artery Stenosis. *Current opinion in nephrology and hypertension*, 22(5):519, 2013.

[17] Mark E. Ladd, Peter Bachert, Martin Meyerspeer, Ewald Moser, Armin M. Nagel, David G. Norris, Sebastian Schmitter, Oliver Speck, Sina Straub, and Moritz Zaiss. Pros and cons of ultra-high-field MRI/MRS for human application. *Progress in Nuclear Magnetic Resonance Spectroscopy*, 109:1–50, 2018.

[18] Christopher Mirfin, Stephen Bawden, Paul Glover, Penny Gowland, and Richard Bowtell. RF Slice Shimming at 7T with Power Control on a Commercial 8-Channel Transmit Coil. *In Proc. ISMRM (Hawaii)*, (5204), 2017.

[19] Hannes Dahnke and T. Schaeffter. Limits of detection of SPIO at 3.0 T using T2* relaxometry. *Magnetic Resonance in Medicine*, 53(5):1202–1206, 2005.

[20] M.A. Fernandez-Seara and F.W. Wehrli. Postprocessing technique to correct for background gradients in image-basedR*2 measurements. *Magnetic Resonance in Medicine*, 44(3):358–366, 2000.

[21] Andrew M. Peters, Matthew J. Brookes, Frank G. Hoogenraad, Penny A. Gowland, Susan T. Francis, Peter G. Morris, and Richard Bowtell. T2* measurements in human brain at 1.5, 3 and 7 T. *Magnetic Resonance Imaging*, 25(6):748–753, 2007.

[22] Devkumar Mustafi, Xiaobing Fan, Urszula Dougherty, Marc Bissonnette, Gregory S Karczmar, Aytekin Oto, John Hart, Erica Markiewicz, and Marta Zamora. High-Resolution Magnetic Resonance Colonography and Dynamic

Contrast-Enhanced Magnetic Resonance Imaging in a Murine Model of Colitis. *Magn Reson Med*, 63(4):922–929, 2010.

[23] R E Naziroglu, Ca J Puylaert, Ja W Tielbeek, J Makanyanga, A Menys, and C Y Ponsioen. automatic bowel wall thickness measurements on MR enterography in patients with Crohn's disease Semi-automatic bowel wall thickness measurements on MR enterography in patients with Crohn's disease. *Br J Radiol*, 90, 2017.

[24] Gregory P Donaldson, S Melanie Lee, and Sarkis K Mazmanian. Gut biogeography of the bacterial microbiota, 2015.

[25] Ryan Brown, Pippa Storey, Christian Geppert, Kellyanne McGorty, Ana Paula Klautau Leite, James Babb, Daniel K. Sodickson, Graham C. Wiggins, and Linda Moy. Breast MRI at 7 Tesla with a bilateral coil and T1-weighted acquisition with robust fat suppression: Image evaluation and comparison with 3 Tesla. *European Radiology*, 23(11):2969–2978, 2013.

[26] Anja Laader, Karsten Beiderwellen, Oliver Kraff, Stefan Maderwald, Karsten Wrede, Mark E. Ladd, Thomas C. Lauenstein, Michael Forsting, Harald H. Quick, Kai Nassenstein, and Lale Umutlu. 1.5 versus 3 versus 7 Tesla in abdominal MRI: A comparative study. *PLoS ONE*, 12(11):1–18, 2017.

[27] Mustafa R. et al. Bashir. Hepatic R2* is more strongly associated with proton density fat fraction than histologic liver iron scores in patients with nonalcoholic fatty liver disease. *Journal of Magnetic Resonance Imaging*, 49(5):1456–1466, 2019.

[28] Sasan Partovi, Anja Carina Schulte, Bjoern Jacobi, Markus Klarhöfer, Alan B. Lumsden, Matthias Loebe, Mark G. Davies, Georg P. Noon, Christof Karmonik, Lisa Zipp, Georg Bongartz, and Deniz Bilecen. Blood oxygenation level-dependent (BOLD) MRI of human skeletal muscle at 1.5 and 3 T. *Journal of Magnetic Resonance Imaging*, 35(5):1227–1232, 2012.

[29] Declan P O'Regan, Martina F Callaghan, Marzena Wylezinska-Arridge, Julie Fitzpatrick, Rossi P Naoumova, Joseph V Hajnal, and Stephan A Schmitz. Liver fat content and T2*: simultaneous measurement by using breath-hold multiecho MR imaging at 3.0 T–Feasibility. *Radiology*, 247(2):550–557, 2008.

[30] José P. Marques, Tobias Kober, Gunnar Krueger, Wietske van der Zwaag, Pierre François Van de Moortele, and Rolf Gruetter. MP2RAGE, a self bias-field corrected sequence for improved segmentation and T1-mapping at high field. *NeuroImage*, 49(2):1271–1281, 2010.

8 Conclusion

This thesis is the result of a PhD research project dedicated to developing abdominal MRI at 7 T. The work presented has included the validation of a newly installed pTx system on a Philips 7 T Achieva MR system and 8 TX/32RX fractionated dipole body array. Different B_1^+ mapping methods were explored for use on pTx systems and techniques to overcome the large dynamic range of B_1^+ and inhomogeneities experienced in whole-body imaging at 7 T were developed and presented.

Efficient RF modelling methods were developed for the work in this thesis, including the validation of a prototype wire dipole coil model and a custom 10-gram averaging algorithm designed for optimised gridding in the underlying EM simulations. A pipeline for modelling local SAR in subject-specific models was implemented and used to study intra-subject variation in B_1^+ and local SAR with respect to respiratory motion; and inter- subject variability of maximum local SAR results in a small library of simplified subject-specific body models. The results concluded that it was not necessary to consider a respiration safety factor when determining the overall safety factor for a given simulation. With respect to inter-subject variability, the peak local SAR values varied across the library of models and RF transmit phase settings such that the current average power limits in place on the 7 T are operating within a 1.6 safety factor. The correlation of these measures with body fat composition and subject BMI was also presented but were inconclusive.

Future work should include expanding the library of body models to include representation of more subjects of different ages and body types. This will provide results that are more representative of a general population and will improve the confidence in peak local SAR measures and both intra- and inter- subject variability. The developed method for subject-specific body model creation, efficient RF modelling and local SAR computation outlined in Chapter 5 can be used to efficiently perform the required analysis when a large enough database of

modelled data can be created, then machine learning approaches to local SAR prediction in the body at 7 T can be considered.

A high-resolution multi-echo time-of-flight angiography protocol was developed in healthy volunteers. The multiple echoes were summed together to increase the SNR in the final images, improving details of the small peripheral vessels in different organs. Initially this protocol was applied to the intrarenal vessels; final angiograms were analysed for SNR, CNR and vessel radii. The vascular network in the liver was also imaged and a preliminary phase contrast angiography protocol was implemented to calculate the flow velocity results in the portal vein and hepatic artery. Finally, the TOF-MRA protocol was applied to the abdominal wall to image the DIEP vessels; these images showed similar image quality at 7 T that is achieved at 1.5 T with contrast-enhanced angiography. This work demonstrated the benefit of the increased intrinsic SNR at 7 T. Expected applications of this protocol for different patient groups were discussed. Future development concerning abdominal angiography at 7 T should include further optimisation of the PCA protocol for the liver and using the multiple echoes to fit for T_2^* values in the kidneys, liver and abdominal wall to visualise and evaluate venous changes and vessel viability in healthy subjects and patient groups.

Preliminary quantitative MRI was performed to collect measures of the T_2^* relaxation time in different abdominal tissues. These measures demonstrated increased contrast between the relaxation properties of abdominal tissue types at 7 T when compared to the same measures in the same subjects at 3 T. The 7 T results will inform future MR sequence optimisation in abdominal applications. Other interesting anatomical findings based on the T_2^* weighted images were presented, along with results from mDixon scans that output fat and water images demonstrating the potential for future fat quantification work at 7 T.

The B_1^+ inhomogeneity and available RF power from the scanner has been challenging throughout this research. Phase-only RF shimming proved sufficient for the in vivo work performed. Future quantitative work will require more robust methods to ensure the homogeneity of the B_1^+ across larger areas of interest.

This should include dynamic pTx methods that also address considerable inter-subject variability in abdominal anatomy. At 3 T, universal pulses designed using a machine learning approach have been shown to produce calibration-free RF pulses that reduce B_1^+ artefacts for routine, clinical, pTx imaging [1].

This will be important for organs such as the liver which is of great interest in other MR techniques such as spectroscopy, magnetisation transfer and chemical exchange saturation transfer imaging. These methods also benefit from higher magnetic field strengths and preliminary work applied as an extension to current 3 T protocols has shown promising results for further implementation at 7 T [2, 3]. These methods will both compliment the imaging protocols developed for this PhD and also rely on the B_1^+ mapping methods and local SAR considerations that were investigated.

References

[1] Raphaël Tomi-Tricot, Vincent Gras, Bertrand Thirion, Franck Mauconduit, Nicolas Boulant, Hamza Cherkaoui, Pierre Zerbib, Alexandre Vignaud, Alain Luciani, and Alexis Amadon. SmartPulse, a machine learning approach for calibration-free dynamic RF shimming: Preliminary study in a clinical environment. *Magnetic Resonance in Medicine*, 82(6):2016–2031, 2019.

[2] Andrew Carradus, Emma Doran, Olivier Mougin, Christopher Mirfin, Hans Hoogduin, Stephen Bawden, and Penny Gowland. The 7T z-spectrum from the human liver in-vivo: observing the effects of a meal. *In Proc. ISMRM (Montreal)*, (5006), 2019.

[3] Hannah G Williams, Emma Doran, Stephen Bawden, Christopher Mirfin, and Penny A Gowland. Liver mDixon at 7T. *In Proc. ISMRM (Montreal)*, (1801), 2019.

A Error Propagation in AFI Sequence

Using the laws of error propagation, the error in the full analytic solution for α can be expressed as:

$$\sigma_\alpha^2 = \left(\frac{d\alpha}{dTR_1}\right)^2 \sigma_{TR_1}^2 + \left(\frac{d\alpha}{dT_1}\right)^2 \sigma_{T_1}^2 + \left(\frac{d\alpha}{dr}\right)^2 \sigma_r^2 + \left(\frac{d\alpha}{dTR_2}\right)^2 \sigma_{TR_2}^2 \quad \text{(A.1)}$$

As TR_1, TR_2 and T_1 are technically known values, their associated errors are equal to zero. Therefore, the error in α can be simplified to the following expression:

$$\sigma_\alpha^2 = \left(\frac{d\alpha}{dr}\right)^2 \sigma_r^2 \quad \text{(A.2)}$$

Therefore, the error in α depends on the error in the ratio, r, of the two signal intensities. The error in r relates to the errors in the measurements of the two source images:

$$\sigma_r^2 = \left(\frac{dr}{dS_1}\right)^2 \sigma_{S_1}^2 + \left(\frac{dr}{dS_2}\right)^2 \sigma_{S_2}^2 \quad \text{(A.3)}$$

The error in each of the measured signal dependencies depends on the following expression:

$$\sigma_{S_1}^2 = \left(\frac{dS_1}{dM_{Z1}}\right)^2 \sigma_{M_{Z1}}^2 + \left(\frac{dS_1}{dTE}\right)^2 \sigma_{TE}^2 + \left(\frac{dS_1}{dT_2^*}\right)^2 \sigma_{T_2^*}^2 + \left(\frac{dS_1}{d\alpha}\right)^2 \sigma_\alpha^2 \quad \text{(A.4)}$$

As TE and T_2^* are known values, their associated errors are equal to zero. At this stage, the error in α can also be treated as zero since it is the reference value for the flip angle. The error in the measurement of S_1 is therefore:

$$\sigma^2_{S_1} = \left(\frac{dS_1}{dM_{Z1}}\right)^2 \sigma^2_{M_{Z1}} \tag{A.5}$$

Similarly, for S_2:

$$\sigma^2_{S_2} = \left(\frac{dS_2}{dM_{Z2}}\right)^2 \sigma^2_{M_{Z2}} \tag{A.6}$$

The error in the measured signal intensities depends on the error in the measurement of the amount of magnetisation present in each voxel:

$$\sigma^2_{M_{Z1}} = \left(\frac{dM_{Z1}}{dM_0}\right)^2 \sigma^2_{M_0} + \left(\frac{dM_{Z1}}{dTR_2}\right)^2 \sigma^2_{TR_2} + \left(\frac{dM_{Z1}}{dT_1}\right)^2 \sigma^2_{T_1} + \left(\frac{dM_{Z1}}{dTR_1}\right)^2 \sigma^2_{TR_1} + \left(\frac{dM_{Z1}}{d\alpha}\right)^2 \sigma^2_{\alpha} \tag{A.7}$$

As TR_1, TR_2, T_1 and α are known quantities, these associated errors can be set to zero and the previous expression can be simplified for the error in M_{Z1} as:

$$\sigma^2_{M_{Z1}} = \left(\frac{dM_{Z1}}{dM_0}\right)^2 \sigma^2_{M_0} \tag{A.8}$$

Similarly, for the error in M_{Z2}:

$$\sigma^2_{M_{Z2}} = \left(\frac{dM_{Z2}}{dM_0}\right)^2 \sigma^2_{M_0} \tag{A.9}$$

The error in the measured magnetisation depends on the error in the initial magnetisation present in the system, M_0. This error is dependent on the SNR of the system:

$$\sigma_{M_0} = \frac{M_0}{SNR} \tag{A.10}$$

Now the error terms are derived, the derivatives that they depend on can now be reached. The derivative of the magnetisation with respect to the initial magnetisation is as follows:

$$\left(\frac{dM_{Z1}}{dM_0}\right)^2 = \left(\frac{d}{dM_0}\left(M_0 \frac{1 - E_2 + (1 - E_1)E_2 cos\alpha}{1 - E_1 E_2 cos^2\alpha}\right)\right)^2 \tag{A.11}$$

$$\left(\frac{dM_{Z1}}{dM_0}\right)^2 = \left(\frac{1 - E_2 + (1 - E_1)E_2 cos\alpha}{1 - E_1 E_2 cos^2\alpha}\right)^2 \tag{A.12}$$

$$\left(\frac{dM_{Z2}}{dM_0}\right)^2 = \left(\frac{1 - E_1 + (1 - E_2)E_1 cos\alpha}{1 - E_1 E_2 cos^2\alpha}\right)^2 \tag{A.13}$$

Now, the error in the measured magnetisation can be expressed as:

$$\sigma^2_{M_{Z1}} = \left(\frac{1 - E_2 + (1 - E_1)E_2 cos\alpha}{1 - E_1 E_2 cos^2\alpha}\right)^2 \left(\frac{M_0}{SNR}\right)^2 \tag{A.14}$$

$$\sigma^2_{M_{Z2}} = \left(\frac{1 - E_1 + (1 - E_2)E_1 cos\alpha}{1 - E_1 E_2 cos^2\alpha}\right)^2 \left(\frac{M_0}{SNR}\right)^2 \tag{A.15}$$

The derivative of the measured signal intensities with respect to the measured magnetisation is:

$$\left(\frac{dS_1}{dM_{Z1}}\right)^2 = \left(\frac{d}{dM_{Z1}}\left(M_{Z1} e^{-\frac{-TE}{T_2^*}} sin\alpha\right)\right)^2 \tag{A.16}$$

$$\left(\frac{dS_1}{dM_{Z1}}\right)^2 = \left(e^{-\frac{-TE}{T_2^*}} sin\alpha\right)^2 \tag{A.17}$$

$$\left(\frac{dS_2}{dM_{Z2}}\right)^2 = \left(e^{-\frac{-TE}{T_2^*}} sin\alpha\right)^2 \tag{A.18}$$

Therefore, the error in each of the measured signal intensities can be expressed as:

$$\sigma_{S_1}^2 = \left(e^{-\frac{-TE}{T_2^*}} sin\alpha\right)^2 \left(\frac{1 - E_2 + (1 - E_1)E_2 cos\alpha}{1 - E_1 E_2 cos^2\alpha}\right)^2 \left(\frac{M_0}{SNR}\right)^2 \tag{A.19}$$

$$\sigma_{S_2}^2 = \left(e^{-\frac{-TE}{T_2^*}} sin\alpha\right)^2 \left(\frac{1 - E_1 + (1 - E_2)E_1 cos\alpha}{1 - E_1 E_2 cos^2\alpha}\right)^2 \left(\frac{M_0}{SNR}\right)^2 \tag{A.20}$$

The derivative of r with respect to the measured signal intensities is as follows:

$$\left(\frac{dr}{dS_1}\right)^2 = \left(\frac{d}{dS_1}\left(\frac{S_2}{S_1}\right)\right)^2 \tag{A.21}$$

$$\left(\frac{dr}{dS_1}\right)^2 = \left(\frac{-S_2}{S_1^2}\right)^2 \tag{A.22}$$

$$\left(\frac{dr}{dS_2}\right)^2 = \left(\frac{d}{dS_2}\left(\frac{S_2}{S_1}\right)\right)^2 \tag{A.23}$$

$$\left(\frac{dr}{dS_2}\right)^2 = \left(\frac{1}{S_1}\right)^2 \tag{A.24}$$

This sets the error in the ratio, r, of the two measured signal intensities to:

$$\sigma_r^2 = \left(\frac{-S_2}{S_1^2}\right)^2 \left(e^{-\frac{-TE}{T_2^*}} sin\alpha\right)^2 \left(\frac{1 - E_2 + (1 - E_1)E_2 cos\alpha}{1 - E_1 E_2 cos^2\alpha}\right)^2 \left(\frac{M_0}{SNR}\right)^2 + \left(\frac{1}{S_1}\right)^2 \left(e^{-\frac{-TE}{T_2^*}} sin\alpha\right)^2 \left(\frac{1 - E_1 + (1 - E_2)E_1 cos\alpha}{1 - E_1 E_2 cos^2\alpha}\right)^2 \left(\frac{M_0}{SNR}\right)^2 \tag{A.25}$$

The following fraction concerning the signal intensities can be expanded as shown:

$$\frac{S_2}{S_1^2} = \frac{\left(\frac{1-E_1+(1-E_2)E_1 cos\alpha}{1-E_1 E_2 cos^2\alpha}\right)}{M_0 \left(\frac{1-E_2+(1-E_1)E_2 cos\alpha}{1-E_1 E_2 cos^2\alpha}\right)^2 e^{-\frac{-TE}{T_2^*}} sin\alpha} \tag{A.26}$$

Similarly, for the second fraction involving the signal intensities:

$$\frac{1}{S_1} = \frac{1}{M_0 \left(\frac{1-E_2+(1-E_1)E_2 cos\alpha}{1-E_1 E_2 cos^2\alpha}\right) e^{-\frac{-TE}{T_2^*}} sin\alpha} \tag{A.27}$$

The following known derivative for the *arccos* function can be used to work out the derivative of α with respect to r.

$$\frac{d}{dx} arccos(u) = \frac{-1}{\sqrt{1 - u^2}} \frac{du}{dx} \tag{A.28}$$

$$\frac{d\alpha}{dr} = \frac{-1}{\sqrt{1-\left[\frac{1-E_1-r-rE_2}{E_1E_2-rE_1E_2+rE_2-E_1}\right]^2}} \times \left(\left(\frac{E_2-1}{E_1E_2-rE_1E_2+rE_2-E_1}\right) + \left(\frac{-(1-E_1-r+rE_2)(E_2-E_1E_2)}{(E_1E_2-rE_1E_2+rE_2-E_1)^2}\right)\right) \tag{A.29}$$

These expressions can then be substituted into the expression for the error in α:

$$\sigma_\alpha^2 = \left[\frac{-1}{\sqrt{1-\left[\frac{1-E_1-r-rE_2}{E_1E_2-rE_1E_2+rE_2-E_1}\right]^2}} \times \left(\left(\frac{E_2-1}{E_1E_2-rE_1E_2+rE_2-E_1}\right) + \left(\frac{-(1-E_1-r+rE_2)(E_2-E_1E_2)}{(E_1E_2-rE_1E_2+rE_2-E_1)^2}\right)\right)\right]^2 \times \left[\left(\frac{-S_2}{S_1^2}\right)^2 \left(e^{-\frac{-TE}{T_2^*}} sin\alpha\right)^2 \left(\frac{1-E_2+(1-E_1)E_2cos\alpha}{1-E_1E_2cos^2\alpha}\right)^2 \left(\frac{M_0}{SNR}\right)^2 + \left(\frac{1}{S_1}\right)^2 \left(e^{-\frac{-TE}{T_2^*}} sin\alpha\right)^2 \left(\frac{1-E_1+(1-E_2)E_1cos\alpha}{1-E_1E_2cos^2\alpha}\right)^2 \left(\frac{M_0}{SNR}\right)^2\right] \tag{A.30}$$

σ_α^2 was used to investigate the random error propagation in the AFI method and to calculate voxel based weighting factors for manipulation of B_1^+ mapping methods (see Chapter 4).